Laterally unconfined neutral or negative buoyancy inflow into a quiescent ambient over sloping bottom

Haoran SHI

École
polytechnique
fédérale
de Lausanne

2023

Acknowledgements

First and foremost, I want to thank my supervisor **David Andrew Barry**, who provided me this precious opportunity to join his lab. During the past four years, we had numerous valuable scientific discussions which guided me throughout my PhD journey. I express my gratitude to **Ulrich Lemmin** for his constructive suggestions on my research. I also thank **Koen Blanckaert** who proposed this interesting program. I still remember the winter of 2020 when I visited Laboratoire des Écoulements Géophysiques et Industriels (LEGI), during which time **Julien Chauchat** patiently taught me the numerical model step by step and **Cyrille Bonamy** helped me with the configuration settings. Without the kind help and guidance of **Eletta Negretti**, **Samuel Viboud** and **Thomas Valran** during my stay in LEGI for the laboratory experiments, the nice experimental results introduced in this thesis can never been achieved. All of the outputs of this thesis rely on dozens of discussions and rounds of review-revision with all of my five advisors: **David Andrew Barry, Ulrich Lemmin, Koen Blanckaert, Julien Chauchat** and **Eletta Negretti**. Words can't adequately express my gratitude to them. I also want to thank **Emil Hopfinger**. Although only twice, the fruitful discussions with him inspired me deeply.

I want to thank all of my colleagues and friends in ECOL: **Benjamin Graf**, **Congrong Yu**, **François Mettra**, **Frédéric Soulignac**, **Htet Kyi Wynn**, **Mahmood Ziabari**, **Mehrshad Foroughan**, **Rafael Reiss**, **Naifu Peng**, **Valentin Kindschi**, **Violaine Piton**, **Zhaoyang Luo** and three hot-pot girls **Qiaoli Wang**, **Shiyu Yan** and **Yuhong Shuai**. They kindly helped me in various aspects and made my four-year PhD journey colorful. I am also grateful for the administrative support from our secretaries: **Marie Sudki**, **Carol Ortega** and **Rima Bermuda**.

I would like to express my gratitude to my jury: **Andrea Rinaldo**, **Giovanni De Cesare**, **Wim Uijttewaal** and **Olivier Eiff**. **Giovanni De Cesare** was also a jury member of my candidacy exam who witnessed my PhD study from the beginning to the end. I also thank **Alexis Berne** and my mentor **Dusan Licina** for their kind help during my PhD.

Lastly, I want to send my deepest love to my families in China. Their love and care helped me overcome all the difficulties. I sincerely thank my girlfriend who is now my wife: **Huazi Zhu**, who supported me in spirit throughout this challenging journey of PhD.

I dedicate this thesis to all my beloved families and friends!

Abstract

This work studies the nearshore hydrodynamics of a shallow turbulent flow entering a laterally unconfined quiescent ambient with a sloping bottom boundary. Examples of such flow are neutrally buoyant ebb tidal jets and hyperpycnal river plumes entering open waters.

Laboratory experiments were applied in a shallow open channel connected to a sloping bottom tank. A three-dimensional (3D) CFD model based on large eddy simulation is established and validated using the experimental data. The validated model not only provides detailed 3D flow field information but also extends the experimentally studied range of initial and boundary conditions.

With neutral buoyancy, turbulent inflow is classified as a tidal jet, whose transverse velocity profile gradually transforms from a top-hat profile into a Gaussian distribution. Bounded by a sloping boundary, the jet extends vertically, resulting in an abrupt decrease in centerline velocity near the channel mouth. Under the combined effects of the vertical extension and lateral entrainment, the jet undergoes lateral contraction before spreading laterally. Shear layers are generated at both sides of the jet, converging towards the centerline with increasing offshore distance. The momentum thickness of the shear layers increases longitudinally until the shear layers from both sides meet and merge at the centerline. Kelvin Helmholtz-type coherent structures (KHCS) develop inside the shear layers, contributing remarkably to turbulent kinetic energy production and momentum transfer (70%–80%). The KHCS enlarge with the growth of the shear layers and extend vertically as the jet spreads in the vertical direction. Nevertheless, the Strouhal number of KHCS remains almost constant (~0.079). After the shear layers from both sides meet at the centerline, the jet undergoes a "flag-like" flapping motion.

With negative buoyancy, the turbulent inflow is classified as a hyperpycnal plume. Examples are cool and sediment-laden river flowing into open water. Under the influence of negative buoyancy, the plume converges and forms a triangular shape on the water surface but spreads laterally near the bottom boundary. At a certain distance

(x_p), the plume is totally submerged and plunges towards the bottom boundary. The discharge of the plume increases during plunging as a result of ambient water entrainment. In a fixed geometry, the mean flow field is controlled by the initial densimetric Froude number ($Fr_{d\text{-}0}$). The x_p value and entrainment coefficient (E, quantifying the entrained ambient water) increase with the $Fr_{d\text{-}0}$ value. The experimental and numerical results are comparable to observations at the Rhône River mouth (Lake Geneva) and field measurements at other similar river mouths in terms of x_p and E values. Shear layers are observed at the two sides of the plume, whose lateral growth is suppressed significantly by negative buoyancy. In a 3D view, the plume-ambient interface is a hooked face under the water surface, and thus the direction of shear-induced vorticity changes with depth, resulting in the unique 3D shapes of KHCS. The Strouhal number of KHCS decreases with increasing local Richardson number, and a coherent region containing KHCS forms and considerably contributes to the total mixing (approximately 40%) between the plume and ambient water in the nearshore region.

Keywords

Résumé

Cette étude a pour thème l'hydrodynamique côtière d'un écoulement turbulent peu profond pénétrant dans un environnement calme et ouvert latéralement sur un fond en pente. Des exemples de ce type d'écoulements peuvent être des jets de jusant (marée descendante) à flottabilité neutre ainsi que des panaches fluviaux hyperpycnaux faisant leur entrée dans des eaux libres.

Un chenal peu profond relié à un réservoir doté d'un fond en pente est employé dans l'optique d'étudier de manière expérimentale l'hydrodynamique côtière. Un modèle en trois dimensions (3D) MFN (mécanique des fluides numérique) se fondant sur la Simulation des grandes structures de la turbulence est créé et validé par le biais des données expérimentales. Le modèle approuvé ne fournit pas seulement des informations plus précises sur les champs d'écoulement 3D, il permet également d'étendre la portée de l'étude à d'autres gammes de conditions initiales et aux bords.

Caractérisé par une flottabilité neutre, l'afflux turbulent peut être considéré comme un jet dont le profil de vitesse transversale évolue progressivement d'une courbe en forme de « chapeau haut-de-forme » à une distribution gaussienne. Compte tenu de la présence d'un fond en pente, le jet s'étire verticalement, résultant en un brusque déclin de la vitesse de l'axe près de l'embouchure du chenal. Sous l'effet conjugué de l'étirement vertical et de l'entraînement horizontal, le jet est soumis à un resserrement latéral avant de se diffuser sur les côtés. Des zones de cisaillement apparaissent aux deux extrémités du jet, celles-ci convergent en direction de l'axe au fur et à mesure de l'augmentation de la distance d'éloignement du rivage. La dynamique de l'épaisseur des zones de cisaillement augmente longitudinalement jusqu'à ce que ces dernières provenant des deux côtés se rencontrent et fusionnent au niveau de l'axe. Des structures cohérentes de type Kelvin-Helmholtz (en anglais KHCS) voient le jour au sein des zones de cisaillement, contribuant ainsi de façon importante à la production d'énergie cinétique turbulente et au transfert de quantité de mouvement (70 ~ 80 %). Ces structures KHCS s'agrandissent proportionnellement à la croissance des zones de cisaillement et

s'étendent dans la même direction que le jet, à savoir verticalement. Néanmoins, le nombre de Strouhal des structures KHCS demeure quasiment constant (~0.079). Après la rencontre au niveau de l'axe des zones de cisaillement des deux extrémités, le jet subit un mouvement de battement s'apparentant à un « drapeau ».

Doté d'une flottabilité négative, l'afflux turbulent entre dans la classification d'un panache hyperpycnal. Parmi les exemples, nous pouvons citer des rivières plus froides et/ou chargées de sédiments s'écoulant dans des eaux libres. En raison de l'influence exercée par la flottabilité négative, le panache converge en une forme triangulaire à la surface de l'eau mais se diffuse de manière latérale à proximité du fond en pente. Après une certaine distance (x_p), le panache se retrouve entièrement submergé et plonge en direction du fond. L'écoulement du panache augmente au cours du processus de plongée à la suite de l'entraînement de l'eau ambiante. Ayant pour caractéristique une géométrie fixe, ce processus de plongée est régi par le nombre de Froude densimétrique initiale (Fr_{d-0}). Aussi bien la variable x_p que le coefficient d'entraînement (E, quantifiant la quantité d'eau ambiante entraînée) augmentent avec Fr_{d-0}. Les résultats numériques et expérimentaux jouissent d'une comparaison favorable, concernant x_p et E, avec les observations effectuées à l'embouchure du Rhône (Léman) ainsi qu'avec les relevés de terrain ayant eu lieu aux embouchures d'autres rivières similaires. Des zones de cisaillement sont également observées aux deux extrémités du panache dont la croissance latérale se voit significativement entravée par la flottabilité négative. Au sein d'une vue en 3D, l'interface entre le panache et l'eau ambiante présente une face recourbée sous la surface de l'eau et, de ce fait, la direction du tourbillonnement induit par le cisaillement varie en fonction de la profondeur, cela résulte en une forme 3D unique des structures KHCS. Le nombre de Strouhal relatif à ces dernières diminue avec l'augmentation du nombre de Richardson local. Une « région cohérente » est formée par les structures KHCS ce qui contribue fortement au mélange total (environ 40%) entre le panache et l'eau ambiante dans le secteur côtier.

Mots clés

Écoulement turbulent peu profond, flottabilité neutre ou négative, environnement récepteur ouvert latéralement, lit en pente, zones de cisaillement, structures cohérentes de type Kelvin-Helmholtz, processus de plongée.

Contents

Chapter 1 Introduction

1.1 Neutrally buoyant tidal jet

Ebb tides flowing away from harbors and in straits can be classified as a neutrally buoyant turbulent flow entering into an open receiving water, namely, a tidal jet (Cohen, 2012; Jiménez-Robles et al., 2017; Ortega-Sánchez et al., 2008; Rowland et al., 2009). Tidal inlets are usually shallow with a large aspect ratio ($B_0/H_0 >> 1$, B_0 and H_0 denote the width and depth, respectively) and the flow is bounded by a solid bottom boundary and an upper free surface (Cohen, 2012; Rowland et al., 2009). An example of such tidal flow is shown in Fig. 1.1, which presents the ebb tide flowing from Harimanada (Seto Inland sea) toward Kii Channel through the Naruto Strait, Japan (Onishi, 1984). Similar flow conditions have been reported worldwide in the literature (Broekema et al., 2018; Cohen, 2012; Fujiwara et al., 1994; Hearn et al., 1985; Old & Vennell, 2001; Spiers et al., 2009; Vennell, 2006). An ebb tide brings various natural and artificial materials (e.g., sediment, nutrition, pollution and fish larvae) into the ocean (Joshi, 1982) and thus, has important influence on port water depth (Buonaiuto & Bokuniewicz, 2008; Spiers et al., 2009), plankton growth (Haigh et al., 1992; Wolanski et al., 1988) and fish recruitment (Brown et al., 2000; Churchill et al., 1999).

Figure 1.1 Satellite image of the ebb tide flowing through Naruto Strait in Japan taken in January 2015 from Google Earth.

In the literature, tidal jets are usually studied with a horizontal solid bottom boundary (Cohen, 2012; Deo et al., 2007, 2008; Dracos et al., 1992; Giger et al., 1991; Jirka, 2001;

Rowland et al., 2009). Assuming homogeneity in the vertical direction, the jet behavior can be considered two-dimensional (2D) and described by 2D theories, and thus classified as a plane jet (e.g., Cohen, 2012; Pope, 2000). With increasing offshore distance, the transverse profile of the longitudinal jet velocity gradually transforms from a top-hat profile in the flow establishment zone into a Gaussian profile in the established flow zone (Pope, 2000). Thereafter, the jet becomes self-similar, and the centerline velocity starts to decrease (Cohen, 2012; Deo et al., 2007; Heskestad, 1965; Pope, 2000; Rowland et al., 2009). Ambient water is entrained at two sides of the jet, continuously increasing the jet width (Cohen, 2012; Pope, 2000; Rowland et al., 2009). Inside the established flow zone, the jet may undergo a "flag-like" jet flapping motion (i.e., meandering), depending on the local aspect ratio and bottom friction (Canestrelli et al., 2014; Jirka, 1994; Socolofsky & Jirka, 2004).

However, in the oceans, a tidal jet usually flows over a sloping bottom, rather than a horizontal bottom (Broekema et al., 2018; Jiménez-Robles et al., 2016; Ortega-Sánchez et al., 2008). The global distribution of nearshore slopes was reported by Athanasiou et al. (2019), showing that 85% of nearshore slopes range from 0° to 8°. Different from the plane jet flowing over a horizontal bottom, which is completely confined in the vertical direction, with a sloping bottom boundary, the jet spreads vertically as it transports longitudinally. Analytical models describing the development of jets considering the sloping bottom were proposed by Özsoy and Ünlüata (1982) and Ortega-Sánchez et al. (2008) based on depth-average Navier–Stokes equations. The analytical models suggested that the jet spreads vertically and the width of the jet first decreases and then increases. Such behavior was observed by a numerical simulation with a 2.2° sloping bottom carried out by Jiménez-Robles et al. (2016).

Although analytical and numerical models are available for a tidal jet flowing over a sloping bottom, they have yet to be validated by experiments. Chapter 2 of this thesis reports the first laboratory experiment of such a flow configuration with a $\beta = 8°$ sloping bottom boundary. The experimental results were used to validate a CFD model based on Large Eddy Simulation using OpenFOAM. With the experimental and validated

numerical data, the development of the jet and its turbulence characteristics (i.e., turbulent kinetic energy, eddy viscosity and anisotropy) under the influence of the sloping bottom were studied, and the limitations of the existing analytical models were discussed.

1.2 Plunging process of a hyperpycnal plume

The situation becomes more complicated when the negative buoyancy is introduced. Such a flow is named as a hyperpycnal plume, describing a turbulent flow with larger density flowing into a quiescent ambient. The hyperpycnal plume is representative for a hyperpycnal river flowing into lakes, reservoirs, or oceans. The excess density of the river plume, compared with the receiving ambient water, may come from a lower temperature (Hogg et al., 2013; Spigel et al., 2005), higher sediment concentration (De Cesare et al., 2001; Kostaschuk et al., 2018; Wright et al., 1986), or both (Best et al., 2005). If the excess density arises mainly from the suspended sediment, then the hyperpycnal plume is also called a turbidity current (He, Xu, et al., 2022; Lamb et al., 2010; Pohl et al., 2020; Schuch et al., 2018; Wright et al., 1986). The hyperpycnal river plumes are an important source of sediment, contaminants, and nutrients into the receiving water body (De Cesare et al., 2001; Turner et al., 1990; Lamb et al., 2010; Pohl et al., 2020; Pope et al., 2022). They are capable of shaping the nearshore geomorphology heavily by means of deposition or erosion (Baas et al., 2004; Curray et al., 2002; Meiburg & Kneller, 2010; Parker et al., 1986; Wells & Dorrell, 2021). Their deposits are also suggested to be a reliable record of river flood dynamics (Lamb & Mohrig, 2009; Mulder et al., 2003). A recent study has also suggested that the hyperpycnal plumes potentially distribute and bury a large amount of microplastics in seafloor sediments (Pohl et al., 2020).

A sloping bottom boundary of the receiving water body is usually applied in studies of hyperpycnal plumes (e.g., Akiyama & Stefan, 1984; Arita & Nakai, 2008; Lamb et al., 2010; Lee & Yu, 1997). The hyperpycnal plume pushes and displaces ambient water in front of it after it enters the receiving water body, during which the momentum of the

plume is gradually lost. A balance between the momentum and the baroclinic pressure from negative buoyancy is reached at a certain distance (i.e., the plunge location $x = x_p$), where the plume starts to plunge toward the bottom (e.g., Figure 6.18 of Fischer et al. (1979)). After the plunging process, the hyperpycnal plume transforms into an underflow at distance x_{ud} from the river mouth. The underflow progresses along the bottom boundary (e.g., Kostaschuk et al., 2018) and may detach from the bottom at the level of neutral density (e.g., Cortés et al., 2014; Piton et al., 2022).

Experimental and numerical studies of the hyperpycnal plume plunging process were usually performed in a laterally confined channel (An & Li, 2010; Arita & Nakai, 2008; Fleenor, 2001; Lamb et al., 2010; Lee & Yu, 1997; Schuch et al., 2018; Singh & Shah, 1971; Zhang et al., 2023). Under such a configuration, the hyperpycnal plume is restrained to spread laterally and can be assumed as uniform in the transversal direction. On this basis, 2D plunging theories were proposed to describe the plunging process based on the momentum equations with respect to selected control volumes (see Akiyama & Stefan, 1984 and Parker & Toniolo, 2007). A conceptual sketch of the 2D plunging hyperpycnal plume is presented in Fig. 1.2. The plunging is expected to occur when the densimetric Froude number (Fr_d) decreases from its initial value at the river mouth (Fr_{d-0}) to a critical value (Fr_{d-p}) at the plunge location ($x = x_p$ with a local water depth of H_p, Fig. 1.2). Fr_{d-p} was proposed to equal to 0.5 according to the theory of Parker & Toniolo (2007) as described by Lamb et al. (2010). The densimetric Froude number is a combined parameter of the Froude number (Fr) and density difference, as follows:

$$Fr_d = \frac{Fr}{\sqrt{R_d}} = \frac{U}{\sqrt{gH\left(\rho_d - \rho_a\right)/\rho_a}} \tag{1.1}$$

where $R_d = (\rho_d - \rho_a)/\rho_a$ is the relative density difference, ρ_d denotes the depth-averaged density of the hyperpycnal plume, ρ_a is the ambient water density, and U represents the depth-averaged velocity. Two different types of plunging plume were observed by Arita and Nakai (2008), depending on different inflow conditions. With a large initial densimetric Froude number ($Fr_{d-0} > 1.4$) and large bottom slope ($\beta > 7°$), a low-velocity

(sometimes even recirculated) region was observed inside the plunging plume near the bottom boundary. By contrast, with small Fr_{d-0} and β, the plunging plume completely attaches the bottom boundary. The discharge of the plume increases during the plunging process due to the entrainment of ambient water. A plunging entrainment coefficient was proposed to describe the increased discharge during the plunging process, as follows:

$$E = \frac{Q_{ud} - Q_0}{Q_0} \tag{1.2}$$

where Q_0 and Q_{ud} are the discharges at the river mouth and after the plunging process ($x = x_{ud}$), respectively. The entrainment coefficient was reported to range between 0.02 and 0.2 in previous experiments (Farrell and Stefan, 1988; Fleenor, 2001; Lee and Yu, 1997). The laterally confined configuration described in this paragraph is suitable for hyperpycnal plumes in river-dammed reservoirs, which are laterally confined by the river valley. Examples are the Whiskeytown Reservoir in US (Fleenor, 2001), Beznar Reservoir in Spain (Cortés et al., 2014), and Xiaolangdi Reservoir in China (Kostaschuk et al., 2018).
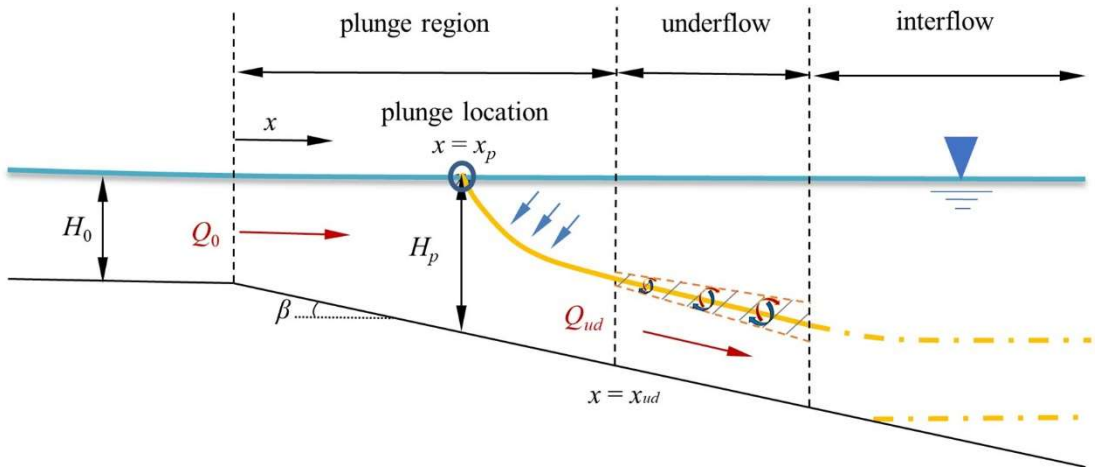

Figure 1.2 Conceptual sketch of 2D hyperpycnal plume plunging. The boundary of the hyperpycnal plume is indicated by the solid and dash-dotted orange lines. The red arrows denote the flow direction of the hyperpycnal plume. The blue arrows present entrainment of ambient water during plunging. The shadowed area bounded by dashed lines presents the shear

layer in the underflow region. Pairs of red and blue arrows denote the Kelvin Helmholtz-type coherent structures (KHCS) in the shear layer.

By contrast, when the receiving water body refers to open waters (e.g., lake or ocean), the hyperpycnal plume is free to spread laterally when it transports longitudinally. Laterally spreading hyperpycnal currents were studied experimentally or numerically by De Cesare and Schleiss (1999), Baas et al. (2004), Georgoulas et al. (2010), and Dai and Huang (2020). However, these studies focus on the underflow rather than the plunging process. The only experimental study on laterally unconfined hyperpycnal plume plunging over a sloping bottom boundary was performed by Hauenstein and Dracos (1984) who also developed an integral model to describe the flow development (e.g., lateral spreading, entrainment and velocity variation). However, only qualitative dye-visualization was conducted in their experiments without detailed flow measurement data. Besides, with a horizontal bottom boundary, Johnson, Ellis, et al. (1987), Johnson et al. (1989), Johnson, Farrell, et al. (1987), and Johnson et al. (1989) performed experimental studies on the plunging process with 3°–90° diverging receiving channels. They concluded that with a diverging angle > 25°, the hyperpycnal plume would detach from the side walls, and thus the receiving channel can be considered an open water. Based on the assumption that the receiving water body has a horizontal bottom, an analytical model was proposed by Hogg et al. (2013) to estimate the plunge location of Canale Italsider entering the Lake Iseo (Italy). The estimated plunge location was more than one time further from the river mouth than their field observations (120 m vs. 50 m). Such an overestimation can be appropriately explained by the unsuitable assumption of horizontal bottom because the measured bathymetry data present a 4.6° sloping bottom in Canale Italsider mouth. Despite this limitation, Hogg et al. (2013)'s model provides a conceptual idea of the laterally unconfined plunging process: The plume slumps laterally under the influence of negative buoyancy when it transports longitudinally and its cross-sections behave similar to a lock-exchange density current (refer to Fig. 3 of Hogg et al. (2013)). As a result of the lateral falling, the plume spreads laterally near the bottom but converges near the water surface (Fig. 1.3), forming a triangular shape on the surface. Such a surface triangular pattern

is illustrated in Fig. 1.4, presenting a satellite image of the hyperpycnal Rhône River plunging into the Lake Geneva, Switzerland. The vertex of the surface triangle represents the plunge location. The unconfined plunging process of a hyperpycnal plume over a sloping bottom was investigated only in numerical studies of Chen et al. (2013) and Tseng and Chou (2018). Chen et al. (2013) applied a hydrostatic model, while Tseng and Chou (2018) suggested that a non-hydrostatic model is required to accurately simulate the vertical motion of the plume during the plunging process. Both models of Chen et al. (2013) and Tseng and Chou (2018) were based on Reynolds-averaged simulation and validated only by laterally confined experiments performed in channels.
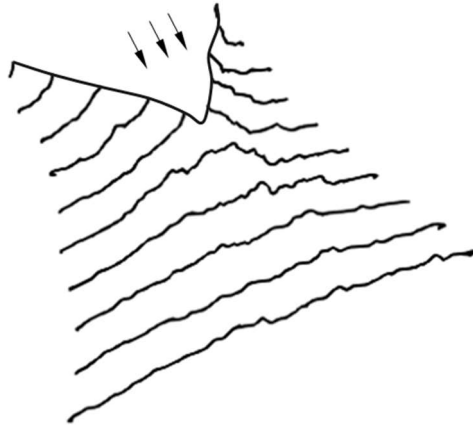
Figure 1.3 Conceptual sketch of the laterally unconfined hyperpycnal plume plunging. Black arrows indicate the inflow direction of the hyperpycnal plume. This sketch is composed of the triangular plume-ambient interfacial curve on the water surface and other interfacial curves in cross-sections.

Thus far, experimental study of a laterally unconfined hyperpycnal plume plunging over a sloping bottom has yet to be reported in the literature. The three-dimensional (3D) hydrodynamics of such a flow are still to be revealed, and existing CFD models are yet to be validated by experiments. Chapter 3 of this thesis introduces the first experimental study to fill the gap. A channel inflow with an aspect ratio of 25 entering an open receiving water body with an 8° sloping bottom was applied in the experiment,

a simplified geometry similar to the Rhône River mouth (Lake Geneva). The measured experimental flow field data were then used to validate a 3D CFD model based on Large Eddy Simulation using OpenFOAM. Extended ranges of inflow and boundary conditions (i.e., Froude and densimetric Froude numbers, density difference and bottom slope) compared with the experiments were applied in the validated numerical model for further analysis. The combined results of the experiments and numerical modeling provided a systematic investigation on the laterally unconfined plunging hydrodynamics, especially the different flow behavior from the classical channelized configuration. The focus was on the identification of the dominant control parameter of the plunging process, the plunging entrainment coefficient, and the influence of the bottom slope on the plunging behavior. The experiment and the numerical modeling were also compared with observations at the Rhône River mouth and field measurements reported in the literature (Hogg et al., 2013; Spigel et al., 2005) in terms of the plunge location and plunging entrainment coefficient.

Figure 1.4 Satellite image of the Rhône River mouth (Lake Geneva), Switzerland, in June 2021 from Google Earth. The Rhône River is sediment-laden, showing a different color from the ambient lake water.

1.3 Shear layers and Kelvin Helmholtz-type coherent structures

Shear layers (also called mixing layers) describe the shearing mechanism between two fluids with different velocities. In the field of hydraulic research, examples of shear layers are widely found in compound open channels (e.g., Dupuis et al., 2023), river confluences (e.g., Lewis & Rhoads, 2015), and canopy flows (e.g., Ghisalberti & Nepf, 2006). Shear layers are usually accompanied with Kelvin Helmholtz-type coherent structures (KHCS), which contribute significantly to the momentum and mass exchange between the two fluids at two sides of the shear layer (Ghisalberti & Nepf, 2005; Lewis & Rhoads, 2015; Truong & Uijttewaal, 2019).

A tidal jet owns two interfaces with the receiving ambient water at its sides. The velocity gradient between the jet and the ambient water forms two symmetric shear layers at the sides of the jet as depicted in Fig. 1.5a, inside of which KHCS develop. Previous jet studies only focused on the coherent structures after the two shear layers meet at the centerline ($x > x_m$) and interact with each other (Deo et al., 2007; Dracos et al., 1992; Jiménez-Robles et al., 2016; Jirka, 2001; Landel et al., 2012; Rowland et al., 2009; Thomas & Goldschmidt, 1986; Weir et al., 1981). However, the development of the shear layers and coherent structures before that location ($x < x_m$), as shown in Figs. 1.1 and 1.5a, was barely discussed. Here, x_m denotes the location where the two shear layers meet at the centerline (Fig. 1.5a), which is also the location where the jet transforms from flow establishment zone to established flow zone. The growth of the shear layers and the development of KHCS in the flow establishment zone were investigated experimentally and numerically in this thesis (Chapter 2), especially considering the situation of a sloping bottom boundary. Specifically, the momentum thickness of the shear layer, the frequency and vertical extension of KHCS, and the contribution of KHCS on the momentum exchange and turbulent kinetic energy production were discussed.
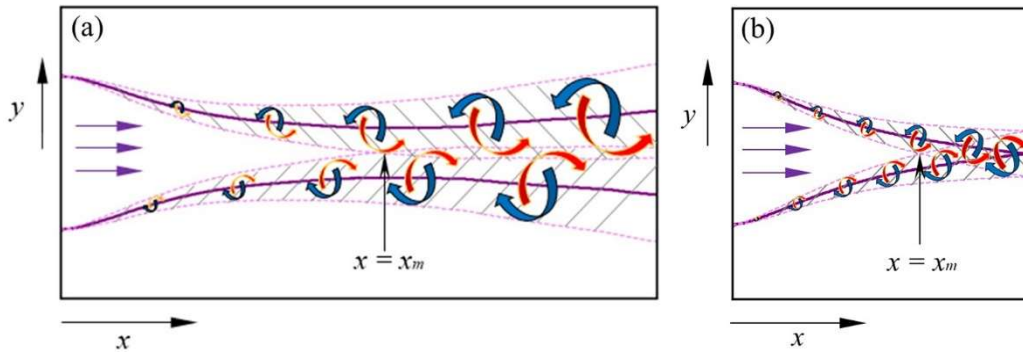
Figure 1.5 Sketches of the shear layers with KHCS developing at two sides of the tidal jet (a) and at two sides of the hyperpycnal plume prior to plunging (b). Sketch (a) presents the sloping-bottom configuration that the jet first converges and then diverges laterally. The purple solid lines represent the interface between the jet or plume and ambient water. The shadowed regions (bounded by the dashed lines) indicate the shear layers. Pairs of red and blue arrows denote the KHCS developing inside the shear layers. The inflow direction is illustrated by the purple arrows.

Shear layers and KHCS also take place in hyperpycnal plumes, but were usually investigated in the underflow region in the literature, as illustrated in Fig. 1.2. (Baas et al., 2005; He, Han, et al., 2022; Kostaschuk et al., 2018; Maggi et al., 2023; Martin et al., 2019; Negretti et al., 2008, 2017; Schuch et al., 2018). The shear layer here spreads vertically and the underflow is stratified. In such a case, KHCS are expected to occur if the shear across the plume-ambient interface is sufficiently strong to overcome the stabilization effect arising from the stratification (i.e., negative buoyancy). The local Richardson number at the interface describes the combined effects of shear and stratification. The criterion that a Richardson number < 0.25 is often used to determine the occurrence of KHCS (Howard, 1961; Miles, 1961).

Differently, the satellite image of the Rhône River mouth (Fig. 1.4) shows shear layers and KHCS developing at two sides of the hyperpycnal plume prior to plunging, which seems to be more similar to the jet case (Fig. 1.5a) rather than the underflow, as shown by the sight of the water surface (Fig. 1.5b). The shear layers illustrated in Fig. 1.5b are more complicated under the water surface because the plume-ambient interface is a

hooked face in a 3D view (Fig. 1.3). Therefore, under the water surface, the flow is stratified; thus, the negative buoyancy can potentially influence the development of the shear layers and shear-induced KHCS. Thus far, the development of the shear layers and coherent structures at the sides of a hyperpycnal plume in the plunge region has yet to be reported in the literature. Chapter 3 addresses this research gap. The validated turbulence-resolving 3D CFD model was applied to provide detailed continuous data of the flow field in the nearshore region before the hyperpycnal plume plunges. These detailed numerical data were used to reveal the 3D characteristics and development of the shear layers and KHCS at the sides of the hyperpycnal plume, especially focusing on the influence of negative buoyancy on the growth of shear layers and KHCS development. The contribution of these KHCS on the mixing between the plume and ambient water was also quantified.

1.4 Research objectives and approach

This thesis aims to reveal the nearshore hydrodynamics of a turbulent flow entering a laterally unconfined quiescent receiving water body with a sloping bottom boundary under the influence of neutral (tidal jet) or negative buoyancy (hyperpycnal plume). In the case of a tidal jet, the focus is on its development and turbulence characteristics under the influence of the sloping bottom boundary, along with the development of shear layers and coherent structures at the sides of the jet. In the case of a hyperpycnal plume, the focus is on its unique 3D plunging process different from laterally confined plumes reported in the literature, along with the influence of negative buoyancy on the development of shear layers and coherent structures at the sides of the plume.

The main approaches applied in this thesis are laboratory experiments and numerical simulation. The experiments were performed in a 13-m diameter circular tank: Coriolis platform (hydralab.eu), using a particle image velocimetry system for velocity measurement and Rhodamine dyeing for flow visualization. The experimental data were then used to validate a turbulence-resolving 3D CFD model based on Large Eddy Simulation using OpenFOAM to provide more detailed instantaneous flow field data

continuously. The combined experimental and numerical data were then used to address hydrodynamic mechanisms of certain topics.

This thesis is structured as follows:

Chapter 2 focuses on the nearshore hydrodynamics in the neutrally buoyant configuration (i.e., tidal jet) using experimental and numerical data. The development of the jet under the influence of a sloping bottom boundary is revealed, focusing on the variation of the jet width, turbulence characteristics (i.e., turbulent kinetic energy, eddy viscosity, and anisotropy), and the growth of the shear layers at the sides of the jet. The characteristics of the KHCS developing inside the shear layers are also investigated in terms of their nondimensionalized frequency (Strouhal number), vertical extension, and contribution on momentum exchange and turbulent kinetic energy production.

Chapter 3 reveals the plunging process of a laterally unconfined hyperpycnal plume based on the experimental and numerical data, compared with laterally confined plunging. The influence of different parameters (Froude number, densimetric Froude number, bottom slope and lateral confinement) on the plunging process is quantified. A comparison of the experimental and numerical results along with field observations reported in the literature and at the Rhône River mouth is also introduced in this chapter.

Chapter 4 is based on the numerical model only. With the detailed instantaneous numerical flow field data, the 3D characteristics of the shear layers and coherent structures developing at the sides of the hyperpycnal plume are investigated, along with the impacts of negative buoyancy on the shear layers and coherent structure development. The contribution of the coherent structures on the mixing between the plume and ambient water is also discussed in this chapter.

Chapter 5 provides a summary of the conclusions drawn by the previous chapters. The limitations of the present study and possible research questions for future studies are also discussed in this chapter.

Chapters 2–4 are based on individual manuscripts published by or to be submitted to peer-reviewed scientific journals. They are presented in the most updated version in this thesis and might be slightly different from the final published version in journals.

References

Akiyama, J., & Stefan, H. G. (1984). Plunging flow into a reservoir: theory. *Journal of Hydraulic Engineering*, *110*(4), 484–499. https://doi.org/10.1061/(ASCE)0733-9429(1984)110:4(484)

An, R., & Li, J. (2010). Characteristic analysis of the plunging of turbidity currents. *Journal of Hydrodynamics*, *22*(2), 274–282. https://doi.org/10.1016/S1001-6058(09)60055-X

Arita, M., & Nakai, M. (2008). Plunging conditions of two-dimensional negative buoyant surface jets released on a sloping bottom. *Journal of Hydraulic Research*, *46*(3), 301–306. https://doi.org/10.3826/jhr.2008.2714

Athanasiou, P., van Dongeren, A., Giardino, A., Vousdoukas, M., Gaytan-Aguilar, S., & Ranasinghe, R. (2019). Global distribution of nearshore slopes with implications for coastal retreat. *Earth System Science Data*, *11*, 1515–1529. https://doi.org/10.5194/essd-11-1515-2019

Baas, J. H., McCaffrey, W. D., Haughton, P. D. W., & Choux, C. (2005). Coupling between suspended sediment distribution and turbulence structure in a laboratory turbidity current. *Journal of Geophysical Research*, *110*(C11), C11015. https://doi.org/10.1029/2004JC002668

Baas, J. H., Van Kesteren, W., & Postma, G. (2004). Deposits of depletive high-density turbidity currents: A flume analogue of bed geometry, structure and texture. *Sedimentology*, *51*(5), 1053–1088. https://doi.org/10.1111/j.1365-3091.2004.00660.x

Best, J. L., Kostaschuk, R. A., Peakall, J., Villard, P. V., & Franklin, M. (2005). Whole flow field dynamics and velocity pulsing within natural sediment-laden underflows. *Geology*, *33*(10), 765-768. https://doi.org/10.1130/G21516.1

Broekema, Y. B., Labeur, R. J., & Uijttewaal, W. S. J. (2018). Observations and analysis of the horizontal structure of a tidal jet at deep scour holes. *Journal of Geophysical Research: Earth Surface*, *123*(12), 3162–3189. https://doi.org/10.1029/2018JF004754

Brown, C. A., Jackson, G. A., & Brooks, D. A. (2000). Particle transport through a narrow tidal inlet due to tidal forcing and implications for larval transport. *Journal of Geophysical Research: Oceans*, *105*(C10), 24141–24156. https://doi.org/10.1029/2000JC000211

Buonaiuto, F. S., & Bokuniewicz, H. J. (2008). Hydrodynamic partitioning of a mixed energy tidal inlet. *Journal of Coastal Research*, *245*, 1339–1348. https://doi.org/10.2112/07-0869.1

Canestrelli, A., Nardin, W., Edmonds, D., Fagherazzi, S., & Slingerland, R. (2014). Importance of frictional effects and jet instability on the morphodynamics of river mouth bars and levees. *Journal of Geophysical Research: Oceans*, *119*(1), 509–522. https://doi.org/10.1002/2013JC009312

Chen, S. N., Geyer, W. R., & Hsu, T. J. (2013). A numerical investigation of the dynamics and structure of hyperpycnal river plumes on sloping continental shelves: dynamics of hyperpycnal river plumes. *Journal of Geophysical Research: Oceans*, *118*(5), 2702–2718. https://doi.org/10.1002/jgrc.20209

Churchill, J. H., Hench, J. L., Luettich, R. A., Blanton, J. O., & Werner, F. E. (1999). Flood tide circulation near Beaufort Inlet, North Carolina: Implications for larval recruitment. *Estuaries*, *22*(4), 1057-1070. https://doi.org/10.2307/1353083

Cohen, C. (2012). Shallow-water plane and tidal jets. Unpublished Ph.D. thesis. *University of Otago*. Otago, New Zealand. https://ourarchive.otago.ac.nz/handle/10523/2493

Cortés, A., Fleenor, W. E., Wells, M. G., de Vicente, I., & Rueda, F. J. (2014). Pathways of river water to the surface layers of stratified reservoirs. *Limnology and Oceanography*, *59*(1), 233–250. https://doi.org/10.4319/lo.2014.59.1.0233

Curray, J. R., Emmel, F. J., & Moore, D. G. (2002). The Bengal Fan: Morphology, geometry, stratigraphy, history and processes. *Marine and Petroleum Geology*, *19*(10), 1191–1223. https://doi.org/10.1016/S0264-8172(03)00035-7

Dai, A., & Huang, Y. L. (2020). Experiments on gravity currents propagating on unbounded uniform slopes. *Environmental Fluid Mechanics*, *20*(6), 1637–1662. https://doi.org/10.1007/s10652-020-09758-2

De Cesare, G., & Schleiss, A. (1999). Physical and numerical modelling of turbidity currents. *Proceedings XXVIII IAHR Congress*, Graz, Austria. https://www.iahr.org/library/infor?pid=13822

De Cesare, G., Schleiss, A., & Hermann, F. (2001). Impact of turbidity currents on reservoir sedimentation. *Journal of Hydraulic Engineering*, *127*(1), 6–16. https://doi.org/10.1061/(ASCE)0733-9429(2001)127:1(6)

Deo, R. C., Mi, J., & Nathan, G. J. (2007). The influence of nozzle-exit geometric profile on statistical properties of a turbulent plane jet. *Experimental Thermal and Fluid Science*, *32*(2), 545–559. https://doi.org/10.1016/j.expthermflusci.2007.06.004

Deo, R. C., Mi, J., & Nathan, G. J. (2008). The influence of Reynolds number on a plane jet. *Physics of Fluids*, *20*(7): 075108. https://doi.org/10.1063/1.2959171

Dracos, T., Giger, M., & Jirka, G. H. (1992). Plane turbulent jets in a bounded fluid layer. *Journal of Fluid Mechanics*, *241*, 587–614. https://doi.org/10.1017/S0022112092002167

Dupuis, V., Schraen, L., & Eiff, O. (2023). Shear layers in two-stage compound channels investigated with LS-PIV. *Experiments in Fluids*, *64*(2), 24. https://doi.org/10.1007/s00348-022-03557-9

Farrell, G. J., & Stefan, H. G. (1988). Mathematical modeling of plunging reservoir flows. *Journal of Hydraulic Research*, *26*(5), 525–537. https://doi.org/10.1080/00221688809499191

Fischer, H. B., List, E., Koh, R., Imberger, J., & Brooks, N. (1979). Mixing in inland and coastal waters. *Academic Press*, San Diego, California. USA. https://doi.org/10.1016/C2009-0-22051-4

Fleenor, W. (2001). Effects and control of plunging inflows on reservoir hydrodynamics and downstream releases. Unpublished Ph.D. thesis. *University of California, Davis*, Davis, California, USA. https://search.library.ucdavis.edu/permalink/01UCD_INST/9fle3i/alma990021089970403126

Fujiwara, T., Nakata, H., & Nakatsuji, K. (1994). Tidal-jet and vortex-pair driving of the residual circulation in a tidal estuary. *Continental Shelf Research*, *14*(9), 1025–1038. https://doi.org/10.1016/0278-4343(94)90062-0

Georgoulas, A. N., Angelidis, P. B., Panagiotidis, T. G., & Kotsovinos, N. E. (2010). 3D numerical modelling of turbidity currents. *Environmental Fluid Mechanics*, *10*(6), 603–635. https://doi.org/10.1007/s10652-010-9182-z

Ghisalberti, M., & Nepf, H. (2005). Mass transport in vegetated shear flows. *Environmental Fluid Mechanics*, *5*(6), 527–551. https://doi.org/10.1007/s10652-005-0419-1

Ghisalberti, M., & Nepf, H. (2006). The structure of the shear layer in flows over rigid and flexible canopies. *Environmental Fluid Mechanics*, *6*(3), 277–301.

https://doi.org/10.1007/s10652-006-0002-4

Giger, M., Dracos, T., & Jirka, G. H. (1991). Entrainment and mixing in plane turbulent jets in shallow water. *Journal of Hydraulic Research*, *29*(5), 615–642. https://doi.org/10.1080/00221689109498980

Haigh, R., Taylor, F. J. R., & Sutherland, T. F. (1992). Phytoplankton ecology of Sechelt Inlet, a fjord system on the British Columbia coast. I. General features of the nano- and microplankton. *Marine Ecology Progress Series*, *89*(2/3), 117–134. https://www.jstor.org/stable/24831781

Hauenstein, W., & Dracos, Th. (1984). Investigation of plunging density currents generated by inflows in lakes. *Journal of Hydraulic Research*, *22*(3), 157–179. https://doi.org/10.1080/00221688409499404

He, Z., Han, D., Lin, Y. T., Zhu, R., Yuan, Y., & Jiao, P. (2022). Propagation, mixing, and turbulence characteristics of saline and turbidity currents over rough and permeable/impermeable beds. *Physics of Fluids*, *34*(6), 066604. https://doi.org/10.1063/5.0095354

He, Z., Xu, B., Okon, S. U., & Li, L. (2022). Numerical investigation of the sediment hyperpycnal flow in the Yellow River estuary. *Journal of Marine Science and Engineering*, *10*(7), 943. https://doi.org/10.3390/jmse10070943

Hearn, C., Hunter, J., Imberger, J., & D. van, S. (1985). Tidally induced jet in Koombana Bay, Western Australia. *Marine and Freshwater Research*, *36*(4), 453-479. https://doi.org/10.1071/MF9850453

Heskestad, G. (1965). Hot-wire measurements in a plane turbulent jet. *Journal of Applied Mechanics*, *32*(4), 721–734. https://doi.org/10.1115/1.3627309

Hogg, C. A. R., Marti, C. L., Huppert, H. E., & Imberger, J. (2013). Mixing of an interflow into the ambient water of Lake Iseo. *Limnology and Oceanography*, *58*(2), 579–592. https://doi.org/10.4319/lo.2013.58.2.0579

Howard, L. N. (1961). Note on a paper of John W. Miles. *Journal of Fluid Mechanics*, *10*(04), 509-512. https://doi.org/10.1017/S0022112061000317

Jiménez-Robles, A. M., Ortega-Sánchez, M., & Losada, M. A. (2016). Effects of basin bottom slope on jet hydrodynamics and river mouth bar formation. *Journal of Geophysical Research: Earth Surface*, *121*(6), 1110–1133. https://doi.org/10.1002/2016JF003871

Jirka, G. H. (1994). Shallow Jets. In: Davies, P.A., Neves, M.J.V. (eds). Recent research advances in the fluid mechanics of turbulent jets and plumes: Vol. 255. (pp. 157–175). *Springer.* Dordrecht. https://doi.org/10.1007/978-94-011-0918-5_10

Jirka, G. H. (2001). Large scale flow structures and mixing processes in shallow flows. *Journal of Hydraulic Research*, *39*(6), 567–573. https://doi.org/10.1080/00221686.2001.9628285

Johnson, T. R., Ellis, C. R., Farrell, G. J., & Stefan, H. G. (1987). Negatively buoyant flow in a diverging channel. II: 3-d flow field descriptions. *Journal of Hydraulic Engineering*, *113*(6), 731–742. https://doi.org/10.1061/(ASCE)0733-9429(1987)113:6(731)

Johnson, T. R., Ellis, C. R., & Stefan, H. G. (1989). Negatively buoyant flow in diverging channel, IV: Entrainment and dilution. *Journal of Hydraulic Engineering*, *115*(4), 437–456. https://doi.org/10.1061/(ASCE)0733-9429(1989)115:4(437)

Johnson, T. R., Farrell, G. J., Ellis, C. R., & Stefan, H. G. (1987). Negatively buoyant flow in a diverging channel. I: Flow regimes. *Journal of Hydraulic Engineering*, *113*(6), 716–730. https://doi.org/10.1061/(ASCE)0733-9429(1987)113:6(716)

Joshi, P. B. (1982). Hydromechanics of tidal jets. *Journal of the Waterway, Port, Coastal and Ocean Division*, *108*(3).239-253. https://doi.org/10.1061/JWPCDX.0000302

Knight, D. W., & Shiono, K. (1990). Turbulence measurements in a shear layer region of a compound channel. *Journal of Hydraulic Research*, *28*(2), 175–196. https://doi.org/10.1080/00221689009499085

Kostaschuk, R., Nasr-Azadani, M. M., Meiburg, E., Wei, T., Chen, Z., Negretti, M. E., Best, J., Peakall, J., & Parsons, D. R. (2018). On the causes of pulsing in continuous turbidity currents. *Journal of Geophysical Research: Earth Surface*, *123*(11), 2827–2843. https://doi.org/10.1029/2018JF004719

Lamb, M. P., McElroy, B., Kopriva, B., Shaw, J., & Mohrig, D. (2010). Linking river-flood dynamics to hyperpycnal-plume deposits: Experiments, theory, and geological implications. *Geological Society of America Bulletin*, *122*(9–10), 1389–1400. https://doi.org/10.1130/B30125.1

Lamb, M. P., & Mohrig, D. (2009). Do hyperpycnal-flow deposits record river-flood dynamics? *Geology*, *37*(12), 1067–1070. https://doi.org/10.1130/G30286A.1

Landel, J. R., Caulfield, C. P., & Woods, A. W. (2012). Meandering due to large eddies and the statistically self-similar dynamics of quasi-two-dimensional jets. *Journal of Fluid Mechanics*, *692*, 347–368. https://doi.org/10.1017/jfm.2011.518

Lee, H., & Yu, W. (1997). Experimental study of reservoir turbidity current. *Journal of Hydraulic Engineering*, *123*(6), 520–528. https://doi.org/10.1061/(ASCE)0733-9429(1997)123:6(520)

Lewis, Q. W., & Rhoads, B. L. (2015). Resolving two-dimensional flow structure in rivers using large-scale particle image velocimetry: An example from a stream confluence. *Water Resources Research*, *51*(10), 7977–7994. https://doi.org/10.1002/2015WR017783

Maggi, M. R., Negretti, M. E., Hopfinger, E. J., & Adduce, C. (2023). Turbulence characteristics and mixing properties of gravity currents over complex topography. *Physics of Fluids*, *35*(1), 016607. https://doi.org/10.1063/5.0132830

Martin, A., Negretti, M. E., & Hopfinger, E. J. (2019). Development of gravity currents on slopes under different interfacial instability conditions. *Journal of Fluid Mechanics*, *880*, 180–208. https://doi.org/10.1017/jfm.2019.713

Meiburg, E., & Kneller, B. (2010). Turbidity currents and their deposits. *Annual Review of Fluid Mechanics*, *42*(1), 135–156. https://doi.org/10.1146/annurev-fluid-121108-145618

Miles, J. W. (1961). On the stability of heterogeneous shear flows. *Journal of Fluid Mechanics*, *10*(04), 496-508. https://doi.org/10.1017/S0022112061000305

Mulder, T., Syvitski, J. P. M., Migeon, S., Faugères, J. C., & Savoye, B. (2003). Marine hyperpycnal flows: Initiation, behavior and related deposits. A review. *Marine and Petroleum Geology*, *20*(6–8), 861–882. https://doi.org/10.1016/j.marpetgeo.2003.01.003

Negretti, M. E., Flòr, J. B., & Hopfinger, E. J. (2017). Development of gravity currents on rapidly changing slopes. *Journal of Fluid Mechanics*, *833*, 70–97. https://doi.org/10.1017/jfm.2017.696

Negretti, M. E., Socolofsky, S. A., & Jirka, G. H. (2008). Linear stability analysis of inclined two-layer stratified flows. *Physics of Fluids*, *20*(9), 094104. https://doi.org/10.1063/1.2980351

Old, C. P., & Vennell, R. (2001). Acoustic Doppler current profiler measurements of the velocity field of an ebb tidal jet. *Journal of Geophysical Research: Oceans*, *106*(C4), 7037–7049.

https://doi.org/10.1029/1999JC000144

Onishi, S. (1984). Study of vortex structure in water surface jets by means of remote sensing. In *Elsevier Oceanography Series* (Vol. 38, pp. 107–132). Elsevier. https://doi.org/10.1016/S0422-9894(08)70607-X

Ortega-Sánchez, M., Losada, M. A., & Baquerizo, A. (2008). A global model of a tidal jet including the effects of friction and bottom slope. *Journal of Hydraulic Research*, *46*(1), 80–86. https://doi.org/10.1080/00221686.2008.9521845

Özsoy, E., & Ünlüata, Ü. (1982). Ebb-tidal flow characteristics near inlets. *Estuarine, Coastal and Shelf Science*, *14*(3), 251-IN3. https://doi.org/10.1016/S0302-3524(82)80015-7

Parker, G., Fukushima, Y., & Pantin, H. M. (1986). Self-accelerating turbidity currents. *Journal of Fluid Mechanics*, *171*(1), 145-181. https://doi.org/10.1017/S0022112086001404

Parker, G., & Toniolo, H. (2007). Note on the analysis of plunging of density flows. *Journal of Hydraulic Engineering*, *133*(6), 690–694. https://doi.org/10.1061/(ASCE)0733-9429(2007)133:6(690)

Piton, V., Soulignac, F., Ulrich, L., Graf, B., Wynn, H. K., Blanckaert, K., & Barry, D. A. (2022). Tracing unconfined nearfield spreading of a river plume interflow in a large lake (Lake Geneva): Hydrodynamics, suspended particulate matter and associated fluxes. *Frontiers in Water*, *4*, 943242. https://doi.org/doi: 10.3389/frwa.2022.943242

Pohl, F., Eggenhuisen, J. T., Kane, I. A., & Clare, M. A. (2020). Transport and burial of microplastics in deep-marine sediments by turbidity currents. *Environmental Science & Technology*, *54*(7), 4180–4189. https://doi.org/10.1021/acs.est.9b07527

Pope, E. L., Cartigny, M. J. B., Clare, M. A., Talling, P. J., Lintern, D. G., Vellinga, A., et. al., (2022). First source-to-sink monitoring shows dense head controls sediment flux and runout in turbidity currents. *Science Advances*, *8*(20), eabj3220. https://doi.org/10.1126/sciadv.abj3220

Pope, S. B. (2000). Turbulent flows. *Cambridge University Press.* Cambridge, UK. https://doi.org/10.1017/CBO9780511840531

Rowland, J. C., Stacey, M. T., & Dietrich, W. E. (2009). Turbulent characteristics of a shallow wall-bounded plane jet: Experimental implications for river mouth hydrodynamics. *Journal of Fluid Mechanics*, *627*, 423–449. https://doi.org/10.1017/S0022112009006107

Schuch, F. N., Pinto, L. C., Silvestrini, J. H., & Laizet, S. (2018). Three-dimensional turbulence-resolving simulations of the plunge phenomenon in a tilted channel. *Journal of Geophysical Research: Oceans*, *123*(7), 4820–4832. https://doi.org/10.1029/2018JC014027

Singh, B., & Shah, C. R. (1971). Plunging phenomenon of density currents in reservoirs. *La Houille Blanche*, *1*, 59–64. https://doi.org/10.1051/lhb/1971005

Socolofsky, S. A., & Jirka, G. H. (2004). Large-scale flow structures and stability in shallow flows. *Journal of Environmental Engineering and Science, 3*(5), 451–462. https://doi.org/10.1139/s04-032

Spiers, K. C., Healy, T. R., & Winter, C. (2009). Ebb-Jet dynamics and transient eddy formation at Tauranga Harbour: Implications for entrance channel shoaling. *Journal of Coastal Research*, *25*(1), 234–247. https://doi.org/10.2112/07-0947.1

Spigel, R. H., Howard-Williams, C., Gibbs, M., Stephens, S., & Waugh, B. (2005). Field calibration of a formula for entrance mixing of river inflows to lakes: Lake Taupo, North Island, New Zealand. *New Zealand Journal of Marine and Freshwater Research*, *39*(4), 785–802.

https://doi.org/10.1080/00288330.2005.9517353

Thomas, F. O., & Goldschmidt, V. W. (1986). Structural characteristics of a developing turbulent planar jet. *Journal of Fluid Mechanics*, *163*, 227–256. https://doi.org/10.1017/S0022112086002288

Truong, S. H., & Uijttewaal, W. S. J. (2019). Transverse momentum exchange induced by large coherent structures in a vegetated compound channel. *Water Resources Research*, *55*(1), 589–612. https://doi.org/10.1029/2018WR023273

Tseng, C. Y., & Chou, Y. J. (2018). Nonhydrostatic simulation of hyperpycnal river plumes on sloping continental shelves: Flow structures and nonhydrostatic effect. *Ocean Modelling*, *124*, 33–47. https://doi.org/10.1016/j.ocemod.2018.02.003

Turner, E. R., Rabalais, N. N., & Zhang, Z. N. (1990). Phytoplankton biomass, production and growth limitations on the Huanghe (Yellow River) continental shelf. *Continental Shelf Research*, *10*(6), 545–571. https://doi.org/10.1016/0278-4343(90)90081-V

Vennell, R. (2006). ADCP measurements of momentum balance and dynamic topography in a constricted tidal channel. *Journal of Physical Oceanography*, *36*(2), 177–188. https://doi.org/10.1175/JPO2836.1

Weir, A. D., Wood, D. H., & Bradshaw, P. (1981). Interacting turbulent shear layers in a plane jet. *Journal of Fluid Mechanics*, *107*(1), 237-260. https://doi.org/10.1017/S0022112081001766

Wells, M. G., & Dorrell, R. M. (2021). Turbulence processes within turbidity currents. *Annual Review of Fluid Mechanics*, *53*(1), 59–83. https://doi.org/10.1146/annurev-fluid-010719-060309

Wolanski, E., Drew, E., Abel, K. M., & O'Brien, J. (1988). Tidal jets, nutrient upwelling and their influence on the productivity of the alga Halimeda in the Ribbon Reefs, Great Barrier Reef. *Estuarine, Coastal and Shelf Science*, *26*(2), 169–201. https://doi.org/10.1016/0272-7714(88)90049-2

Wright, L. D., Yang, Z. S., Bornhold, B. D., Keller, G. H., Prior, D. B., & Wiseman, W. J. (1986). Hyperpycnal plumes and plume fronts over the Huanghe (Yellow River) delta front. *Geo-Marine Letters*, *6*(2), 97–105. https://doi.org/10.1007/BF02281645

Zhang, R., Wu, B., & Zhang, B. (2023). Sensitivity analysis of a three-dimensional simulation of turbidity currents in a sloping flume. *Journal of Hydraulic Research*, *61*(1), 18–33. https://doi.org/10.1080/00221686.2022.2106590

Chapter 2 Tracking the as yet unknown nearfield evolution of a neutrally-buoyant tidal jet over a sloping bottom boundary

H. Shi[1], M. E. Negretti[2], J. Chauchat[2], K. Blanckaert[3], U. Lemmin[1], D. A. Barry[1]

[1]Ecological Engineering Laboratory (ECOL), Environmental Engineering Institute (IIE), Faculty of Architecture, Civil and Environmental Engineering (ENAC), École Polytechnique Fédérale de Lausanne (EPFL), Lausanne, Switzerland

[2]Université Grenoble Alpes, CNRS, Grenoble INP, LEGI UMR 5519, Grenoble, France

[3]Research Unit Hydraulic Engineering, Institute of Hydraulic Engineering and Water Resources Management, Technische Universität Wien, Vienna, Austria

Shi, H., Negretti, M. E., Chauchat, J., Blanckaert, K., Lemmin, U., & Barry, D. A. (2023). Tracking the as yet unknown nearfield evolution of a neutrally-buoyant tidal jet over a sloping bottom boundary. *Water Resources Research*. (Under review).

Key Points

- Combined physical/numerical experiments allowed the first characterization of a sloping bottom tidal jet.

- The influence of the sloping boundary on mean flow-field development and turbulence characteristics of the jet is demonstrated.

- Coherent structures in the shear layers and their importance for turbulent kinetic energy production and momentum exchange are revealed.

Abstract

Experimental studies on the evolution of an initially shallow, neutrally-buoyant tidal jet, bounded by a sloping, solid bottom boundary (Sloping Bottom Jet; SBJ) and a free surface, that issues into a laterally-unconfined quiescent ambient, have yet to be reported. This study investigates the nearfield of such a flow experimentally and numerically, comparing it with a plane jet flowing over a horizontal bottom (Horizontal Bottom Jet; HBJ) with the same flow configuration. As the transverse profile of the longitudinal velocity gradually transforms from a top-hat profile into a Gaussian distribution, the SBJ width decreases and centerline velocity first sharply decreases, then gradually increases, whereas the HBJ width continuously increases, and the centerline velocity remains constant. Once the Gaussian distribution is established, both SBJ and HBJ diverge and the centerline velocity decreases. Shear layers are generated on the sides of both jets with Kelvin Helmholtz-type Coherent Structures (KHCS) developing inside. KHCS produce periodic velocity fluctuations with a Strouhal number of ~0.079 and contribute significantly to momentum exchange and production of turbulent kinetic energy. Different from the HBJ, the vertical thickness of the SBJ increases longitudinally, and as a result, the thickness of KHCS also increase. At a certain distance, the two shear layers on the sides of the jet meet and merge at the centerline, causing a flapping motion of the jet. This location, however, is much closer to the jet mouth in SBJ than in HBJ. These findings demonstrate that a sloping bottom modifies the flow field from quasi-2D in HBJ to strongly 3D in SBJ.

2.1 Introduction

Tidal ebb jets are formed when seawater passes through shallow harbor entrances or straits into the open sea during ebb (Broekema et al., 2018; Cohen, 2012; Fujiwara et al., 1994; Hearn et al., 1985; Old & Vennell, 2001; Onishi, 1984; Spiers et al., 2009; Vennell, 2006). If the amount of freshwater input in a tidal inlet is negligible compared to the harbor's tidal flux, the tidal ebb flow can be approximated by a shallow neutrally-buoyant jet flow, bounded by a solid bottom boundary and an upper free surface, which issues from a wide, rectangular cross-section opening into a quiescent ambient (Cohen, 2012; Jiménez-Robles et al., 2016; Ortega-Sánchez et al., 2008; Rowland et al., 2009; Fig. 2.1a, b).

In previous laboratory studies, the jet was bounded by parallel horizontal boundaries (free surface and/or solid horizontal wall(s); Cohen, 2012; Deo et al., 2007, 2008; Dracos et al., 1992; Giger et al., 1991; Jirka, 2001; Rowland et al., 2009). Assuming homogeneity in the vertical direction, the jet could be treated as (quasi) two-dimensional (2D). The jet mean flow is longitudinal, and ambient fluid is entrained on both sides resulting in an increase of the jet width (Fig. 2.1a). Shear layers develop on both sides of the jet, generating Kelvin Helmholtz-type Coherent Structures (KHCS) with vertical axes. The transverse profile of the longitudinal jet velocity gradually transforms from a top-hat profile in the flow establishment zone into a Gaussian profile in the established flow zone (Pope, 2000). Thereafter, the jet becomes self-similar and the centerline velocity decreases (Cohen, 2012; Deo et al., 2007; Heskestad, 1965; Pope, 2000; Rowland et al., 2009). At the location where the Gaussian profile is reached, the shear layers at the sides of the jet join at the centerline, which may cause the meandering of the jet, a phenomenon known as "jet flapping" (Cohen, 2012; Deo et al., 2007; Dracos et al., 1992; Landel et al., 2012; Thomas & Goldschmidt, 1986). Analytical solutions for the main characteristics of quasi-2D plane jets (i.e., width, centerline velocity, transverse velocity profile and turbulent viscosity) that predict their variations in the longitudinal direction are available in the literature (Cohen, 2012; Deo et al., 2007; Heskestad, 1965; Pope, 2000; Rowland et al., 2009).
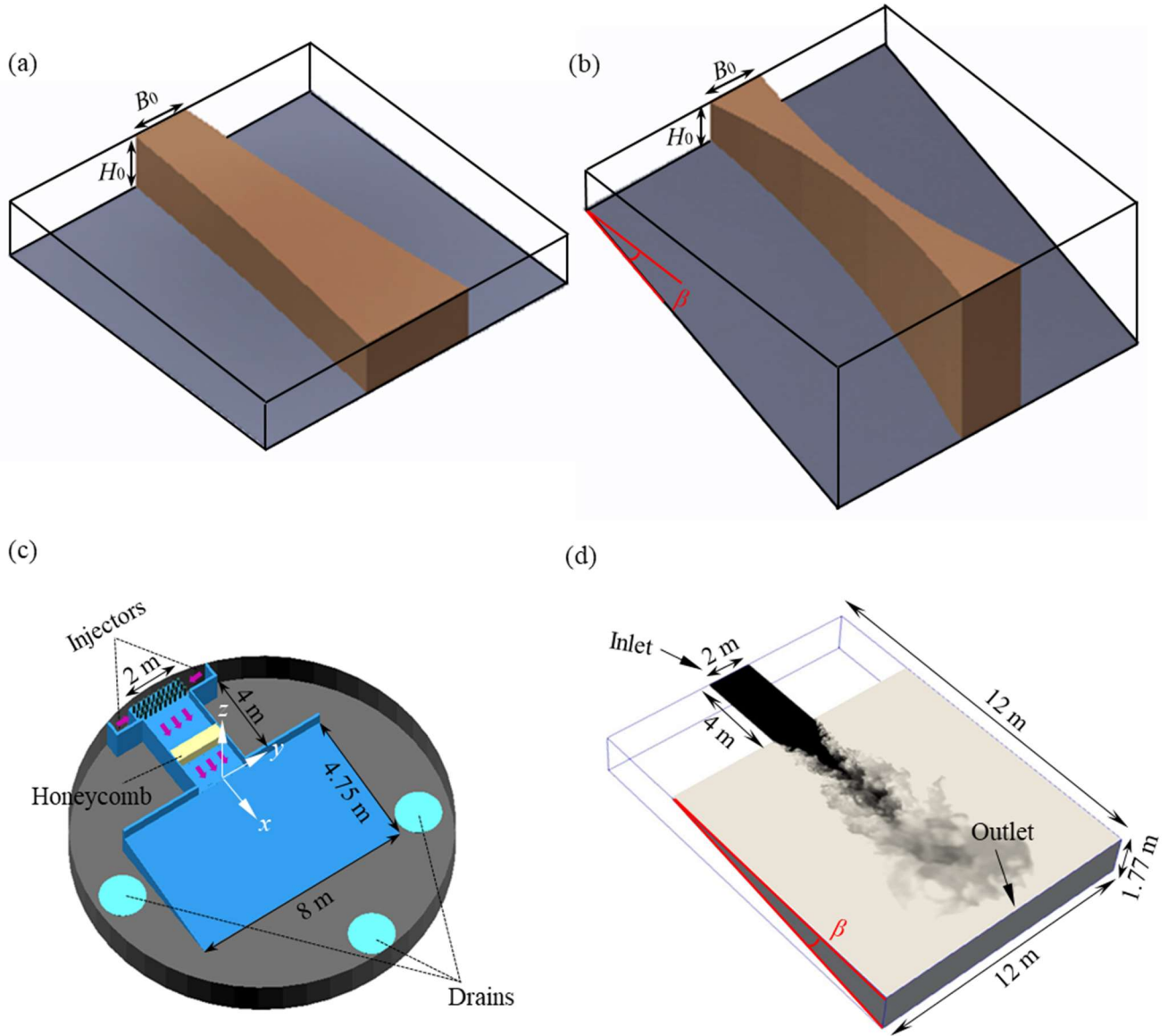
Figure 2.1 Three-dimensional (3D) depth-exaggerated sketch of a neutrally buoyant jet flowing: (a) over a horizontal bottom and (b) over a sloping bottom. (c) Experimental setup inside the Coriolis Platform. The jet flow was generated in a 4-m long free-surface inlet channel, which entered the wide ambient water body with a sloping bottom. The white arrows indicate the coordinate system. Its origin is located in the center at the surface end of the inflow channel. (d) 3D sketch of the simplified geometry used in the numerical model. The jet is colored in black, and the ambient water, in white.

However, unlike the horizontal bottom plane jets discussed above, tidal jets often flow over a sloping bottom boundary (Fig. 2.1b) and behave differently from classic 2D

plane jets (Broekema et al., 2018; Jiménez-Robles et al., 2016; Ortega-Sánchez et al., 2008), since they gradually spread in the vertical direction (Fig. 2.1b). Analytical models describing the development of jets flowing over sloping boundaries were established by Özsoy and Ünlüata (1982) and Ortega-Sánchez et al. (2008). Ortega-Sánchez et al. (2008) suggested that, unlike horizontal bottom plane jets, sloping bottom jets first undergo a horizontal contraction as a result of their vertical extension, before spreading laterally due to entrainment.

In contrast to horizontal bottom plane jets, which have been extensively investigated, experimental studies of initially shallow jets (initial aspect ratio: $B_0/H_0 \gg 1$) flowing over a sloping bottom have yet to be reported in the literature, and validated numerical and analytical models for such a configuration are not available. Here, B_0 and H_0 denote the initial width and depth of the jet, respectively. This study reports the first combined investigation of laboratory experiments and numerical modeling of an initially shallow, free-surface neutrally-buoyant jet flowing from a horizontal rectangular channel onto a sloping solid bottom (8°) boundary in an unconfined ambient. Certain findings are compared with those obtained from a numerical, horizontal bottom plane jet study with the same flow configuration. The findings of the present study have broad applications since globally 85% of nearshore slopes in oceans are reported to be < 8° (Athanasiou et al., 2019). The following questions are addressed:

- What are the similarities and differences between a jet flowing over a sloping bottom and a quasi-2D plane jet flowing over a horizontal bottom in terms of mean flow development?

- Can the features of a jet flowing over a sloping bottom, suggested by existing analytical models, be verified by our experiments and numerical modeling results? If not, what are the limitations of the analytical models?

- Are the characteristics of the shear layers and Kelvin Helmholtz-type Coherent Structures (KHCS) affected by the bottom slope?

- What contributions do KHCS make to the momentum exchange across the jet-ambient interface and the production of turbulent kinetic energy?

The Supporting Information (SI) provides texts and figures (with prefix S) with additional details and clarifications of certain topics discussed in the main text.

2.2 Materials and Methods

2.2.1 Laboratory experiments

The laboratory experiments were carried out in the 1.2-m deep circular tank (diameter 13 m) of the Coriolis Platform at LEGI (Université Grenoble Alpes, CNRS, Grenoble, France) (Fig. 2.1c). The same experimental set-up and measurement techniques were used as in Shi et al. (2022), who investigated negatively-buoyant plumes. Water was discharged from a horizontal 2-m wide (B_0), 4-m long and 0.08-m deep (H_0), straight inflow channel into an unconfined ambient (8-m wide × 4.75-m long) with an inclined bottom boundary (8° slope). The water depth was kept constant during the experiment (0.08 m in the inflow channel and 0.75 m in the circular tank) by extracting water at the same volume flux as the inflow (Q_0) through three outlet drains positioned at the sides and below the sloping boundary on the tank floor (Fig. 2.1c; for more details, see Text S2.1). No experiments were carried out for the horizontal bottom case.

The instantaneous velocity field in the horizontal plane at $z/H_0 = -0.5$ with a spatial resolution of ~0.01 m × 0.01 m was obtained from Particle Image Velocimetry (PIV) measurements. The measurement error for the instantaneous velocities was estimated to be ~3% (details in Text S2.1). A Cartesian coordinate system (x: longitudinal, y: transversal, z: vertical) is applied (Fig. 2.1c); its origin (0, 0, 0) is located at the water surface and at the centerline at the downstream end of the inlet channel. Velocities in the x, y and z directions are $u = \overline{u} + u'$, $v = \overline{v} + v'$, and $w = \overline{w} + w'$, respectively; the overbar denotes time-averaged values and the prime, velocity fluctuations.

Two cases (hereinafter referred to as Case 1 and Case 2) with different inflow velocities (Table 2.1) were investigated resulting in two different inflow Froude numbers ($Fr_0 = U_0 / \sqrt{gH_0}$ equal to 0.08 for Case 1 and 0.13 for Case 2), which are within the range of Froude numbers (0.08 – 0.18) reported in the literature for tidal ebb jets (Broekema et al., 2018; Cohen, 2012; Onishi, 1984). Here, U_0 is the bulk average

velocity of the jet at the channel mouth and g is the magnitude of gravitational acceleration.

Table 2.1 Summary of parameters used in experimental and numerical cases.

Case	Q_0 (L s^{-1})	U_0 (m s^{-1})	Fr_0	Re_0	β (°)
1	18	0.115	0.13	9,000	8
2	12	0.075	0.08	6,000	8
rf	18	0.115	0.13	9,000	0

2.2.2 Numerical model

To simulate the experiments, a three-dimensional (3D) numerical model using Large Eddy Simulation (LES) based on the open-source CFD package OpenFOAM (De Lorenzis and Düster, 2020; Jasak, 2009; Weller et al., 1998) was adapted using the validated model configuration of Shi et al. (2022). A simplified geometry consisting of a rectangular inlet channel connected to a receiving tank with an 8° sloping bottom (Fig. 2.1d) was applied to represent the geometry of the laboratory experiment. Two different inflow configurations for the jet over a sloping bottom were investigated (Cases 1 and 2 in Table 2.1). A reference case with a horizontal bottom geometry (i.e., $\beta = 0°$) was also studied (Case rf in Table 2.1). For more details of the model configuration, see Text S2.2. Text S2.3 gives further verification and validation of the model that includes a grid convergence index analysis and a comparison with experimental data of a shallow plane jet flowing over a horizontal bottom reported by Cohen (2012). Simulations based on the validated numerical model not only allowed obtaining 3D flow field data at different depths, but also extending the range of the investigated domain in the offshore direction, beyond that of the experimental investigations.

2.3 Results and Discussion

2.3.1 Mean flow characteristics and their comparison with theories

Time-averaged quantities are similar for the two sloping bottom cases. Therefore, the focus will mainly be on Case 1 and the comparison with horizontal bottom Case rf. The measured mean velocity field at $z/H_0 = -0.5$ shows that, in contrast to the classical quasi-2D horizontal bottom plane jet, the jet in Case 1 converges laterally near the

channel mouth (Fig. 2.2a). The longitudinal velocity profile along the centerline ($y = 0$) drops steeply until $x/B_0 = 0.5$. It then slightly increases and decreases again before reaching $x/B_0 = 1.6$ (Fig. 2.2b). The transverse velocity distributions at $x/B_0 = 0.4$ and 0.8 present a top-hat profile with a central region of laterally uniform longitudinal velocity (Fig. 2.2c). The velocity profile gradually transforms. At $x/B_0 = 1.2$, the top-hat region becomes much smaller and then disappears in the established flow zone at $x/B_0 = 1.6$, at the limit of the measured domain. The half width of the top-hat region (r) gradually decreases from $0.5B_0$ at the channel mouth to zero at $x/B_0 = 1.6$.

The jet in Case rf differs from Case 1 in that it spreads laterally from the channel mouth (Fig. 2.3a). With increasing offshore distance, a bottom boundary layer gradually develops as shown in Fig. 2.3b, where the velocity distribution in the central section ($y/B_0 = 0$) is presented. For sloping bottom Case 1, the numerical velocity distribution at $z/H_0 = -0.5$ (Fig. 2.3c) is very similar to that observed in the experiment (Fig. 2.2a). Beyond $x/B_0 > 1.6$, the jet starts to diverge. The velocity field obtained in an inclined plane parallel to and 2 cm above the sloping bottom boundary (Fig. 2.3d) features a region of low velocity inside the jet (dashed-lined triangle in Fig. 2.3d), resulting from the angle between the inflow velocity and the sloping bottom. A similar low velocity region at that location was also observed by Shi et al. (2022) for negatively-buoyant plumes over a sloping bottom boundary. The depth-averaged velocity distribution for Case 1 (Fig. 2.3e) is similar to the one close to the water surface (Fig. 2.3c) but has a smaller magnitude. The jet in Case 1 spreads vertically, and thus velocity in the central section ($y/B_0 = 0$) decreases with depth (Fig. 2.3f). Profiles of transversal velocity show no clear transversal velocity in Case rf (Fig. 2.4a), whereas there is strong evidence of non-negligible transversal velocity towards the centerline in Case 1 (Fig. 2.4c). In both cases, the transverse profile of longitudinal velocity gradually transforms from a top-hat profile into a Gaussian distribution (Fig. 2.4b, d), matching well with the Gaussian profile for a quasi-2D plane jet proposed in the literature (Deo et al., 2008):

$$U(y)/U_c = \exp\left[-(y/b)^2 \ln 2\right] \tag{2.1}$$
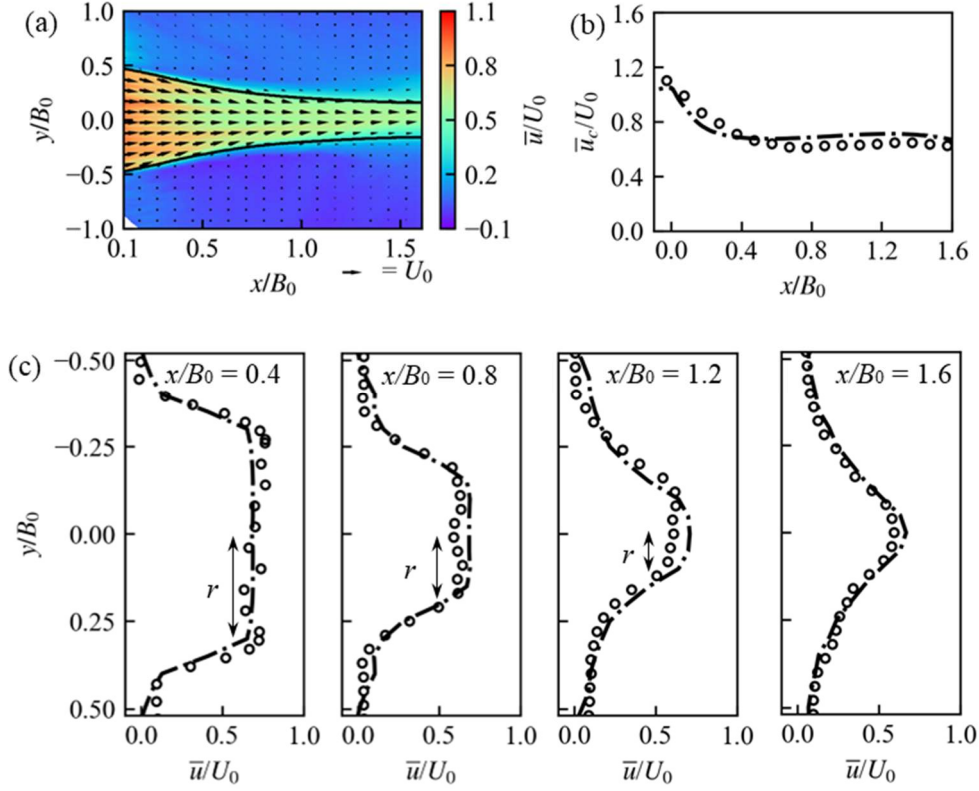
Figure 2.2 Velocity distributions in Case 1 at $z/H_0 = -0.5$. (a) Measured velocity distribution. The black solid line marks the boundary of the jet based on its width b calculated from the numerical model (see Fig. 2.4e). (b) Measured (circles) and modeled (dashed-dotted line) longitudinal velocity profile along the centerline. (c) Measured (circles) and modeled (dashed-dotted lines) transverse profiles of the longitudinal velocity at $x/B_0 = 0.4$, 0.8, 1.2 and 1.6; r indicates the half-width of the top-hat velocity profile.

The location where the Gaussian profile is reached defines the transition point (x_T) from the flow establishment zone to the established flow zone. This transition point is much closer to the channel mouth in Case 1 ($x_T/B_0 \approx 1.6$) than in Case rf ($x_T/B_0 \approx 4$). Cohen (2012) also obtained $x_T/B_0 \approx 4$ for the location of the transition point for the plane jet over a horizontal bottom from experiments. Based on the transverse profile of longitudinal velocity (Fig. 2.4b, d), the jet width b was calculated and is shown in Fig. 2.4e; $b = 2|y_{0.5}|$ where $y_{0.5}$ denotes the transverse coordinate where the longitudinal velocity is 50% of the centerline velocity, U_c. The jet thickness, h_c, in the central section ($y/B_0 = 0$) was calculated following Lee and Yu (1997): $h_c = \left(\int_{z_b}^{0} \overline{u}_c dz \right)^2 \Big/ \int_{z_b}^{0} \overline{u}_c^2 dz$, with u_c

being the centerline velocity and z_b the bottom depth. In Case rf, the jet thickness is constant ($\approx H_0$) while its width increases due to entrainment of ambient fluid (e.g., Pope, 2000; Fig. 2.4e, dashed lines). In the presence of a sloping bottom, fluid momentum is also spread in the vertical direction (h_c increases) and thus width b decreases (Fig. 2.4e, solid lines). The jet thickness is close to the local water depth ($H = x \tan\beta + H_0$, Fig. 2.4e, grey dash-dotted line). As the jet vertical thickness increases, the shear surface between the jet and ambient water increases, resulting in more entrainment of ambient water into the jet. The two competing effects (i.e., vertical extension and lateral entrainment) balance each other at a certain distance (here at $x/B_0 \approx 1.6$). Thereafter, entrainment becomes the dominant mechanism, and the width b slightly increases as in Case rf (Fig. 2.4e, red solid line). A comparison between Case rf and Case 1 in terms of depth-averaged centerline velocity and discharge per unit width in the central section ($q_c = U_c H$) shows that in Case rf, U_c and q_c remain almost constant (Fig. 2.4f). In contrast, in Case 1, a sharp decrease in U_c is observed in the range $0 < x/B_0 < 0.5$ due to the increase of the jet thickness (Fig. 2.4e, blue line). After that, it undergoes a slight increase in the range $0.5 < x/B_0 < 1.6$ because q_c increases. The increase of q_c is triggered by transversal velocities directed towards the centerline (Fig. 2.4c). For $x/B_0 > 1.6$, the transversal velocity becomes negligible, and thus, q_c remains almost constant and U_c decreases again.
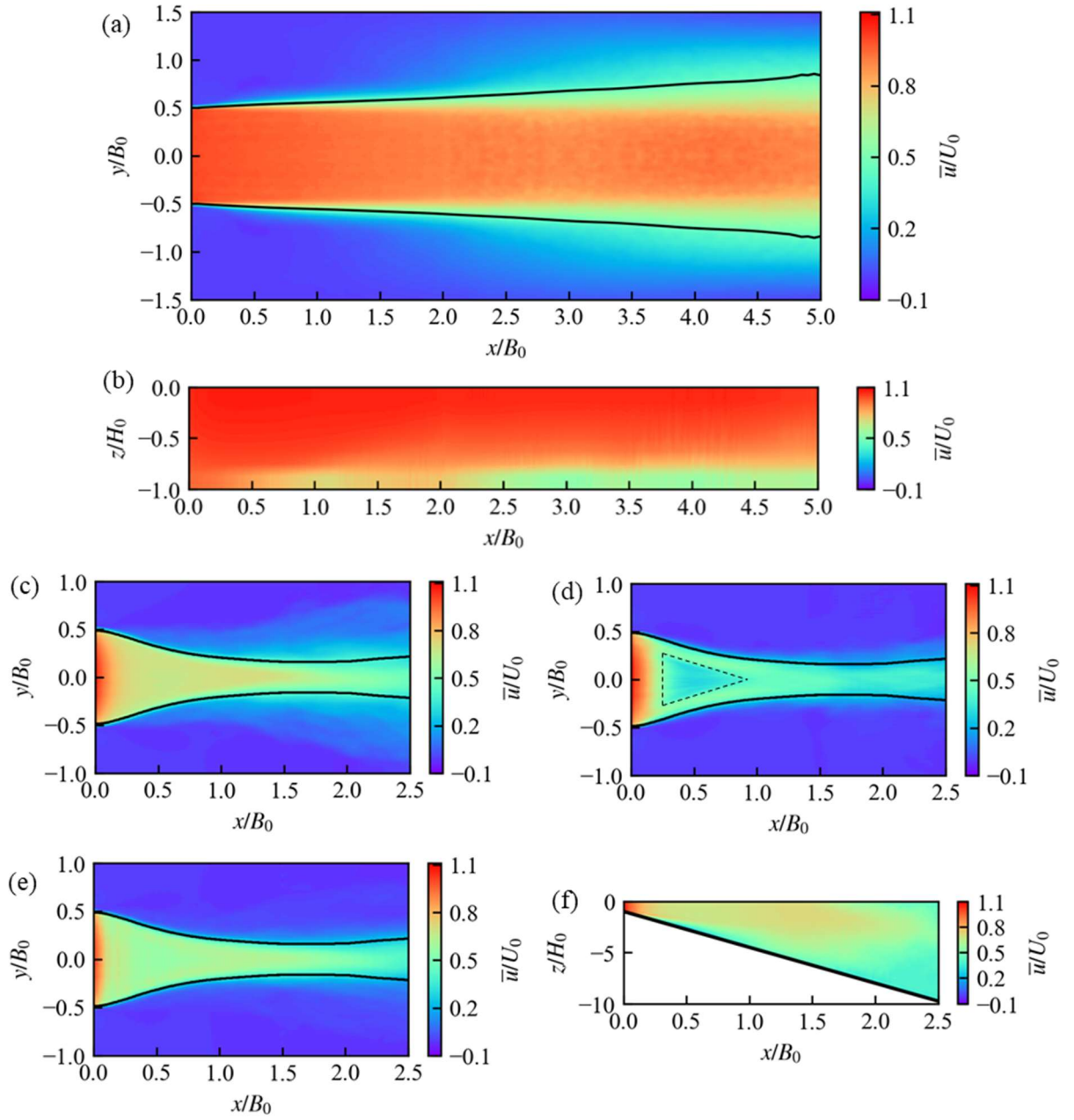
Figure 2.3 Time-averaged velocity distribution for Case rf: (a) In a horizontal plane at $z/H_0 = -0.5$ (solid lines give the jet width) and (b) at the central-section ($y/B_0 = 0$). (c–e) Time-averaged velocity distribution for numerical Case 1: (c) In a horizontal plane at $z/H_0 = -0.5$, (d) In an inclined plane parallel to and 2 cm above the sloping bottom boundary. Dashed-lined triangle: region with relatively lower velocity inside the jet. (e) Depth-averaged velocity field. (f) Velocity distribution at the central section ($y/B_0 = 0$) for numerical Case 1.
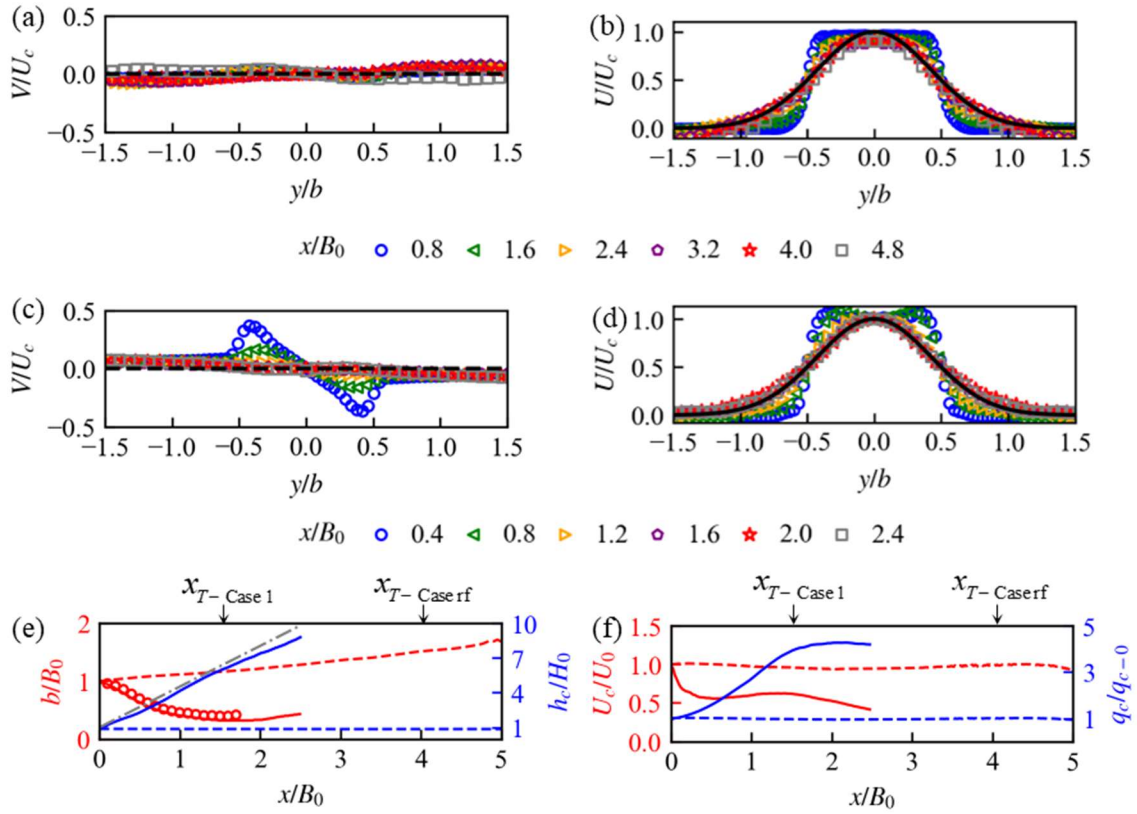
Figure 2.4 Transverse distribution of depth-averaged transversal and longitudinal velocity for numerical Case rf (a, b) and Case 1 (c, d). Black dashed line in (a) and (c) is zero. Black solid line in (b) and (d): Gaussian profile (Eq. 2.1). Legends for (a–d): symbols related to the longitudinal coordinates. (e) Variations of the jet width (red) and jet thickness (blue) in numerical Case 1 (solid lines) compared with reference Case rf (dashed lines). The red circles denote the jet width obtained from the measured velocity field at $z/H_0 = -0.5$. Grey dash-dotted line: increase of the local water depth ($H = x \tan\beta + H_0$) for Case 1. (f) Variations of the depth-averaged centerline velocity (U_c/U_0; red) and discharge per unit width in the central section (blue; right vertical axis) for numerical Case rf (dashed lines) and Case 1 (solid lines).

Analytical models for the variation of jet width and centerline velocity for the sloping bottom case were proposed by Özsoy and Ünlüata (1982) and Ortega-Sánchez et al. (2008). Unlike the present study where $y_{0.5}$ is used to measure the jet width, they defined a jet half-width $\tilde{b}$ as the distance from the centerline to the location where the longitudinal velocity is equal to zero. They proposed the following relationship for the transverse profile of the longitudinal velocity:

$$U(y)/U_c = F(\eta) = \begin{cases} 0 & \eta \geq 1 \\ \left(1-\eta^{1.5}\right)^2 & 0 < \eta < 1 \\ 1 & \eta \leq 0 \end{cases} \qquad \eta = \frac{|y|/\tilde{b} - r/\tilde{b}}{1 - r/\tilde{b}} \qquad (2.2)$$

with η being a similarity variable (Ortega-Sánchez et al., 2008). According to the definition, $U/U_c = 0.5$ when $y = \pm 0.5b$. Inserting this definition into Eq. 2.2, the following relation between $\tilde{b}$ and b is obtained: $b = 0.88\tilde{b} + 1.12r$. This relationship and Eq. 2.2 are compared with the present numerical data (Fig. 2.5a, b). The abovementioned analytical models are based on time- and depth-averaged mass and momentum equations and include the bottom friction term expressed with the Darcy-Weisbach friction factor, which is set to $f_n = 0.02$ here. This corresponds to a Manning coefficient $n = H_0^{1/6} (8g/f_n)^{-0.5} \approx 0.01$, a typical value for smooth polyvinylchloride (PVC) surfaces. According to Ortega-Sánchez et al. (2008), the analytical model is not sensitive to f_n for slopes > 3˚. In the flow establishment zone, where $r > 0$, the models of Özsoy and Ünlüata (1982) and Ortega-Sánchez et al. (2008) are identical, and assume that the centerline velocity remains constant. For the established flow zone, where $r = 0$, the results of Özsoy and Ünlüata (1982) and Ortega-Sánchez et al. (2008) are similar, even though different similarity functions were used. The present numerical results are compared with the analytical model results of Özsoy and Ünlüata (1982) in Fig. 2.5c–f. The analytical results underestimate jet width and overestimate centerline velocity. Errors are due to the model assumption that there is a constant centerline velocity in the flow establishment zone ($x/B_0 < 1.6$). However, the numerical results (Fig. 2.5e, f) and measurements (Fig. 2.2b) demonstrate that the centerline velocity is not constant. In the established flow zone ($x/B_0 > 1.6$), the model roughly captures the variation of the jet width and centerline velocity if the curves are shifted upwards to compensate for the initial errors.
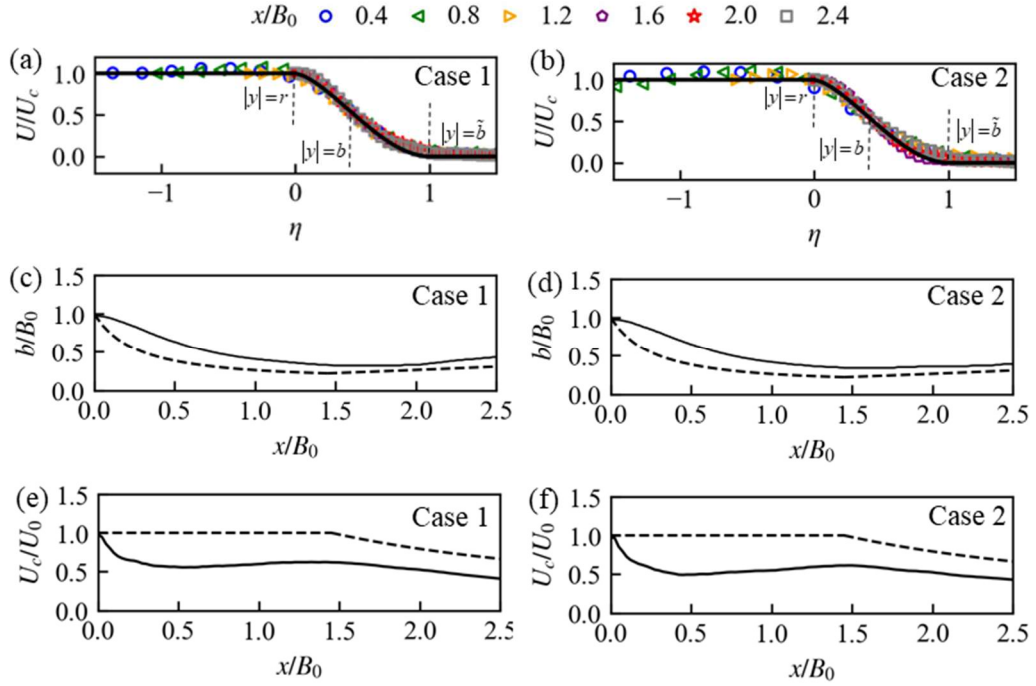
Figure 2.5 Transverse profiles of the longitudinal velocity for: (a) Case 1 and (b) Case 2 at different locations (x/B_0) indicated by colored symbols above the panels. Symbols: numerical data. Solid lines: results of Eq. 2.2. Three typical locations $|y|=r$, b, and $\tilde{b}$ are identified by vertical dashed lines. Variation of jet width for: (c) Case 1 and (d) Case 2. Variation of centerline velocity for: (e) Case 1 and (f) Case 2. Solid lines: data from the numerical model. Dashed lines: predictions of the analytical model (Özsoy & Ünlüata, 1982).

2.3.2 Turbulence characteristics

Figures 2.6a, b present the distribution of horizontal Turbulent Kinetic Energy (TKE), $k_H = 0.5\left(\overline{u'u'}+\overline{v'v'}\right)$, at $z/H_0 = -0.5$ for Case rf and Case 1. The vertical component of TKE is not available from the experimental data, but numerical model results confirm that the TKE is dominated by the horizontal components (Text S2.4). Shear layers with large k_H values are observed along each side of the jet. The two shear layers in Case rf remain almost parallel to each other. However, since they grow laterally with increasing offshore distance, the inner boundaries of the two shear layers (dash-dotted line, representing $k_H/U_0^2 = 0.01$) move towards the centerline and meet at $x/B_0 = 3.6$ which is close to the transition point from the flow establishment zone to the established flow zone ($x_T/B_0 \approx 4$). In contrast, the jet undergoes a lateral convergence in sloping bottom

Case 1. As a result, the shear layers meet at $x/B_0 = 1.55$, which is much closer to the channel mouth, and is again very close to the transition point from the flow establishment zone to the established flow zone ($x_T/B_0 \approx 1.6$). Similar to Case rf, the width of the region with high k_H values widens with increasing offshore distance, indicating that the lateral shear layers are spreading. The close resemblance between experimental and numerical transverse profiles of k_H (Fig. 2.6c), confirms that the numerical model can reproduce the main turbulence features. The magnitudes of $\overline{u'u'}$, $\overline{v'v'}$ and $\overline{w'w'}$ are compared in Fig. 2.6d based on the numerical data to identify the anisotropy of the jet. In Case rf, $\overline{u'u'}$ and $\overline{v'v'}$ are similar in magnitude and larger than $\overline{w'w'}$. In Case 1, however, both $\overline{v'v'}$ and $\overline{w'w'}$ are much smaller than $\overline{u'u'}$. The anisotropy of the jet is further discussed in Text S2.4.

Below, the focus is on the turbulence characteristics of the shear layers in the flow establishment zone before they merge with each other. Production (P) of turbulent kinetic energy describes the energy transfer from the mean velocity gradients (working against the Reynolds stresses) to fluctuating velocity fields. This is generally positive and thus a source of TKE (Hinze, 1975; Pope, 2000):

$$P = -\overline{u'_i u'_j} \frac{\partial \overline{u_i}}{\partial x_j} \tag{2.3}$$

The production term was determined based on the measured and modeled horizontal velocity fields, since vertical velocities were not measured, and the horizontal components are the main source due to anisotropy (Text S2.4). In Case rf and Case 1, production is strong inside the shear layer, in particular, close to the channel mouth (Fig. 2.7a, c and e). Further away from the channel mouth as the shear layer develops, production decreases because of the decrease of the velocity gradient (Fig. 2.3a, c). Similar to TKE (Fig. 2.6a, b), the horizontal Reynolds stress ($\overline{u'v'}$) at $z/H_0 = -0.5$ is high in the shear layer (Fig. 2.7b, d and f). In the region $0.75 < x/x_T < 1.0$ in Case 1 where the two shear layers are close to each other, the magnitude of the Reynolds stress is larger than near the channel mouth. This phenomenon is not observed in the horizontal bottom Case rf.
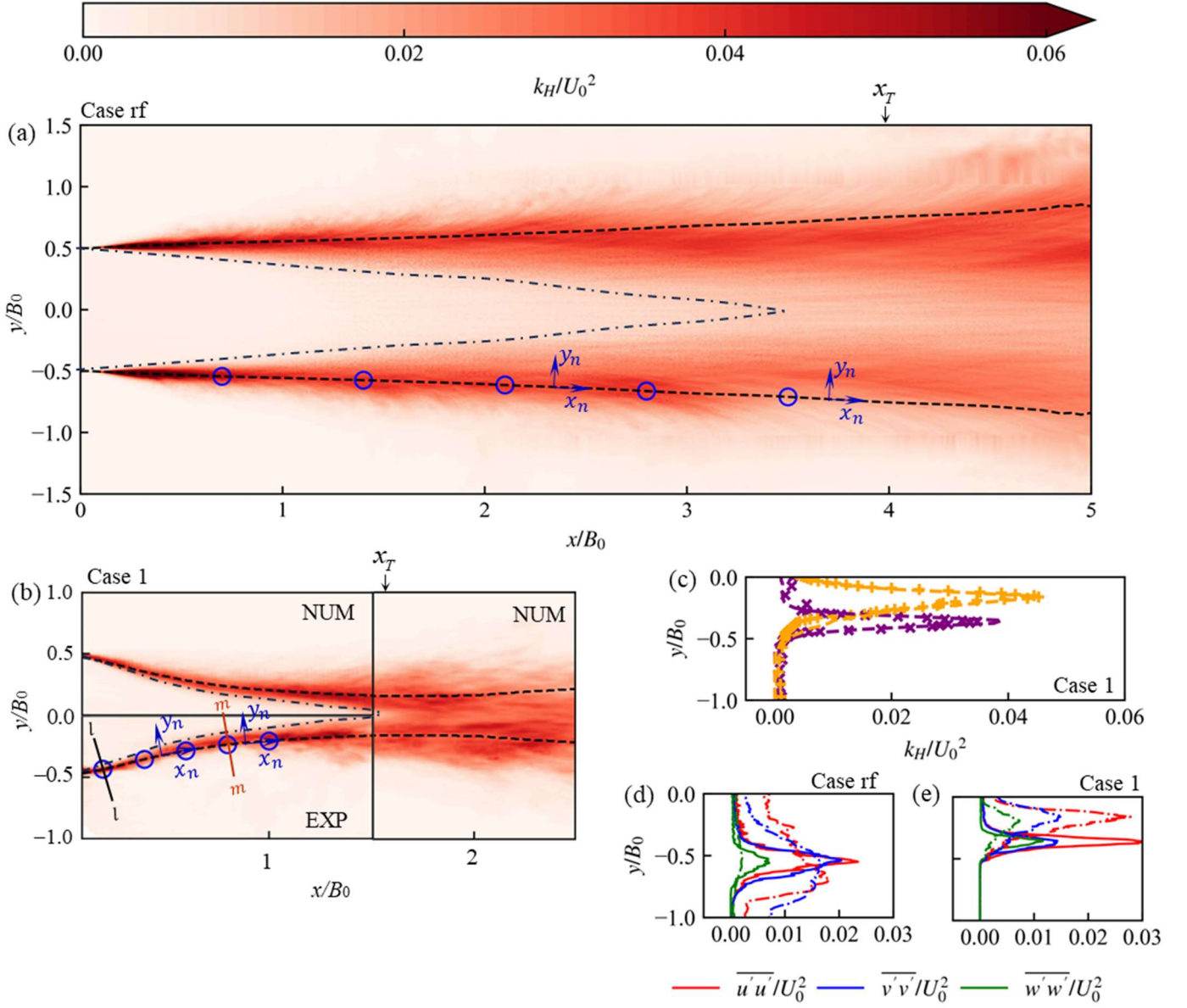
Figure 2.6 Distribution of horizontal turbulent kinetic energy k_H at $z/H_0 = -0.5$ for: (a) Case rf and (b) Case 1. For Case 1, in the region $x/B_0 < 1.5$, the upper half of the panel presents the numerical results (NUM), and the lower one, the experimental (EXP) data. In the region $x/B_0 > 1.5$, only numerical data are available. Dashed lines: jet width b. Dash-dotted lines: inner boundary of the shear layers, defined by $k_H/U_0^2 = 0.01$. Five points (P1–P5) on the jet width curve are shown by the blue circles in (a) and (b). For Case rf, these points are located at $x/B_0 = 0.7, 1.4, 2.1, 2.8$ and 3.5; for Cases 1, these points are located at $x/B_0 = 0.2, 0.4, 0.6, 0.8$ and 1.0. Case 2 shows a similar pattern of turbulent kinetic energy as Case 1 (data not shown) and thus the locations of P1-P5 are also the same as in Case 1. A coordinate system corresponding

to the jet width curve is represented by the blue arrows (x_n, y_n). In Case 1, lines *l-l* and *m-m* are two lines perpendicular to the jet width curve with intersections located at $x/B_0 = 0.2$ and 0.8, respectively. (c) Lateral distributions of k_H at $z/H_0 = -0.5$ at $x/B_0 = 0.4$ (purple), 1.2 (orange). Symbols: experimental data. Dashed lines: numerical data. Numerical transverse profiles of $\overline{u'u'}$ (red), $\overline{v'v'}$ (blue) and $\overline{w'w'}$ (green) for: (d) Case rf at $x/B_0 = 1$ (solid lines) and $x/B_0 = 3$ (dashed lines), and (e) Case 1 at $x/B_0 = 0.4$ (solid lines) and $x/B_0 = 1.2$ (dashed lines). In plots (c–e), only half of the jet is presented.

Turbulent viscosity $\upsilon_t = \overline{u'v'}\big/\left(\partial\overline{u}/\partial y\right)$ is an important parameter that is often used for shear stress closure (e.g., Odier et al., 2012; Shih et al., 1995; Shiono & Knight, 1991). It can be nondimensionalized into a turbulent Reynolds number $R_T = \left(0.5b - r\right)\overline{u}_c\big/\upsilon_t$ (Pope, 2000). Considering that measured/modeled values of turbulent viscosity are not reliable close to the lateral boundary of a shear layer (Odier et al. 2012), R_T is averaged inside the shear layers between $y_{0.8}$ and $y_{0.2}$ (Fig. 2.7g); $y_{0.8}$ and $y_{0.2}$ represent the locations of 80% and 20% of the centerline velocity $\overline{u}_c$, respectively. No clear difference between Case rf and Cases 1 and 2 is observed in terms of R_T in the flow establishment zone (Fig. 2.7g). Combing all experimental and numerical data, an averaged value of $R_T \approx 47 \pm 14$ was obtained (Fig. 2.7g). This value is larger than the theoretical value $R_T \approx 31$ proposed by Pope (2000) for the established flow zone but of the same order of magnitude.

2.3.3 Characterization of the shear layers

A new coordinate system (x_n, y_n) is defined as one that follows the jet width curve (dashed lines in Fig. 2.6a and b) with corresponding velocities $u_n = \overline{u}_n + u'_n$ tangent to the curve, and $v_n = \overline{v}_n + v'_n$ perpendicular to the curve. Directions of (x_n, y_n) do not show a big difference with the original coordinates (x, y) in Case rf. However, in Case 1, (x_n, y_n) is a curvilinear coordinate system with changing directions because the jet converges. Following the y_n direction, velocity $\overline{u}_n$ must increase from a small value $\overline{u}_{n-a}$ (at y_{n-a}) in the ambient water to a large value $\overline{u}_{n-c}$ inside the jet (at y_{n-c}). Typical profiles of measured $\overline{u}_n$ in Case 1 are plotted in Fig. 2.8a.
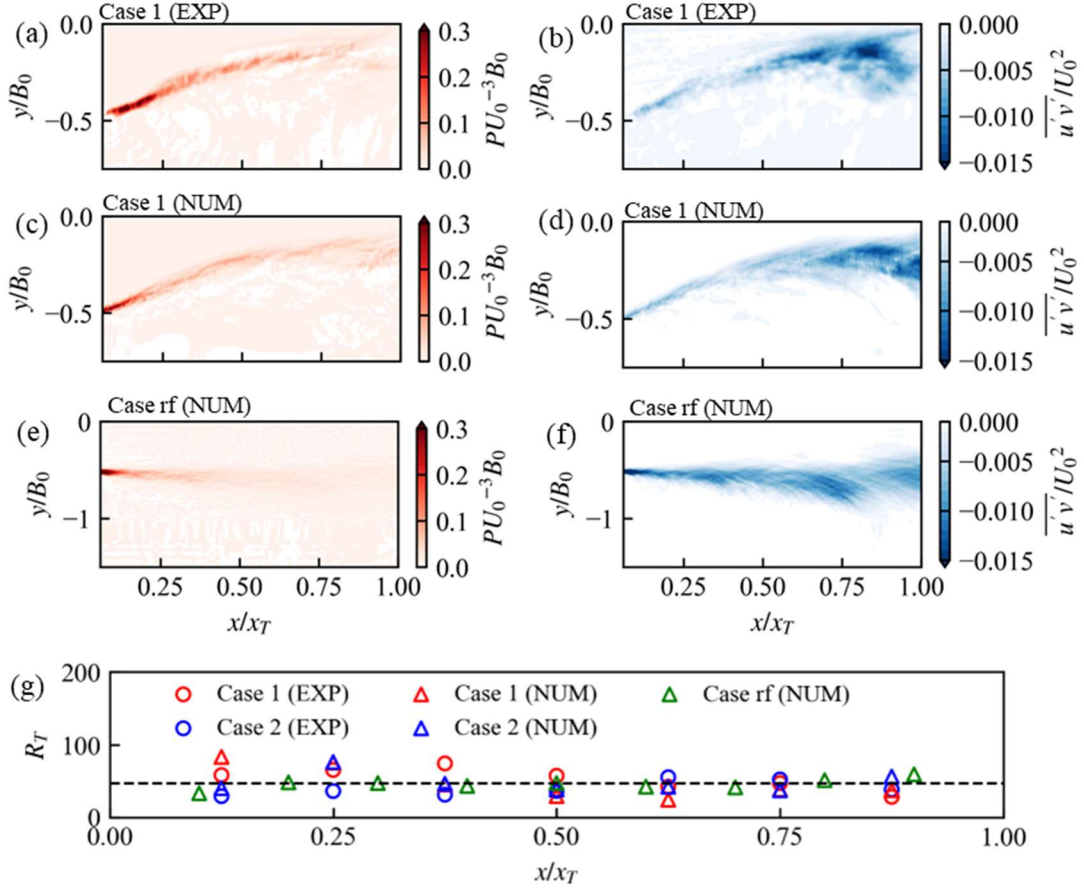
Figure 2.7 Left column (a, c, e): Production (P) of turbulent kinetic energy at $z/H_0 = -0.5$ for: (a) Case 1 experimental (EXP) data, (b) Case 1 numerical (NUM) data, and (e) Case rf numerical data. Right column (b, d, f): Reynolds shear stress at $z/H_0 = -0.5$ for: (b) Case 1 experimental data, (d) Case 1 numerical data, and (f) Case rf numerical data. Considering that the system is symmetric, only half of the domain ($y < 0$) is plotted. (g) Turbulent Reynolds number averaged over the shear layers at $z/H_0 = -0.5$. Black horizontal dashed line in (g): average value of R_T over all datasets in this panel (see legend).

Momentum thickness θ is a characteristic length scale that describes the width of a shear layer (Ho & Huang, 1982; Rogers & Moser, 1992):

$$\theta = \int_{y_{n-a}}^{y_{n-c}} \left[\frac{1}{4} - \left(\frac{\overline{u}_n - \overline{u}_{n-o}}{\overline{u}_{n-c} - \overline{u}_{n-a}} \right)^2 \right] dy_n \tag{2.4}$$

where $\overline{u}_{n-o}$ is the arithmetic mean of $\overline{u}_{n-a}$ and $\overline{u}_{n-c}$. The variation of θ along x was calculated using the experimental and numerical velocity fields (Fig. 2.8b). The

momentum thickness continuously increases with x in Case rf. In the sloping bottom cases, it first increases and then becomes almost constant after $x/x_T > 1$. The momentum thickness is comparatively smaller in Case 1 with larger Fr_0 and Re_0 than Case 2 (Table 2.1), which is consistent with previous findings in slowly spreading shear layers (Dimotakis, 1991).
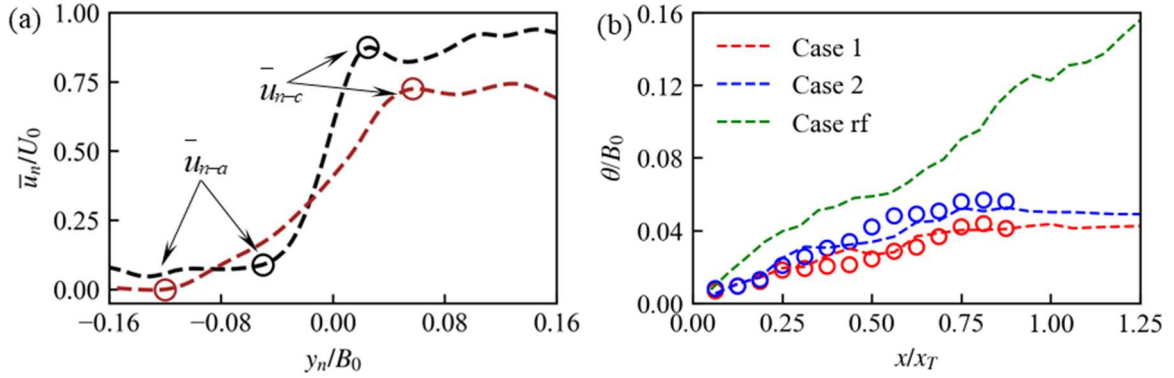
Figure 2.8 (a) Typical velocity profiles along lines *l-l* (black) and *m-m* (brown) shown in Fig. 2.6b for Case 1. Ambient waters ($\bar{u}_{n-a}$) and jet ($\bar{u}_{n-c}$) values are marked by circles. (b) Variations of the shear-layer momentum thickness. Symbols: experimental data. Curves: numerical data. Red: Case 1. Blue: Case 2. Green: Case rf.

2.3.4 Turbulent coherent structures

2.3.4.1 Structure identification and Strouhal numbers

Kelvin Helmholtz-type Coherent Structures (KHCS) are often observed in shear layers (Brown & Roshko, 1974). The transient iso-concentration surface ($c = 0.7$) in numerical Case 1 indicates the occurrence of KHCS (Fig. 2.9). Concentration c is determined by the degree of mixing of two fluids, i.e., $c = 1$ inside the inflow channel, and $c = 0$ in the ambient water (see Text S2.2). Thus, the iso-concentration surface ($c = 0.7$) in Fig. 2.9 is composed of 70% inflow fluid and 30% ambient water. The turbulent structures generate nearly periodic local velocity fluctuations in the velocity time series (Fig. 2.10a, b). The Power Spectral Density (PSD) is obtained from the velocity signals at locations P1–P5 (blue circles in Fig. 2.6a, b) on the jet-ambient interface determined by the jet width (dashed lines in Fig. 2.6a, b); the Strouhal number $St_\theta = f\theta / \bar{u}_{n-c}$ is used as

the nondimensional frequency (Ho & Huerre, 1984). All spectra have a strong peak close to $St_\theta = 0.079$ indicating the dominant KHCS frequency. This Strouhal number (~0.079) is consistent with the typical value of KHCS in slowly spreading shear layers (Ho & Huerre, 1984; Ho & Huang, 1982).

2.3.4.2 Contribution of KHCS to momentum exchange and energy production

KHCS contribute to the momentum exchange and production of TKE in shear layers (Taborda et al., 2022; Truong & Uijttewaal, 2019; White & Nepf, 2008). The momentum exchange between the jet and ambient waters is mainly represented by the horizontal Reynolds stress $\tau = -\overline{u_n' v_n'}$ at the interface ($y_n = 0$) (Truong & Uijttewaal, 2019; Taborda et al., 2022). Production P_n in the curvilinear coordinate system (neglecting vertical components) is given by,

$$P_n = -\left(\overline{u'_n u'_n} \frac{\partial \overline{u}_n}{\partial x_n} + \overline{v'_n v'_n} \frac{\partial \overline{v}_n}{\partial y_n} + \overline{u'_n v'_n} \frac{\partial \overline{u}_n}{\partial y_n} + \overline{u'_n v'_n} \frac{\partial \overline{v}_n}{\partial x_n} \right) \qquad (2.5)$$

In order to compare the contribution of KHCS and small-scale turbulence to momentum exchange and energy production, it is necessary to separate the velocity fluctuations associated with KHCS from those associated with small-scale turbulence. This analysis was only based on the experimental data of Case 1. Case rf could not be investigated, because the LES model does not directly resolve small-scale turbulence; instead, it uses a sub-grid model.

Two different methods were proposed in the literature to quantify the contribution of KHCS: The first method uses a simple low-pass filter to separate low-frequency (associated with KHCS) from small-scale, turbulence-induced high-frequency velocity signals (Truong & Uijttewaal, 2019; Li et al., 2022). Examples of filtered velocity signals are shown in Fig. 2.10a and b (using a low-pass filter, $f_{filter} = 4f_{cs}$ following Truong and Uijttewaal (2019); f_{cs} is the dominant frequency of KHCS, i.e., peak frequency in Fig. 2.10c before nondimensionalization.

In the second method, the measured flow field is reconstructed based on conditionally-averaging in order to smooth out small-scale turbulence (Shi et al., 2023; Taborda et al.,

2022; Yuan & Horner-Devine, 2017). The conditionally-averaging approach identifies KHCS using three consecutive zero-crossings of low-pass filtered v_n' (Taborda et al., 2022; White & Nepf, 2008), based, for example, on the velocity signal at P1 (Fig. 2.10b). A typical KHCS (Fig. 2.10b) lasts for a time period of T_i and contains a sweep ($Q4$) and an ejection ($Q2$) event distinguished using quadrant analysis (Bagherimiyab & Lemmin, 2018; Huai et al., 2019; Nezu & Nakagawa, 1993; White & Nepf, 2008). Results of a quadrant analysis of velocity signals are given in Text S2.5. A series of KHCS is identified based on low-pass filtered data, which provide the starting and ending time of a given structure (Taborda et al., 2022). The measured flow field (before low-pass filtering) of the identified structures along line l-l during their periods T_i is then rescaled into a new time coordinate $t_A = T_d(t - t_0)/T_i$, where $T_d = 1/f_{cs}$. Here, t is the instantaneous raw time and t_0 is the time when the structure first appears (Taborda et al. 2022). Rescaled velocity signals of the identified structures are then averaged to obtain the conditionally-averaged data. Note that the conditionally-averaged velocity field obtained here is based on the "raw" measured data rather than on the low-filtered data; the low-filtered data is only used to identify coherent structures. According to Taylor's frozen hypothesis, the structures are advected mainly by the mean velocity. The conditionally-averaged velocity field relative to a reference frame moving with a velocity $\overline{u}_{n-o}$ is obtained by subtracting this reference velocity. The same procedure is also applied to the velocity signals of P4 to determine the structures on line m-m.

The conditionally-averaged flow field provides streamline patterns of the KHCS (Fig. 2.11). Compared with the structure at line l-l, the structure at m-m is larger in both the x_n (L_x) and y_n (L_y) directions. Since coherent structures are induced by shear and located inside the shear layer, the size of the structure defined by L_x and L_y scales with the width of the shear layer, i.e., $L_x \sim L_y \sim \theta$. Thus, the time period of the structure is $T_d = 1/f_{cs} = L_x/\overline{u}_{n-o} \sim \theta/\overline{u}_{n-o}$, which explains why the Strouhal number remains almost constant (Fig. 2.10c).
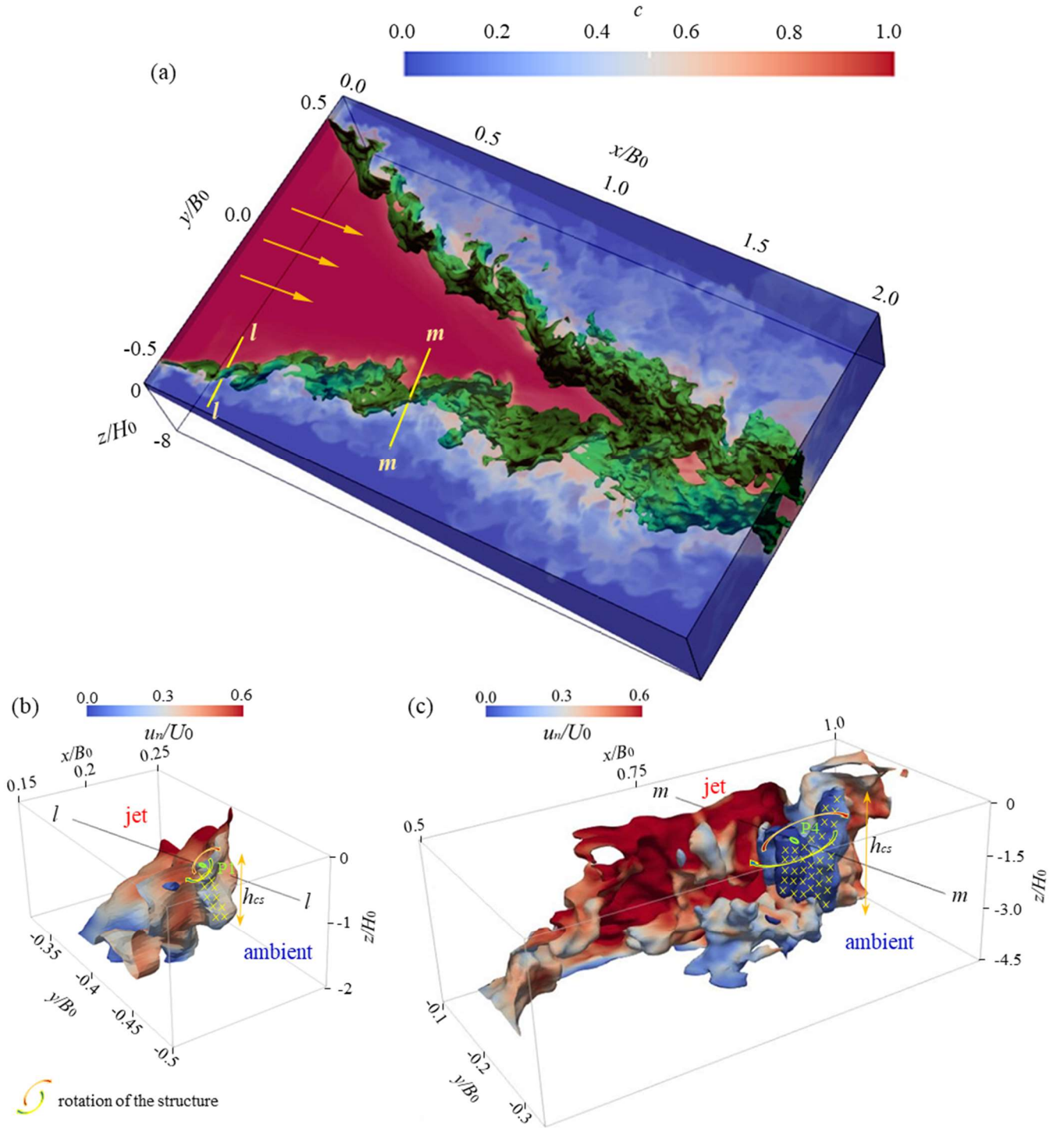
Figure 2.9 (a) Instantaneous concentration field for numerical Case 1. The translucent background color (from blue to red) illustrates the concentration distribution in the 3D field. The iso-concentration surface for $c = 0.7$ is highlighted in green. Arrows: inflow direction.

Details of the iso-concentration surface $c = 0.7$: (b) in the region of line l-l, and (c) in the region of line m-m; see colorbar for u_n. Regions with relatively small u_n values (sometimes even turning backwards) of Kelvin Helmholtz-type Coherent Structures (KHCS) are highlighted by yellow crosses. The KHCS height is given by h_{cs}. The sense of rotation and the size of the KHCS are indicated by the curved arrows.
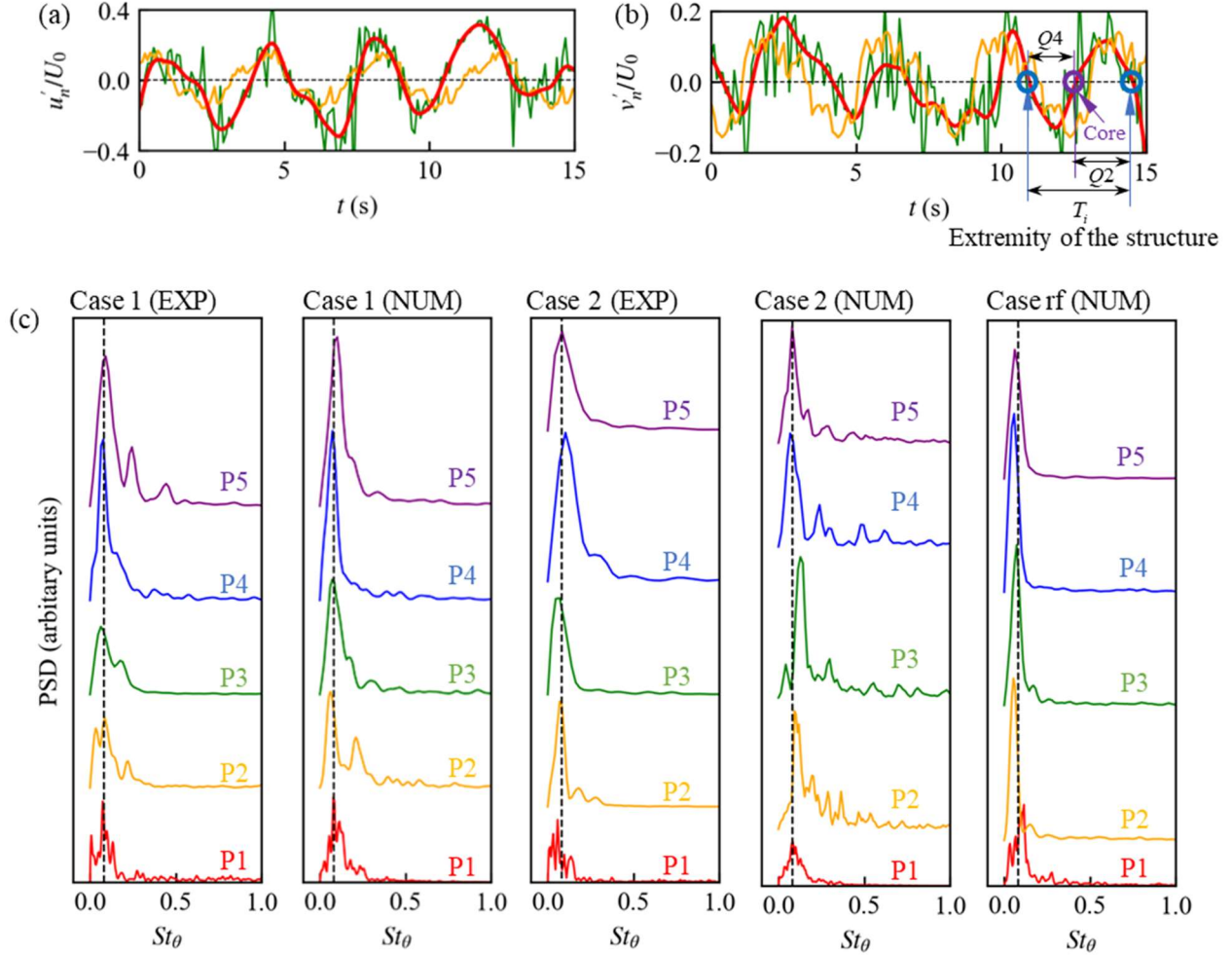
Figure 2.10 (a) and (b): Fluctuating velocities measured at P1 (for location of P1, see Fig. 2.6b) for experimental Case 1. Green lines: raw data. Red lines: low-pass filtered data. Orange lines: conditionally-averaged data. Horizontal dashed lines represent zero. $Q2$: Quadrant 2 (ejection), $Q4$: Quadrant 4 (sweep). (c) Power spectral density of experimental (EXP) and numerical (NUM) velocity fluctuations at locations P1–P5 as a function of the nondimensionalized frequency, i.e., Strouhal number, for Cases 1, 2 and rf (for locations of P1–5, see Fig. 2.6a, b). The vertical dashed lines represent $St_\theta = 0.079$.
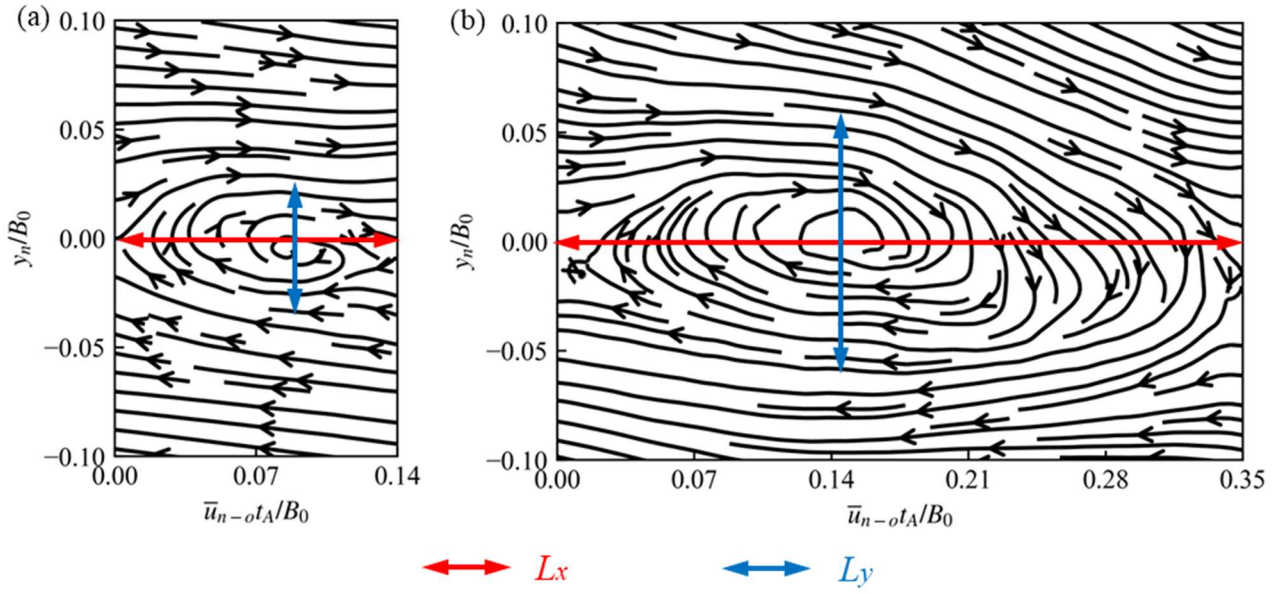
Figure 2.11 Streamlines of the conditionally-averaged velocity field relative to a reference frame moving with the Kelvin Helmholtz-type Coherent Structures (KHCS). (a) Structure passing line *l-l*. (b) Structure passing line *m-m*. Results are based on experimental data from Case 1; for location of lines *l-l* and *m-m,* see Fig. 2.6b. *Lx* and *Ly* give the dimensions of the KHCS along (red) and across (blue) the interface between the jet and the ambient waters. Note that *Lx* and *Ly* are scaled differently.

Low-pass filtered or conditionally-averaged flow fields were used to calculate Reynolds stress and second-order terms in P_n (i.e., $\overline{u'_n u'_n}$, $\overline{u'_n v'_n}$, $\overline{v'_n v'_n}$) associated with KHCS (Fig. 2.12). Based on the low-pass filtering method, low-frequency signals contribute 78% and 79% of the total momentum exchange at P1 and P4, respectively. These values change, respectively, to 63% and 68%, if the conditionally-averaged method is applied. For the production of TKE, the integral of P_n from $y_n/B_0 = -0.15$ to 0.15 was calculated. Based on the low-pass filtering method, the low-frequency signals contributed 72% and 79% to the total production at lines *l-l* and *m-m*, respectively. If the conditional-averaging method is applied, these values are 45% and 50%, respectively.

The processed velocity data obtained by the two abovementioned methods are compared in Fig. 2.10a and b. Using the low-pass filter, the velocity signals are

smoothed, but the variations of the KHCS are preserved, i.e., the three KHCS identified in Fig. 2.10b have slight differences in terms of time period and fluctuation amplitude. Such variability of KHCS is smoothed out when the conditionally-averaged method is used. This explains why KHCS-associated momentum exchange and production based on conditionally-averaged data are underestimated.
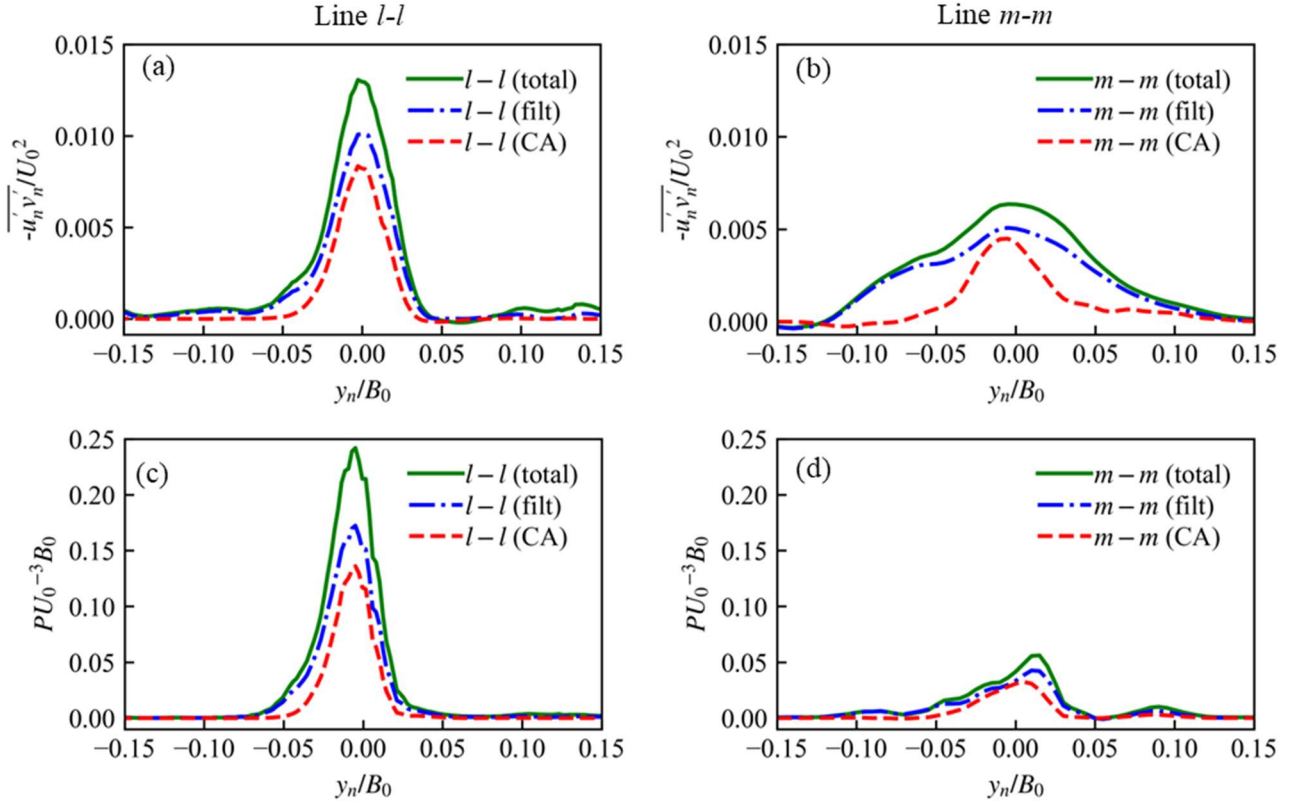
Figure 2.12 Horizontal Reynolds stress (top panels) and production of turbulent kinetic energy (bottom panels) induced by the Kelvin Helmholtz-type coherent structures compared to total horizontal Reynolds stress and production for experimental Case 1. Left panels: along line *l-l*. Right panels: along line *m-m* (for location, see Fig. 2.6b). Green solid lines: total values. Blue dashed-dotted lines: low-pass filtered values (filt). Red dashed lines: conditionally-averaged values (CA).

2.3.4.3 Vertical extension of KHCS

The vertical thickness of the plane jet for the horizontal-bottom case remains constant (equal to H_0; Fig. 2.4e, blue dashed line). The jet over a sloping bottom, on the other

hand, spreads vertically with increasing water depth (Fig. 2.4e, blue line). Therefore, the vertical thickness (h_{cs}) of KHCS increases with the increase of jet thickness (Fig. 2.9). KHCS are characterized by regions with relatively small u_n (sometimes even turning backwards; see yellow crosses in Fig. 2.9b and c). In addition to autocorrelations of the modeled concentration c at P1 and P4 (at $z_c/H_0 = –0.5$), cross-correlations R_{zz} with points at different depths are determined (Bagherimiyab & Lemmin, 2018; Nezu & Nakagawa, 1993) as:

$$R_{zz}\left(x,y,z_c:z,\sigma\right) = \frac{\overline{c'\left(x,y,z_c,t\right)c'\left(x,y,z,t+\sigma\right)}}{\sqrt{\overline{\left[c'\left(x,y,z_c,t\right)\right]^2}\overline{\left[c'\left(x,y,z,t+\sigma\right)\right]^2}}} \tag{2.6}$$

where σ is the time lag, and c' is concentration fluctuation. The cross-correlation decreases with increasing distance between the locations (Fig. 2.13a, b), indicating that coherence is gradually lost. However, the loss of coherence at P4 (Fig. 2.13b) is more gradual than at P1 (Fig. 2.13a), confirming that the vertical thickness of the coherent structures increases with increasing distance from the channel mouth. Using $R_{zz} = 0.3$ as a threshold, the KHCS thickness increases from $1.25H_0$ (73% of local depth) at P1 to $2.75H_0$ (72% of local depth) at P4. The correlation time scale at P4 is longer than at P1. Moreover, a progressively larger positive time shift is observed when z increases. A positive time shift indicates that the concentration signal at a higher location correlates with the signal at a lower location at a later time. This suggests that the coherent structures are inclined, since $\overline{u}_n$ is comparatively larger close to the water surface (Fig. 2.13c).
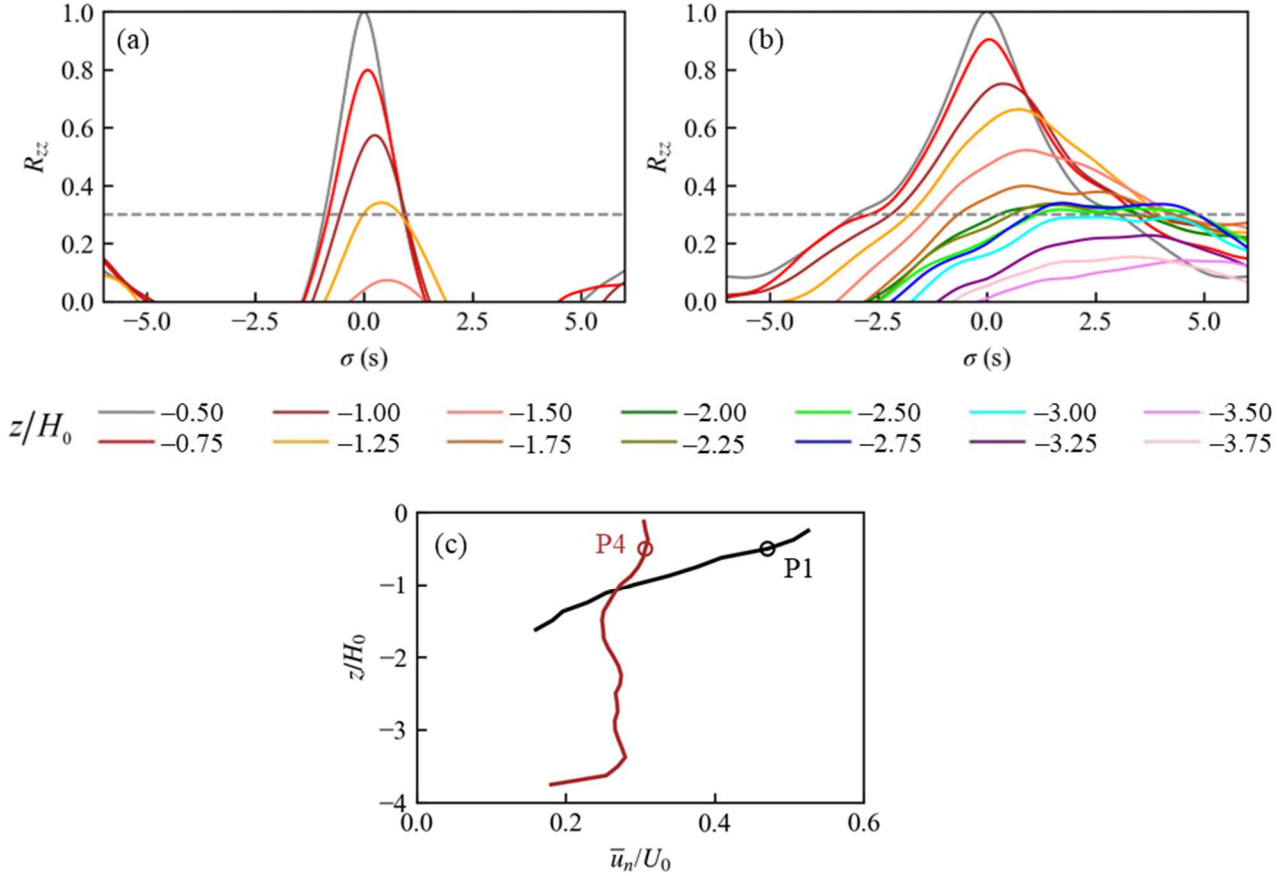
Figure 2.13 Autocorrelation for concentration signals at $z_c/H_0 = -0.5$ and cross-correlation values between $z_c/H_0 = -0.5$ and locations below $z_c/H_0 = -0.5$, at: (a) P1 and (b) P4. The correlation values are calculated based on numerical data over 200 s (100 Hz) for Case 1. Horizontal dashed lines: threshold $R_{zz} = 0.3$. (c) Vertical profiles of the velocity $\bar{u}_n$ passing through points P1 (black line) and P4 (brown line); the points are marked by circles on the profiles (for location, see Fig. 2.6b).

2.3.5 Merging of lateral shear layers

When the jet reaches the established flow zone, the two shear layers meet and merge at the centerline (Fig. 2.6a, b). After the shear layers merge, the jet may manifest a "flag-like" flapping motion (Antonia et al., 1983; Cohen, 2012; Oler & Goldschmidt, 1982; Rowland et al., 2009). Comparing the times series of depth-averaged concentration (c_d) at $x/x_T = 0.5$ and $x/x_T = 1$ for Case 1 and Case rf (Fig. 2.14), it can be seen that at $x/x_T = 0.5$, for both cases, the central part of the jet is stable and the KHCS only generate

fluctuations at the sides of the jet. At $x/x_T = 1$, however, the jet flaps, showing a meandering pattern. The frequency of the jet flapping motion (f_j) was obtained from spectral analysis of the velocity at the centerline (i.e., the peak of PSD of the depth-averaged transversal velocity signal at $x/x_T = 1$, $y = 0$). It is usually nondimensionalized as $f_j b/U_c$ (Jirka, 2001) or $f_j b_0/U_0$ (Cohen, 2012; Deo et al., 2007), and ranges between 0.08 and 0.5 (Cohen, 2012). The numerical results gave $f_j b/U_c \sim 0.3$ for both Case 1 and Case rf, within the range reported in the literature. The jet flapping motion also brings ambient water to the centerline (Fig. 2.14d), resulting in a decreased depth-averaged concentration at ($x/x_T = 1$, $y = 0$) in Case 1 (equal to 0.86 after time-averaging). In contrast, the jet flapping motion in Case rf is not strong enough to influence the centerline concentration, and at ($x/x_T = 1$, $y = 0$), the time-averaged concentration is still equal to 1. Previous studies pointed out that the instability of a jet is related to aspect ratio b/H and bottom friction (Canestrelli et al., 2014; Jirka, 1994; Socolofsky & Jirka, 2004), i.e., the jet flapping motion is expected to be stronger with a smaller aspect ratio and smaller bottom friction. The main difference between Case 1 and Case rf is the aspect ratio at $x/x_T = 1$, which is only $b/H = 1.2$ in Case 1, but can be as large as $b/H = 37.5$ in Case rf.
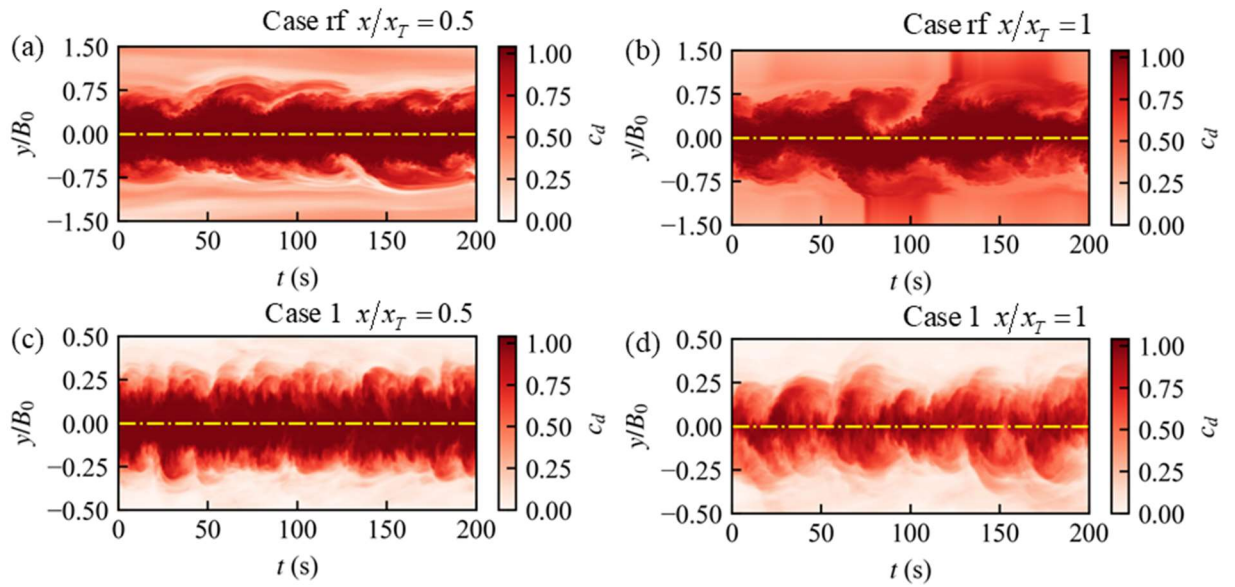

Figure 2.14 Time series of depth-averaged instantaneous concentration at $x/x_T = 0.5$ (left panels) and $x/x_T = 1$ (right panels) for Case rf (top panels) and Case 1 (bottom panels).

Colorbars: range of the concentration. Yellow dash-dotted lines represent the centerline: $y/B_0 =$ 0.

2.4 Summary and Conclusions

This paper presents the first laboratory study that documents the evolution of an initially shallow, neutrally-buoyant tidal jet, bounded by a sloping, solid bottom boundary and an upper free surface, that issues into a laterally-unconfined, quiescent ambient. A 3D numerical model using Large Eddy Simulation (LES) was developed and validated with the experimental data. Furthermore, a comparison was made with a plane jet flowing over a horizontal bottom with the same flow conditions. Based on the experimental and numerical results, the following conclusions can be drawn:

Mean field development and turbulence characteristics

- In the nearfield, the transverse profile of the longitudinal jet velocity transforms from a top-hat profile (flow establishment zone) into a Gaussian distribution (established flow zone) for sloping bottom and horizontal bottom jets.

- For the sloping bottom jet, the transition to the Gaussian distribution occurs at a distance from the channel mouth which is 0.4 times that of the horizontal bottom jet. Thus, the length of the flow establishment zone is significantly reduced for the sloping bottom jet.

- Shear layers develop and grow on both sides of the jet due to the presence of the velocity gradient between the jet and ambient water for both types of jets.

- Different from a plane jet over a horizontal bottom, the jet over a sloping bottom spreads vertically. Under the combined influence of the vertical spreading and lateral entrainment, the jet first contracts and then spreads laterally.

- Different from existing analytical models that assume a constant centerline velocity in the nearfield of sloping bottom jets, the vertical spreading actually results in an abrupt decrease of centerline velocity near the channel mouth, since fluid momentum also spreads in the vertical direction. This is also different from the horizontal bottom jet where the centerline velocity remains constant.

- Turbulence exhibits significant anisotropy in both jets and strong signals of

turbulent kinetic energy are observed in the shear layers.

- The momentum thickness of the shear layers increases with distance in the flow establishment zone and then remains almost constant thereafter in the sloping bottom case. In the horizontal bottom case, however, the momentum thickness continuously increases in the flow establishment zone and in the established flow zone.

Kelvin Helmholtz-type coherent structures

- In the shear layers, Kelvin Helmholtz-type Coherent Structures (KHCS) are generated, resulting in quasi-periodic velocity fluctuations at the interface between the jet and ambient water. A nearly constant Strouhal number of ~0.079 is observed for KHCS in horizontal bottom and sloping bottom jets.

- Different from the horizontal bottom jet, the size of KHCS in the sloping bottom jet increases with increasing distance from the channel mouth, not only horizontally, but also vertically because of the vertical spreading of the jet.

- KHCS in sloping bottom jets are the main contributor to momentum exchange and production of turbulent kinetic energy inside shear layers, consistent with previous studies on 2D shear layers.

- After the shear layers merge at the centerline (at around $x/x_T = 1$), both jets start flapping. However, the flapping motion of the jet over the sloping bottom is strong enough to influence the centerline concentration, whereas it is not for the jet over the horizontal bottom.

This study demonstrates that unlike the horizontal bottom jet that behaves like a (quasi) 2D plane jet, the flow field of the sloping bottom jet is clearly 3D. These experimentally-verified results can be expected to have broad applications, in particular, those of the sloping bottom case, since they resemble ebb tide flows away from harbors, and 85% of nearshore slopes are reported to be < 8°, the slope angle of this investigation.

Acknowledgements

Open Research

Data reported in this paper can be downloaded from the following link in zenodo: https://doi.org/10.5281/zenodo.8183701.

References

Antonia, R. A., Browne, L. W. B., Rajagopalan, S., & Chambers, A. J. (1983). On the organized motion of a turbulent plane jet. *Journal of Fluid Mechanics*, *134*(1), 49-66. https://doi.org/10.1017/S0022112083003213

Athanasiou, P., van Dongeren, A., Giardino, A., Vousdoukas, M., Gaytan-Aguilar, S., & Ranasinghe, R. (2019). Global distribution of nearshore slopes with implications for coastal retreat. *Earth System Science Data*, *11*, 1515–1529. https://doi.org/10.5194/essd-11-1515-2019

Bagherimiyab, F., & Lemmin, U. (2018). Large-scale coherent flow structures in rough-bed open-channel flow observed in fluctuations of three-dimensional velocity, skin friction and bed pressure. *Journal of Hydraulic Research*, *56*(6), 806–824. https://doi.org/10.1080/00221686.2017.1416686

Broekema, Y. B., Labeur, R. J., & Uijttewaal, W. S. J. (2018). Observations and analysis of the horizontal structure of a tidal jet at deep scour holes. *Journal of Geophysical Research: Earth Surface*, *123*(12), 3162–3189. https://doi.org/10.1029/2018JF004754

Brown, G. L., & Roshko, A. (1974). On density effects and large structure in turbulent mixing layers. *Journal of Fluid Mechanics*, *64*(4), 775–816. https://doi.org/10.1017/S002211207400190X

Canestrelli, A., Nardin, W., Edmonds, D., Fagherazzi, S., & Slingerland, R. (2014). Importance of frictional effects and jet instability on the morphodynamics of river mouth bars and levees. *Journal of Geophysical Research: Oceans, 119*(1), 509–522. https://doi.org/10.1002/2013JC009312

Cohen, C. (2012). Shallow-water plane and tidal jets. Unpublished Ph.D. thesis. *University of Otago*. Otago, New Zealand. https://ourarchive.otago.ac.nz/handle/10523/2493

De Lorenzis, L., & Düster, A. (2020). Modeling in engineering using innovative numerical methods for solids and fluids. CISM International Centre for Mechanical Sciences (Vol. 599). *Springer International Publishing*, Cham, Switzerland. https://doi.org/10.1007/978-3-030-37518-8

Deo, R. C., Mi, J., & Nathan, G. J. (2007). The influence of nozzle-exit geometric profile on statistical properties of a turbulent plane jet. *Experimental Thermal and Fluid Science*, *32*(2), 545–559. https://doi.org/10.1016/j.expthermflusci.2007.06.004

Deo, R. C., Mi, J., & Nathan, G. J. (2008). The influence of Reynolds number on a plane jet. *Physics of Fluids, 20*, 075108. https://doi.org/10.1063/1.2959171

Dimotakis, P. E. (1991). Turbulent free shear layer mixing and combustion. In: High Speed Flight Propulsion Systems (pp. 265–340). *American Institute of Aeronautics and Astronautics*. Washington DC, USA. https://doi.org/10.2514/4.866104

Dracos, T., Giger, M., & Jirka, G. H. (1992). Plane turbulent jets in a bounded fluid layer. *Journal of Fluid Mechanics*, *241*, 587–614. https://doi.org/10.1017/S0022112092002167

Fujiwara, T., Nakata, H., & Nakatsuji, K. (1994). Tidal-jet and vortex-pair driving of the residual circulation in a tidal estuary. *Continental Shelf Research*, *14*(9), 1025–1038. https://doi.org/10.1016/0278-4343(94)90062-0

Giger, M., Dracos, T., & Jirka, G. H. (1991). Entrainment and mixing in plane turbulent jets in shallow water. *Journal of Hydraulic Research, 29*(5), 615–642. https://doi.org/10.1080/00221689109498980

Hearn, C., Hunter, J., Imberger, J., & Senden, D van. (1985). Tidally induced jet in Koombana Bay, Western Australia. *Marine and Freshwater Research*, *36*(4), 453-479. https://doi.org/10.1071/MF9850453

Heskestad, G. (1965). Hot-wire measurements in a plane turbulent jet. *Journal of Applied Mechanics*, *32*(4), 721–734. https://doi.org/10.1115/1.3627309

Hinze, J. O. (1975). Turbulence (2nd Edition). *McGraw-Hill Inc.* US. https://openlibrary.org/books/OL5186579M/Turbulence

Ho, C. M, & Huerre, P. (1984). Perturbed free shear layers. *Annual Review of Fluid Mechanics*, *16*(1), 365–422. https://doi.org/10.1146/annurev.fl.16.010184.002053

Ho, C. M., & Huang, L. S. (1982). Subharmonics and vortex merging in mixing layers. *Journal of Fluid Mechanics*, *119*, 443–473. https://doi.org/10.1017/S0022112082001438
Huai, W. X., Zhang, J., Wang, W. J., & Katul, G. G. (2019). Turbulence structure in open channel flow with partially covered artificial emergent vegetation. *Journal of Hydrology*, *573*, 180–193. https://doi.org/10.1016/j.jhydrol.2019.03.071

Jasak, H. (2009). OpenFOAM: Open source CFD in research and industry. *International Journal of Naval Architecture and Ocean Engineering*, *1*(2), 89–94. https://doi.org/10.2478/IJNAOE-2013-0011

Jiménez-Robles, A. M., Ortega-Sánchez, M., & Losada, M. A. (2016). Effects of basin bottom slope on jet hydrodynamics and river mouth bar formation. *Journal of Geophysical Research: Earth Surface*, *121*(6), 1110–1133. https://doi.org/10.1002/2016JF003871

Jirka, G. H. (1994). Shallow jets. In: Davies, P.A., Neves, M.J.V. (eds). Recent research advances in the fluid mechanics of turbulent jets and plumes: Vol. 255. (pp. 157–175). *Springer.* Dordrecht. https://doi.org/10.1007/978-94-011-0918-5_10

Jirka, G. H. (2001). Large scale flow structures and mixing processes in shallow flows. *Journal of Hydraulic Research*, *39*(6), 567–573. https://doi.org/10.1080/00221686.2001.9628285

Landel, J. R., Caulfield, C. P., & Woods, A. W. (2012). Meandering due to large eddies and the statistically self-similar dynamics of quasi-two-dimensional jets. *Journal of Fluid Mechanics, 692*, 347–368. https://doi.org/10.1017/jfm.2011.518

Lee, H., & Yu, W. (1997). Experimental study of reservoir turbidity current. *Journal of Hydraulic Engineering*, *123*(6), 520–528.https://doi.org/10.1061/(ASCE)0733-9429(1997)123:6(520)

Li, D., Liu, M., & Huai, W. (2022). Modeling transverse momentum exchange in partially vegetated flow. *Physics of Fluids*, *34*(2), 025124. https://doi.org/10.1063/5.0081202

Nezu, I., & Nakagawa, H. (1993). Turbulence in Open-Channel Flows. *IAHR,* A.A. Balkema, Rotterdam, Netherlands. https://doi.org/10.1201/9780203734902

Odier, P., Chen, J., & Ecke, R. E. (2012). Understanding and modeling turbulent fluxes and entrainment in a gravity current. *Physica D: Nonlinear Phenomena, 241*(3), 260–268. https://doi.org/10.1016/j.physd.2011.07.010

Old, C. P., & Vennell, R. (2001). Acoustic Doppler current profiler measurements of the velocity field of an ebb tidal jet. *Journal of Geophysical Research: Oceans*, *106*(C4), 7037–7049. https://doi.org/10.1029/1999JC000144

Oler, J. W., & Goldschmidt, V. W. (1982). A vortex-street model of the flow in the similarity region of a two-dimensional free turbulent jet. *Journal of Fluid Mechanics, 123,* 523–535. https://doi.org/10.1017/S0022112082003188

Onishi, S. (1984). Study of vortex structure in water surface jets by means of remote sensing. *Elsevier Oceanography Series, 38*, 107-132. https://doi.org/10.1016/S0422-9894(08)70607-X

Ortega-Sánchez, M., Losada, M. A., & Baquerizo, A. (2008). A global model of a tidal jet including the effects of friction and bottom slope. *Journal of Hydraulic Research*, *46*(1), 80–86. https://doi.org/10.1080/00221686.2008.9521845

Özsoy, E., & Ünlüata, Ü. (1982). Ebb-tidal flow characteristics near inlets. *Estuarine, Coastal and Shelf Science, 14*(3), 251-IN3. https://doi.org/10.1016/S0302-3524(82)80015-7

Pope, S. B. (2000). Turbulent flows. *Cambridge University Press.* UK. https://doi.org/10.1017/CBO9780511840531

Rogers, M. M., & Moser, R. D. (1992). The three-dimensional evolution of a plane mixing layer: The Kelvin–Helmholtz rollup. *Journal of Fluid Mechanics*, *243*(1), 183-226. https://doi.org/10.1017/S0022112092002696

Rowland, J. C., Stacey, M. T., & Dietrich, W. E. (2009). Turbulent characteristics of a shallow wall-bounded plane jet: Experimental implications for river mouth hydrodynamics. *Journal of Fluid Mechanics*, *627*, 423–449. https://doi.org/10.1017/S0022112009006107

Shi, H., Negretti, M. E., Chauchat, J., Blanckaert, K., Lemmin, U., & Barry, D. A. (2022). Unconfined plunging of a hyperpycnal river plume over a sloping bed and its lateral spreading: Laboratory experiments and numerical modeling. *Water Resources Research*, *58*. e2022WR032633. https://doi.org/10.1029/2022WR032633

Shi, H., Zhang, J., & Huai, W. (2023). Experimental study on velocity distributions, secondary currents, and coherent structures in open channel flow with submerged riparian vegetation. *Advances in Water Resources*, *173*, 104406. https://doi.org/10.1016/j.advwatres.2023.104406

Shih, T. H., Liou, W. W., Shabbir, A., Yang, Z., & Zhu, J. (1995). A new k-ϵ eddy viscosity model for high Reynolds number turbulent flows. *Computers & Fluids*, *24*(3), 227–238. https://doi.org/10.1016/0045-7930(94)00032-T

Shiono, K., & Knight, D. W. (1991). Turbulent open-channel flows with variable depth across the channel. *Journal of Fluid Mechanics*, *222*(1), 617-646. https://doi.org/10.1017/S0022112091001246

Socolofsky, S. A., & Jirka, G. H. (2004). Large-scale flow structures and stability in shallow flows. *Journal of Environmental Engineering and Science, 3*(5), 451–462. https://doi.org/10.1139/s04-032

Spiers, K. C., Healy, T. R., & Winter, C. (2009). Ebb-jet dynamics and transient eddy formation at Tauranga Harbour: Implications for entrance channel shoaling. *Journal of Coastal Research, 25*(1), 234–247. https://doi.org/10.2112/07-0947.1

Taborda, C., Fael, C., Ricardo, A. M., & Ferreira, R. M. L. (2022). Wave-like motion and secondary currents in arrays of emergent cylinders induced by large scale eddying motion. *Environmental Fluid Mechanics, 22*(2–3), 403–428. https://doi.org/10.1007/s10652-022-09863-4

Thomas, F. O., & Goldschmidt, V. W. (1986). Structural characteristics of a developing turbulent planar jet. *Journal of Fluid Mechanics, 163*, 227–256. https://doi.org/10.1017/S0022112086002288

Truong, S. H., & Uijttewaal, W. S. J. (2019). Transverse momentum exchange induced by large coherent structures in a vegetated compound channel. *Water Resources Research*, *55*, 589–612. https://doi.org/10.1029/2018WR023273

Vennell, R. (2006). ADCP measurements of momentum balance and dynamic topography in a constricted tidal channel. *Journal of Physical Oceanography, 36*(2), 177–188. https://doi.org/10.1175/JPO2836.1

Weller, H. G., Tabor, G., Jasak, H., & Fureby, C. (1998). A tensorial approach to computational continuum mechanics using object-oriented techniques. *Computers in Physics*, *12*(6), 620-631. https://doi.org/10.1063/1.168744

White, B. L., & Nepf, H. M. (2008). A vortex-based model of velocity and shear stress in a partially vegetated shallow channel. *Water Resources Research*, *44*, W01412. https://doi.org/10.1029/2006WR005651

Yuan, Y., & Horner-Devine, A. R. (2017). Experimental investigation of large-scale vortices in a freely spreading gravity current. *Physics of Fluids, 29*(10), 106603. https://doi.org/10.1063/1.5006176

Supporting Information for Chapter 2

Table of Contents

Text S2.1 Laboratory experiments

S2.1.1 Experimental setup

The tank was first filled with water to a depth of 0.75 m such that the water depth inside the inflow channel was $H_0 = 0.08$ m. Then, fluid with the same density was injected at constant water discharge Q_0 through a gravity feeding system to the upstream end of the inflow channel via two injectors. An array of plastic vertical cylinders (Fig. 2.1c) over the full depth of the channel was placed in the upstream portion of the channel, followed by a 0.5-m long honeycomb 1.5-m upstream from the downstream end of the channel. These elements ensured a near-uniform velocity distribution across the channel width and a fully developed turbulent flow near the downstream end of the inlet channel, which was confirmed by preliminary measurements taken with an Acoustic Doppler Velocimeter (ADV; see Shi et al., 2022 for further details). Three outlet drains positioned at the sides and below the sloping boundary on the tank floor were used to maintain the water depth inside the channel and in the tank by extracting water at the same volume flux as the inflow (Q_0) without disturbing the jet flow. Measurements started 6 min after the commencement of the experiment, to make sure the jet had reached steady state.

The Particle Image Velocimetry (PIV) system consisted of a light source, light sheet optics, seeding particles, cameras and PCs equipped with a frame grabber and image acquisition software. Horizontal laser sheets scanning a two-dimensional (2D) field of view of -0.1 m $< x <$ 3.3 m by -2.26 m $< y <$ 2.30 m were used to measure the horizontal plane at $z/H_0 = -0.5$. Images of 4.5 m $\times$ 3.5 m were taken with a high-resolution SCMOS camera (JAI SP12000, resolution of 4096 $\times$ 3072 pixels) at a frame rate of 10 Hz. The measurements were performed twice; each time 450 images were taken over 45 s (in total, 900 images). Velocity fields obtained from the PIV measurements were computed using a cross-correlation PIV algorithm (UVMAT, http://servforge.legi.grenoble-inp.fr/projects/soft-uvmat). An adaptive multi-pass routine was used, overlapping 70% of an interrogation window of 45 $\times$ 21 pixels, resulting in a spatial resolution of ~0.01 m $\times$ 0.01 m.

S2.1.2 Error analysis of velocity data

Three sources of error in the PIV measurements were analyzed: velocity gradients, particle diameter, and Adaptive Gaussian Window (AGW) interpolation, using the results of Cowen et al. (1997) and Prasad et al. (1992). The error from the velocity gradients was estimated by computing the mean values of the largest velocity gradients in the streamwise and spanwise directions from the raw PIV data (about 2%). The particles used in the experiments had a size of 60 μm, giving a non-dimensional particle diameter of 0.06 pixels/pixel. Note that particles smaller than one pixel always occupy one pixel in a PIV image; thus, the true position of a particle within a pixel cannot be resolved. According to Fig. 13 in Prasad et al. (1992), errors associated with a particle diameter of 0.06 pixels are 20% larger than the errors associated with a particle diameter of 1 pixel. However, light defocusing of the camera helped to increase the optical size of the particle, resulting in particles that were globally larger than one pixel. The error due to AGW interpolation was estimated from Fig. 5f of Cowen and Monismith (1997). The total error in the velocity arising from velocity gradients, particle size, and AGW interpolation was then estimated to be ~0.176 pixels. Given the range of velocities in the experiments, the experimental error in the instantaneous velocity would range between 1% and 6%. An error of 6% is the worst-case scenario for slow velocities. The PIV correlations were also computed doubling the time step, thus increasing the displacement between the two considered images. The velocity difference using the two methods was less than 3%. Therefore, the average error in the instantaneous velocity field measurements was estimated to be ~3%.

Text S2.2 Numerical model configuration

The numerical model solves the following governing equations,

$$\nabla \cdot \langle \mathbf{u} \rangle = 0 \qquad (S2.1)$$

$$\frac{\partial \langle \mathbf{u} \rangle}{\partial t} + \nabla \cdot \left(\langle \mathbf{u} \rangle \otimes \langle \mathbf{u} \rangle \right) = -\nabla \left(\frac{\langle p \rangle}{\rho_0} \right) + \frac{1}{\rho_0} \nabla \cdot \left(\boldsymbol{\tau} + \boldsymbol{\tau_t} \right) + \mathbf{g} \qquad (S2.2)$$

where $\langle ... \rangle$ denotes the LES space scale filter (a filter based on grid size is applied), **u**

the velocity vector, t time, p pressure, $\boldsymbol{\tau}$ resolved stress tensor, $\boldsymbol{\tau}_t$ sub-grid scale (SGS) turbulent stress tensor, ρ_0 fluid density and $\mathbf{g}$ gravitational acceleration. A conservative tracer was added into the numerical model, whose transportation and mixing were described by,

$$\frac{\partial \langle c \rangle}{\partial t} + \mathbf{u} \cdot \nabla \langle c \rangle = \nabla^2 \left(\alpha_{eff} \langle c \rangle \right) \tag{S2.3}$$

In solving Eq. S.2.3, concentrations were normalized such that $c = 1$ is the concentration in the inflow channel and $c = 0$, the initial concentration of the ambient water. The effective diffusivity is given by $\alpha_{eff} = v/Sc + v_t/Sc_t$, with $Sc = v/D$ being the Schmidt number and $Sc_t = v_t/K$, the turbulent Schmidt number. Here, v and D respectively denote molecular viscosity and diffusivity, v_t turbulent viscosity and K turbulent diffusivity. Sc was assumed to be unity in the model since molecular diffusion was negligible (Ooi et al., 2009). The model used $Sc_t = 0.85$ following Shi et al. (2022), which is within the range (0.7–0.9) commonly used in the literature (Tominaga and Stathopoulos, 2007). Numerical results were not sensitive to Sc_t according to preliminary tests.

The dynamic one-equation eddy viscosity Sub-Grid-Scale (SGS) model (*dynamicKEqn*) was applied to solve the filtered Navier-Stokes equations (Kim and Menon, 1995). Below, the terms in italics are functions and submodules in OpenFOAM. A transient solver for incompressible turbulent flow, "*BuoyantBoussinesqPimpleFoam*", was used. Considering that the jet is neutrally buoyant, the thermal expansion coefficient was set to be zero. The same boundary conditions as in Shi et al. (2022) were applied.

For the inlet, the inflow velocity was assumed to follow a log-wake law in the vertical direction (obtained from the ADV measurements) and to be uniform in the transverse direction. The Divergence Free Synthetic Eddy Method (*turbulentDFSEMInlet*) was applied to impose synthetic eddies at the inlet in order to generate a similar turbulent intensity as measured in the experiments. For the outlet, *inletoutlet* (a generic outflow condition with specified inflow if there are return flows) for velocity and *advective* (advective outflow condition) for tracer concentration were applied. The free surface

was treated as a rigid lid and set as a slip boundary. For the bottom and side walls, slip boundary conditions for the inlet channel and no-slip boundary conditions for the receiving tank were used.

Grids near the bottom boundary were refined to reach a $\delta_z^+ = u_*\delta_z/v$ close to 1, where δ_z denotes the vertical size of the cell close to the bottom boundary and u_* is the bed shear velocity. Thus, the numerical model can resolve the viscous sublayer close to the bottom boundary. In the horizontal-bottom case (Case rf) for example, the numerical model gives a bed shear stress close to 2×10^{-5} ($m^2\,s^{-2}$) in the flow establishment zone which is equivalent to a Manning coefficient close to 0.01.

The *Gauss linear* scheme (second-order centered) was used for the velocity divergence and all gradient terms, whereas the *Gauss limitedLinear* scheme (a combination of second-order centered and first-order upwind) was applied for the kinetic energy divergence (subgrid scale model) and concentration. The *backward* scheme (second order) was applied for all time derivatives.

Text S2.3 Model validation

S2.3.1 Grid convergence index

The Grid Convergence Index (*GCI*) based on the generalized theory of Richardson Extrapolation is often applied to uniformly report grid-convergence tests (Roache, 1997). In the present study, we carried out the *GCI* analysis based on three different grids for numerical Case 1: fine ($i = 1$), medium ($i = 2$) and coarse ($i = 3$) with a fixed grid-refinement ratio $\Gamma = \sqrt{2}$ (in all the three directions). The fine grid ($7.5 \times 10 \times 5$ mm) was used in the analysis in the main text. Figure S2.1 presents the modeled turbulent kinetic energy ($k = \overline{u'u'} + \overline{v'v'} + \overline{w'w'}$) at $z/H_0 = -0.5$ in the three grids. Differences are clearly observed between the coarse grid and the other two. The integrated value of the turbulent kinetic energy at $z/H_0 = -0.5$ was used for the grid convergence analysis:

$$IT_k = \frac{\int_{x/B_0=0}^{x/B_0=1.6} \int_{y/B_0=-0.6}^{y/B_0=0.6} k\,dxdy}{U_0^2 B_0^2} \tag{S2.4}$$

A monotonic convergence condition is reached when the convergence ratio $0 < \Phi < 1$ (Table S2.1):

$$\Phi = \frac{\varphi_2 - \varphi_1}{\varphi_3 - \varphi_2} \tag{S2.5}$$

where φ_i represents the target parameter calculated from the ith grid. Then, the GCI is calculated using (Roache, 1994):

$$GCI_{i+1,i} = \frac{1.25 \left| \left(\varphi_i - \varphi_{i+1} \right) / \varphi_i \right|}{\Gamma^{\psi} - 1} \tag{S2.6}$$

where ψ is the order of accuracy (Roache, 1997):

$$\xi = \ln \left(\frac{\varphi_3 - \varphi_2}{\varphi_2 - \varphi_1} \right) \Big/ \ln \Gamma \tag{S2.7}$$

As listed in Table S2.1, the $GCI_{2,1}$ is about one order of magnitude smaller than $GCI_{3,2}$ indicating that the calculations are mesh-convergent and further grid refinement will not significantly change the simulation results.

Table S2.1 Grid Convergence Index (GCI)

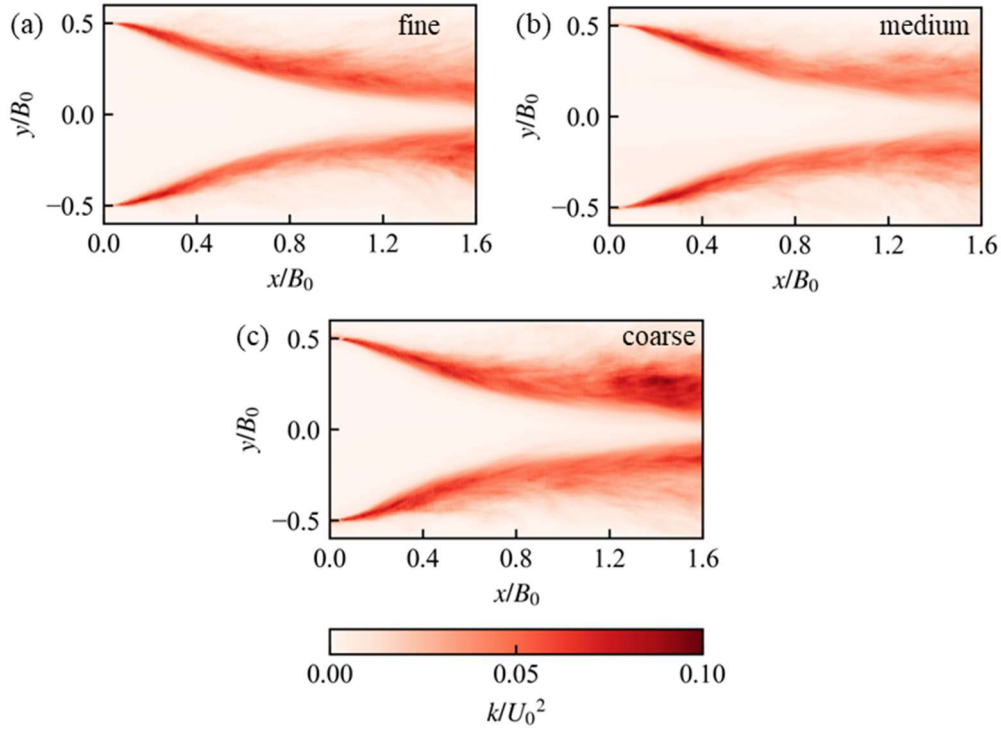|	Fine	Medium	Coarse	Φ	ξ	$GCI_{2,1}$	$GCI_{3,2}$
IT_k ($\times 10^{-3}$)	2.59	2.67	3.52	0.08	7.15	0.003	0.037

Figure S2.1 Turbulent kinetic energy at $z/B_0 = -0.5$ modeled by the numerical model using three different grids (fine, medium, coarse).

S2.3.2 Comparison with Cohen's experiment

The numerical modeling results are compared with the experiment of Cohen (2012), who reported mean and turbulent fields of a shallow plane jet flowing over a horizontal bottom. The geometry of the numerical model was modified according to that experimental setup (a 1.3-m long, 0.25-m wide inlet channel connected with a 4.3-m long, 3-m wide horizontal-bottom tank, see Fig. 4.1 in Cohen, 2012). Data for the experiment with an initial aspect ratio of 1:0.15, $Re_0 = 9,000$ and $Fr_0 = 0.42$ was chosen since both the mean velocity and turbulent intensity data were reported. Figure S2a presents the variation of the centerline longitudinal velocity on the water surface while Fig. S2.2b illustrates the variation of the jet width. These two plots confirm the good capability of the numerical model to simulate the time-averaged velocity field with mean relative errors of 6% and 7% for centerline velocity and jet width, respectively. Figure S2.2c presents the transverse profile of turbulent intensity on the water surface at $x/B_0 = 8.44$ (the furthest profile of the experimental measurement),

nondimensionalized by the centerline velocity $\bar{u}_c$,

$$TI_u = \sqrt{\frac{\overline{u'u'}}{\bar{u}_c^2}} \tag{S2.8}$$

An overall good comparison between the experimental and numerical profiles is obtained (Fig. S2.2c) with a mean relative error of 22%, although the numerical model slightly overestimates the turbulent intensity at the centerline.
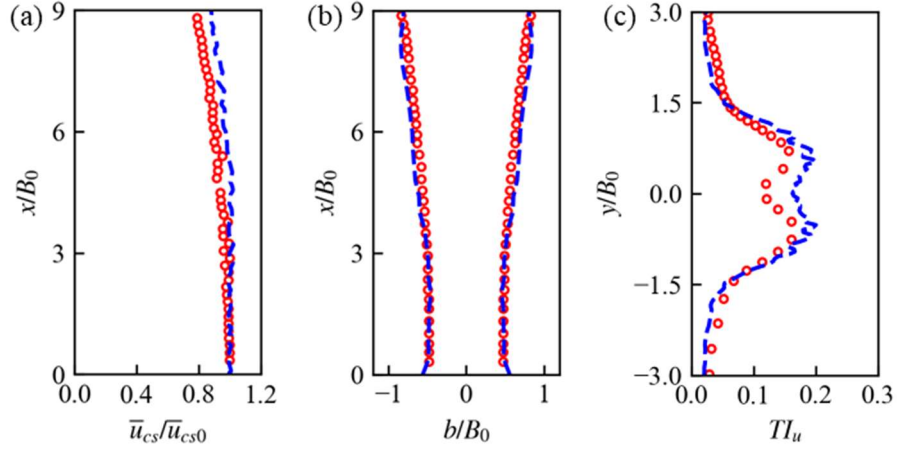
Figure S2.2 Comparison between the numerical results and the experimental data of Cohen (2012). (a) Variation of the centerline velocity on the water surface. (b) Variation of the jet width. (c) Transverse profile of the turbulent intensity at $x/B_0 = 8.44$ on the water surface. Red circles are experimental data and blue curves are numerical results.

Text S2.4 Anisotropy of the jet

Figure S2.3 compares components of the turbulent kinetic energy in numerical Case 1 at $z/H_0 = -0.5$. The vertical component ($\overline{w'w'}$) is much smaller than the horizontal components ($\overline{u'u'}$ and $\overline{v'v'}$) since the shear between the jet and ambient water is mainly produced in the horizontal plane. Horizontal energy ($k_H = \overline{u'u'} + \overline{v'v'}$) contributes 84% of the total turbulent kinetic energy in the plotted region at $z/H_0 = -0.5$. Figure S2.4 presents the turbulent kinetic energy production (with or without vertical components) at $z/H_0 = -0.5$ in numerical Case 1. The two-dimensional production contributes 77% of the total energy production in the plotted region at $z/H_0 = -0.5$, indicating that the two-dimensional PIV measurement captures the main source of turbulent kinetic energy

production. The same analysis was also performed for Case rf (Figs. S2.5 and S2.6) where horizontal energy contributes 94% of the total energy and two-dimensional production contributes 71% of the total production in the plotted region at $z/H_0 = -0.5$.

Figure S2.3 Comparison of the three components (indicated in the upper right corner of the panels) of turbulent kinetic energy in numerical Case 1 at $z/H_0 = -0.5$. x_T marks the location of the transition from the flow establishment zone to the established flow zone.

Figure S2.4 Production of turbulent kinetic energy in numerical Case 1 at $z/H_0 = -0.5$. (a) Two-dimensional production without vertical components. (b) Vertical components. (c) Three-dimensional production. x_T marks the location of the transition from the flow establishment zone to the established flow zone.
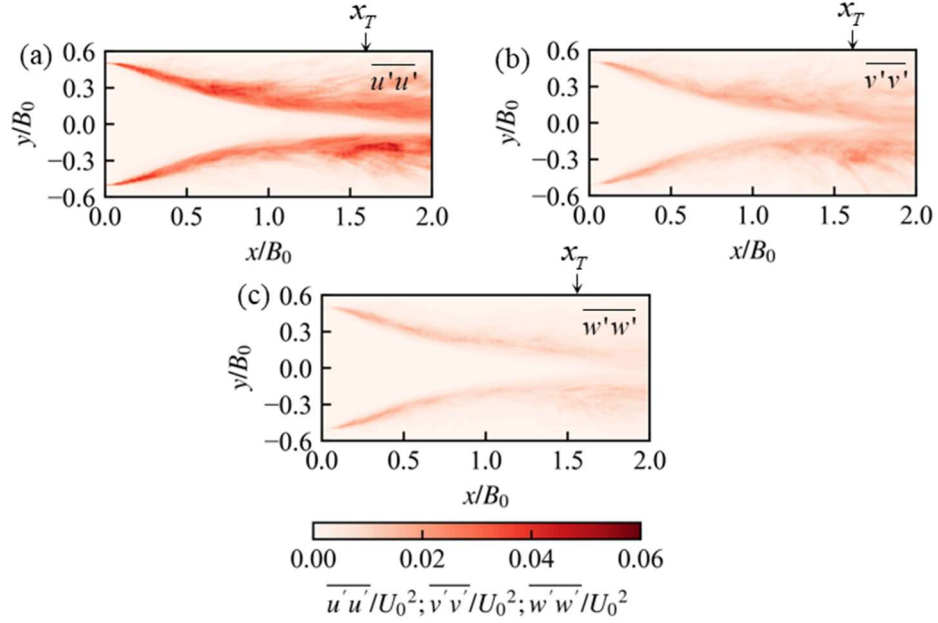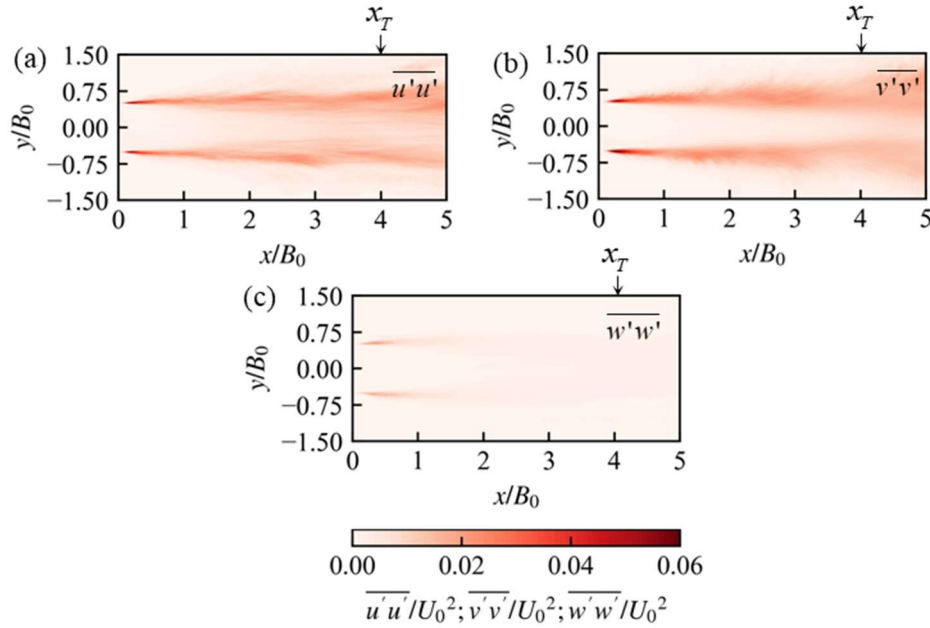

Figure S2.5 Comparison of the three components (indicated in the upper right corner of the panels) of turbulent kinetic energy in numerical Case rf at $z/H_0 = -0.5$. x_T marks the location of the transition from the flow establishment zone to the established flow zone.
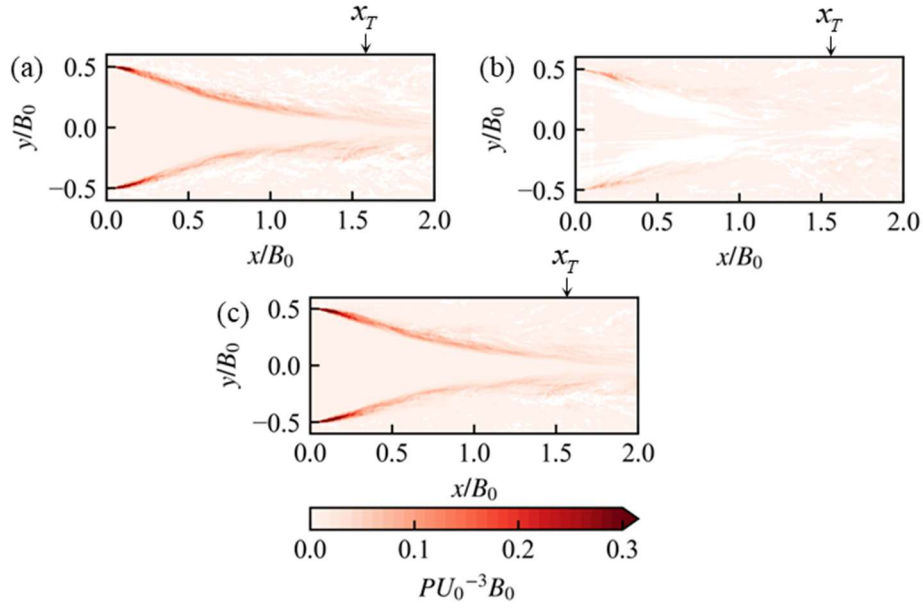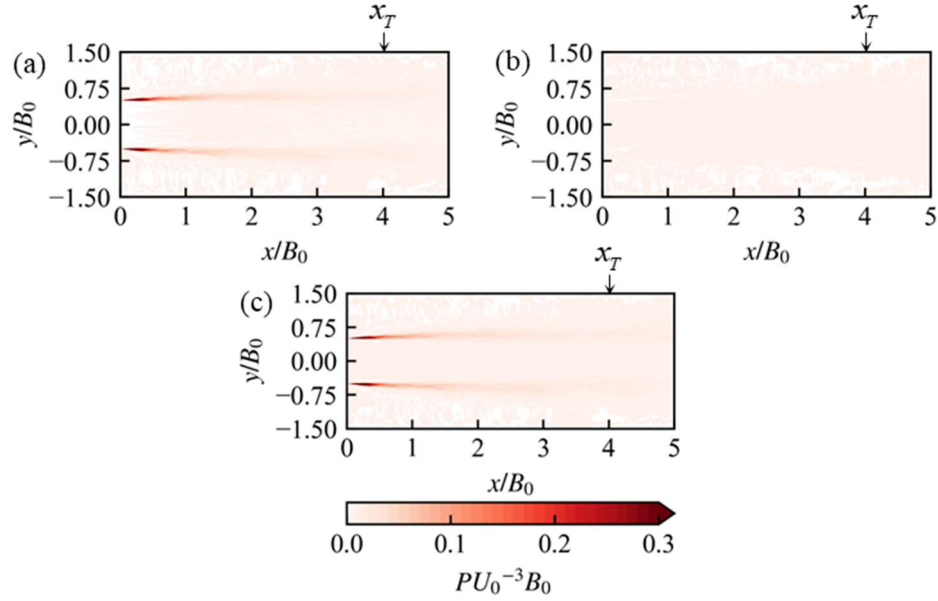
Figure S2.6 Production of turbulent kinetic energy in numerical Case rf at $z/H_0 = -0.5$ for: (a) Two-dimensional production without vertical components, (b) vertical components, and (c) three-dimensional production. x_T marks the location of the transition from the flow establishment zone to the established flow zone.

Text S2.5 Quadrant analysis

The quadrant analysis technique (Bagherimiyab & Lemmin, 2018) divides turbulence into four quadrant events: $Q1$ (outward interaction: $u'_n > 0$ and $v'_n > 0$), $Q2$ (ejection: $u'_n < 0$ and $v'_n > 0$), $Q3$ (inward interaction: $u'_n < 0$ and $v'_n < 0$) and $Q4$ (sweep: $u'_n > 0$ and $v'_n < 0$). This analysis was carried out for the measured velocity data along line l-l in experimental Case 1 (Fig. S2.7), indicating that the Kelvin Helmholtz-type Coherent Structures (KHCS) are predominantly composed of $Q2$ and $Q4$ events, which mainly contribute to the Reynolds stress.
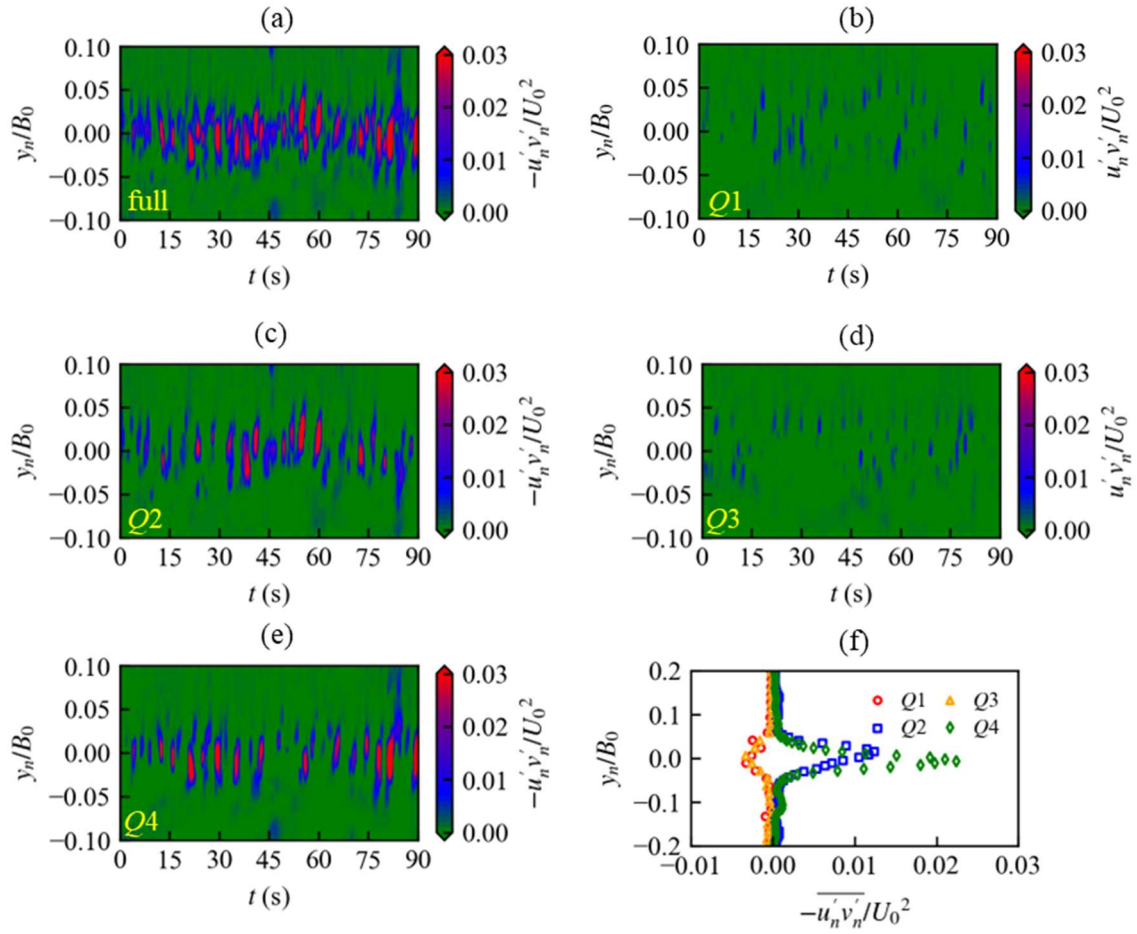
Figure S2.7 Quadrant (Q) analysis along line *l-l* for experimental Case 1. (a)–(e) Time series of the covariance term for: (a) Full dataset, (b) Quadrant 1, (c) Quadrant 2, (d) Quadrant 3, and (e) Quadrant 4. (f) Contribution of the different quadrant events on Reynolds stress. For location of line *l-l,* see Fig. 2.6b in main text.

References

Bagherimiyab, F., & Lemmin, U. (2018). Large-scale coherent flow structures in rough-bed open-channel flow observed in fluctuations of three-dimensional velocity, skin friction and bed pressure. *Journal of Hydraulic Research*, *56*(6), 806–824. https://doi.org/10.1080/00221686.2017.1416686

Cohen, C. (2012). Shallow-water plane and tidal jets. Unpublished Ph.D. thesis. *University of Otago*. Otago, New Zealand. https://ourarchive.otago.ac.nz/handle/10523/2493

Cowen, E. A., Monismith, S. G., Cowen, E. A., & Monismith, S. G. (1997). A hybrid digital particle tracking velocimetry technique. *Experiments in Fluids*, *22*(3), 199–211. https://doi.org/10.1007/s003480050038

Kim, W. W., & Menon, S. (1995). A new dynamic one-equation subgrid-scale model for large eddy simulations. *33rd Aerospace Sciences Meeting and Exhibit*. Reno, Nevada, USA. https://doi.org/10.2514/6.1995-356

Ooi, S. K., Constantinescu, G., & Weber, L. (2009). Numerical simulations of lock-exchange compositional gravity current. *Journal of Fluid Mechanics*, *635*, 361–388. https://doi.org/10.1017/S0022112009007599

Prasad, A. K., Adrian, R. J., Landreth, C. C., & Offutt, P. W. (1992). Effect of resolution on the speed and accuracy of particle image velocimetry interrogation. *Experiments in Fluids*, *13*(2–3), 105–116. https://doi.org/10.1007/BF00218156

Roache, P. J. (1994). Perspective: A method for uniform reporting of grid refinement studies. *Journal of Fluids Engineering*, *116*(3), 405–413. https://doi.org/10.1115/1.2910291

Roache, P. J. (1997). Quantification of uncertainty in computational fluid dynamics. *Annual Review of Fluid Mechanics*, *29*(1), 123–160. https://doi.org/10.1146/annurev.fluid.29.1.123

Shi, H., Negretti, M. E., Chauchat, J., Blanckaert, K., Lemmin, U., & Barry, D. A. (2022). Unconfined plunging of a hyperpycnal river plume over a sloping bed and its lateral spreading: Laboratory experiments and numerical modeling. *Water Resources Research*, *58*, e2022WR032633. https://doi.org/10.1029/2022WR032633

Tominaga, Y., & Stathopoulos, T. (2007). Turbulent Schmidt numbers for CFD analysis with various types of flow field. *Atmospheric Environment*, *41*(37), 8091–8099. https://doi.org/10.1016/j.atmosenv.2007.06.054

Chapter 3 Unconfined plunging of a hyperpycnal river plume over a sloping bed and its lateral spreading: Laboratory experiments and numerical modeling

H. Shi[1], M. E. Negretti[2], J. Chauchat[2], K. Blanckaert[3], U. Lemmin[1], D. A. Barry[1]

[1]Ecological Engineering Laboratory (ECOL), Environmental Engineering Institute (IIE), Faculty of Architecture, Civil and Environmental Engineering (ENAC), École Polytechnique Fédérale de Lausanne (EPFL), Lausanne, Switzerland

[2]Université Grenoble Alpes, CNRS, Grenoble INP, LEGI UMR 5519, Grenoble, France

[3]Research Unit Hydraulic Engineering, Institute of Hydraulic Engineering and Water Resources Management, Technische Universität Wien, Vienna, Austria

Key Points

- Main features of unconfined plunging are investigated experimentally and numerically

- The inflow densimetric Froude number is a primary control parameter for plunging behavior

- Entrainment in unconfined plunging is much larger than in confined plunging

Abstract

Hyperpycnal (negatively-buoyant) river inflow into lakes and oceans often develops three-dimensional (3D) plunging flow patterns when laterally unconfined. To determine the 3D flow pattern characteristics, laboratory experiments of laterally unconfined plunging on a sloping bed were carried out using salinity to control the density difference. The experiments were complemented by numerical modeling based on a high-resolution Computational Fluid Dynamics model. As is the case for confined plunging plumes, it was found that in unconfined plunging, the inflow densimetric Froude number $Fr_{d\text{-}0}$ at the river mouth and the bed slope of the receiving water body β are the dominant control parameters. However, the results documented that the hydrodynamics of laterally unconfined plunging are fundamentally different: The hyperpycnal plume in unconfined configurations forms a triangle on the surface in the plunge zone due to its convergence near the surface and lateral spreading near the bottom. The triangular pattern extends further into the receiving water when $Fr_{d\text{-}0}$ increases or the bottom slope decreases. The unconfined entrainment coefficient, which quantifies the amount of ambient water entrained into the plunging plume, also increases with increasing $Fr_{d\text{-}0}$. In general, entrainment is much higher in unconfined than in confined plunging. The plunging densimetric Froude number $Fr_{d\text{-}p}$ takes a constant value of ~0.5 in confined plunging, whereas it increases with increasing $Fr_{d\text{-}0}$ and can be $\gg 1$ in unconfined plunging. Complex patterns of secondary currents occur in the plunging plume. A low-velocity zone whose size increases with $Fr_{d\text{-}0}$ is observed near the centerline above the bed.

3.1 Introduction

River inflows carry sediments, contaminants and nutrients into reservoirs, lakes or oceans (Branch et al., 2020; Lamb et al., 2010; Pope et al., 2022; Scheu et al., 2018). The present paper focuses on river inflows that have a higher density (ρ_0) than the receiving waters (ρ_a), hereinafter referred to as hyperpycnal (negatively-buoyant) river inflows. The excess density may result from lower temperatures (Hogg et al., 2013; Spigel et al., 2005), suspended sediments (Wright et al., 1986; Kostaschuk et al., 2018; De Cesare et al., 2001), or both (Best et al., 2005). Understanding how hyperpycnal river inflows transport and how they mix with ambient waters is essential for predicting and modeling the fate of fluvial materials (e.g., dissolved salts, heat, chemicals, biological particles, sediment) and thus for determining how they will affect water quality, local ecosystems and morphological evolution.

Upon entering the receiving water body, the hyperpycnal discharge displaces ambient water and then plunges below the surface at the plunge location ($x = x_p$), which is determined by a balance between the momentum of the inflow and the baroclinic pressure resulting from the density difference (e.g., Figure 6.18 of Fischer et al., 1979; see also Figs. 3.1 and 3.2 below). After plunging, the hyperpycnal plume transforms into an underflow at distance x_{ud} from the river mouth. Thus, the plunge region can be divided into two parts: from the river mouth to the plunge location ($0 < x \leq x_p$) and from the plunge location to the location where the plunging plume has transformed into an underflow ($x_p < x \leq x_{ud}$). The underflow progresses along the bottom boundary (e.g., Kostaschuk et al., 2018) and may detach from the bottom at the level of neutral buoyancy (e.g., Cortés et al., 2014).

Sediment-laden hyperpycnal plumes can cause turbidity currents. If the hyperpycnal plume gradually loses momentum, suspended sediment can settle out (Lamb et al., 2010), which reduces the excess density. On the other hand, the hyperpycnal plume can also pick up sediment from the bottom and thereby increase its excess density, potentially leading to self-acceleration (Parker et al., 1986; Sequeiros et al., 2009). Both sediment deposition and pick-up can induce morphological modifications in the receiving water body.

The dynamics of the hyperpycnal plume are dominated by its buoyancy and momentum.

Buoyancy is expressed as the depth-averaged relative density difference R_d, and momentum, by the Froude number Fr. From the river mouth to the plunge location, R_d and Fr are defined as $R_d = (\rho_d - \rho_a)/\rho_a$ and $Fr = U/\sqrt{gH}$. Here, U and ρ_d are, respectively, the depth-averaged velocity and density of the hyperpycnal current, H is the local water depth and g is the magnitude of gravitational acceleration. Fr and R_d are often combined in the densimetric Froude number Fr_d (e.g., Akiyama and Stefan, 1984; Sequeiros, 2012),

$$Fr_d = \frac{Fr}{\sqrt{R_d}} = \frac{U}{\sqrt{gH(\rho_d - \rho_a)/\rho_a}}\bigg|_{y/B_0=0} \tag{3.1}$$

These parameters are calculated at the central plane ($y/B_0 = 0$; B_0 is the width of the river channel at the mouth and y is the distance along the transverse axis in a Cartesian coordinate system, Fig. 3.1a). The subscript "0" denotes initial parameters at the river mouth. Most previous laboratory studies focused on laterally confined receiving waters (Singh and Shah, 1971; Akiyama and Stefan, 1984; Lee and Yu, 1997; Fleenor, 2001; Arita and Nakai, 2008; Lamb et al., 2010; Fig. 3.1), where plunging occurs when Fr_d decreases from Fr_{d-0} at the river mouth to a critical value called the plunging densimetric Froude number, Fr_{d-p} (e.g., Akiyama and Stefan, 1984). Laterally confined configurations may occur in river-dammed reservoirs where the original riverbed formed a subaqueous channel and the reservoir is laterally confined by the slowly diverging river valley, e.g., the Beznar Reservoir, Spain (Cortes et al., 2014) and Xiaolangdi Reservoir, China (Kostaschuk et al., 2018). For constant-width geometries and no sediment deposition, the variation of Fr_d until the plunge location can be expressed as (Arita and Nakai, 2008):

$$Fr_d(x) = Fr_{d-0}\left(\frac{H_0}{H_0 + x\tan\beta}\right)^{3/2} \tag{3.2}$$

where β is the bottom slope. To determine the plunge location, a layer-averaged thickness $h_c(x)$ that describes the vertical extent of the confined hyperpycnal plume was defined by Lee and Yu (1997):

$$h_c = \left.\frac{\left(\int_{z_b}^{z_o} \overline{u}\,dz\right)^2}{\int_{z_b}^{z_o} \overline{u}^{-2}\,dz}\right|_{y/B_0=0} \tag{3.3}$$

Here, z_b represents the depth of the bottom boundary and z_o denotes the depth of the position where $\overline{u}$, the time-averaged longitudinal velocity, decreases to zero. In confined plunging, $h_c(x)$ first increases because of the sloping boundary, then reaches a local maximum. Thereafter, it decreases to a local minimum, before finally again increasing due to the entrainment of ambient water (Lee and Yu, 1997). The location of the local maximum of $h_c(x)$ defines the location of the plunge ($x = x_p$), while its local minimum defines the location where the plunging plume is transformed into an underflow ($x = x_{ud}$). The plunging densimetric Froude number Fr_{d-p} is calculated from Equation 3.1 with parameters at the plunge location. Hereinafter, the subscript "p" denotes the parameters at $x = x_p$. In confined plunging, it is often assumed that Fr_{d-p} is a constant with a value close to 0.5, although values in the range 0.4 to 0.8 have been reported in the literature (Singh and Shah, 1971; Akiyama and Stefan, 1984; Lee and Yu, 1997; Fleenor, 2001; Parker and Toniolo, 2007; Lamb et al., 2010).

Different inlet and boundary conditions inside the plunging hyperpycnal plume cause two different types of flow (Spigel et al., 2005; Arita and Nakai, 2008): (i) the plume attaches to the bottom boundary, or (ii) the plume separates from the bottom and forms a recirculation zone below it. Based on laboratory experiments, Arita and Nakai (2008) concluded that the latter case occurs when $Fr_{d-0} > 1.4$ and $\beta > 7°$.

During the plunging process, the hyperpycnal plume entrains ambient waters. As a result, the underflow discharge Q_{ud} at $x = x_{ud}$ is larger than the inflow discharge. The underflow discharge can be obtained from:

$$Q_{ud} = \int_A \overline{u}\,dA \ \text{ at } x = x_{ud} \tag{3.4}$$

where A represents the cross-sectional area of the hyperpycnal plume defined by a specific density contour (e.g., Tseng and Chou, 2018). The entrainment coefficient, E, describes the amount of ambient water transported across the density interface into the hyperpycnal plume during plunging:

$$E = \frac{Q_{ud} - Q_0}{Q_0} \tag{3.5}$$

Laboratory experiments on confined plunging reported values for E in the range 0.02 to 0.2 (Farrell and Stefan, 1988; Fleenor, 2001; Lamb et al., 2010; Lee and Yu, 1997).
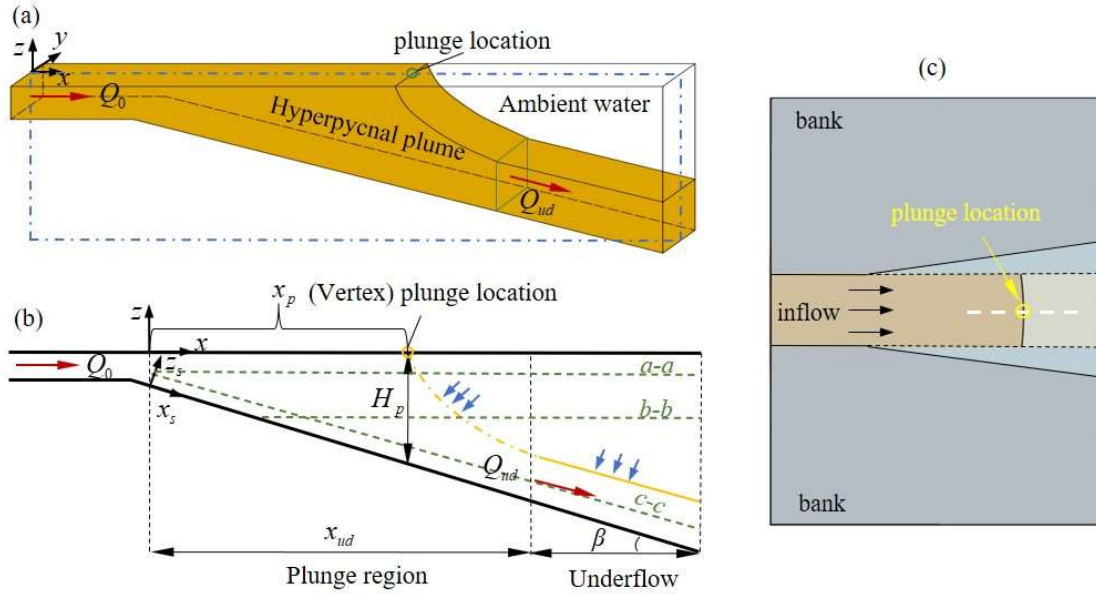
Figure 3.1 (a) Sketch of the confined plunging process on a sloping bed with inflow discharge Q_0 and underflow discharge Q_{ud}. (b) Sketch of the central plane ($y/B_0 = 0$, B_0 is the width of the inflow) identified by the blue dash-dotted lined box in (a). The orange line indicates the limits of the plunging plume and the blue arrows indicate entrainment. This sketch also describes the central plane of unconfined plunging (Fig. 3.2). The transversal planes passing through (*a-a*, *b-b* and *c-c*) are the locations of the PIV sheets in the laterally unconfined experiments, the results of which are shown in Fig. 3.5. (c) Plan view sketch of the confined plunging process.

In lakes or oceans, river inflow can develop laterally after leaving the inflow channel (Fig. 3.2); thus, the plunging of a hyperpycnal inflow can be three-dimensional (3D). Examples of unconfined plunging are the Lillooet River entering Lillooet Lake (Canada; Best et al., 2005), the Slims River flowing into Kluane Lake (Canada; Crookshanks and Gilbert, 2008) and the Rhône River plunging into Lake Geneva (Switzerland; Soulignac et al., 2021; Piton et al., 2022). Figure 3.2a gives an aerial view of the Rhône River mouth showing a triangular pattern on the water surface. A sketch of the unconfined plunging process is shown in Fig. 3.2b. In unconfined plunging, Hogg et al. (2013)

defined the plunge location as the place on the surface where the ambient waters from both sides of the progressively plunging plume meet, i.e., the vertex of the surface triangle. Hereinafter, this location is referred to as the vertex plunge point in the unconfined case to distinguish it from the plunge location in confined plunging. Hogg et al. (2013) presented a theoretical approach to predict the shape of the triangle and the vertex plunge point as a function of the inflow parameters for the case of a horizontal bottom.
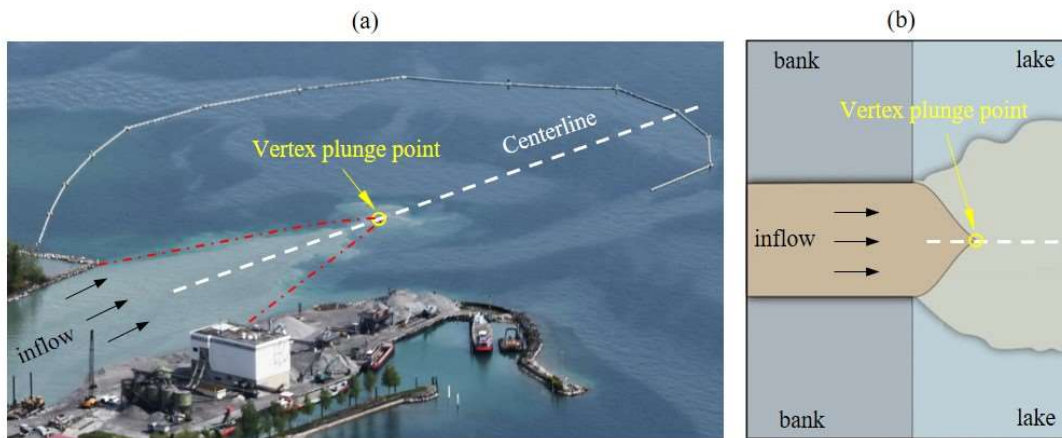
Figure 3.2 (a) Aerial view of the Rhône River mouth (inflow) in Lake Geneva taken on 1 May 2017 at 16:34 (local time). The mean surface triangular pattern (red dashed lines) of the unconfined plunging and vertex plunge point were determined from the difference in colors of the turbid sediment-laden river flow and the clear ambient water. The grey circular structure is a floating barrier (about 1 m deep) used to retain driftwood. (b) Plan view sketch of an unconfined plunging river plume.

Thus far, no detailed measurements of the velocity and density fields in the unconfined plunging zone are available in the literature. Yet, such data are needed to quantify the main characteristics of unconfined plunging, i.e., the location of the vertex plunge point, plunging densimetric Froude number and entrainment coefficient and how they are related to control parameters such as the inflow densimetric Froude number Fr_{d-0} and bottom slope β. Laboratory experiments were conducted by Hauenstein and Dracos (1984) using dye and fine sediments to visualize the spreading of unconfined plunging plumes over a sloping bottom. They proposed an integral model to estimate the lateral spreading and entrainment of the hyperpycnal plume. Johnson et al. (1987a, b, 1989)

and Stefan and Johnson (1989) experimentally investigated plunging currents in diverging channels (3–90°) with a horizontal bottom. They observed that the plunging current separates from the sidewalls and becomes laterally unconfined when the diverging angle exceeds 25°, while $Fr_{d\text{-}p}$ depends on $Fr_{d\text{-}0}$ and the diverging angle. Chen et al. (2013) and Tseng and Chou (2018) showed numerically that the dynamics of the plunging are substantially modified by a sloping bottom. However, their (Reynolds-averaged) models were validated only with laboratory data from confined experiments.

In this paper, results from laboratory experiments and numerical modeling of unconfined plunging are presented. These allow for a systematic characterization of this 3D process. The detailed velocity and density fields obtained from the experiments are used to quantify the main characteristics of the plunging plume and to validate the numerical model. The validated model is then applied to investigate an extended range of initial and boundary conditions for additional quantitative analyses (e.g., to determine the role of control parameters). The results for unconfined 3D plunging are also compared with results from laterally confined, two-dimensional (2D) cases. In particular, we focus on the following questions:

- How do 3D flow patterns in unconfined plunging differ from 2D confined plunging patterns?

- How does the flow inside the unconfined plunging hyperpycnal plume develop? Does flow separation occur near the bottom boundary?

- What are the control parameters of the unconfined plunging process and how do they affect the plunging dynamics?

- Do characteristics of confined plunging, such as constant $Fr_{d\text{-}p}$ and limited entrainment $E < 0.2$ also apply to unconfined plunging?

Figures and text with the prefix S, which provide details and clarifications of topics discussed in the main text, are found in the Supporting Information (SI) section.

3.2 Materials and methods

3.2.1 Control parameters and their investigated range

The dynamics of unconfined plunging depends on g, B_0, H_0, β, ρ_0, ρ_a, U_0, and the kinematic viscosity υ. According to the Buckingham Pi-theorem (Garrett, 1960), these

can be grouped into independent nondimensional parameters, e.g., the aspect ratio H_0/B_0, the bottom slope β, the Reynolds number $Re_0 = U_0H_0/\upsilon$, the Froude number Fr_0 and the relative density excess R_0. The latter two can be combined into $Fr_{d\text{-}0}$ (Equation 3.1). It is important to determine whether $Fr_{d\text{-}0}$ is the only dominant control parameter, or if both of its constituents Fr_0 and R_0 must be considered. The range of investigated control parameters in the present laboratory experiments and numerical investigations is summarized in Table 3.1.

This investigation was motivated by ongoing ECOL field studies of the negatively-buoyant Rhône River inflow into Lake Geneva (e.g., Piton et al., 2022; Soulignac et al., 2021). The river channel aspect ratio $H_0/B_0 = 0.04$ and lake bottom slope of $\beta = 8°$ were reproduced in the laboratory experiments. Four experimental cases were investigated with relative density difference R_0 ranging between 8×10^{-4} and 4×10^{-3}, and with two Froude numbers Fr_0 (0.08 and 0.13), resulting in two sets of $Fr_{d\text{-}0}$ values (2 and 3, Cases 1–4, Table 3.1.A). The corresponding inflow Reynolds numbers in laboratory experiments are inherently several orders of magnitude smaller than those under field conditions. The values of Re_0 between 6,000 and 9,000 are, however, large enough to guarantee turbulent flow conditions.

After the numerical model was validated with the experimental data (Table 3.1.A), it was applied to expanded ranges of control parameters (Table 3.1.B) and also a confined configuration (Table 3.1.C):

(i) $Fr_{d\text{-}0}$ values from 2 to 6 were investigated based on a variety of combinations of Fr_0 and R_0 values. This range of $Fr_{d\text{-}0}$ values is representative of the Rhône River inflow into Lake Geneva. Only cases with $Fr_{d\text{-}0} > 1$ were considered since the plunge is expected to occur inside the inlet channel if $Fr_{d\text{-}0} < 1$ (Johnson et al., 1987; Spigel et al., 2005).

(ii) The influence of the bottom slope angle β was investigated numerically by also considering a smaller bottom slope ($\beta = 4°$) and a horizontal bottom ($\beta = 0°$).

(iii) Confined plunging was simulated using the validated numerical model for the same range of $Fr_{d\text{-}0}$ (from 2 to 6) for a comparison with unconfined plunging.

Table 3.1. Summary of parameters used in experimental and numerical cases.

Case	Q_0 (l s^{-1})	$10^3 R_0$	$Fr_{d\text{-}0}$	Fr_0	Re_0	β (°)
A. Experimental and corresponding numerical cases for unconfined plunging						
1	12	1.9	2	0.08	6,000	8
2	18	4.09	2	0.13	9,000	8
3	12	0.8	3	0.08	6,000	8
4	18	1.9	3	0.13	9,000	8
B. Extended numerical cases for unconfined plunging						
5	6	0.45	2	0.04	3,000	8
6	24	7.2	2	0.17	12,000	8
7	6	0.2	3	0.04	3,000	8
8	24	3.2	3	0.17	12,000	8
9	12	0.45	4	0.08	6,000	8
10	12	0.29	5	0.08	6,000	8
11	6	0.05	6	0.04	3,000	8
12	12	0.2	6	0.08	6,000	8
13	18	0.45	6	0.13	9,000	8
14	24	0.8	6	0.17	12,000	8
15	12	1.9	2	0.08	6,000	4
16	12	1.9	2	0.08	6,000	0
C. Numerical cases for confined plunging						
17	12	1.9	2	0.08	6,000	8
18	12	0.8	3	0.08	6,000	8
19	12	0.45	4	0.08	6,000	8
20	12	0.29	5	0.08	6,000	8
21	12	0.2	6	0.08	6,000	8

3.2.2 Laboratory experiments

The laboratory experiments were carried out in the Coriolis Platform, a 13-m diameter by 1.2-m deep circular tank at LEGI (Laboratoire des Écoulements Géophysiques et Industriels, Université Grenoble Alpes, CNRS, Grenoble, France). A sketch of the experimental set-up is shown in Fig. 3.3a; more details are given in Text S3.1 and Fig. S3.1.1. The Rhône River inflow into Lake Geneva was simulated at a scale of 1:60 by a 2-m wide by 4-m long straight inflow channel with a rectangular cross-section and horizontal bottom that was positioned 0.67 m above the bottom of the tank. The water depth inside the inlet channel was maintained at $H_0 = 0.08$ m, resulting in an aspect ratio $H_0/B_0 = 0.04$. The channel's downstream end was centered with respect to an inclined flat plate ($\beta = 8°$ slope, 8-m wide by 4.75-m long).

During the experiments, the tank was first filled with water with density ρ_0. After that, saline water with density ρ_a was fed at the upstream end of the inlet channel via two lateral injectors (Fig. 3.3a). In order to produce a near-uniform velocity distribution across the channel width, a rectangular manifold consisting of an array of full-depth plastic grids (Fig. 3.3a) was installed, followed by a 0.5-m thick honeycomb placed 1.5-m upstream from the discharge plane. With a constant water discharge Q_0, a stable water flow in the inlet channel was established and verified in preliminary tests (Text S3.1.1). A constant water depth in the basin was maintained by extracting water (at rate Q_0) from outlets in the bottom of the tank. These outlets were positioned at the side and below the sloping boundary to minimize perturbations to the hyperpycnal plume. More details of the experimental procedure are given in Text S3.1. The Cartesian coordinate system used in this study (x: longitudinal, y: transversal, z: vertical) has its origin (0, 0, 0) on the centerline of the inlet channel at the beginning of the sloping boundary and at the water surface (Fig. 3.3a). The respective time-averaged $(\bar{u}, \bar{v}, \bar{w})$ and transient velocities (u, v, w) are in the (x, y, z) directions. A second Cartesian coordinate system (x_s, $y_s = y$, z_s) with corresponding velocities $(\bar{u}_s, \bar{v}_s = \bar{v}, \bar{w}_s)$ and (u_s, $v_s = v$, w_s) was applied as shown in Fig. 3.1b. For the "s" coordinate system, the longitudinal and vertical coordinates are, respectively, parallel and perpendicular to the bottom slope of the inclined flat plate.

For Cases 1 and 3 (Table 3.1), flow visualization was realized by injecting fluorescent dye (Rhodamine 6G) at different times during the experiment. A 25-W Yag laser operating at a wavelength of $\lambda = 532$ nm was set horizontally and moved vertically (from $z = -0.04$ to -0.29 m) to scan the whole volume of the hyperpycnal plume. Images were captured with GoPro and Nikon D5 cameras.

Particle Image Velocimetry (PIV) was used for flow visualization and instantaneous velocity determination. The PIV measurements in the plunge region started when this region reached steady state, which was 3 min after the onset of the experiment. Velocity fields were computed from PIV measurements using a cross-correlation PIV algorithm encoded with the UVMAT software (http://servforge.legi.grenoble-inp.fr/projects/soft-uvmat). For this purpose, an adaptive multi-pass routine was used, starting with an

interrogation window of 45 × 31 pixels and a final window size of 31 × 21 pixels, with a 70% window overlap. Each element of the resulting vector field represents an area of roughly 0.01 × 0.01 m. The maximum instantaneous velocity error is estimated to be ~3%. Detailed information about the PIV configuration is provided in Text S3.1.3.
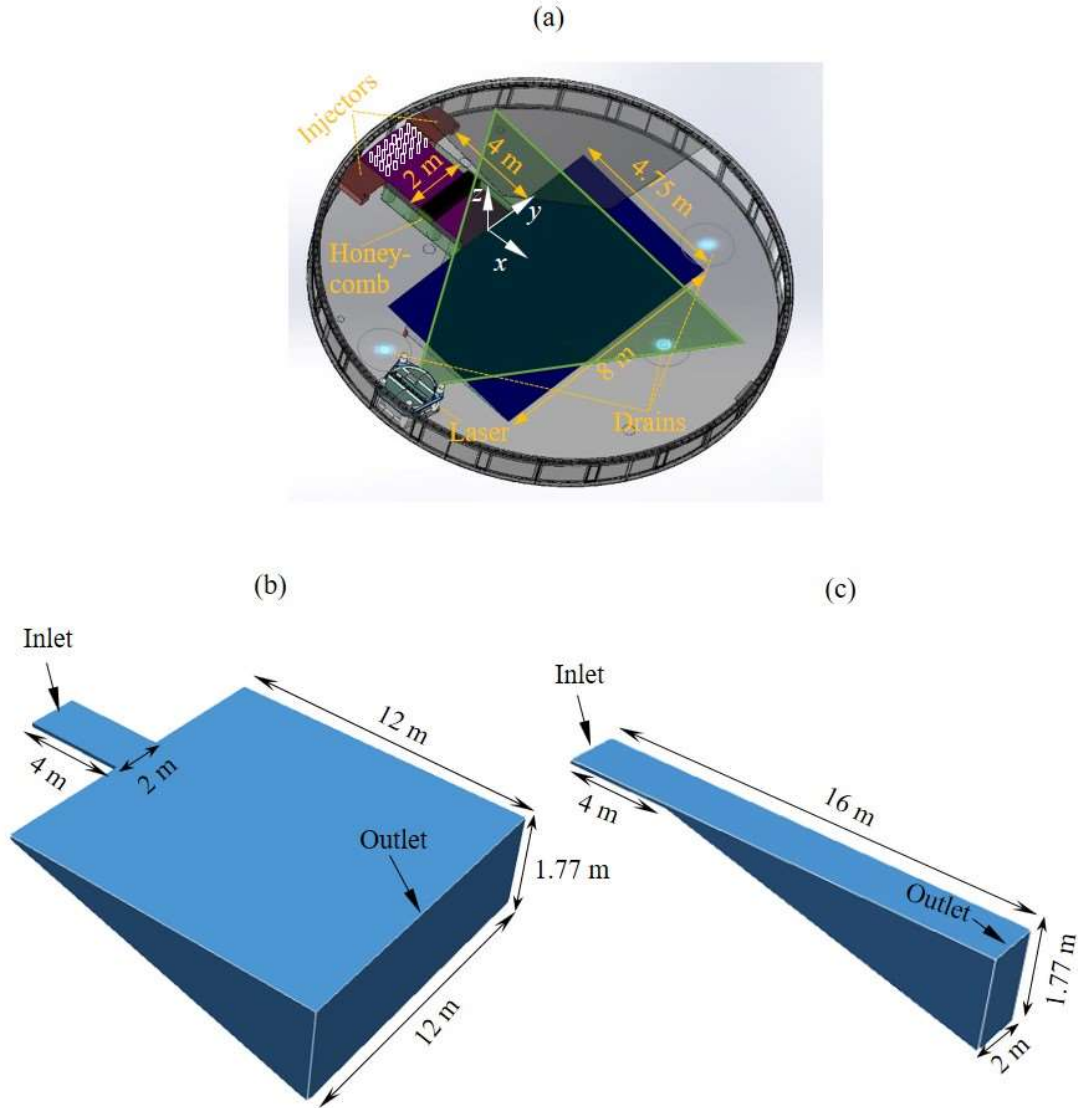
Figure 3.3 Sketches of the Coriolis Platform (LEGI, Université Grenoble Alpes) and the numerical domain. (a) The experimental set-up consists of injectors, an inlet channel, a sloping bottom plate (inclination 8°) and three drains. The origin of the coordinate system is at the surface of the inlet channel. The large green triangle represents the PIV laser sheet. (b) Numerical domain for unconfined plunging composed of an inlet channel with a horizontal bottom and a receiving domain with a sloping bottom. (c) Numerical domain for confined plunging composed of a 4-m long inlet channel and a 12-m channelized receiving domain.

3.2.3 Numerical model

A numerical model based on the open-source CFD package <u>OpenFOAM</u> (Weller et al., 1998; Jasak, 2009; De Lorenzis and Düster, 2020) was developed to simulate the experimental configurations using a transient solver "*BuoyantBoussinesqPimpleFoam*" for incompressible turbulent flow. The geometry used in the model represents the relevant geometry of the laboratory experiment, consisting of an inlet channel plus a receiving tank with an 8° bottom slope (Fig. 3.3b). The mass and momentum conservation equations are, respectively:

$$\nabla \cdot \langle \mathbf{u} \rangle = 0 \tag{3.6}$$

$$\frac{\partial \langle \mathbf{u} \rangle}{\partial t} + \nabla \cdot \left(\langle \mathbf{u} \rangle \otimes \langle \mathbf{u} \rangle \right) = -\nabla \left(\frac{\langle p \rangle}{\rho_a} \right) + \frac{1}{\rho_a} \nabla \cdot \left(\boldsymbol{\tau} + \boldsymbol{\tau}_{\mathbf{t}} \right) + \left(\langle R \rangle + 1 \right) \mathbf{g} \tag{3.7}$$

where $\langle ... \rangle$ denotes the LES space scale filter, $\mathbf{u}$ the velocity vector, t time, p pressure, $\boldsymbol{\tau}$ the resolved stress tensor, $\boldsymbol{\tau}_t$ the sub-grid scale (SGS) turbulent stress tensor, ρ the local density, $R = (\rho - \rho_a)/\rho_a$ the relative density difference and $\mathbf{g}$ the gravitational acceleration. The momentum equation is based on the Boussinesq approximation, i.e., density variations are considered only in the buoyancy term (e.g., Gray and Giorgini, 1976; Mayeli and Sheard, 2021). Transport of salt was computed using the incompressible mass diffusion equation (Cantero et al., 2007),

$$\frac{\partial R}{\partial t} + \mathbf{u} \cdot \nabla R = \nabla^2 \left(\alpha_{eff} R \right) \tag{3.8}$$

where $\alpha_{eff} = \upsilon/Sc + \upsilon_t/Sc_t$ is the effective diffusivity with $Sc = \upsilon/D$ being the Schmidt number and $Sc_t = \upsilon_t/K$ the turbulent Schmidt number. Here, υ is kinematic viscosity, υ_t is turbulent viscosity, D is molecular diffusivity and K is eddy diffusivity. Following previous studies on density currents (e.g., Cantero et al., 2007; Härtel et al., 2000; Ooi et al., 2009; Özgökmen et al., 2004), Sc is assumed to be unity, which has almost no effect on the numerical results if $R \ll 1$ (Ooi et al., 2009), since molecular diffusion is negligible. Most previous studies took the turbulent Schmidt number, Sc_t, in the range 0.7 to 0.9 (Tominaga and Stathopoulos, 2007). Here, $Sc_t = 0.85$ was applied.

The computational domains for the unconfined and confined geometries are shown in Fig. 3.3. Comparisons of the unconfined and confined plunging were likewise

performed, with the domain shown in Fig. 3.3c for the latter case. The domain for confined plunging is a 2-m wide channel with two sections: a 4-m long inlet with a horizontal bottom and a 12-m long receiving section with an 8° sloping bottom. Additional details of the numerical model set-up (e.g., numerical schemes, treatment of boundary conditions and grid independence test) are provided in Text S3.2.

3.3 Results and Discussion

3.3.1 Main features of velocity and density patterns

In all experimental and numerical cases investigated (Table 3.1), qualitatively similar results of velocity and density patterns were obtained. In this section, details of the flow field and the density field development will first be shown for Case 3 as a representative example to present the 3D flow patterns of unconfined plunging. Thereafter, results from all cases will be combined to determine the parameters that control the plunging process in Sections 3.2 and 3.3.

3.3.1.1 Density field at different vertical levels

Figure 3.4a shows the dye-visualized images at three depths in experimental Case 3. For comparison, the density distributions at the same planes calculated from the numerical model are illustrated in Fig. 3.4b. Figures 3.4a, b present the changes in the structure of the plunge region below the water surface. With increasing depth, the core of the triangular surface pattern gradually decreases due to buoyancy-induced plunging of the inflow and entrainment of ambient water. The numerical model also provides a more detailed 3D shape of the plunge region for a specific isopycnic surface ($R = 0.2R_0$) as shown in Fig. 3.4c. The hyperpycnal plume converges toward the centerline near the water surface after entering the ambient waters (Fig. 3.4). It forms a triangle at the surface but spreads laterally close to the bottom (Fig. 3.4c). This behavior is markedly different from confined plunging.
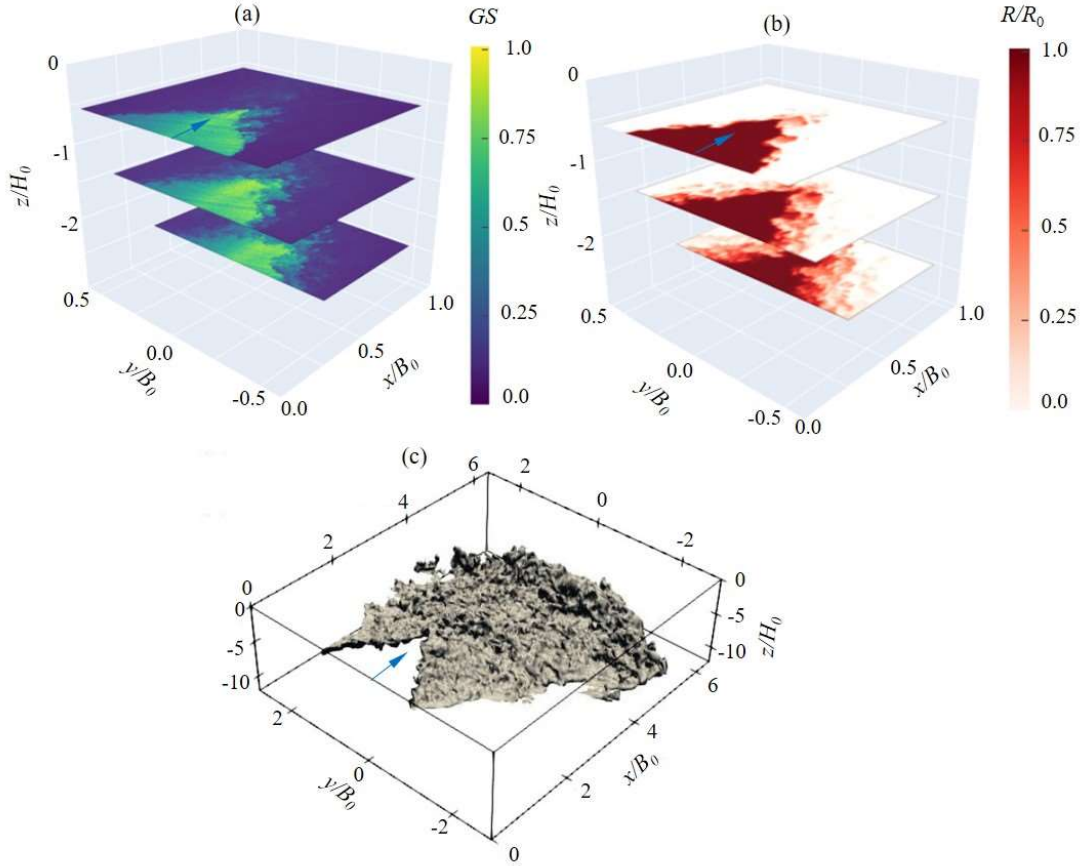
Figure 3.4 (a) Dye-visualized images of the hyperpycnal plume taken at three different depths in experimental Case 3 (Table 3.1). (b) Density patterns of the hyperpycnal current on the same three planes calculated from the numerical model. (c) 3D shape of the hyperpycnal current as delineated by an isopycnic surface ($R = 0.2R_0$) in the numerical model. The blue arrows in the plots indicate the inflow direction. In (a), the colorbar presents the dimensionless Gray Scales (*GS*), nondimensionalized by the maximum gray scales of each image. In (b) the colorbar presents the density ratio R/R_0.

3.3.1.2 Comparison of measured and modeled mean velocity fields

Figures 3.5a–c present the time-averaged (over 50 s) velocity distributions on different planes for Case 3. The location of the vertex plunge point (x_p) and the location where the plunging plume transforms into an underflow (x_{ud}) are discussed in more detail in Section 3.2. Since the inlet flow and the plunging process can be assumed to be symmetrical (Hauenstein, 1982; Hauenstein and Dracos, 1984), the symmetry of each panel in Fig. 3.5 illustrates the good agreement between the numerical model results and the experimental data. The distribution of longitudinal velocities at $z = –0.5H_0$ is

also triangular (Fig. 3.5a). The boundary of the triangle extracted from the dye-visualized images (uppermost layer in Fig. 3.4a) is plotted for comparison (red stars; for details refer to Text S3.3). In the deeper section at $z = -2H_0$ (Fig. 3.5b), a larger triangle is identified. Inside this triangle, a region with reduced velocity (low-velocity region) exists, marked by the brown dashed lines. Close to the bottom (Fig. 3.5c), this low-velocity region is still evident in the plunging region ($0 < x \leq x_{ud}$). In the underflow region after plunging ($x \geq x_{ud}$) (Fig. 3.5c), the largest longitudinal velocities are located at the centerline ($y/B_0 = 0$) and the current spreads laterally outward on both sides.

Figures 3.6a and b compare the velocity along the centerline on the plane a-a ($z = -0.5H_0$) and 0.04 m above the sloping bottom on plane c-c. On plane a-a, the horizontal velocity decreases with distance from the end of the inlet channel due to loss of momentum, and eventually reaches zero. Near the bottom, the centerline current velocity parallel to the bottom slope first decreases rapidly and then increases again, indicating the zone with reduced velocity inside the plunging plume, marked by brown dashed lines in Fig. 3.5c. In the underflow region ($x \geq x_{ud}$), the longitudinal velocity $\overline{u}_s$ near the bottom at the centerline tends towards a constant value (Figs. 3.5c, 6b) due to the combined effect of acceleration ($Rg\sin\beta$) and entrainment.
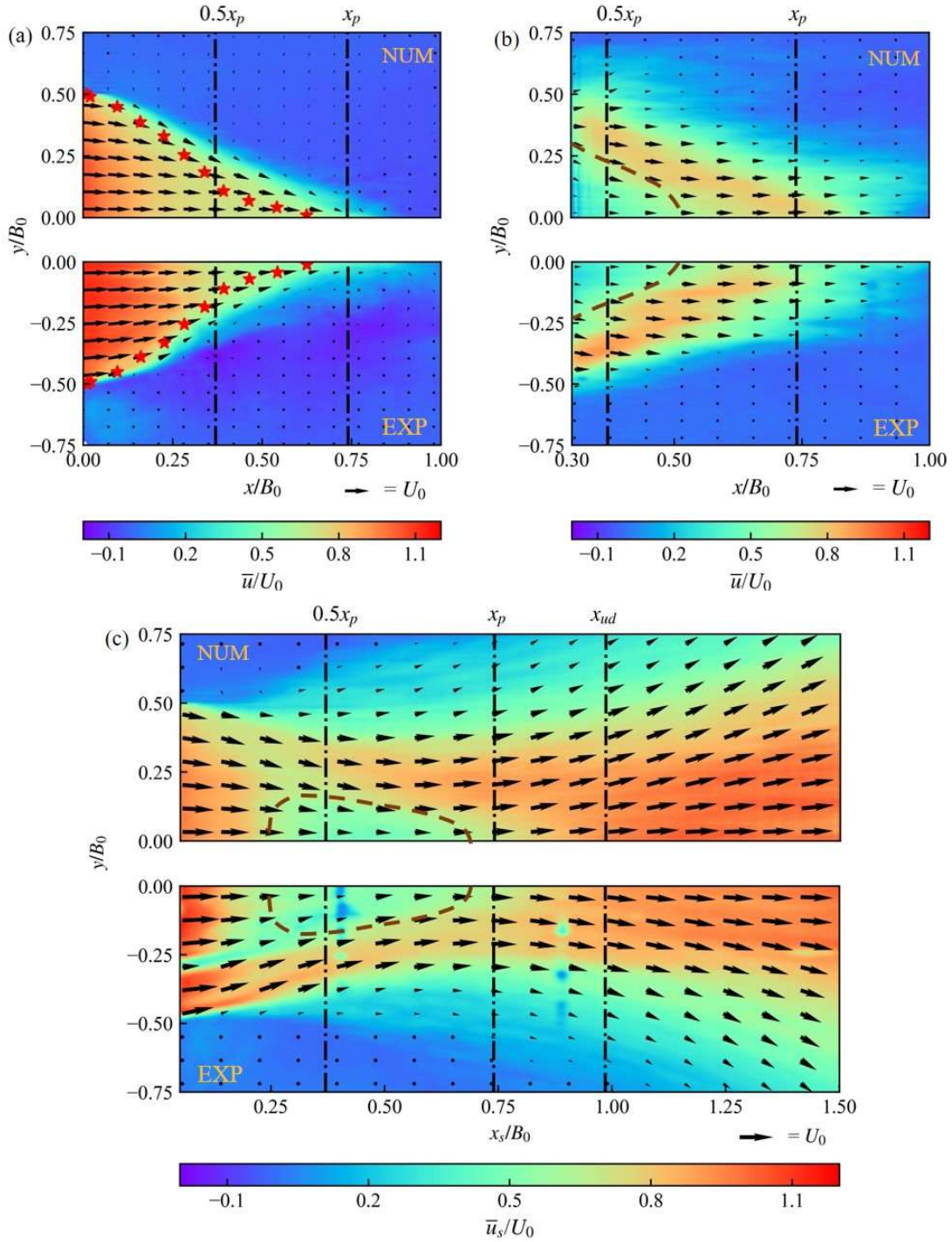
Figure 3.5 Longitudinal (time-averaged) velocity distribution for Case 3 in the: (a) first plane ($z = -0.5H_0$, plane *a-a* in Fig. 3.1b), (b) deeper plane ($z = -2H_0$, plane *b-b* in Fig. 3.1b), and (c) near-bottom inclined plane parallel to the slope (0.04 m above the bed, plane *c-c* in Fig. 3.1b). The red stars in (a) indicate the triangular pattern obtained from dye-visualized images (for details, see Text S3.3). The low-velocity region inside the plunging current is marked by the brown dashed lines in (b) and (c). The black dash-dotted vertical lines present the locations of

$x = 0.5x_p$ inside the plunge region, $x = x_p$ at the vertex plunge point, and $x = x_{ud}$ where the plunging plume transforms into an underflow. The top half of each panel presents numerical modeling results (NUM), and the bottom half, experimental results (EXP). Black arrows give the mean flow direction and colorbars, the range of velocity. The resolution of this figure is 0.01 m × 0.01 m.

Transversal profiles of the longitudinal, transversal and vertical velocity components at $x = 0.5x_p$ and $z = -0.5H_0$ are plotted in Fig. 3.6c. In this panel, the longitudinal velocity has a nearly constant value inside the triangular region and decreases quickly outside it. On each side, the transversal velocity points inwards towards the centerline with maximum (positive) and minimum (negative) values located near the edge of the surface triangle. This inward transversal velocity results from the transverse lock-exchange type flow generated by the lateral pressure gradient between the hyperpycnal plume and ambient water as discussed by Hogg et al. (2013) and Tseng and Chou (2018). The superposition of the longitudinal and inward transversal velocity components results in a velocity direction that follows the edge of the surface velocity triangle at the interface (Fig. 3.5a). The vertical velocity (green line, Fig. 3.6c), obtained from the numerical model, is directed downward in the whole transect with two peaks near the edges of the surface triangle. Figure 3.6d presents the near-bottom downslope velocity profiles (plane c-c) at $x = 0.5x_p$ and $x = x_{ud}$. At $x = 0.5x_p$, inside the plunging region (purple), two local velocity maxima delimit a lower velocity region near the centerline. Again, this behavior is due to the low-velocity zone observed in Figs. 3.5b, c. At $x = x_{ud}$ (orange), however, the current is an underflow, and the velocity profile only has one maximum at the centerline. The 3D shape of the low-velocity zone can be visualized by the iso-surface of $\bar{u} = 0.6U_0$ in Fig. 3.6e (numerical results).
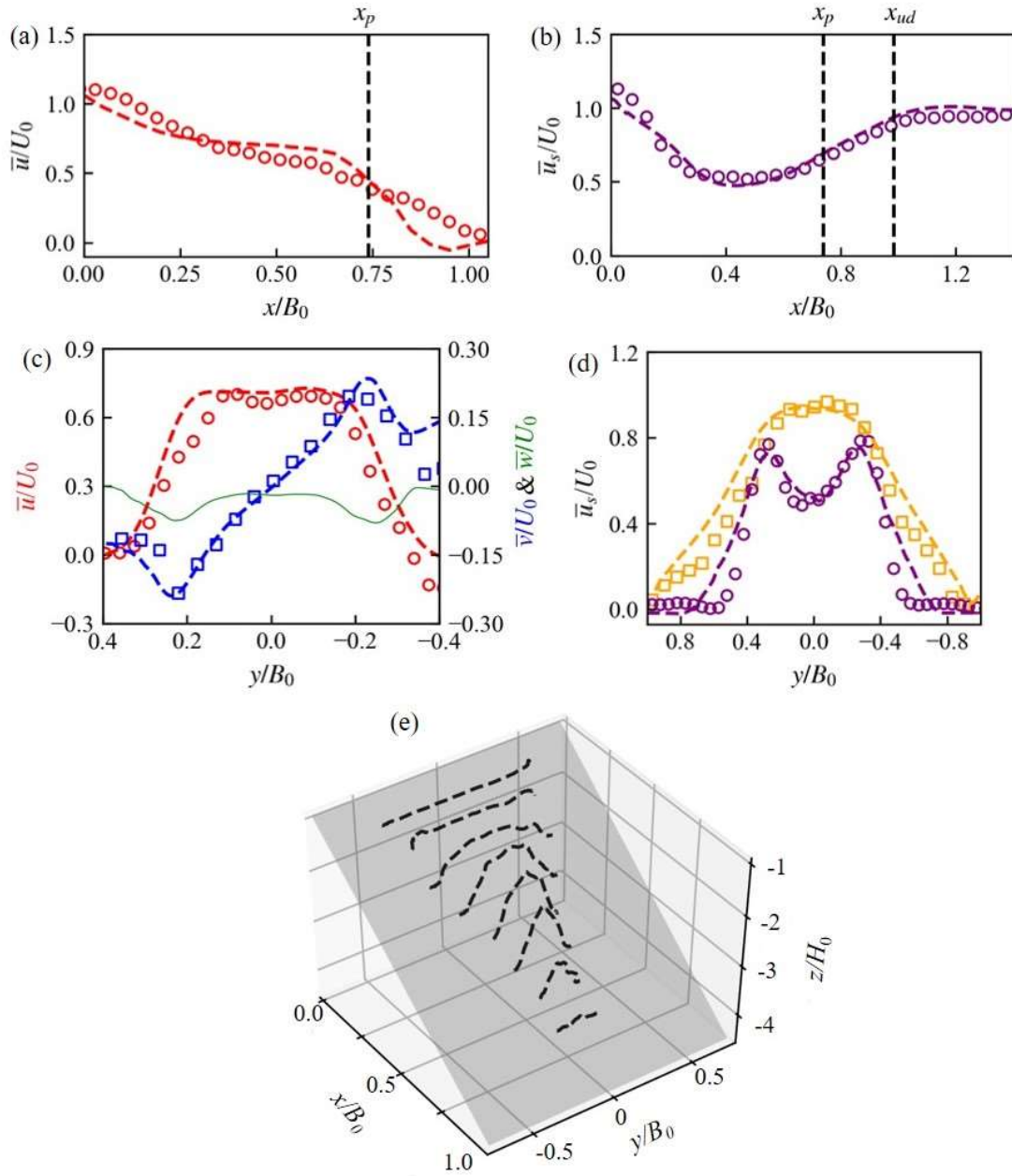
Figure 3.6 Comparison of numerical results (lines) and experimental results (circles and squares) for Case 3: (a) Centerline longitudinal velocity at $z = –0.5H_0$. (b) Centerline velocity parallel to and 0.04 m above the sloping bottom. The locations of the vertex plunge point (x_p) and where the plunging plume transforms into an underflow (x_{ud}) are marked by the black dashed lines. (c) Transversal profiles of velocities at ($x/x_p = 0.5$; $z/H_0 = –0.5$). Red and blue present the longitudinal and transversal velocities, respectively. For the vertical velocity, only numerical data are available (green line). (d) Transversal profiles of experimental and numerical $\bar{u}_s$ at 0.04 m above the bottom (plane c-c, Fig. 3.1) inside the plunge region at $x = 0.5x_p$ (purple) and in the underflow region at $x = x_{ud}$ (orange). (e) 3D shape of the low-velocity

zone defined by the iso-surface of $\overline{u} = 0.6U_0$ based on the numerical results. Note that the axes have different ranges in the panels.

3.3.1.3 Modeled mean velocity fields in the central plane and cross-sections

Model results for the velocity distribution clearly show a low-velocity zone around the centerline (Fig. 3.7a, b). However, the time-averaged relative density field ($\overline{R}$) in the corresponding sections indicate that the density in this low-velocity zone is uniform (= R_0; Fig. 3.7c, d). The low-velocity zone is created by flow separation that occurs when the slope changes at the junction of the inlet channel and the sloping bed of the receiving waters. Blanckaert (2015) divided the flow separation process into two stages: In the first stage, the velocity profile develops a deficit but remains oriented downward, followed by the second stage where flow reversal occurs near the boundary and a recirculation zone develops. Only the first stage separation occurs in the cases considered here. The density distribution remains uniform within the plunging flow whereas it is diluted due to entrainment of ambient water across the interface (Fig. 3.7c, d). Figure 3.7b presents the transverse and vertical velocities at $x = 0.5x_p$. Near the bottom, the density difference between the hyperpycnal plume and ambient water causes a lateral pressure gradient. This results in an outward transversal flow on both sides near the bottom (red dash-lined boxes). As a consequence, similar to lock-exchange flow (e.g., Shin et al., 2004), an inward transversal flow toward the centerline is generated near the surface (red dotted-lined boxes) to keep the mass balance. Interestingly, transverse velocities converging towards the center of the plunging flow are also observed in the region $-0.3 < y/B_0 < 0.3$ near the bottom, as already reported in the numerical study of Tseng and Chou (2018) and confirmed by the experimental data in Fig. 3.5c. In the area $0.25 < x/B_0 < 0.5$, $-0.3 < y/B_0 < -0.1$, the quiver plot shows transverse velocities directed towards the centerline. These near-bottom converging velocities occur due to the much higher downward velocity at the two sides ($y/B_0 \approx \pm 0.3$) compared with the centerline.

After plunging, the hyperpycnal plume flows down the slope in the underflow region. Figure 3.7e, f present the density and velocity fields at $x = x_{ud}$. Most of the dense fluid is found in a thin layer at the bottom (Fig. 3.7e). In contrast to the plunging region (Fig.

3.7d), only downward-outward secondary velocities were observed inside the hyperpycnal plume (Fig. 3.7f), which explains the lateral spreading of the underflow (Fig. 3.5c).

In both cross-sections, at $x = 0.5x_p$ and $x = x_{ud}$, secondary circulations at the dense/ambient flow interfaces are observed, highlighted by the circles in Figs. 3.7b, f (clockwise on the left side and counterclockwise on the right). Figures 3.7g, h present the time-averaged vorticity field, $\overline{\omega}_i = \partial\overline{w}/\partial y - \partial\overline{v}/\partial z$, in these two sections. High values on both sides of the hyperpycnal plume indicate rotating secondary circulations.

3.3.2 Determination of parameters x_p, x_{ud}, $Fr_{d\text{-}p}$ and E

Although the location of the vertex plunge point can be estimated from specific contours of velocity and/or density at the surface, the results will depend on the threshold value used in the definition. In confined plunging, Lee and Yu (1997) suggested that x_p and x_{ud} can be determined from variation of the layer-averaged thickness of the hyperpycnal plume $h_c(x)$ along the central plane ($y/B_0 = 0$) (details in Section 3.1). In the present study, this method is also applied to the numerical unconfined cases. Figure 3.8 illustrates the variation of $h_c(x)$ in the unconfined numerical Case 3. The local maximum of $h_c(x)$ gives the value of x_p, while the local minimum gives the location where the plunging plume transforms into an underflow (x_{ud}). After x_p and x_{ud} are determined, the plunging densimetric Froude number is calculated using Equation 3.1 and the entrainment coefficient is obtained by Equations 3.4 and 3.5 using $\overline{R} = 0.2R_0$ to determine the cross-sectional area A.
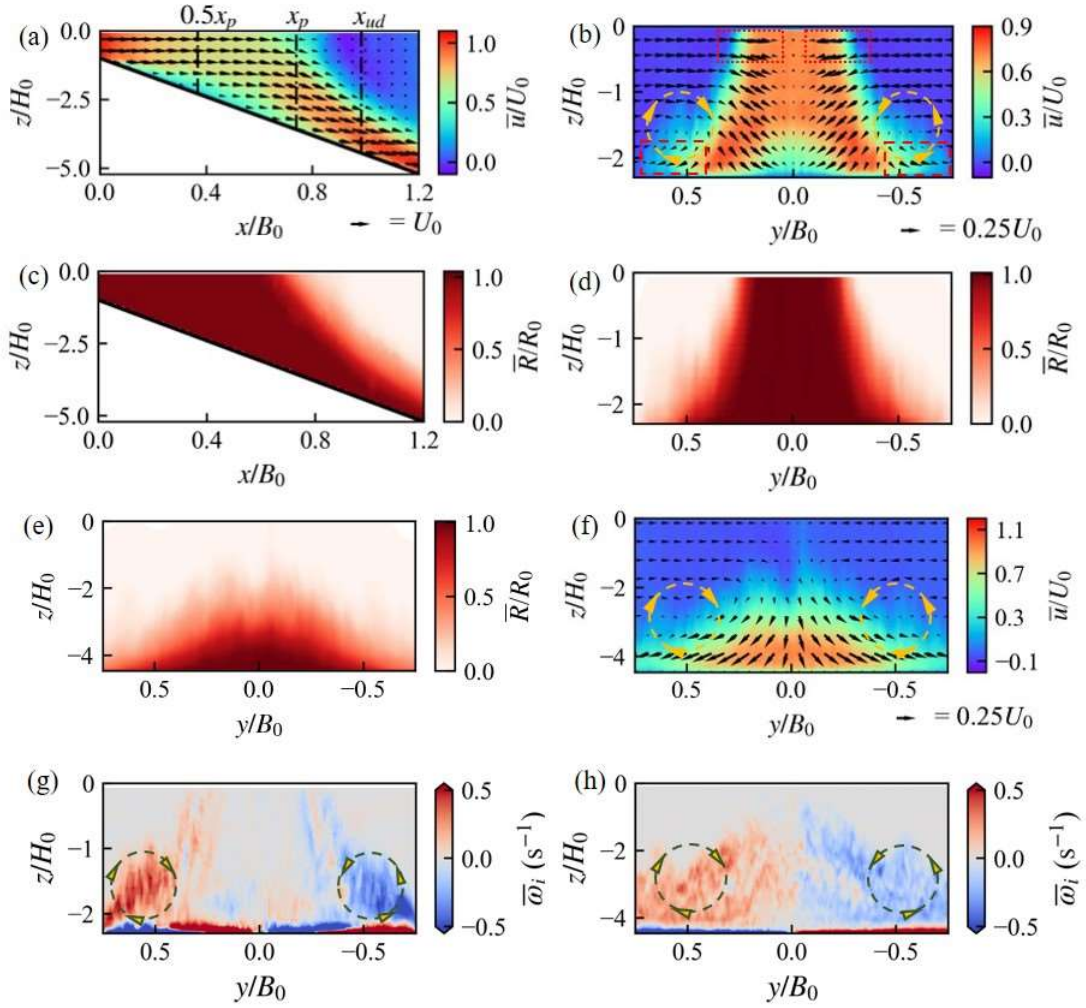
Figure 3.7 Numerically determined velocity and density fields for Case 3. (a) Velocity and (c) density fields in the central plane $y/B_0 = 0$. The three black dash-dotted lines mark the locations where $x = 0.5x_p$, $x = x_p$ and $x = x_{ud}$. (b) Velocity and (d) density fields in the cross-section at $x = 0.5x_p$. (e) Density and (f) velocity fields in the cross-section at $x = x_{ud}$. (g) Vorticity in the cross-section at $x = 0.5x_p$ and (h) vorticity at $x = x_{ud}$. Circles in (b) and (f) – (h) show suggested secondary circulations.
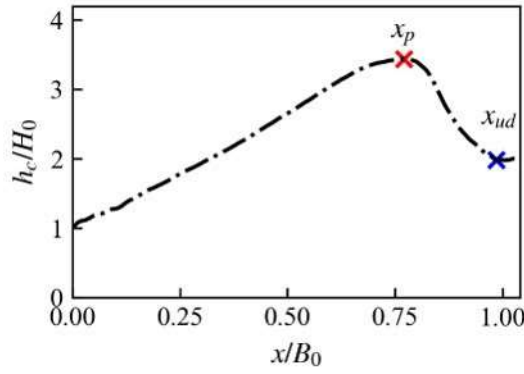
Figure 3.8 Modeled variations of layer-averaged hyperpycnal current thickness in the central section of Case 3. The red cross indicates the vertex plunge point (x_p) and the blue cross marks the location where the plunging plume transforms into an underflow (x_{ud}).

3.3.3 Parameters dominating the plunging process

Since the results obtained for all cases were similar to those of Case 3 discussed above, they were combined in order to determine their dependence on Fr_0, R_0, Fr_{d-0}, β and the lateral confinement, which are assumed to be the main controls.

3.3.3.1 Influence of Fr_0, R_0 and Fr_{d-0}

Figure 3.9a shows half of the modeled density contour ($\overline{R} = 0.95R_0$) at $z = -0.5H_0$, for cases with different values of Fr_{d-0}, Fr_0 and R_0 (Table 3.1). Experimental data from the dye-visualized images are also depicted in this figure for comparison (grey scales of the dye images are approximately linked to the density; see Text S3.3 for details). Figure 3.9b presents half of the velocity contour ($\overline{u} = 0.3U_0$) at $z = -0.5H_0$ in the experiments compared with the corresponding numerical cases. It is evident that the size of the triangle strongly depends on Fr_{d-0}. As Fr_{d-0} increases, the vertex plunge point moves further away from the river mouth, resulting in a larger x_p.

Although different combinations of Fr_0 and R_0 can result in the same Fr_{d-0}, the size of the surface triangle does not change (Fig. 3.9) for given values of Fr_{d-0}. Figure 3.10 presents the measured and modeled centerline longitudinal velocity at $z = -0.5H_0$ for Cases 1–4. Similar to the surface triangle size, the variation of this centerline velocity is again dependent only on Fr_{d-0} rather than Fr_0 and R_0. Furthermore, the length of the low-velocity zone inside the plunging plume also increases with Fr_{d-0} (Fig. 3.11).
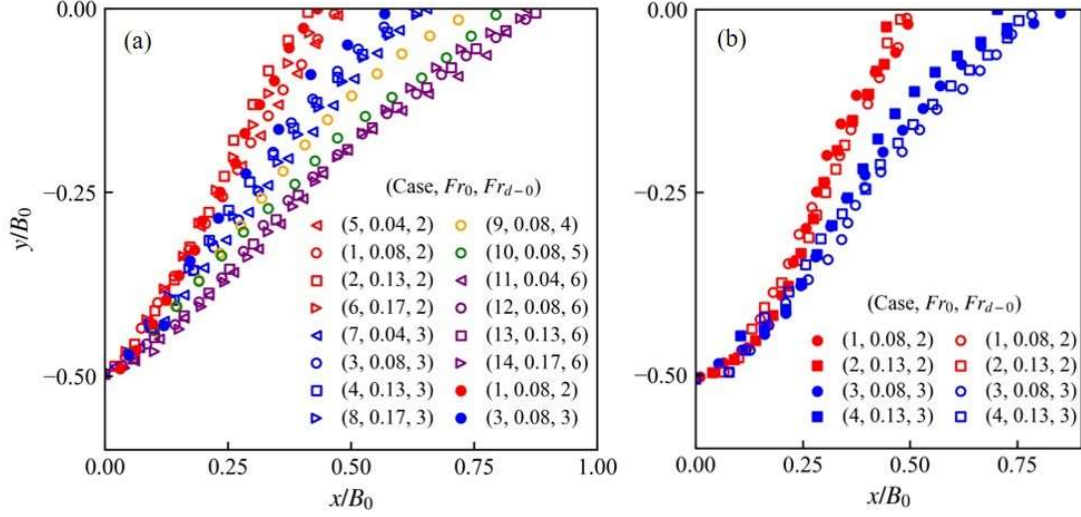
Figure 3.9 (a) Points on the density contours $(\overline{R} = 0.95R_0)$ at $z = -0.5H_0$ for Cases 1–14 (Table 3.1). (b) Points on the velocity contours $(\overline{u} = 0.3U_0)$ at $z = -0.5H_0$ for Cases 1–4. In both panels, each case is identified by Case, Fr_0 and Fr_{d-0} values in the legend (corresponding R_0 values are given in Table 3.1). Open and filled symbols present the numerical and experimental data, respectively. Symbols indicate cases with different Fr_0, and colors give cases with different Fr_{d-0}.

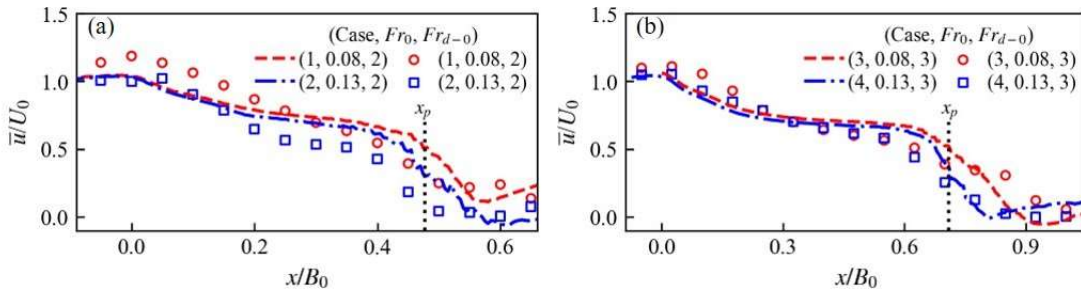**Figure 3.10** Measured and modeled centerline longitudinal velocity at $z = -0.5H_0$ for a) Cases 1 and 2 and b) Cases 3 and 4 (identified by Case, Fr_0 and Fr_{d-0} values in the legend, Table 3.1). Symbols represent experimental data while lines are numerical results. The vertical dotted lines locate the vertex plunge point (x_p) obtained numerically. Note that the x/B_0 axes have different ranges.
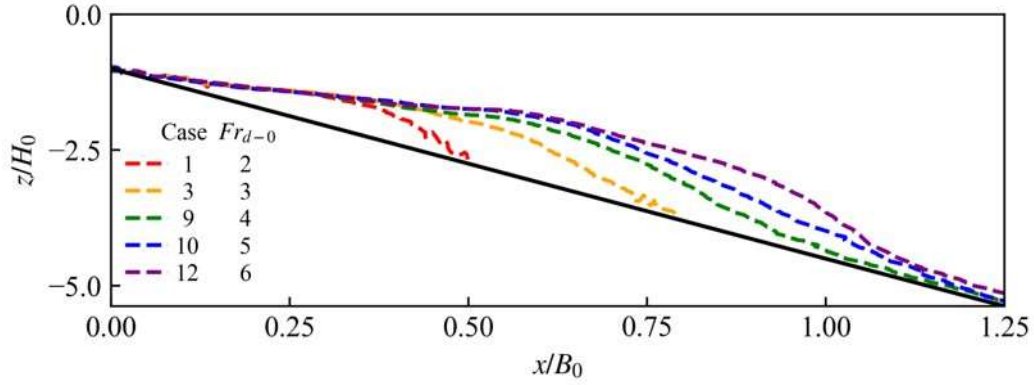
Figure 3.11 Variation of the length of the low-velocity zone in the central plane, defined by the contour $\bar{u} = 0.6U_0$, in unconfined plunging for numerical cases with $Fr_0 = 0.08$.

3.3.3.2 Influence of the bottom slope

Figure 3.12 presents the modeled surface density contour ($\bar{R} = 0.95R_0$) for three numerical cases with the same inlet condition ($Fr_0 = 0.08$, $Fr_{d-0} = 2$), but with different bottom slopes (β). Investigated bottom slopes include a horizontal bottom, a bottom slope of 4° and the experimentally investigated bottom slope of 8°. A large difference between the surface triangles is apparent in Fig. 3.12, which shows that the unconfined hyperpycnal plume plunges closer to the river mouth when the bottom boundary slope is larger, as was previously observed by Tseng and Chou (2018). A similar result was reported in confined cases (Arita and Nakai, 2008). The results of the numerical simulation of the horizontal case were compared with the analytical prediction of the surface triangle by Hogg et al. (2013):

$$y = \pm\left(\frac{B_0}{2} - \frac{x\sqrt{g'_0 H_0}}{2\bar{u}_{os}} \right) \tag{3.9}$$

where $\bar{u}_{os}$ denotes the inlet velocity at the surface. The numerical results of this study agree well with their model (Fig. 3.12). Equation 3.9 is based on the assumptions that the centerline velocity on the water surface remains almost constant up to the vertex plunge point and that the lateral converging velocity of the surface triangle follows the law obtained from lock-exchange density currents: $\bar{v}_e = \sqrt{g'_0 H_0}/2$. Both of these assumptions are invalid if the bottom boundary is inclined. A comparable analytical solution to Equation 3.9 for a non-zero bottom slope is not available.
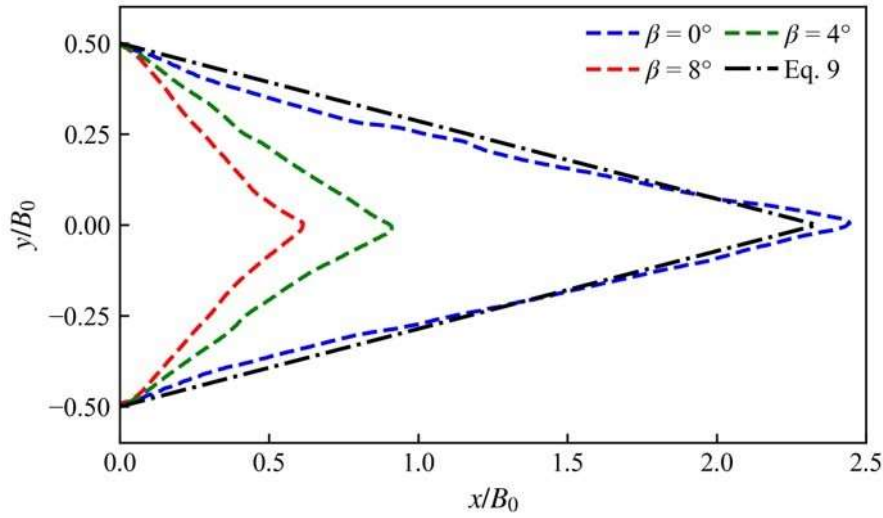
Figure 3.12 Surface density contours ($\overline{R} = 0.95 R_0$) for the numerical cases with the same $Fr_0 = 0.08$ and $Fr_{d\text{-}0} = 2$, but with different bottom slopes (i.e., 0°, 4° and 8° for Cases 16, 15 and 1 (Table 3.1), respectively, as indicated by the colors in the legend). The black dash-dotted lines are the prediction of Equation 3.9 for the horizontal bottom Case 16.

3.3.3.3 Influence of lateral confinement

Figure 3.13a presents the variation of Fr_d in confined numerical cases with an 8° bottom slope and $Fr_0 = 0.08$. Fr_d is calculated based on the velocity and density data in the central plane (Equation 3.1). In the longitudinal direction, Fr_d decreases due to the bottom slope following Equation 3.2 as suggested by Arita and Nakai (2008). The numerical simulations indicate that the plunge occurs when Fr_d decreases to a critical value close to 0.5, which is consistent with the value obtained by Lamb et al. (2010) using the theoretical model of Parker and Toniolo (2007). When $Fr_{d\text{-}0}$ increases, the plunge occurs further away from the river mouth. The decrease of Fr_d is slower in unconfined plunging than in confined plunging (Figs. 3.13a, b), implying that Equation 3.2 is not valid in unconfined cases. Equation 3.2 is based on the assumption that the discharge per unit width in the central plane (q_c) remains constant before the plunge location, i.e., $U_0 H_0 = U_c(x) H(x)$. This is valid in confined plunging, for example in Case 21, where $q_c/q_{c\text{-}0}$ remains nearly constant at around unity (Fig. 3.13c, black circles). However, in unconfined plunging, q_c increases longitudinally since the transversal secondary velocity is directed towards the centerline as shown in Fig. 3.7b. The increase

of q_c slows down the decrease of Fr_d. As a result, Fr_d at the location where the confined hyperpycnal plume plunges, is still greater than 0.5 in the corresponding unconfined case (same value of $Fr_{d\text{-}0}$, compare Figs. 3.13a, b). Thereafter, Fr_d continues to decrease in the unconfined case. At the vertex plunge point, $Fr_{d\text{-}p}$ in the unconfined cases is still substantially greater than the critical value of ~0.5 that is characteristic of confined plunging. Moreover, $Fr_{d\text{-}p}$ is found to increase with $Fr_{d\text{-}0}$ and can be larger than unity. These results indicate that the unconfined plunge is not only controlled by a critical value of $Fr_{d\text{-}p}$, but also by the three-dimensional flow patterns inside the plunge region. Indeed, the plunge occurs where the two sides of the hyperpycnal plume meet at the centerline on the surface, even though Fr_d is still greater than the critical value for confined cases.

Figure 3.14a presents the increase of discharge in the plunge region (from $x = 0$ to $x = x_{ud}$) due to entrainment in four unconfined numerical cases with the same $Fr_{d\text{-}0} = 3$, but different combinations of Fr_0 and R_0. For the cases considered, Fr_0 and R_0 have no influence on the entrainment since $Fr_{d\text{-}0}$ does not change. Figure 3.14b shows the variation of the entrainment coefficient E with $Fr_{d\text{-}0}$ in confined and unconfined numerical cases with $Fr_0 = 0.08$. In confined plunging, E values are found within a narrow range (0.05–0.15), which is similar to results reported in previous experimental studies ranging from 0.02 to 0.2 (Farrell and Stefan, 1988; Lee and Yu, 1997; Fleenor, 2001; Lamb et al., 2010). In unconfined plunging, however, E values are not only significantly larger, but also increase with increasing $Fr_{d\text{-}0}$ from 0.4 to 0.7 (Fig. 3.14b). The increase of E with $Fr_{d\text{-}0}$ in unconfined cases can be explained by the downstream shift of the vertex plunge point with increasing $Fr_{d\text{-}0}$. This results in a larger interface area along which the entrainment between the riverine inflow and the ambient water occurs.
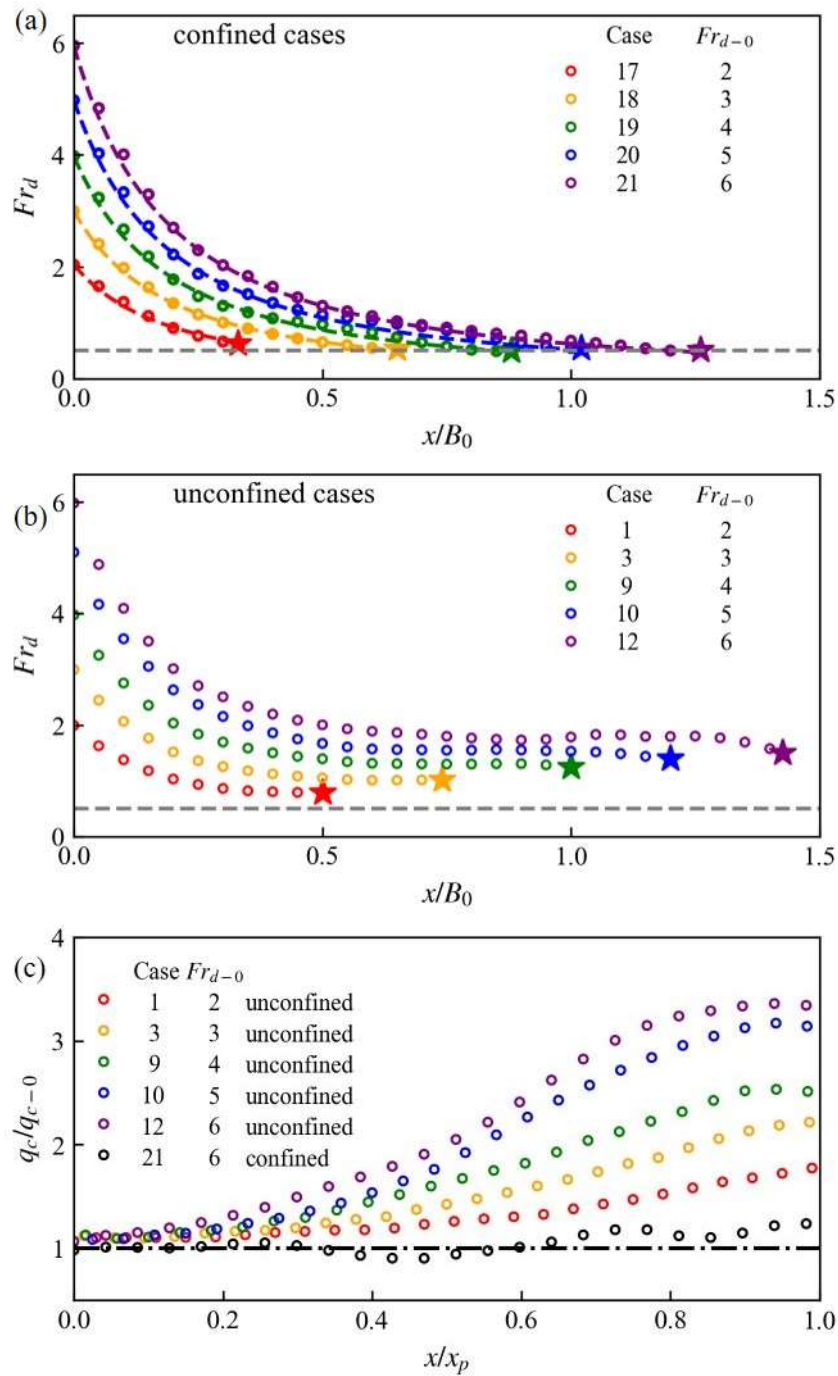
Figure 3.13 Variation of Fr_d in the central plane from the river mouth to the plunge location (or the vertex plunge point) in the (a) confined and (b) unconfined numerical cases with $Fr_0 = 0.08$. The end point (star) of each curve marks x_p (Fig. 3.1). (c) Modeled variations of discharge per unit width q_c in the central plane of the unconfined cases with $Fr_0 = 0.08$. Modeled variations of q_c in the confined case with $Fr_{d-0} = 6$ and $Fr_0 = 0.08$ (black circles, Case 21, Table 3.1) are also included and compared with the theoretical result $q_c(x) = q_{c-0}$ (black dash-dotted line).

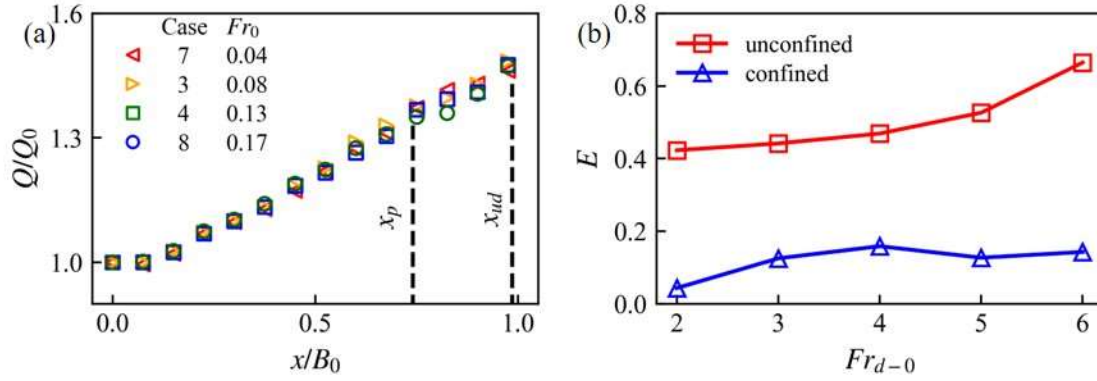**Figure 3.14** (a) Variations of the normalized discharge Q/Q_0 in four unconfined numerical cases with $Fr_{d\text{-}0} = 3$ but different combinations of Fr_0 and R_0. The black dashed lines give the vertex plunge point and the location where the plunging plume has transformed into an underflow. (b) Comparison of the entrainment coefficient E between the confined (blue, Cases 17–21, Table 3.1) and unconfined (red, Cases 1, 3, 9, 10 and 12) numerical cases with the same $Fr_0 = 0.08$.

3.3.4 Generalization of results

Field measurements of unconfined temperature-induced plunging were made in the Canale Italsider mouth (Lake Iseo, Italy) by Hogg et al. (2013) and in the Tokaanu Tailrace mouth (Lake Taupo, New Zealand) by Spigel et al. (2005). The related geometry and inlet conditions are listed in Table 3.2. Numerical simulations for Lake Iseo and Lake Taupo were performed using simplified geometries similar to Fig. 3.3b based on geometric (1:20 scale) and Froude similarity (Table 3.2). The numerical model predicts $x_p/B_0 = 0.8$ for the Canale Italsider mouth, consistent with the range of 0.6–1.0 reported by Hogg et al. (2013). Hogg et al. (2013) applied Equation 3.9 to estimate the vertex plunge point ($x_{up} = \bar{u}_{os} B_0 / \sqrt{g'_0 H_0}$; they further assumed that $\bar{u}_{os} = U_0$), resulting in $x_p/B_0 = 2.4$, which is more than double the measured value. This overestimation of x_p is due to the simplifying assumption that the lake bottom is horizontal. For the Tokaanu Tailrace mouth, the numerical model gave $x_p/B_0 = 1.0$, which agrees with the range ($x_p/B_0 = 0.8$–1.0) reported by Spigel et al. (2005). They calculated an entrainment coefficient $E = 1.9$, which is about double the value ($E = 1.1$) determined numerically using Equation 3.4 to calculate Q_{ud}. This difference is due to the different methods used to obtain Q_{ud}. Spigel et al. (2005) assumed that Q_{ud} = discharge per unit width in the central plane × plume width, which overestimates Q_{ud}

since the velocity in the central plane of the underflow region is considerably higher than on the two sides as shown in Fig. 3.5c. If their method is applied to the numerical data, $E = 1.7$ is obtained which is quite close to the value ($E = 1.9$) they reported.

The inflow of the Rhône River (Lake Geneva) is sediment-laden, and both the suspended sediment and temperature contribute to the excess density of the hyperpycnal plume. Figure 3.2a shows the surface triangle at the Rhône River mouth. This image was taken on a day when $Fr_{d\text{-}0} \approx 3.2$ and gives an estimation of the vertex plunge point as $x_p/B_0 \approx 1.0$. The numerical and experimental Case 3 have an $Fr_{d\text{-}0}$ value close to this and further that $x_p/B_0 = 0.75$. The underestimation of x_p may result from sediment deposition that is not included in the experiments or the numerical model. As the hyperpycnal plume develops, it loses momentum, which leads to the deposition of larger-sized suspended sediment, reducing the relative density difference (Piton et al., 2022). Sedimentation may also reduce the bottom slope angle. Both of these mechanisms can lead to a larger x_p in hyperpycnal plunging.

3.4. Summary and Conclusions

By combining detailed laboratory measurements of the velocity fields and 3D numerical modeling, this study allowed the first characterization of 3D unconfined plunging of a hyperpycnal river plume over a sloping bed and its lateral spreading. The numerical modeling was based on a Computational Fluid Dynamics (CFD) model, which was validated with the experimental results, thus demonstrating that the model is suitable for realistically simulating the unconfined plunging process.

Table 3.2. Comparison between the numerical model (NUM) and field measurements.

	U_0 (m s^{-1})	H_0 (m)	B_0 (m)	ρ_a (kg m^{-3})	ρ_0 (kg m^{-3})	β (°)	x_p/B_0	$Fr_{d\text{-}0}$	E	scale
				Canale Italsider mouth (Hogg et al., 2013)						
Field	0.48	1.7	49	997.3	999.4	4.6	0.6–1.0	2.6	-	20
NUM	0.107	0.085	2.45	997.3	999.4	4.6	0.8	2.6	0.5	
				Tokaanu Tailrace mouth (Spigel et al., 2005)						
Field	0.63	1.42	96	999.56	999.98	5.5	0.8–1.0	8.2	1.9[a]	20
NUM	0.141	0.071	4.8	999.56	999.98	5.5	1.0	8.2	1.1(1.7[a])	
				Rhône River mouth						
Field	0.14	4.8	120	999.76	999.80	8	1.0	3.2	-	60

[a]Entrainment coefficient using the method in Spigel et al., (2005) to estimate Q_{ud}

The results of this study reveal that the 3D unconfined plunging process is different from confined (essentially 2D) plunging. In the unconfined plunging process, 3D flow structures are observed: As the hyperpycnal plume is advected longitudinally, currents in the cross-sections are directed downwards and form transversal lock-exchange type flows on each side of the plunge. This causes the current to converge towards the centerline on the surface creating a triangular shape of velocity/density fields, while spreading laterally near the bottom. The near-bottom lateral spreading further generates secondary circulations on both sides of the hyperpycnal plume.

Inside the unconfined plunging plume, a low-velocity zone exists due to flow separation induced by the transition from the horizontal bottom of the inflow channel to the sloping bed of the receiving waters.

Similar to confined plunging, the inflow densimetric Froude number Fr_{d-0} and the bottom slope β in the receiving water body are the dominant control parameters in unconfined plunging. The same value of Fr_{d-0} can be obtained from different combinations of its constituents Fr_0 and R_0. The results show that plunging characteristics only depend on Fr_{d-0} irrespective of Fr_0 and R_0. Decreasing Fr_{d-0} or increasing the bottom slope causes plunging to occur closer to the river mouth.

In confined plunging, the plunge occurs when the densimetric Froude number Fr_{d-0} decreases to a critical value close to 0.5 and the amount of ambient water entrained into the hyperpycnal plume is quite limited. In unconfined plunging, however, the vertex plunge point is where the two sides of the hyperpycnal plume meet at the centerline on the surface, even if Fr_d is still larger than the critical value of unconfined plunging. Since ambient waters can be entrained from both sides into the hyperpycnal current, the entrainment coefficient E in unconfined plunging is found to be much larger than in confined plunging.

This study has made evident the following similarities and differences between confined and unconfined plunging:

Similarities

- From the river mouth, the layer-averaged thickness h_c of the hyperpycnal current in the central section first increases, and then decreases rapidly after the initiation

of plunging, followed by another increase due to entrainment. The variations of h_c can be applied to determine x_{up} and x_{ud}.

- The distance from the river mouth to the plunge location (or the vertex plunge point) increases with increasing $Fr_{d\text{-}0}$ and decreasing bottom slope β.

Differences

- Unconfined (3D) plunging flow patterns are different to those of confined (2D) cases.

- The discharge per unit width at the central section q_c increases longitudinally in unconfined plunging but is constant in confined cases.

- In confined plunging, the plunge occurs when Fr_d decreases to the critical value (i.e., $Fr_{d\text{-}p} \approx 0.5$). In unconfined cases, however, the vertex plunge point is located where the two sides of the hyperpycnal plume meet at the centerline on the surface.

- In unconfined plunging, much more entrainment takes place resulting in significantly larger entrainment coefficient E values than in confined cases.

The numerical model results agreed well with previous field observations of unconfined plunging flow. This unique combination of laboratory experiments, numerical modeling and previous field observations improves the understanding and the characterization of unconfined hyperpycnal river plunging dynamics.

Unconfined hyperpycnal river plume plunging is often observed in lakes. Taking into consideration unconfined plunging processes allows for better understanding of how plunging inflows transport materials and how they mix with ambient waters, and as a result, how they affect water quality, local ecosystems and morphological evolution. Therefore, the results of the present study can contribute to the development of effective lake management concepts. These findings can also be expected to be applicable to other water bodies where unconfined hyperpycnal river-plume plunging occurs.

Acknowledgements

Open Research

Data reported in this paper and the original image of the Rhône River mouth (Fig. 3.2a) can be downloaded from https://doi.org/10.5281/zenodo.6940788 or https://gitlab.epfl.ch/hashi/wrrdata.git.

References

Akiyama, J., & Stefan, H. G. (1984). Plunging flow into a reservoir: Theory. *Journal of Hydraulic Engineering*, *110*(4), 484–499. https://doi.org/10.1061/(ASCE)0733-9429(1984)110:4(484)

Arita, M., & Nakai, M. (2008). Plunging conditions of two-dimensional negative buoyant surface jets released on a sloping bottom. *Journal of Hydraulic Research, 46*(3), 301–306. https://doi.org/10.3826/jhr.2008.2714

Best, J. L., Kostaschuk, R. A., Peakall, J., Villard, P. V., & Franklin, M. (2005). Whole flow field dynamics and velocity pulsing within natural sediment-laden underflows. *Geology*, *33*(10), 765-768. https://doi.org/10.1130/G21516.1

Blanckaert, K. (2015). Flow separation at convex banks in open channels. *Journal of Fluid Mechanics*, *779*, 432–467. https://doi.org/10.1017/jfm.2015.397

Branch, R. A., Horner-Devine, A. R., Kumar, N., & Poggioli, A. R. (2020). River plume liftoff dynamics and surface expressions. *Water Resources Research*, *56*, e2019WR026475. https://doi.org/10.1029/2019WR026475

Cantero, M. I., Balachandar, S., & Garcia, M. H. (2007). High-resolution simulations of cylindrical density currents. *Journal of Fluid Mechanics*, *590*, 437–469. https://doi.org/10.1017/S0022112007008166

Chen, S. N., Geyer, W. R., & Hsu, T. J. (2013). A numerical investigation of the dynamics and structure of hyperpycnal river plumes on sloping continental shelves: Dynamics of hyperpycnal river plumes. *Journal of Geophysical Research: Oceans*, *118*(5), 2702–2718. https://doi.org/10.1002/jgrc.20209

Cortés, A., Fleenor, W. E., Wells, M. G., de Vicente, I., & Rueda, F. J. (2014). Pathways of river water to the surface layers of stratified reservoirs. *Limnology and Oceanography*, *59*(1), 233–250. https://doi.org/10.4319/lo.2014.59.1.0233

Crookshanks, S., & Gilbert, R. (2008). Continuous, diurnally fluctuating turbidity currents in Kluane Lake, Yukon Territory. *Canadian Journal of Earth Sciences*, *45*(10), 1123–1138. https://doi.org/10.1139/E08-058

De Cesare, G., Schleiss, A., & Hermann, F. (2001). Impact of turbidity currents on reservoir sedimentation. *Journal of Hydraulic Engineering, 127*(1), 6–16. https://doi.org/10.1061/(ASCE)0733-9429(2001)127:1(6)

De Lorenzis, L., & Düster, A. (2020). Modeling in engineering using innovative numerical methods for solids and fluids. CISM International Centre for Mechanical Sciences (Vol. 599). *Springer International Publishing*, Cham, Switzerland. https://doi.org/10.1007/978-3-030-37518-8

Farrell, G. J., & Stefan, H. G. (1988). Mathematical modeling of plunging reservoir flows. *Journal of Hydraulic Research*, *26*(5), 525–537. https://doi.org/10.1080/00221688809499191

Fischer, H. B., List, E., Koh, R., Imberger, J., & Brooks, N. (1979). Mixing in inland and coastal waters. *Academic Press*, San Diego, California. USA. https://doi.org/10.1016/C2009-0-22051-4

Fleenor, W. (2001). Effects and control of plunging inflows on reservoir hydrodynamics and downstream releases. Unpublished Ph.D. thesis. *University of California, Davis*, Davis, California, USA.

https://search.library.ucdavis.edu/permalink/01UCD_INST/9fle3i/alma990021089970403126

Garrett, B. (1960). Hydrodynamics (Second Edition). *Princeton University Press*. Princeton, New Jersey, USA. https://press.princeton.edu/books/ebook/9781400877775/hydrodynamics

Gray, D. D., & Giorgini, A. (1976). The validity of the Boussinesq approximation for liquids and gases. *International Journal of Heat and Mass Transfer*, *19*(5), 545–551. https://doi.org/10.1016/0017-9310(76)90168-X

Härtel, C., Meiburg, E., & Necker, F. (2000). Analysis and direct numerical simulation of the flow at a gravity-current head. Part 1. Flow topology and front speed for slip and no-slip boundaries. *Journal of Fluid Mechanics*, *418*, 189–212. https://doi.org/10.1017/S0022112000001221

Hauenstein, W. (1982). *Zuflussbedingte Dichteströmungen in Seen*. Unpublished Ph.D. thesis. *ETH Zürich*. Zürich, Switzerland.
https://eth.swisscovery.slsp.ch/permalink/41SLSP_ETH/lshl64/alma990003139310205503

Hauenstein, W., & Dracos, Th. (1984). Investigation of plunging density currents generated by inflows in lakes. *Journal of Hydraulic Research*, *22*(3), 157–179.
https://doi.org/10.1080/00221688409499404

Hogg, C. A. R., Marti, C. L., Huppert, H. E., & Imberger, J. (2013). Mixing of an interflow into the ambient water of Lake Iseo. *Limnology and Oceanography*, *58*(2), 579–592.
https://doi.org/10.4319/lo.2013.58.2.0579

Jasak, H. (2009). OpenFOAM: Open source CFD in research and industry. *International Journal of Naval Architecture and Ocean Engineering*, *1*(2), 89–94. https://doi.org/10.2478/IJNAOE-2013-0011

Johnson, T. R., Ellis, C. R., Farrell, G. J., & Stefan, H. G. (1987a). Negatively buoyant flow in a diverging channel. II: 3-d flow field descriptions. *Journal of Hydraulic Engineering*, *113*(6), 731–742.
https://doi.org/10.1061/(ASCE)0733-9429(1987)113:6(731)

Johnson, T. R., Ellis, C. R., & Stefan, H. G. (1989). Negatively buoyant flow in diverging channel, IV: Entrainment and dilution. *Journal of Hydraulic Engineering*, *115*(4), 437–456.
https://doi.org/10.1061/(ASCE)0733-9429(1989)115:4(437)

Johnson, T. R., Farrell, G. J., Ellis, C. R., & Stefan, H. G. (1987b). Negatively buoyant flow in a diverging channel. I: Flow regimes. *Journal of Hydraulic Engineering*, *113*(6), 716–730.
https://doi.org/10.1061/(ASCE)0733-9429(1987)113:6(716)

Kostaschuk, R., Nasr-Azadani, M. M., Meiburg, E., Wei, T., Chen, Z., Negretti, M. E., Best, J., Peakall, J., & Parsons, D. R. (2018). On the causes of pulsing in continuous turbidity currents. *Journal of Geophysical Research: Earth Surface*, *123*(11), 2827–2843.
https://doi.org/10.1029/2018JF004719

Lamb, M. P., McElroy, B., Kopriva, B., Shaw, J., & Mohrig, D. (2010). Linking river-flood dynamics to hyperpycnal-plume deposits: Experiments, theory, and geological implications. *Geological Society of America Bulletin*, *122*(9–10), 1389–1400. https://doi.org/10.1130/B30125.1

Lee, H., & Yu, W. (1997). Experimental study of reservoir turbidity current. *Journal of Hydraulic Engineering*, *123*(6), 520–528. https://doi.org/10.1061/(ASCE)0733-9429(1997)123:6(520)

Mayeli, P., & Sheard, G. J. (2021). Buoyancy-driven flows beyond the Boussinesq approximation: A brief review. *International Communications in Heat and Mass Transfer*, *125*, 105316.
https://doi.org/10.1016/j.icheatmasstransfer.2021.105316

Ooi, S. K., Constantinescu, G., & Weber, L. (2009). Numerical simulations of lock-exchange compositional gravity current. *Journal of Fluid Mechanics*, *635*, 361–388.

https://doi.org/10.1017/S0022112009007599

Özgökmen, T. M., Fischer, P. F., Duan, J., & Iliescu, T. (2004). Three-dimensional turbulent bottom density currents from a high-order nonhydrostatic spectral element model. *Journal of Physical Oceanography*, *34*(9), 2006–2026. https://doi.org/10.1175/1520-0485(2004)034<2006:TTBDCF>2.0.CO;2

Parker, G., Fukushima, Y., & Pantin, H. M. (1986). Self-accelerating turbidity currents. *Journal of Fluid Mechanics*, *171*(1), 145-181. https://doi.org/10.1017/S0022112086001404

Parker, G., & Toniolo, H. (2007). Note on the analysis of plunging of density flows. *Journal of Hydraulic Engineering*, *133*(6), 690–694. https://doi.org/10.1061/(ASCE)0733-9429(2007)133:6(690)

Piton, V., Soulignac, F., Ulrich, L., Graf, B., Wynn, H. K., Blanckaert, K., & Barry, D. A. (2022). Tracing unconfined nearfield spreading of a river plume interflow in a large lake (Lake Geneva): Hydrodynamics, suspended particulate matter and associated fluxes. *Frontiers in Water*, *4*: 943242. https://doi.org/doi: 10.3389/frwa.2022.943242

Pope, E. L., Cartigny, M. J. B., Clare, M. A., Talling, P. J., Lintern, D. G., Vellinga, A., et al. (2022). First source-to-sink monitoring shows dense head controls sediment flux and runout in turbidity currents. *Science Advances*, *8*(20), eabj3220. https://doi.org/10.1126/sciadv.abj3220

Scheu, K. R., Fong, D., Monismith, S. G., & Fringer, O. B. (2018). Modeling sedimentation dynamics of sediment-laden river intrusions in a rotationally-influenced, stratified lake. *Water Resources Research*, *54*, 4084–4107. https://doi.org/10.1029/2017WR021533

Sequeiros, O. E. (2012). Estimating turbidity current conditions from channel morphology: A Froude number approach: Gravity flow estimation Froude approach. *Journal of Geophysical Research: Oceans*, *117*(C4), C04003. https://doi.org/10.1029/2011JC007201

Sequeiros, O. E., Naruse, H., Endo, N., Garcia, M. H., & Parker, G. (2009). Experimental study on self-accelerating turbidity currents. *Journal of Geophysical Research, 114*(C5), C05025. https://doi.org/10.1029/2008JC005149

Shin, J. O., Dalziel, S. B., & Linden, P. F. (2004). Gravity currents produced by lock exchange. *Journal of Fluid Mechanics*, *521*, 1–34. https://doi.org/10.1017/S002211200400165X

Singh, B., & Shah, C. R. (1971). Plunging phenomenon of density currents in reservoirs. *La Houille Blanche*, *1*, 59–64. https://doi.org/10.1051/lhb/1971005

Soulignac, F., Lemmin, U., Ziabari, S. M. H., Wynn, H. K., Graf, B., & Barry, D. A. (2021). Rapid changes in river plume dynamics caused by advected wind-driven coastal upwelling as observed in Lake Geneva. *Limnology and Oceanography*, *66*(8), 3116–3133. https://doi.org/10.1002/lno.11864

Spigel, R. H., Howard-Williams, C., Gibbs, M., Stephens, S., & Waugh, B. (2005). Field calibration of a formula for entrance mixing of river inflows to lakes: Lake Taupo, North Island, New Zealand. *New Zealand Journal of Marine and Freshwater Research*, *39*(4), 785–802. https://doi.org/10.1080/00288330.2005.9517353

Stefan, H. G., & Johnson, T. R. (1989). Negatively buoyant flow in diverging channel. III: Onset of underflow. *Journal of Hydraulic Engineering*, *115*(4), 423–436. https://doi.org/10.1061/(ASCE)0733-9429(1989)115:4(423)

Tominaga, Y., & Stathopoulos, T. (2007). Turbulent Schmidt numbers for CFD analysis with various types of flowfield. *Atmospheric Environment*, *41*(37), 8091–8099. https://doi.org/10.1016/j.atmosenv.2007.06.054

Tseng, C. Y., & Chou, Y. J. (2018). Nonhydrostatic simulation of hyperpycnal river plumes on sloping continental shelves: Flow structures and nonhydrostatic effect. *Ocean Modelling*, *124*, 33–47. https://doi.org/10.1016/j.ocemod.2018.02.003

Weller, H. G., Tabor, G., Jasak, H., & Fureby, C. (1998). A tensorial approach to computational continuum mechanics using object-oriented techniques. *Computers in Physics*, *12*(6), 620-631. https://doi.org/10.1063/1.168744

Wright, L. D., Yang, Z. S., Bornhold, B. D., Keller, G. H., Prior, D. B., & Wiseman, W. J. (1986). Hyperpycnal plumes and plume fronts over the Huanghe (Yellow River) delta front. *Geo-Marine Letters*, *6*(2), 97–105. https://doi.org/10.1007/BF02281645

Supporting Information for Chapter 3

Table of Contents

Text S3.1 Laboratory Experiments

S3.1.1 Preliminary tests

Figure S3.1.1 presents a photo of the experimental set up in the Coriolis Platform at LEGI (Université Grenoble Alpes, Grenoble, France). The inlet conditions were measured by Particle Image Velocimetry (PIV) and an Acoustic Doppler Velocity (ADV) meter during preliminary tests using pure water. The laser sheet was positioned horizontally at a depth of $z = -0.035$ m. It has a view of -0.3 m $< x < 0$ m and -1 m $< y < 1$ m. Images of 2 m $\times$ 2.5 m were taken by a high-resolution SCMOS camera (PCO edge 5.5) with a resolution of 2160 $\times$ 2560 pixels at a frame rate of 10 Hz. Figure S3.1.2a presents the transversal profiles of time-averaged velocity $\bar{u}$ near the end of the inlet channel at $(x, z) = (-0.3, -0.035)$ m when experiments for the two different Q_0 values were performed. Although fluctuations were observed, the transversal velocity profiles can be assumed to be uniform. Figure S3.1.2b presents the transversal profiles of velocity root mean square (u_{rms}) at the same location, showing that the turbulent intensity (u_{rms}/U_0) ranged between 3% and 6% with a mean value of 4%. This information was used to set the magnitude of inlet turbulence generated by the *turbulentDFSEMInlet* function in the numerical model (OpenFOAM). The detailed Reynolds stress data required for *turbulentDFSEMInlet* function was obtained from a preliminary numerical case and enlarged proportionally to ensure u_{rms}/U_0 is close to 4%. ADV measurements were also taken during the preliminary tests. The ADV probe was fixed at $(x, y) = (-1, 0)$ m, but could be moved vertically to measure the vertical velocity profile in the inlet flow (Fig. S3.1.3). At each measuring point, the ADV measured velocities for 2 min with an acquisition frequency of 200 Hz. The vertical velocity profile of the time-averaged velocity ($\bar{u}$) in the inlet channel (Fig. S3.1.3) was well fitted by a log-wake law (Nezu and Nakagawa, 1993):

$$\frac{\bar{u}(z - z_b)}{u_*} = \frac{1}{\kappa} \ln \left[\frac{(z - z_b) u_*}{\nu} \right] + C + \frac{2\Pi}{\kappa} \sin^2 \left[\frac{\pi (z - z_b)}{2 H_0} \right] \tag{S3.1}$$

where κ, C and Π are, respectively, the von Karman constant, integration constant and wake strength parameter. Also, u_* denotes the shear velocity, z_b the depth of the bottom boundary, H_0 the inflow water depth and ν the kinematic viscosity. The shear Reynolds

number ($Re_\tau = u_* H_0/v$) was estimated to be close to 1500 in the inlet channel for both discharges.
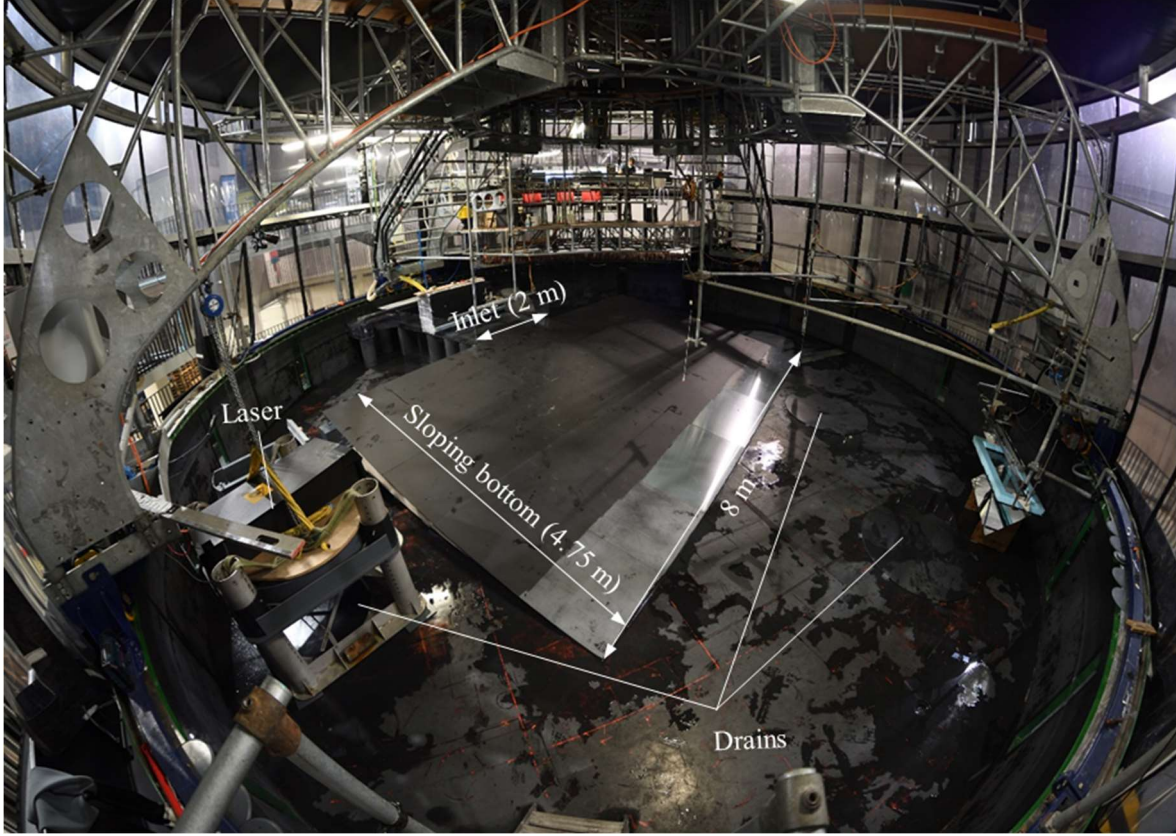

Figure S3.1.1 Photograph of the experimental set-up in the circular tank of the Coriolis Platform composed of a horizontal inlet channel, a sloping flat plate, three drains and a laser. The (inclined) horizontal laser sheets are emitted from the Laser (see Fig. 3.3a in main text for details).

S3.1.2 Onset and maximum duration of each experiment

During the experiments, two PME Micro-Scale Conductivity Instruments 125 (MSCTI, PME Vista, California, USA) were installed in the inlet channel at $(x, y) = (-1, 0 \text{ m})$ to monitor the density at two vertical levels ($z = -0.06$ and -0.01 m), and served to determine the onset of experiments based on the formation of a uniform saline injection over the full depth. PIV measurements started 3 min after the onset of each experiment. A third conductivity probe was fixed in the tank above the sloping bottom at $(x, y, z) = (3.35, 0.10, -0.22)$ m and a fourth probe was installed at $(x, y) = (4.95, 2.00)$ m mounted on a 1-m axis. The fourth probe was moved vertically between $z = -0.74$ to -0.04 m

during experiments at a rate of 0.01 m s^{-1} to track the evolution of the downstream conditions (mixing). The measurements of the third and fourth probes were used to determine the maximum experimental duration, which lasted until the ambient density field was modified by the hyperpycnal inflow.

S3.1.3 Particle Image Velocimetry (PIV) configuration

The PIV set-up consisted of a light source, light sheet optics, seeding particles, three cameras, and PCs equipped with a frame grabber and image acquisition software. Polyamide particles (Orgasol) with a mean diameter of 60 μm and a specific density of 1.016 kg m^{-3} were added to the ambient water and in the injected saline water as tracer material for the PIV measurements. The laser provided a continuous light source. The beam passed through an optical lens with an angle of 75° that diverged the laser sheet in the area of interest. Two different PIV scanning configurations were performed. In the first configuration, horizontal laser sheets scanned a field of view of –0.1 m $< x <$ 3.3 m and –2.26 m $< y <$ 2.30 m for the plunging and underflow area measurements. Images of 4.5 m × 3.5 m were taken with a high-resolution SCMOS camera (JAI SP12000) with a resolution of 4096 × 3072 pixels. The laser system could be moved vertically along a linear axis to scan the water depth, yielding laser sheets at five horizontal levels at z = –0.04, –0.08, –0.12, –0.16, –0.22 m. At each level, two scans were made, and during each scan, 496 images were taken at a frequency of 10 Hz. In the second configuration, the laser sheet was parallel to the bottom slope. A total of 15 sections ranging from 0.01 m to 0.15 m above the bottom slope, covering a field of view of –0.1 m $< x_s <$ 3.3 m and –2.26 m $< y_s <$ 2.30 m, were measured.

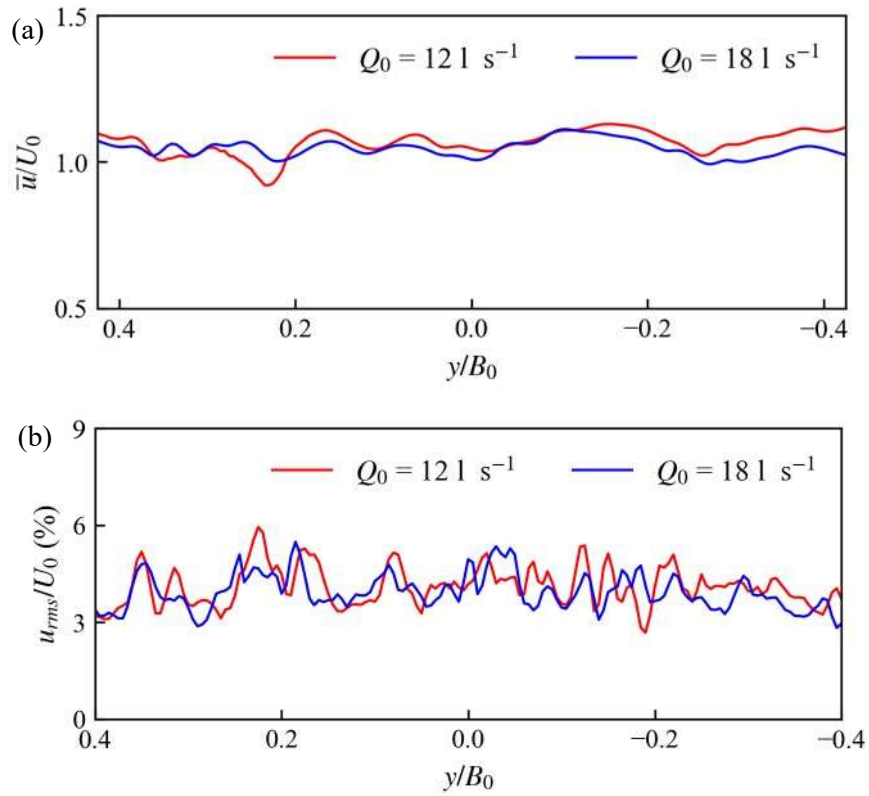**Figure S3.1.2** Transversal profiles of (a) mean velocity and (b) turbulent intensity in the inlet channel measured at $(x, z) = (-0.3, -0.035)$ m, for the two inflow discharges. Measurements were taken in preliminary tests.
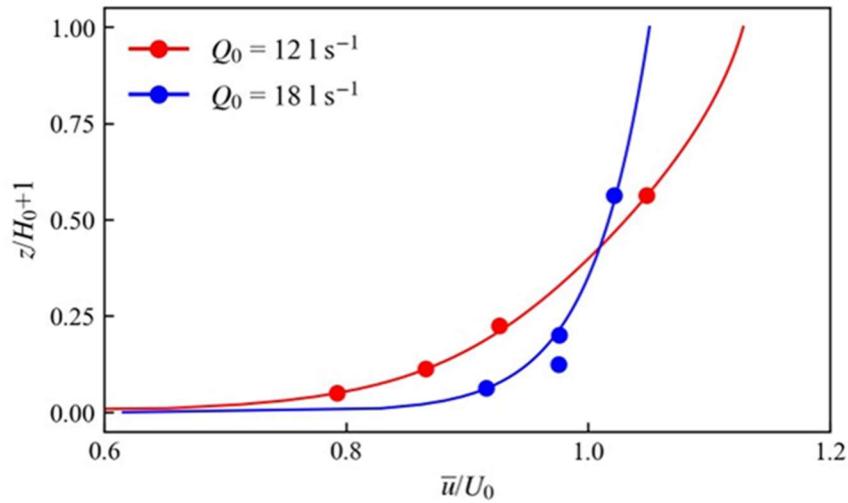

Figure S3.1.3 Measured vertical velocity profiles (circles) in the inlet channel $(x, y) = (-1, 0)$ m for two different flow rates compared with the fitted log-wake law (lines). Red and blue

represent data for $Q_0 = 12$ l s^{-1} and 18 l s^{-1}, respectively. The velocity profile is nondimensionalized by the inlet bulk velocity U_0.

Text S3.2 Numerical modeling

S3.2.1 Numerical model configurations

In OpenFOAM, a simple filter based on grid size and the dynamic one-equation eddy viscosity (*dynamicKEqn*) SGS model (Kim and Menon, 1995) were applied to solve the Navier-Stokes equations. During the simulation, the time step was adapted to keep the Courant number smaller than 0.5. As mentioned above, the inlet flow was introduced by a pumping system and then stabilized using in-channel structures. Instead of directly simulating the real inlet channel configuration, the vertical velocity profiles measured with the ADV near the end of the inlet channel were fitted by a log-wake law (Nezu and Nakagawa, 1993) and put directly into the numerical model's inlet face while the transversal distribution was assumed to be uniform (Text S3.1.1). The Divergence Free Synthetic Eddy Method (*turbulentDFSEMInlet*) of Poletto et al. (2013) was also adopted at the inlet face to provide structured eddies and turbulence whose intensity was of the same order as that measured (Text S3.1.1).

For the boundary condition in the inlet channel, preliminary numerical tests showed that the no-slip condition resulted in the generation of artificial boundary layers, and a velocity distribution that was considerably different to that measured at the end of the inlet channel. To avoid the effect of artificial boundary layers, a slip boundary condition was chosen for the bottom and the side walls of the inlet channel. Within the receiving water body, the no-slip boundary condition was chosen for the bottom and the side walls. At the free water surface, a slip boundary was adopted according to the rigid lid hypothesis. For the outlet, the OpenFOAM *inletoutlet* boundary condition was used for the velocity. This is a generic outflow condition with the specified inflow if there are return flows. The *advective* boundary condition was applied for density. The *Gauss linear* scheme (a second-order centered scheme) was used for the velocity divergence and all gradient terms, whereas the *Gauss limitedLinear* scheme (a combination of a second-order centered and a first-order upwind scheme) was chosen for the divergence of density and kinetic energy. The *backward* scheme (a second-order scheme) is

adopted for all gradient terms over time. In the inlet channel and the plunging region, the majority of grid cells were 0.015 m × 0.02 m × 0.01 m. The model had ~10^7 cells in total, and a typical simulation time of ~8 h using 224 computational cores. In the numerical cases of confined plunging (Table 3.1.C in the main text), slip boundary conditions were chosen for the side walls of the whole channel to exclude the influence of side wall friction. Inlet conditions and other settings were the same as for unconfined plunging (Table 3.1.C). All numerical results were postprocessed using ParaView (https://www.paraview.org/) and fluidfoam (Bonamy et al., 2020).

S3.2.2 Grid independence

In order to ensure that the numerical model results were grid-independent, the numerical results of Case 1 (the production model, PDM) with coarser (cell size doubled in each direction) and finer (cell size halved in each direction) meshes were compared. The coarse model did not converge. In PDM, the values of $\delta_x^+ = u_* \, \delta_x/\upsilon$ and $\delta_y^+ = u_* \, \delta_y/\upsilon$ were close to 250 and 350, respectively, whereas in the fine model these values are half as large. The cells near the bottom boundary were refined in the vertical direction, and as a result, in PDM, $\delta_z^+ = u_* \, \delta_z/\upsilon$ was close to 2, and in the fine model, it was close to unity. Here, δ_x, δ_y and δ_z denote, respectively, the size of the cell in the x, y, and z directions close to the bottom boundary. Results of the fine model are compared with the production model in Figs. S3.2.1 and S3.2.2. Figure S3.2.1 presents the velocity fields on two horizontal planes ($z = -0.5H_0$ and $-2H_0$) and the central plane ($y/B_0 = 0$). A more detailed comparison of the transversal and longitudinal velocity profiles at different locations is given in Fig. S3.2.2. In general, the results of the production and fine meshes are almost the same, indicating that the presented numerical results are grid independent.
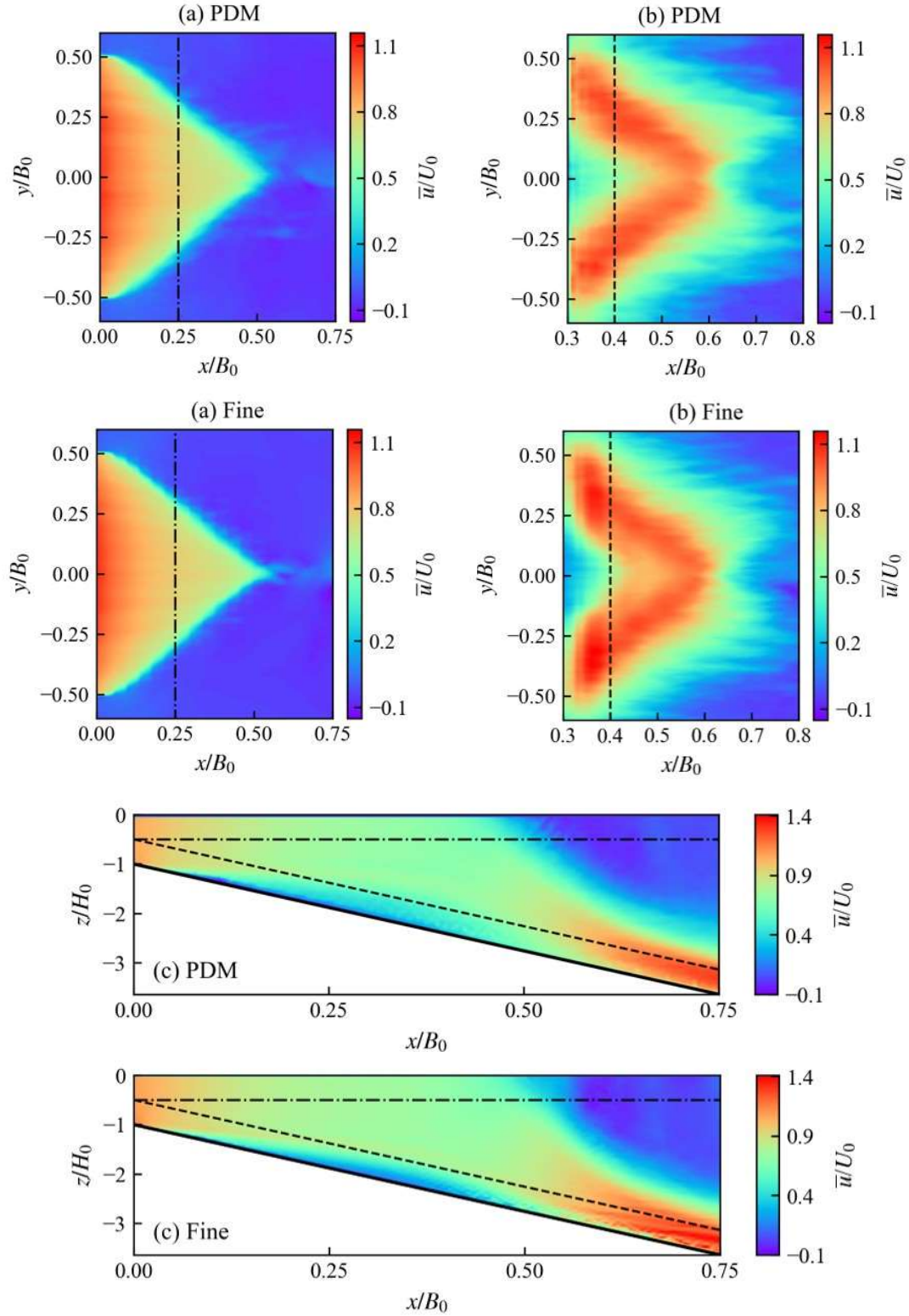
Figure S3.2.1 Comparison between the production model (PDM) and the finer mesh model (Fine) for numerical Case 1 (Table 3.1 in the main text). (a) Velocity distribution in the horizontal plane $z = -0.5H_0$. (b) Velocity distribution in the horizontal plane $z = -2H_0$. (c)

Velocity distribution in the central plane $y/B_0 = 0$. Velocity profiles along the dashed and dash-dotted lines are presented in Fig. S3.2.2. Colorbars indicate the velocity range.
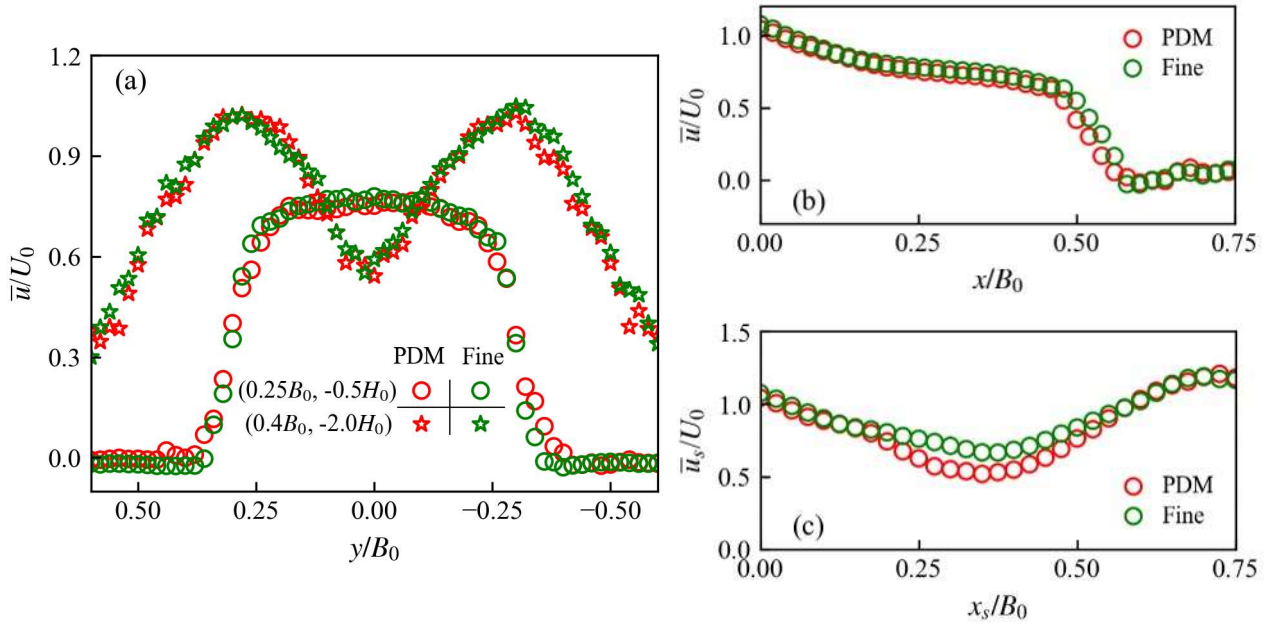

Figure S3.2.2 Comparison between the production model (red symbols, PDM) and finer mesh model (green symbols, Fine) for numerical Case 1. (a) Transversal velocity profiles (circles) at $(x = 0.25B_0, z = -0.5H_0)$ along the dash-dotted lines in Fig. S3.2.1a and transversal velocity profiles (stars) at $(x = 0.4B_0, z = -2H_0)$ along the dashed lines in Fig. S3.2.1b. (b) Longitudinal velocity profiles at $(y = 0, z = -0.5H_0)$ along the dash-dotted lines in Fig. S3.2.1c. (c) Longitudinal velocity profiles near the bottom slope (0.04 m above, along the dashed lines in Fig. S3.2.1c).

Text S3.3 Dye-visualized image analysis

In experimental Cases 1 and 3 (Table 3.1), flow visualization was performed using fluorescent dye, which provided 50 transient images of the plunge region at $z = -0.5H_0$. These images were transformed into gray scale data using the Python library Pillow (https://pillow.readthedocs.io), then averaged, based on gray scales, to obtain a mean image showing the distribution of Rhodamine; as an example, see the mean image for Case 1 in Fig. S3.3.1a. Following a ray of light (for example line m or line n) from its origin at the laser, the dye concentration must initially be zero. It increases rapidly when it reaches the dyed hyperpycnal current, attaining a maximum and then remains approximately constant. The variation of gray scale in the mean image following the

ray of light behaves similarly as shown in Fig. S3.3.1b. The only difference is that, after the rapid increase, the gray scale starts to decrease due to attenuation of the light. A fixed relationship between gray scales and dye concentration is not available. Instead, a gray scale threshold can be applied to define approximately the boundary of the triangle in Fig. S3.3.1a. For this, 95% of the maximum gray scale on each ray of light was applied to compare with the modeled density contours $(\overline{R}=0.95R_0)$ in Fig. 3.9a. As a result, the red stars in Fig. S3.3.1a, which approximately present the boundary of the triangle, were obtained. This method only can be used for the right side of the current due to the light source location. For the left side, it was assumed that the boundary is symmetric.
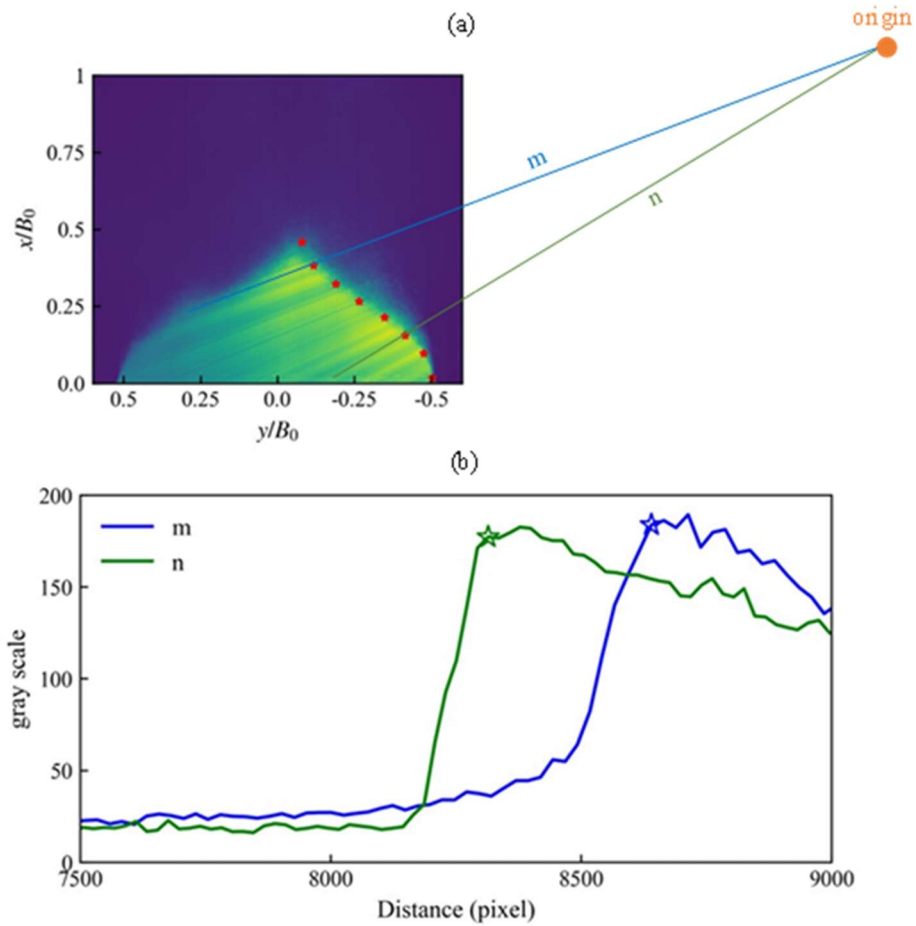
Figure S3.3.1 Method to obtain the boundary of the triangle from dye-visualized images. (a) Mean image at $z = -0.5H_0$ for experimental Case 1. Two typical rays of light from the laser are denoted by lines m and n. Red stars indicate the triangle boundary determined with 95% of the

maximum gray scales as the threshold. (b) Variation of gray scale along the two light rays. The two stars (blue and green) correspond to the red stars in (a) on the triangle boundary.

References

Bonamy, C., Chauchat, J., Augier, P., Mathieu, A., Clemencot, Q., Chassagne, R., et al. (2020). fluiddyn/fluidfoam: Release v0.2.3 (v0.2.3). https://doi.org/10.5281/zenodo.6453090

Kim, W., & Menon, S. (1995). A new dynamic one-equation subgrid-scale model for large eddy simulations. *33rd Aerospace Sciences Meeting and Exhibit*. https://doi.org/10.2514/6.1995-356

Nezu, I., & Nakagawa, H. (1993). Turbulence in open-channel flows. *IAHR, A. A. Balkema*, Rotterdam, Netherlands. https://doi.org/10.1201/9780203734902

Poletto, R., Craft, T., & Revell, A. (2013). A new divergence free synthetic eddy method for the reproduction of inlet flow conditions for LES. *Flow, Turbulence and Combustion*, *91*(3), 519–539. https://doi.org/10.1007/s10494-013-9488-2

Additional comparison with the Rhône River mouth

This additional comparison was presented in *7th IAHR Europe Congress* (Athens, Greek, 2022).

Shi, H., Negretti, M. E., Chauchat, J., Blanckaert, K., Lemmin, U., & Barry, D. A. (2022). The surface pattern of unconfined, hyperpycnal river plume plunging. *7th IAHR Europe Congress*, Athens, Greek. https://www.iahr.org/library/infor?pid=22271

Section 3.3.4 made a comparison between the plunge location determined by the experiment/model and that from a remoting sensing image by an RGB camera taken at the Rhône River mouth (Lake Geneva) on 1 May 2017. In addition to the RGB camera, a thermal camera was also installed at the same location to monitor the surface patterns at the Rhône River mouth (Fig. A3.1a, for example). Images taken from June 2019 to June 2020 were used to determine the daily plunge locations, except foggy days. The daily plunge location was averaged from 24 images (every hour). Discharge, temperature and suspended sediment concentration of the river inflow and temperature of the ambient lake water were obtained from local hydrological stations to determine the initial densimetric Froude number at the river mouth. The comparison between the observed plunge location compared with that from experiments and numerical models is generally good as depicted in Fig. A3.1, although it seems that the x_p is slightly larger in the field. This difference may be due to the deposition of large-size suspended sediments and the evolution of bed morphology as discussed in Section 3.3.4.
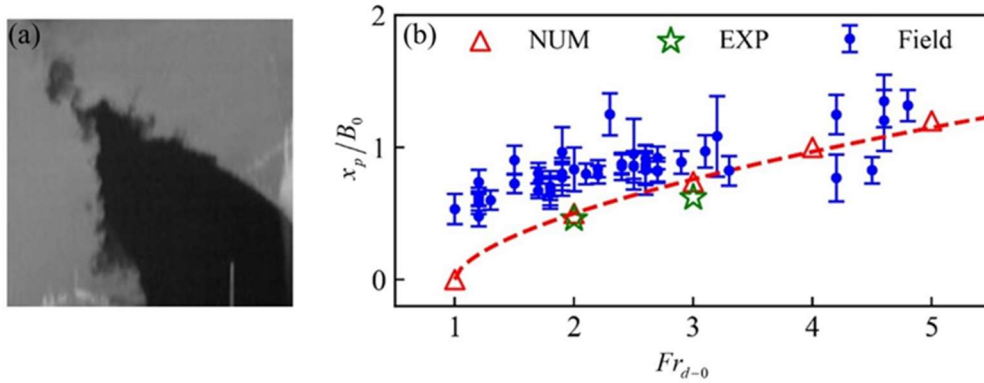

Figure A3.1 (a) A thermal image taken at the Rhône River mouth on 25 July 2019 at 3 am (local time). The image has been postprocessed to give a vertical top view. (b) Variations of the plunge location with initial densimetric Froude number obtained from the numerical model (triangles), experimental measurement (stars) and field observations (circles).

Chapter 4 Impacts of negative buoyancy on the development of shear layers and coherent structures at the interface between a hyperpycnal plume and the quiescent receiving ambient

Key Points

- A turbulence-resolving CFD model is established to simulate the nearshore hydrodynamics of a hyperpycnal river plume.

- The development of shear layers at the sides of the plume under the influence of negative buoyancy is studied.

- Characteristics of 3D Kelvin Helmholtz-type coherent structures developing in shear layers are revealed.

Abstract

Kelvin Helmholtz-type Coherent Structures (KHCS) developing inside shear layers are an important mechanism for the mixing of two fluids. The present study uses a turbulence-resolving CFD model based on Large Eddy Simulation to simulate the nearshore flow fields of a river plume entering into a laterally unconfined quiescent ambient. Shear layers are observed at two sides of the plume whose growth is suppressed by the negative buoyancy arising from higher density of the river plume than the ambient water. The plume-ambient interface is a hooked face because the negatively buoyant plume slumps laterally. As a result, the shear-induced vorticity changes its direction from vertical near the water surface to transversal near the bottom, leading to specific three-dimensional shapes of KHCS, which present a half crescent shape in transects. KHCS generate nearly periodic velocity fluctuations at the plume-ambient interface whose nondimensionalized frequency (Strouhal number) decreases with the increase of local Richardson number. A quadrant analysis shows that the ejection ($Q2$) and sweep ($Q4$) events associated with KHCS dominate the mass and

momentum exchange between the plume and ambient water. With the existence of KHCS, a coherent region is formed, remarkably contributing to the total mixing (approximately 40%) between the plume and ambient water in the nearshore region.

4.1 Introduction

Hyperpycnal river plumes arise from negatively buoyant river inflows into a receiving ambient. Examples of such currents can be found worldwide when a river with relatively low temperature and/or high sediment concentration flows into a lake or an ocean (Best et al., 2005; De Cesare et al., 2001; Soulignac et al., 2021; Spigel et al., 2005; Talling et al., 2022; Vandekerkhove et al., 2020; Wang et al., 2010). Hogg et al. (2013) and Shi et al. (2022) proposed that the river plume would slump laterally and establish a triangular pattern on the water surface due to the negative buoyancy when the ambient environment is laterally unconfined, as illustrated in Fig. 4.1a. The figure presents a satellite image of the hyperpycnal Rhône River entering Lake Geneva in Switzerland/France. Such a triangular pattern is also observed in the laboratory study of Shi et al. (2022), who reproduced the Rhône River mouth at the laboratory scale (Fig. 4.1b). After the plunge location (i.e., the vertex of the surface triangle), the hyperpycnal river plunges toward the lake bottom and transforms into an underflow (Hogg et al., 2013; Shi et al., 2022).

At the edge of the surface triangles, vertically oriented turbulent coherent structures are clearly identified in the field and in the laboratory experiment (Fig. 4.1a, b). These intermediate scale coherent structures induced from shearing indicate a shear layer at the plume-ambient interface arising from the velocity gradient between the river plume and ambient water. Similar structures have been widely observed and studied in other geophysical problems with shear layers. Examples include compound channel flows (e.g., Proust et al., 2017; Stocchino & Brocchini, 2010), tidal ebb jets (e.g., Cohen, 2012 and Shi, Negretti, et al. 2023), and river confluences (e.g., Biron et al., 2019; Lewis & Rhoads, 2015). These shear-induced vertically oriented coherent structures are classified as Kelvin Helmholtz-type structures and are believed to play an important role in mass and momentum transfer, including the exchange of sediment, pollutants,

and nutrients between the two sides of a shear layer.

The situation at the hyperpycnal river mouth is more complicated under the water surface. As the hyperpycnal river plume slumps laterally, the interface between the plume and ambient is curvilinear in cross-section rather than a vertical line when the density difference is not introduced (red dashed lines in Fig. 4.1c, d). With such a curved interface, the negative buoyancy is expected to influence the development of the shear layer and shear-induced intermediate scale coherent structures. However, such an impact has yet to be classified. The characteristics and development of the shear layers and coherent structures are still to be revealed in such a configuration, especially under the water surface.
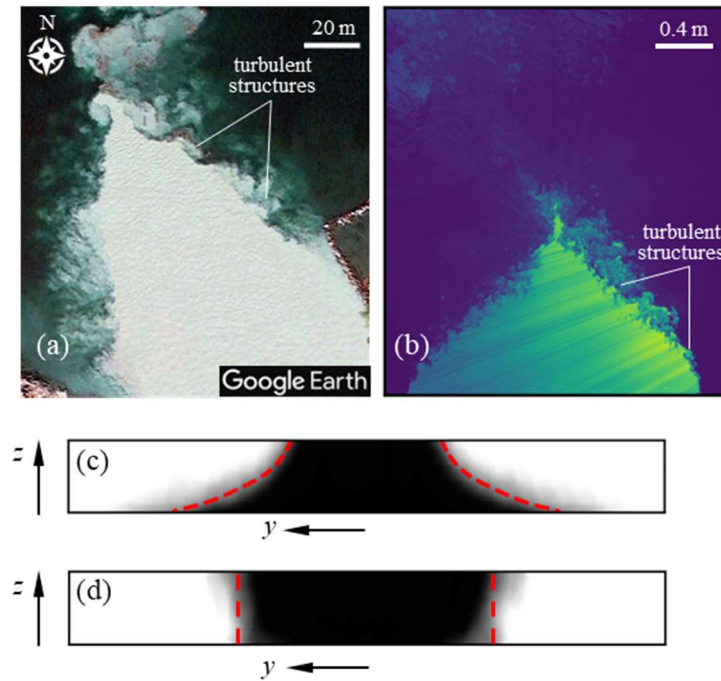
Figure 4.1 (a) Satellite image of the Rhône River mouth (Lake Geneva) in September 2018 from Google Earth. (b) Dye-visualized image captured during the laboratory experiment of Shi et al. (2022). The inflow was visualized by Rhodamine (refer to their Fig. 4a for details). (c) Sketch of a hyperpycnal river plume cross-section. (d) Sketch of a neutrally buoyant river plume cross-section. In (c) and (d), the river plume is colored black and the ambient water is white. The red dashed lines present the interface between the river plume and ambient water.

Details of the shear layers and intermediate scale coherent structures are difficult to measure in the field, considering the complexity of the hydrodynamic environment at a hyperpycnal river mouth (e.g., unsteady river inflow, complex topography, background currents, wind effects) and limited time-space resolution of measuring equipment. These difficulties can be partially resolved in laboratory experiments, but the laboratory measuring techniques can only provide datasets over a line (using Acoustic Doppler Velocity Profiler) or a plane (using Particle Image Velocimetry), which cannot sufficiently unravel the three-dimensional (3D) coherent structures. This study aims to use a turbulence-resolving model based on Large Eddy Simulation (LES) to simulate the nearshore hydrodynamics of a hyperpycnal river mouth, which is able to provide continuous high-resolution 3D datasets of the velocity and density fields and thus able to capture the development of shear layers and coherent structures. The following scientific questions are addressed:

- What is the influence of the negative buoyancy on the shear layer development?

- What are the 3D characteristics of those shear-induced coherent structures, especially under the water surface?

- How does the negative buoyancy influence the coherent structures development?

- What contribution do these coherent structures make to the mixing between the river plume and ambient water?

4.2 Numerical model

The numerical model used in the present study, as detailed in Shi et al. (2022) and Shi, Negretti, et al. (2023), solves the incompressible Navier–Stokes equations using a transient solver "*BuoyantBoussinesqPimpleFoam*" provided by the open-source CFD package OpenFOAM (De Lorenzis and Düster, 2020; Jasak, 2009; Weller et al., 1998), while the turbulence is resolved using LES. The computational domain of the model is identical to that of Shi et al. (2022) and Shi, Negretti, et al. (2023), consisting of a rectangular inlet channel ($B_0 = 2$ m wide, $H_0 = 0.08$ m deep) connected to a receiving tank with an 8°-sloping bottom (Fig. 4.2). A Cartesian coordinate system whose origin (0, 0, 0) is located at the water surface and downstream end of the inlet channel is

applied. Longitudinal ($u = \bar{u} + u'$), transversal ($v = \bar{v} + v'$), and vertical velocities ($w = \bar{w} + w'$) follow x, y, and z directions, respectively. Time-averaged values are denoted by the overbar, and fluctuations by the prime. The mesh used in the model has a resolution of $0.007 \times 0.01 \times 0.005$ m, which has been proven to be sufficiently fine to capture intermediate scale coherent structures (Shi, Negretti, et al., 2023). For other configurations of the model, including governing equations, subgrid-scale model, inlet/outlet conditions, boundary conditions, and numerical schemes, the reader is referred to the abovementioned previous work (Shi et al., 2022; Shi, Negretti, et al., 2023). The model was validated with experimental data of Shi et al. (2022) when the river plume is negatively buoyant and with data of Shi, Negretti, et al. (2023) when the river plume is neutrally buoyant. The validation, detailed in Shi et al. (2022) and Shi, Negretti, et al. (2023), ensures the capability and accuracy of the numerical approach to simulate the mean fields of the river plume and the characteristics of intermediate scale coherent structures.

Four numerical cases were established, where the initial relative density difference between the river plume and ambient water $R_0 = (\rho_0 - \rho_a)/\rho_a$ (ρ_0 denotes the initial density of the river plume, and ρ_a is the density of ambient water) increases from 0% to 0.2%, thereby decreasing the initial densimetric Froude number from infinity to 2 (Table 4.1). The densimetric Froude number follows $Fr_{d-0} = Fr_0 / \sqrt{R_0} = U_0 / \sqrt{g H_0 R_0}$, where U_0 and H_0 are the initial bulk velocity and water depth of the river inflow, respectively. Hereafter, the subscript "0" denotes the initial parameters at the river mouth. Shi et al. (2022) proved that the plunging hydrodynamics of the hyperpycnal river plume is controlled by the initial densimetric Froude number (Fr_{d-0}) rather than the Froude number (Fr_0). Thus, Fr_0 is maintained constant at 0.08 in the present study. The numerical model provides datasets of velocity, density, and concentration. The concentration (c) here indicates the proportion of the fluid originating from the river plume, that is, $c = 1$ for the inflow and $c = 0$ for the ambient water. For Cases 2–4 when $R_0 > 0$, $c \approx R/R_0$.

Table 4.1. Summary of parameters in numerical cases.

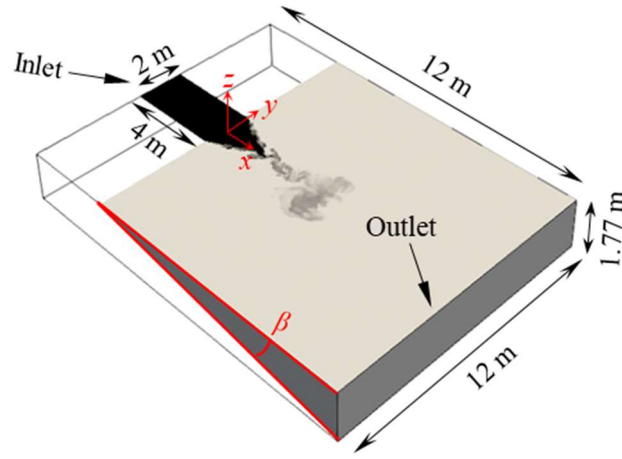| Case	Q_0 (L s^{-1})	U_0 (m s^{-1})	R_0	Fr_0	$Fr_{d\text{-}0}$	β (°)	x_m/B_0
1	12	0.075	0	0.08	∞	8	1.24
2	12	0.075	1.12e–4	0.08	8	8	0.97
3	12	0.075	4.5e–4	0.08	4	8	0.72
4	12	0.075	2e–3	0.08	2	8	0.45

Figure 4.2 Geometry used in the numerical model, consisting of an inlet channel and a receiving tank. The river plume is colored in black and the ambient water, in white. The same geometry was applied by our previous studies (Shi et al., 2022; Shi, Negretti, et al., 2023).

4.3 Results and Discussion

4.3.1 Shear layer and coherent structures observed on the water surface

Shear layers (also called mixing layers) are formed by the velocity gradient between two fluids. Figure 4.3(i), presents the time-averaged velocity distribution of the four numerical cases on the water surface ($z/H_0 = 0$). A velocity gradient is clearly observed between the river plume and ambient water. Figure 4.3(ii), illustrates the time-averaged concentration field on the water surface, showing a similar pattern to the velocity field. Figure 4.3 (iii), depicts the distribution of turbulent kinetic energy $k = 0.5\left(\overline{u'u'} + \overline{v'v'} + \overline{w'w'}\right)$ on the water surface, highlighting the shear layers. The time-averaged concentration contour ($\bar{c} = 0.5$) is used to represent the interface

between the river plume and ambient water, which is located at the center of the shear layers (Fig. 4.3(iii)). Shear layers approcach the centerline in Case 1 due to the convergence of the river plume induced by the bottom sloping boundary as explained by Shi, Negretti, et al. (2023). The convergence of the shear layers is even stronger in Cases 2–4 as a result of the lateral slumping of the hyperpycnal river plume induced by negative buoyancy (Hogg et al., 2013; Shi et al., 2022). Following Shi, Negretti, et al. (2023), we define a curvilinear coordinate system (x_n, y_n) along the plume-ambient interface, as shown in Fig. 4.3 (iii), with corresponding velocities $u_n = \bar{u}_n + u'_n$ and $v_n = \bar{v}_n + v'_n$, tangent and perpendicular to the interface curve, respectively. As the system is symmetric along the centerline ($y = 0$), only half of the system ($y < 0$) is considered in the following analysis. The velocity gradient between the river plume and ambient water is illustrated by the velocity profile along a representative line perpendicular to the interface curve (dashed lines in Fig. 4.3(iii)). The selected line intersects with the interface curve at $x = 0.5x_m$, where x_m represents the place where the two shear layers meet at the centerline, estimated as the location when the centerline concentration starts to decrease (Fig. 4.3(iv)). As the velocity $\bar{u}_n$ increases from $\bar{u}_{n-a}$ (at y_{n-a}) inside the ambient water to $\bar{u}_{n-c}$ (at y_{n-c}) inside the river plume, the momentum thickness of the shear layer is calculated as:

$$\theta_s = \int_{y_{n-a}}^{y_{n-c}} \left[\frac{1}{4} - \left(\frac{\bar{u}_n - \bar{u}_{n-o}}{\bar{u}_{n-c} - \bar{u}_{n-a}} \right)^2 \right] dy_n \qquad (4.1)$$

where $\bar{u}_{n-o}$ is the arithmetic mean of $\bar{u}_{n-a}$ and $\bar{u}_{n-c}$. The variation of the shear layer momentum thickness along the interface curve is calculated and plotted in Fig. 4.4a. With the increasing distance from the river mouth, the momentum thickness increases as the shear layers develop due to mixing. However, such growth is suppressed when the negative buoyancy is introduced.
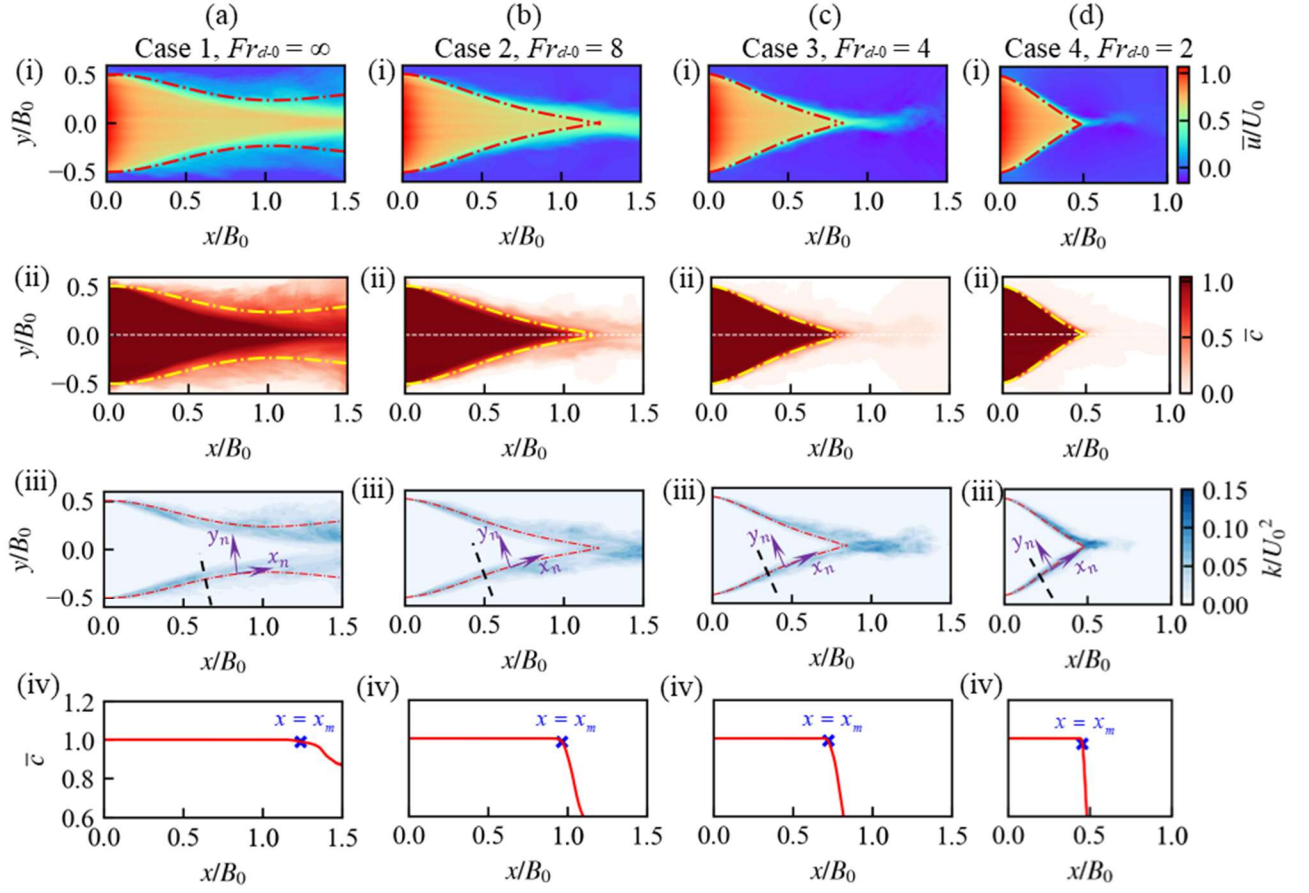
Figure 4.3 Each panel (a–d) presents one numerical case. Subplots (i) and (ii): Time-averaged velocity (i) and concentration (ii) fields on the water surface. Subplot (iii): Turbulent kinematic energy distribution on the water surface. The dash-dotted lines present the interface between the river plume and ambient water. The black dashed line in subplot (iii) is perpendicular to the plume-ambient interface whose intersection with the interface is located at $x = 0.5x_m$. Subplot (iv) presents the concentration profile along the surface centerline ($y = 0$, $z = 0$). The crosses indicate the location where the shear layers from both sides meet at the centerline.

Figure 4.4 (a) Typical velocity profile across the plume-ambient interface (along the black dashed lines in Fig. 4.3(iii)). (b) Variation of the momentum thickness on the water surface with the development of the shear layer. Different cases are labelled as follows: (Case number, Fr_{d-0}).

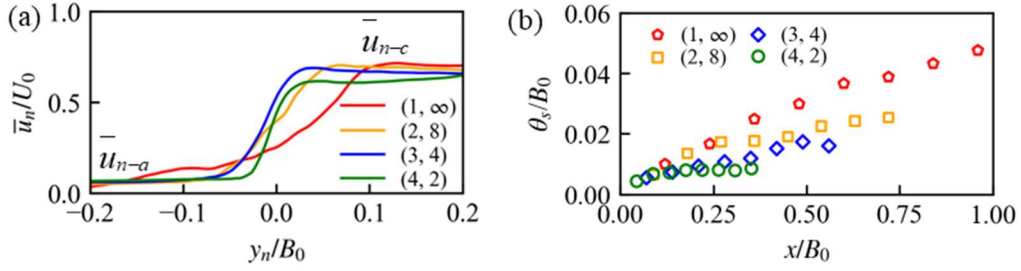Vertically oriented coherent structures are observed at the two sides of the surface triangle, as shown in Figs. 4.5a–d. These structures inside the shear layers are induced by the velocity gradient between the river plume and ambient water, and thus supposed to Kelvin Helmholtz-type structures (Brown & Roshko, 1974). The rotation of these structures is illustrated by the vorticity field in Figs. 4.5e–h, clockwise ($\omega_k < 0$) in the right-side shear layer ($y < 0$) and counterclockwise ($\omega_k > 0$) in the left side shear layer ($y > 0$). These structures are smaller in cases with smaller initial densimetric Froude number because the growth of the shear layers is suppressed by negative buoyancy (Fig. 4.4). The vorticity of these coherent structures is controlled by a balance between advection, baroclinic production, dissipation, stretching and tilting (Cantero et al., 2007; Yuan & Horner-Devine, 2017). The stretching and tilting term describes the lengthening of vortices, which is absent in two-dimensional flows (Tennekes & Lumley, 1972) and thus reflects the three-dimensionality of the flow. Figures 4.6a and b compare the instantaneous distribution of vertical vorticity stretching (ψ) on the water surface in Cases 1 and 4, as follows:

$$\psi = \omega_i \frac{\partial w}{\partial x} + \omega_j \frac{\partial w}{\partial y} + \omega_k \frac{\partial w}{\partial z} \tag{4.2a}$$

$$\overline{\psi}_{ave} = \int_{-5\theta}^{5\theta} \overline{\psi} dy_n \Big/ 10\theta \tag{4.2b}$$

where $\omega_{i,j,k}$ denotes the three components of the vorticity. In both cases, vorticity stretching is observed mainly inside the shear layers. Compared with Case 1 without buoyancy, the vorticity stretching is much stronger in Case 4 as the negative buoyancy enhances the three-dimensionality of the flow and coherent structures. Figure 4.6c presents the time-averaged vorticity stretching ($\overline{\psi}$) along the representative line perpendicular to the plume-ambient interface (Fig. 4.3(iii), for the location of the line). $\overline{\psi}$ is negative in Cases 2–4 (the same sign as the vorticity, Figs. 4.5e–h), that is, is a source of voriticty. By contrast, both positive and negative values of $\overline{\psi}$ are observed in Case 1, which are interpreted as fluctuations due to the heterogeneity of the flow fields (Yuan & Horner-Devine, 2017). The values of $\overline{\psi}$ presented in Fig. 4.6c are then averaged over the shear layer (Eq. 4.2b, Fig. 4.6d), whose magnitude increases with the decrease of initial densimetric Froude number (Fr_{d-0}). This finding indicates that the negative buoyancy enhances the three-dimensionality of the coherent structures and thus enhances the vertical voriticty stretching.
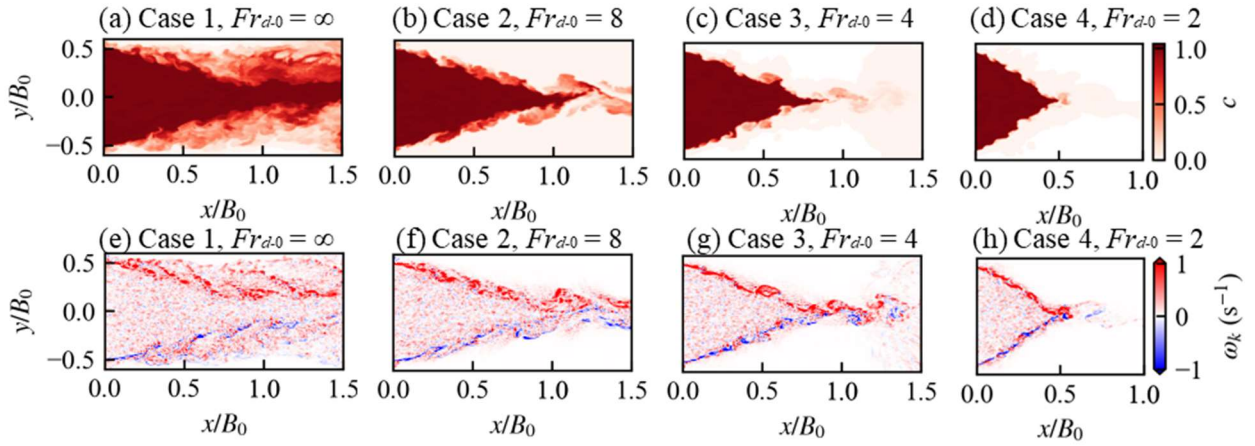

Figure 4.5 Transient fields of concentration (a)–(d) and vorticity (e)–(h) on the water surface.
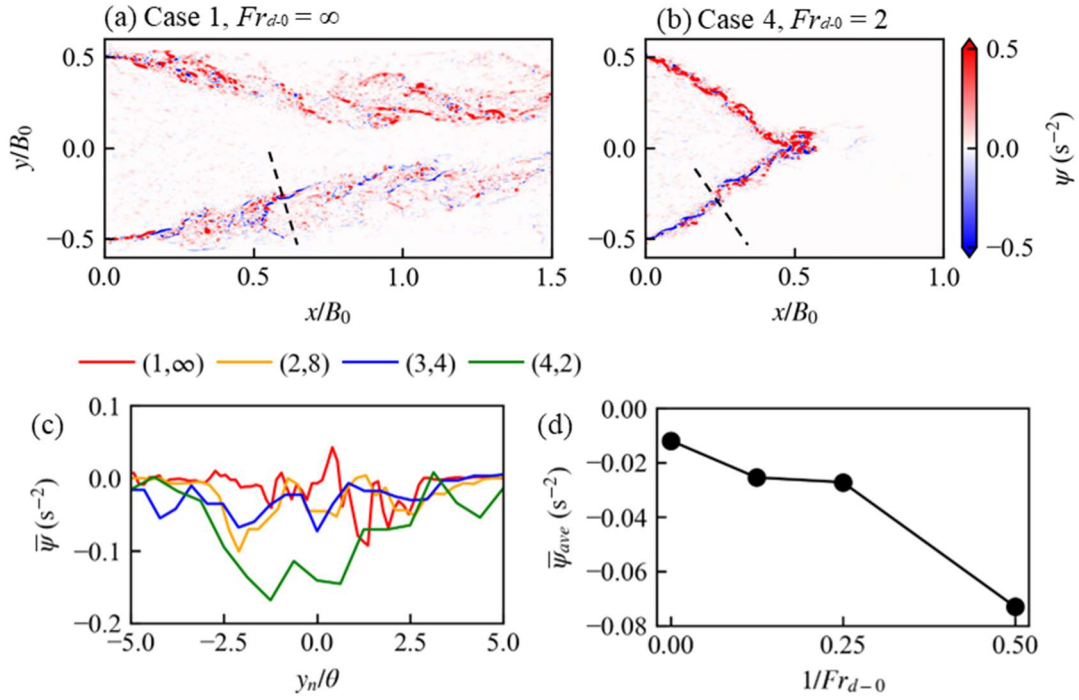
Figure 4.6 (a–b) Instantaneous distribution of vertical vorticity stretching (ψ) on the water surface. (c) Time-averaged vertical vorticity stretching along the representative line perpendicular to the plume-ambient interface (dashed lines in Fig. 4.6a, b). (d) Averaged vertical vorticity stretching $\overline{\psi}_{ave}$ in different cases. In plot (c), different cases are labeled as (Case number, Fr_{d-0}).

4.3.2 3D shape of the coherent structures

Coherent structures developing in shear layers are presented by the transient iso-surface of $c = 0.5$, as shown in Fig. 4.7(i), which is rough and wrinkled. Each wrinkle indicates a coherent structure. Figure 4.7(ii), presents the time-averaged iso-surface of $\overline{c} = 0.5$, which locates the 3D interface between the river plume and the ambient. In Case 1 with neutral buoyancy, this interface is oriented vertically but becomes hooked in other cases under the influence of negative buoyancy because the river plume slumps laterally. The comparison of the subplots in Fig. 4.7 indicates that the mixing term ($\overline{c'c'}$, refer to Duguay et al., 2022) is larger in the region where the coherent structures are found. A representative transect is selected for further analysis (represented by red parallelograms in Fig. 4.7(ii) such that it is perpendicular to the plume-ambient

interface curve on the water surface (dash-dotted lines in Fig. 4.3) with an intersection at $x = 0.5x_m$. The selected transect ends at $x = x_m$ given that we only consider the nearshore region ($0 < x < x_m$) in the present study. Flow patterns in the representative transect are shown in Fig. 4.8, which contains four panels corresponding to the four numerical cases. The velocity difference between the plume and ambient water is illustrated in subplot (i), indicating a strong shear between the two fluids. The plume-ambient interface inside the selected transects is determined based on the concentration contour $\bar{c} = 0.5$ (denoted by dash-dotted lines in Fig. 4.8), consistent with the velocity distribution in subplot (i). Following Duguay et al., (2022), the fluid is considered mixed when the concentration $\bar{c}$ ranges between 5% and 95%. Figure 4.8(ii) shows that the mixing term is negligible out of the mixed region ($\bar{c} < 5\%$ or $\bar{c} > 95\%$). The coherent structures are expected to develop inside the mixed region ($5\% < \bar{c} < 95\%$), forming a coherent region. The coherent region is determined based on the Pearson correlation function r_{cc}. The time-series of the concentration fluctuating signal c' (over 100 s at 10 Hz) at the point on the plume-ambient interface curve and close to the water surface is selected as the basic signal (at $y_n \approx 0$ and $z \approx 0$, orange circles in Fig. 4.8(ii)). The Pearson correlation function between the basic signal and time-series of c' at other locations inside the selected transects (over the same time period) is determined using:

$$r_{cc}\left(y_n, z\right) = \frac{\overline{c'\left(y_n, z, t\right) c'\left(y_n \approx 0, z \approx 0, t\right)}}{\sqrt{\overline{\left[c'\left(y_n, z, t\right)\right]^2}\overline{\left[c'\left(y_n \approx 0, z \approx 0, t\right)\right]^2}}} \tag{4.3}$$

The distribution of r_{cc} is plotted in Fig. 4.8(iii). The coherent region is determined using the contour $r_{cc} = 0.3$ (Shi, Negretti, et al., 2023), which is located inside the mixed region ($5\% < \bar{c} < 95\%$). The shape of the coherent region becomes a half crescent under the influence of the negative buoyancy (Cases 2–4), indicating that the coherent structures are distorted and thus the vorticity direction is not always vertical. Figure 4.9 presents the variation of time-averaged vorticity direction along the plume-ambient interface in the representative transect (Fig. 4.8) in Cases 1 and 4. This direction is determined from the ratio between its vertical component ($\partial \bar{u}_n / \partial y_n$) and transversal component ($\partial \bar{u}_n / \partial z$). In Case 1 without buoyancy, this vorticity direction

approximately follows the $-z$ direction. By contrast, in Case 4, this direction changes gradually from $-z$ to $-y_n$ along the plume-ambient interface.
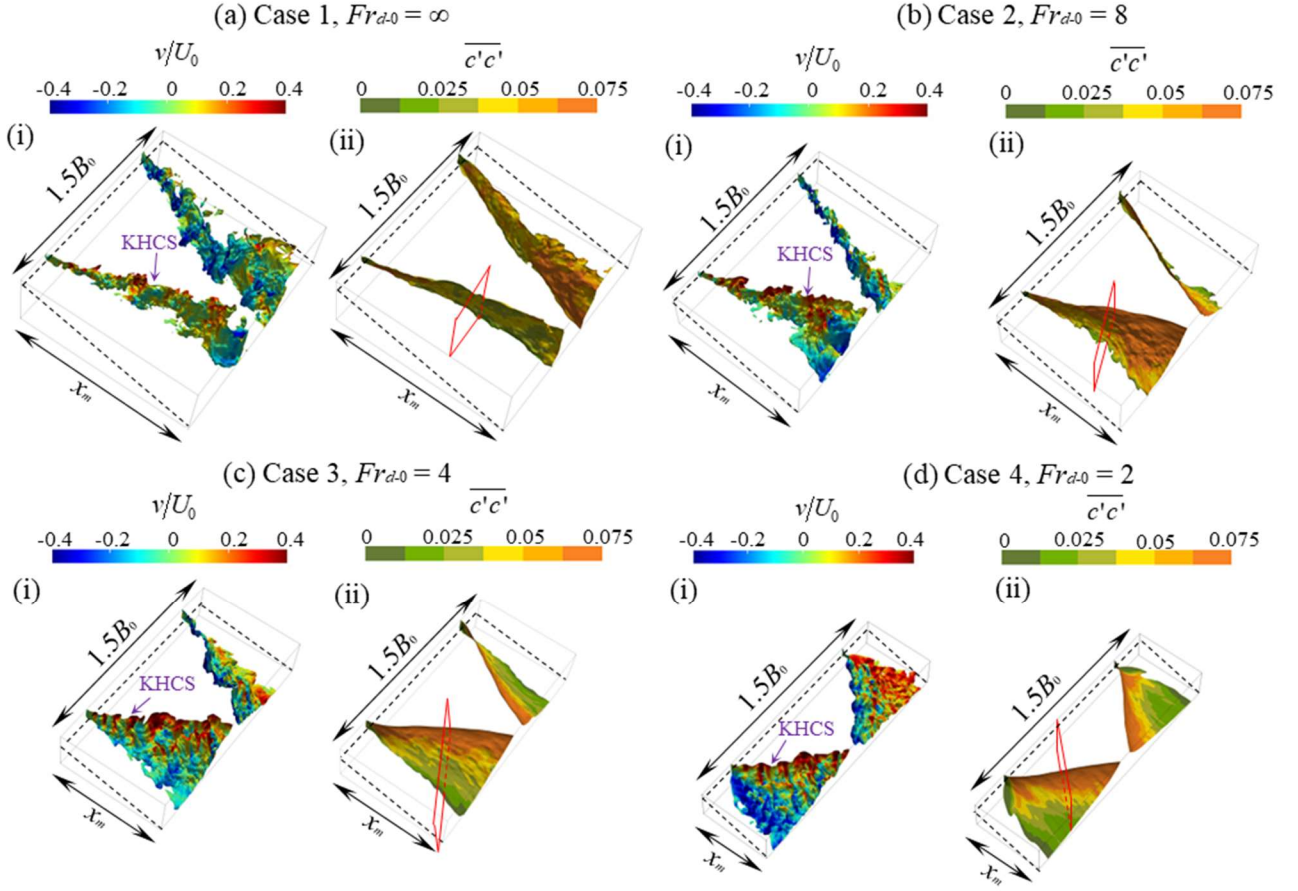
Figure 4.7 Each panel (a–d) presents one numerical case. Subplot (i) of each panel presents a transient iso-surface of $c = 0.5$, colored by transient transversal velocity at the same time. Subplot (ii) of each panel presents the time-averaged (over 100 s) iso-surface $\bar{c} = 0.5$, colored by the mixing term $\overline{c'c'}$. The sloping bottom boundary is highlighted by the dashed lines. Red parallelograms illustrate planes perpendicular to the plume-ambient interface curve on the water surface with an intersection at $x = 0.5x_m$.

Figure 4.8 Each panel represents data of a certain numerical case. Every panel contains four subplots: (i) Time-averaged velocity distribution at the representative transect. (ii) Distribution of the mixing term ($\overline{c'c'}$) at the representative transect. The dotted lines in (i) and (ii) present the contours $\overline{c} = 0.05$ and $\overline{c} = 0.95$. (iii) Distribution of the correlation function at the

representative transect. The black dash-dotted curves in (i)–(iii) show the plume-ambient interface (i.e., $\overline{c}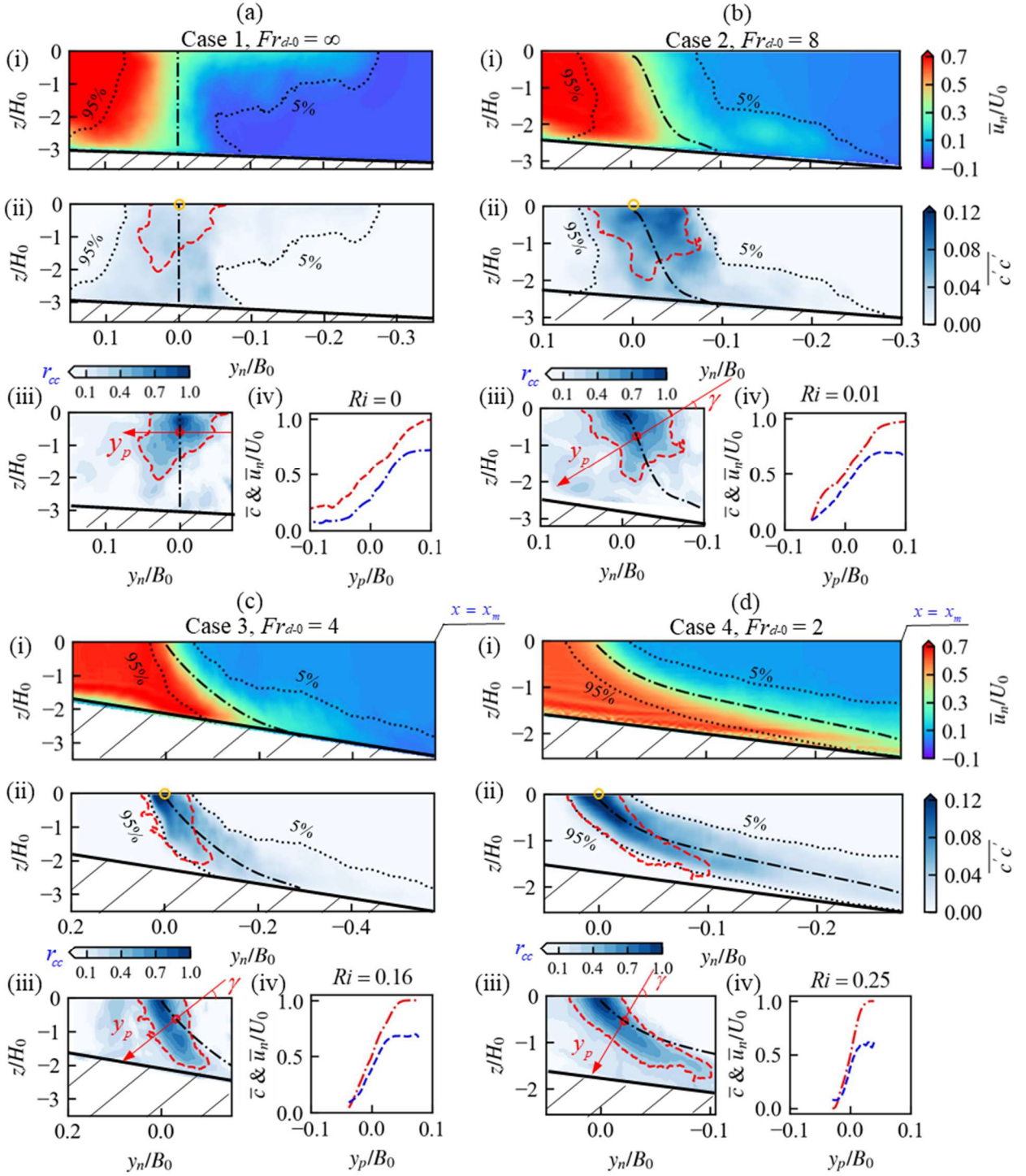 = 0.5$). The red dashed curve in (ii) and (iii) denotes the contour $r_{cc} = 0.3$. The red arrow in (iii) shows the coordinate y_p, which is perpendicular to the plume-ambient interface and crosses the central point (marked by the red circle) of the coherent structure. This coordinate y_p is identical to y_n in Case 1 and forms an angle of γ with y_n in other cases. (iv) Profiles of time-averaged density (red line) and velocity (blue line) along the y_p coordinate, based on which the Richardson number (Ri) is calculated. The central point is located at $y_p = 0$.
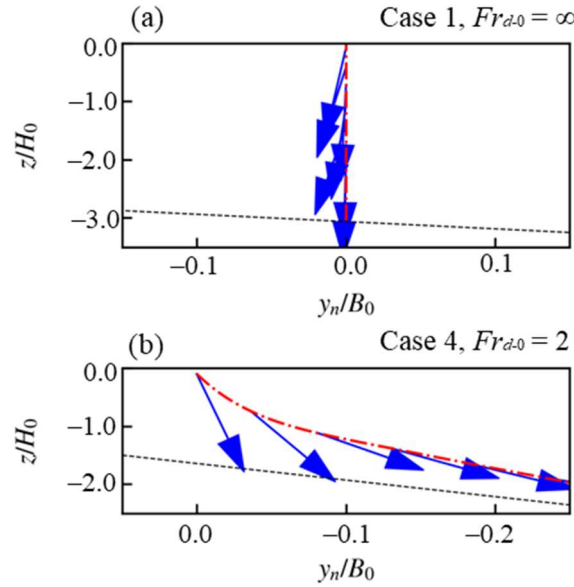
Figure 4.9 Variations of the shear-induced vorticity direction along the plume-ambient interface at the representative transect in Case 1 (a) and Case 4 (b). The location of the representative transect is presented in Fig. 4.7. The dashed line presents the bottom boundary.

4.3.3 Richardson and Strouhal numbers

A portion of the plume-ambient interface curve in the transect (black dash-dotted lines, Fig. 4.8) is located inside the coherent region, as shown in Fig. 4.8(iii). The geometric midpoint of this portion is defined as the central point of the coherent region. A new coordinate (y_p), which is perpendicular to the plume-ambient interface curve in the transect and crosses the central point, is proposed. This coordinate forms an angle γ with y_n, which equals to zero in Case 1 but is larger in other cases. The velocity and concentration profiles along the y_p coordinate are depicted in Fig. 4.8(iv), based on

which the local Richardson number at the central point is calculated, as follows:

$$Ri = R_0 \sin\gamma \, \frac{\partial \bar{c}/\partial y_p}{\partial \bar{u}_n/\partial y_p} \tag{4.4}$$

Similar transects perpendicular to the plume-ambient interface on the water surface (dash-dotted line in Fig. 4.3) with an intersection of $x = (0.2\sim0.8)x_m$ are then analyzed using the same procedure. Figure 4.10a exhibits the Richardson numbers at the central points in these transects. In Case 1 (with neutral buoyancy), the Richardson number remains zero. By contrast, in other cases with negative buoyancy, positive Richardson numbers are observed. Most Richardson numbers are smaller than 0.25, indicating that those shear-induced coherent structures are Kelvin Helmholtz-type (e.g., Negretti et al., 2017; Parker et al., 2019; Yuan & Horner-Devine, 2017). The few exceptions in Case 4 (with a maximum value of 0.27) may be due to the uncertainties when calculating gradients of velocity and density.

Kelvin Helmholtz-type coherent structures (KHCS) usually induce periodic velocity fluctuations in the shear layer, which can be detected by the power spectrum (e.g., Akula et al., 2017; Truong & Uijttewaal, 2019). Figure 4.11 presents the power spectra of the crossing-interface velocity signal v_p (along the y_p direction) at the central point in the same transects as shown in Fig. 4.8 (i.e., velocity signals at the red circles in Fig. 4.8(iii)). The frequency is nondimensionalized into the Strouhal number: $St = f\theta/\bar{u}_{n-o}$ (Ghisalberti & Nepf, 2005; Ho & Huerre, 1984), where the momentum thickness θ and arithmetic mean velocity $\bar{u}_{n-o}$ are calculated based on the local velocity profile (blue lines in Fig. 4.8(iv)) using Eq. 4.1. Instead of the typical $-5/3$ slope of isotropic turbulence energy cascade, the spectra in Fig. 4.11 follow the -3 slope corresponding to shear-induced KHCS (Truong & Uijttewaal, 2019; Uijttewaal & Booij, 2000). All the spectra are unimodal with a fundamental peak (St_{cs}) presenting the dominant frequency of the coherent structures (e.g., Deo et al., 2008; Shi, Negretti, et al., 2023; Shi, Zhang, et al., 2023; White & Nepf, 2008). St_{cs} was also calculated for the central points at other transects perpendicular to the surface plume-ambient interface (Fig. 4.10b). In shear layers without any buoyancy effect, the Strouhal number associated

with the KHCS was reported to be a constant close to 0.079 (Ho & Huerre, 1984; Ho & Huang, 1982; Shi, Negretti, et al., 2023). By contrast, as shown in Fig. 4.10b, with the increase in the local Richardson number, St_{cs} decreases because the negative buoyancy limits the development of the coherent structures. An empirical relationship between Ri and St_{cs} is obtained from the plotted datasets ($St_{cs} = 0.8Ri^2 - 0.4Ri + 0.079$), presented by the dashed line in Fig. 4.10b with a correlation function square equal to 0.8.
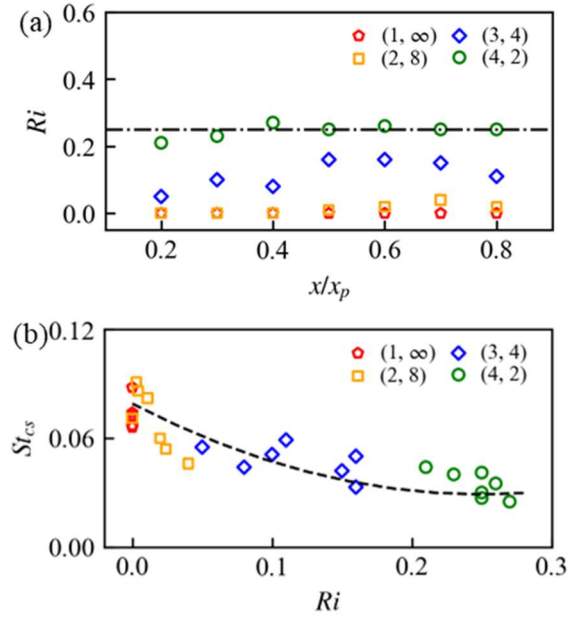

Figure 4.10 (a) Variations of the Richardson number at the central points in transects. The dash-dotted line denotes the critical Richardson number $Ri = 0.25$ for KHCS. (b) Variations of the Strouhal number associated with KHCS with the local Richardson number. The dashed line presents the empirical relationship. Datasets are labelled with (Case number, $Fr_{d\text{-}0}$) in legends.
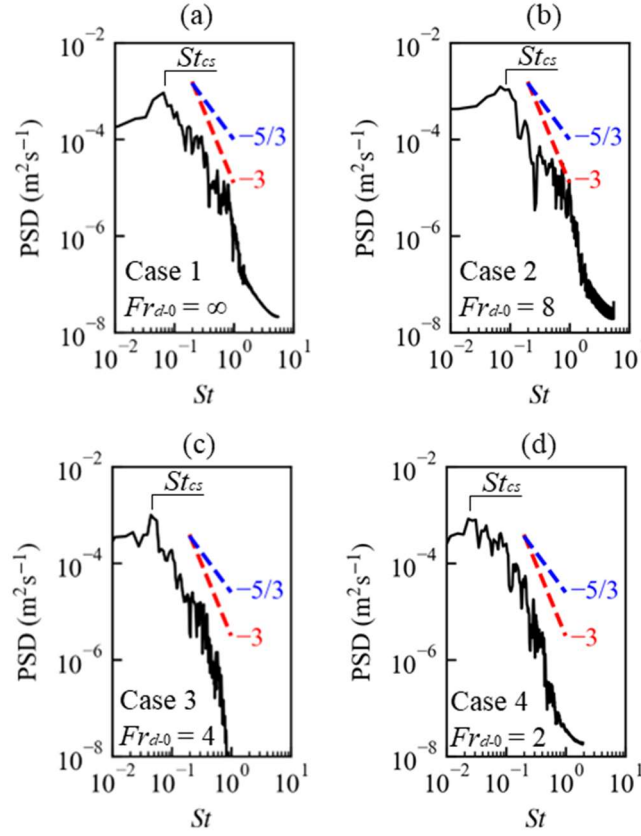
Figure 4.11 Power spectrum density of the crossing-interface velocity signal v_p at the central points in the four numerical cases. The locations of the central points are denoted by the red circles in Fig. 4.8(iii). Dashed lines present slopes of the energy cascade −5/3 (blue) and −3 (red).

4.3.4 Quadrant analysis

Figures 4.5–7 depict the KHCS at a certain time. These coherent structures can also be detected in time series of concentration or velocity signals (e.g., Kostaschuk et al., 2018; Shi, Negretti, et al., 2023). Figure 4.12(i) and (ii) present the time series data of concentration and v'_p along the y_p coordinate (Fig. 4.8), displaying the occurrence of KHCS. The largest (in y_p direction) coherent structures are observed in Case 1 without density difference. Sizes of the structures are smaller in cases with smaller $Fr_{d\text{-}0}$ given that the growth of the mixing layer is suppressed by the negative buoyancy. A quadrant analysis is applied for further analysis on the coherent structures; it was initially proposed to analyze coherent structures in open channel flow induced by channel bed

roughness (Bagherimiyab & Lemmin, 2018; Nezu & Nakagawa, 1993; Wallace, 2016; Willmarth & Lu, 1972). Later, it was applied in shear layers to analyze shear-induced coherent structures, especially their contribution to momentum and mass exchange between the two sides of a shear layer (Guan et al., 2018; Huai et al., 2019; Truong & Uijttewaal, 2019; Variano & Cowen, 2013; White & Nepf, 2008; Yue et al., 2007). Quadrant analysis has also been applied to LES data, showing good comparison with direct numerical simulation and laboratory experiments (e.g., Kim & Moin, 1986; Yue et al., 2007). In the present study, the quadrants are defined using velocity fluctuations u'_n and v'_p: ejection ($Q2$: $u'_n < 0$ and $v'_p > 0$), sweep ($Q4$: $u'_n > 0$ and $v'_p < 0$), and interactions ($Q1$: $u'_n > 0$ and $v'_p > 0$ and $Q3$: $u'_n < 0$ and $v'_p < 0$). Two covariance terms ($\overline{u'_n v'_p}$ and $\overline{c'v'_p}$) were proposed in the literature to describe the momentum and mass exchange (e.g., Variano & Cowen, 2013; Wallace, 2016; White & Nepf, 2007). Figure 4.12 (iii) and (iv) present the profiles of $\overline{u'_n v'_p}$ and $\overline{c'v'_p}$, respectively. The momentum exchange term is nondimensionalized by the shear velocity at the central point (Fig. 4.8(iii)). The shear velocity is defined as $u_{*s}^2 = -\overline{u'_n v'_p}$ (White & Nepf, 2007). Similarly, the mass exchange term $\overline{c'v'_p}$ is nondimensionalized by $\iota_*^2 = -\overline{c'v'_p}$ at the central point. The ejection ($Q2$, orange lines) and sweep ($Q4$, green lines) events are induced by the KHCS (Shi, Negretti, et al., 2023; Taborda et al., 2022; White & Nepf, 2008). They are much stronger than the interactions ($Q1$ and $Q3$, red and blue lines) and dominate the momentum and mass exchange as reported in the literature for other shear layers (e.g., Guan et al., 2018; Variano & Cowen, 2013; White & Nepf, 2008).
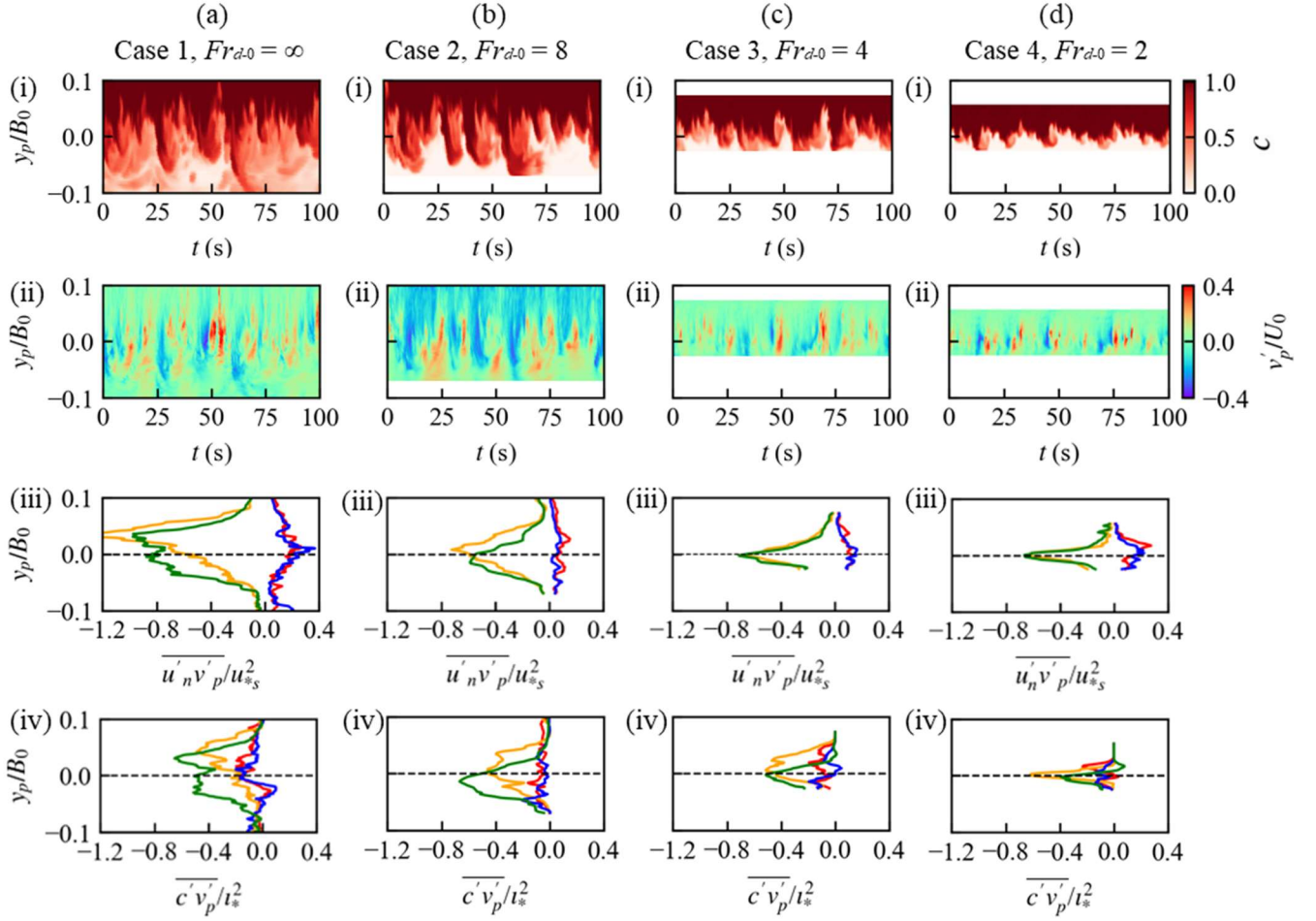
Figure 4.12 Each panel represents one numerical case. Subplots (i) and (ii) present the time series of concentration c and velocity v_p, respectively, along the representative line perpendicular to the plume-ambient interface (y_p in Fig. 4.8(iii)). Subplots (iii) and (iv) illustrate the time-averaged covariance terms $\overline{u'_n v'_p}$ and $\overline{c'v'_p}$ along the representative line in different quadrant events: $Q1$ (red), $Q2$ (orange), $Q3$ (blue), and $Q4$ (green).

4.3.5 Contribution of the coherent region on mixing

Figure 4.8(iii), shows that large values of the mixing term ($\overline{c'c'}$) are observed in the coherent region. Here, we compare the area proportion and the mixing proportion of the coherent region in the transect shown in Fig. 4.8 and other transects perpendicular to the surface plume-ambient interface with an intersection of $x = (0.2\sim0.8)x_m$. The area proportion occupied by the coherent region compared with the total mixed region inside the selected transect is calculated as follows:

$$s_A = \frac{\left[\iint dy_n dz\right]_{r_{cc}>0.3}}{\left[\iint dy_n dz\right]_{5\%<\bar{c}<95\%}} \tag{4.5}$$

The contribution of the coherent region on mixing compared with the total mixed region inside the same transect is calculated as follows:

$$s_M = \frac{\left[\iint \overline{c'c'} dy_n dz\right]_{r_{cc}>0.3}}{\left[\iint \overline{c'c'} dy_n dz\right]_{5\%<\bar{c}<95\%}} \tag{4.6}$$

In some transects, the mixed region extends out of the nearshore region ($0 < x < x_m$). For example, in Case 4, as shown by Fig. 4.8d(ii), the mixed region ($5\% < \bar{c} < 95\%$) is not closed on the right side. In such a case, only the $x < x_m$ part of the mixed region is counted when calculating s_A and s_M. Averaging over the four cases, the mixing contribution s_M ($40 \pm 11\%$, mean value $\pm$ standard deviation) is evidently larger than the area proportion s_A ($25 \pm 9\%$), suggesting that the coherent region contributes considerably to mixing.
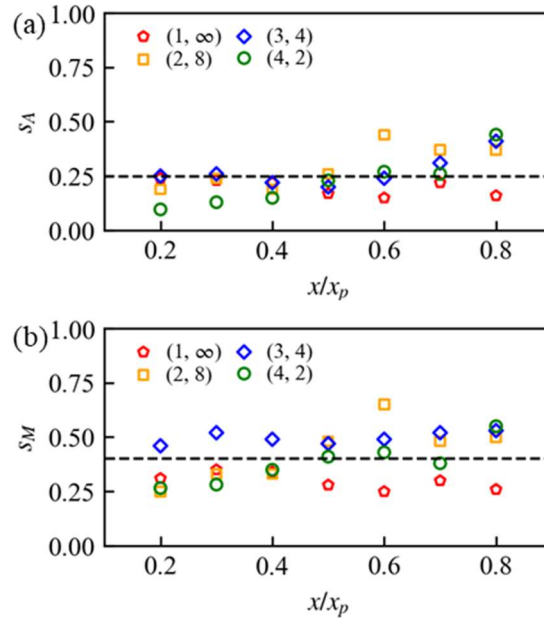

Figure 4.13 (a) Area proportion and (b) mixing proportion of the coherent region. Dashed lines present the mean value of s_A and s_M. Datasets are labelled with (Case number, Fr_{d-0}) in legends.

4.4 Conclusions

River inflows are a significant source of nutrition, pollution, and sediment to the receiving water body (i.e., lakes, reservoirs, or oceans). Its transportation and mixing with the receiving ambient water are important mechanisms for the material transport and nearshore environment. The present study performs a turbulence-resolving numerical model based on LES approach to simulate the shear layers and shear-induced coherent structures at the side interface between a neutrally/negatively buoyant river plume and quiescent receiving water. Such shear layers and coherent structures have yet to be discussed in the literature because they do not exist if the receiving water body is laterally confined, which is commonly applied in previous studies for hyperpycnal currents (e.g., Kostaschuk et al., 2018; Lamb et al., 2010; Schuch et al., 2018), but different from the actual river mouths connected with lakes or oceans (e.g., Best et al., 2005; Shi et al., 2022).

With the advantage of accessing all quantities of the flow field continuously, the numerical model can capture the detailed 3D characteristics of the shear layers and coherent structures at the sides of the river plume and characterize/quantify the influence of negative buoyancy on their development. The high-resolution numerical data show that the negative buoyancy suppresses the growth of the shear layer but enhances the three-dimensionality of the flow field by modifying the plume-ambient interface from a vertically standing face in the neutrally buoyant case into a hooked face (Fig. 4.8). With a hooked interface in the negatively buoyant situation, the shear direction changes from vertical (near water surface) to transversal (near bottom) in transects, contrary to the neutrally buoyant case, where the shear is always vertical (Fig. 4.9). The shear between plume and ambient water generates KHCS whose nondimensionalized frequency (i.e., Strouhal number) decreases with the increase in the local Richardson number. A quadrant analysis shows that the ejection ($Q2$) and sweep ($Q4$) events induced by the KHCS dominate the momentum and mass exchange inside the shear layers. KHCS also create a coherent region, where strong signals of mixing are observed. The coherent region occupies approximately 40% of the total

mixing in the nearshore region ($0 < x < x_m$).

References

Akula, B., Suchandra, P., Mikhaeil, M., & Ranjan, D. (2017). Dynamics of unstably stratified free shear flows: An experimental investigation of coupled Kelvin-Helmholtz and Rayleigh-Taylor instability. *Journal of Fluid Mechanics*, *816*, 619–660. https://doi.org/10.1017/jfm.2017.95

Bagherimiyab, F., & Lemmin, U. (2018). Large-scale coherent flow structures in rough-bed open-channel flow observed in fluctuations of three-dimensional velocity, skin friction and bed pressure. *Journal of Hydraulic Research*, *56*(6), 806–824. https://doi.org/10.1080/00221686.2017.1416686

Best, J. L., Kostaschuk, R. A., Peakall, J., Villard, P. V., & Franklin, M. (2005). Whole flow field dynamics and velocity pulsing within natural sediment-laden underflows. *Geology*, *33*(10), 765. https://doi.org/10.1130/G21516.1

Biron, P. M., Buffin-Bélanger, T., & Martel, N. (2019). Three-dimensional turbulent structures at a medium-sized confluence with and without an ice cover. *Earth Surface Processes and Landforms*, *44*(15), 3042–3056. https://doi.org/10.1002/esp.4718

Brown, G. L., & Roshko, A. (1974). On density effects and large structure in turbulent mixing layers. *Journal of Fluid Mechanics*, *64*(4), 775–816. https://doi.org/10.1017/S002211207400190X

Cantero, M. I., Balachandar, S., & Garcia, M. H. (2007). High-resolution simulations of cylindrical density currents. *Journal of Fluid Mechanics*, *590*, 437–469. https://doi.org/10.1017/S0022112007008166

Cohen, C. (2012). Shallow-water plane and tidal jets. Unpublished Ph.D. thesis. *University of Otago*. Otago, New Zealand. https://ourarchive.otago.ac.nz/handle/10523/2493

De Cesare, G., Schleiss, A., & Hermann, F. (2001). Impact of turbidity currents on reservoir sedimentation. *Journal of Hydraulic Engineering*, *127*(1), 6–16. https://doi.org/10.1061/(ASCE)0733-9429(2001)127:1(6)

De Lorenzis, L., & Düster, A. (2020). Modeling in engineering using innovative numerical methods for solids and fluids. CISM International Centre for Mechanical Sciences (Vol. 599). *Springer International Publishing*, Cham, Switzerland. https://doi.org/10.1007/978-3-030-37518-8

Deo, R. C., Mi, J., & Nathan, G. J. (2008). The influence of Reynolds number on a plane jet. *Physics of Fluids*, *20*(075108). https://doi.org/10.1063/1.2959171

Duguay, J., Biron, P. M., & Lacey, J. (2022). Impact of density gradients on the secondary flow structure of a river confluence. *Water Resources Research*, *58*, e2022WR032720. https://doi.org/10.1029/2022WR032720

Ghisalberti, M., & Nepf, H. (2005). Mass transport in vegetated shear flows. *Environmental Fluid Mechanics*, *5*(6), 527–551. https://doi.org/10.1007/s10652-005-0419-1

Guan, D., Agarwal, P., & Chiew, Y. M. (2018). Quadrant analysis of turbulence in a rectangular cavity with large aspect ratios. *Journal of Hydraulic Engineering*, *144*(7), 04018035. https://doi.org/10.1061/(ASCE)HY.1943-7900.0001480

Ho, C. M, & Huerre, P. (1984). Perturbed free shear layers. *Annual Review of Fluid Mechanics*, *16*(1), 365–422. https://doi.org/10.1146/annurev.fl.16.010184.002053

Ho, C. M., & Huang, L. S. (1982). Subharmonics and vortex merging in mixing layers. *Journal of Fluid Mechanics*, *119*, 443–473. https://doi.org/10.1017/S0022112082001438

Hogg, C. A. R., Marti, C. L., Huppert, H. E., & Imberger, J. (2013). Mixing of an interflow into the ambient water of Lake Iseo. *Limnology and Oceanography*, *58*(2), 579–592. https://doi.org/10.4319/lo.2013.58.2.0579

Huai, W. X., Zhang, J., Wang, W. J., & Katul, G. G. (2019). Turbulence structure in open channel flow with partially covered artificial emergent vegetation. *Journal of Hydrology*, *573*, 180–193. https://doi.org/10.1016/j.jhydrol.2019.03.071

Jasak, H. (2009). OpenFOAM: Open source CFD in research and industry. *International Journal of Naval Architecture and Ocean Engineering*, *1*(2), 89–94. https://doi.org/10.2478/IJNAOE-2013-0011

Kostaschuk, R., Nasr-Azadani, M. M., Meiburg, E., Wei, T., Chen, Z., Negretti, M. E., Best, J., Peakall, J., & Parsons, D. R. (2018). On the causes of pulsing in continuous turbidity currents. *Journal of Geophysical Research: Earth Surface*, *123*(11), 2827–2843. https://doi.org/10.1029/2018JF004719

Lamb, M. P., McElroy, B., Kopriva, B., Shaw, J., & Mohrig, D. (2010). Linking river-flood dynamics to hyperpycnal-plume deposits: Experiments, theory, and geological implications. *Geological Society of America Bulletin*, *122*(9–10), 1389–1400. https://doi.org/10.1130/B30125.1

Lewis, Q. W., & Rhoads, B. L. (2015). Resolving two-dimensional flow structure in rivers using large-scale particle image velocimetry: An example from a stream confluence. *Water Resources Research*, *51*(10), 7977–7994. https://doi.org/10.1002/2015WR017783

Negretti, M. E., Flòr, J. B., & Hopfinger, E. J. (2017). Development of gravity currents on rapidly changing slopes. *Journal of Fluid Mechanics*, *833*, 70–97. https://doi.org/10.1017/jfm.2017.696

Nezu, I., & Nakagawa, H. (1993). Turbulence in open-channel flows. *IAHR, A.A. Balkema*, Rotterdam, Netherlands. https://doi.org/10.1201/9780203734902

Parker, J. P., Caulfield, C. P., & Kerswell, R. R. (2019). Kelvin–Helmholtz billows above Richardson number 1/4. *Journal of Fluid Mechanics*, *879*, R1. https://doi.org/10.1017/jfm.2019.725

Proust, S., Fernandes, J. N., Leal, J. B., Rivière, N., & Peltier, Y. (2017). Mixing layer and coherent structures in compound channel flows: Effects of transverse flow, velocity ratio, and vertical confinement. *Water Resources Research*, *53*(4), 3387–3406. https://doi.org/10.1002/2016WR019873

Schuch, F. N., Pinto, L. C., Silvestrini, J. H., & Laizet, S. (2018). Three-dimensional turbulence-resolving simulations of the plunge phenomenon in a tilted channel. *Journal of Geophysical Research: Oceans*, *123*(7), 4820–4832. https://doi.org/10.1029/2018JC014027

Shi, H., Negretti, M. E., Chauchat, J., Blanckaert, K., Lemmin, U., & Barry, D. A. (2022). Unconfined plunging of a hyperpycnal river plume over a sloping bed and its lateral spreading: laboratory experiments and numerical modeling. *Water Resources Research*, *58*, e2022WR032633. https://doi.org/10.1029/2022WR032633

Shi, H., Negretti, M. E., Chauchat, J., Blanckaert, K., Lemmin, U., & Barry, D. A. (2023). Tracking the as yet unknown nearfield evolution of a shallow, neutrally-buoyant plane jet over a sloping bottom boundary. Submitted to *Water Resources Research*. (Under Review).

Shi, H., Zhang, J., & Huai, W. (2023). Experimental study on velocity distributions, secondary currents, and coherent structures in open channel flow with submerged riparian vegetation. *Advances in Water Resources, 173*, 104406. https://doi.org/10.1016/j.advwatres.2023.104406

Soulignac, F., Lemmin, U., Ziabari, S. M. H., Wynn, H. K., Graf, B., & Barry, D. A. (2021). Rapid changes in river plume dynamics caused by advected wind-driven coastal upwelling as observed in Lake Geneva. *Limnology and Oceanography*, *66*(8), 3116–3133. https://doi.org/10.1002/lno.11864

Spigel, R. H., Howard-Williams, C., Gibbs, M., Stephens, S., & Waugh, B. (2005). Field calibration of a formula for entrance mixing of river inflows to lakes: Lake Taupo, North Island, New Zealand. *New Zealand Journal of Marine and Freshwater Research*, *39*(4), 785–802. https://doi.org/10.1080/00288330.2005.9517353

Stocchino, A., & Brocchini, M. (2010). Horizontal mixing of quasi-uniform straight compound channel flows. *Journal of Fluid Mechanics*, *643*, 425–435. https://doi.org/10.1017/S0022112009992680

Taborda, C., Fael, C., Ricardo, A. M., & Ferreira, R. M. L. (2022). Wave-like motion and secondary currents in arrays of emergent cylinders induced by large scale eddying motion. *Environmental Fluid Mechanics*, *22*(2–3), 403–428. https://doi.org/10.1007/s10652-022-09863-4

Talling, P. J., Baker, M. L., Pope, E. L., Ruffell, S. C., Jacinto, R. S., Heijnen, M. S., et al. (2022). Longest sediment flows yet measured show how major rivers connect efficiently to deep sea. *Nature Communications*, *13*(1), 4193. https://doi.org/10.1038/s41467-022-31689-3

Tennekes, H., & Lumley, J. L. (1972). A first course in turbulence. *The MIT Press*. Cambridge, Massachusetts and Longdon, England. https://mitpress.mit.edu/9780262536301/a-first-course-in-turbulence/

Truong, S. H., & Uijttewaal, W. S. J. (2019). Transverse momentum exchange induced by large coherent structures in a vegetated compound channel. *Water Resources Research*, *55*(1), 589–612. https://doi.org/10.1029/2018WR023273

Uijttewaal, W. S. J., & Booij, R. (2000). Effects of shallowness on the development of free-surface mixing layers. *Physics of Fluids*, *12*(2), 392–402. https://doi.org/10.1063/1.870317

Vandekerkhove, E., Bertrand, S., Crescenzi Lanna, E., Reid, B., & Pantoja, S. (2020). Modern sedimentary processes at the heads of Martínez Channel and Steffen Fjord, Chilean Patagonia. *Marine Geology*, *419*, 106076. https://doi.org/10.1016/j.margeo.2019.106076

Variano, E. A., & Cowen, E. A. (2013). Turbulent transport of a high-Schmidt-number scalar near an air–water interface. *Journal of Fluid Mechanics*, *731*, 259–287. https://doi.org/10.1017/jfm.2013.273

Wallace, J. M. (2016). Quadrant analysis in turbulence research: History and evolution. *Annual Review of Fluid Mechanics*, *48*(1), 131–158. https://doi.org/10.1146/annurev-fluid-122414-034550

Wang, H., Bi, N., Wang, Y., Saito, Y., & Yang, Z. (2010). Tide-modulated hyperpycnal flows off the Huanghe (Yellow River) mouth, China. *Earth Surface Processes and Landforms*, *35*(11), 1315–1329. https://doi.org/10.1002/esp.2032

Weller, H. G., Tabor, G., Jasak, H., & Fureby, C. (1998). A tensorial approach to computational continuum mechanics using object-oriented techniques. *Computers in Physics*, *12*(6), 620. https://doi.org/10.1063/1.168744

White, B. L., & Nepf, H. M. (2007). Shear instability and coherent structures in shallow flow adjacent to a porous layer. *Journal of Fluid Mechanics*, *593*, 1–32. https://doi.org/10.1017/S0022112007008415

White, B. L., & Nepf, H. M. (2008). A vortex-based model of velocity and shear stress in a partially vegetated shallow channel. *Water Resources Research*, *44*(1), W01412. https://doi.org/10.1029/2006WR005651

Willmarth, W. W., & Lu, S. S. (1972). Structure of the Reynolds stress near the wall. *Journal of Fluid Mechanics*, *55*(1), 65–92. https://doi.org/10.1017/S002211207200165X

Yuan, Y., & Horner-Devine, A. R. (2017). Experimental investigation of large-scale vortices in a freely spreading gravity current. *Physics of Fluids*, *29*(10), 106603. https://doi.org/10.1063/1.5006176

Yue, W., Meneveau, C., Parlange, M. B., Zhu, W., Van Hout, R., & Katz, J. (2007). A comparative quadrant analysis of turbulence in a plant canopy. *Water Resources Research*, *43*, W05422. https://doi.org/10.1029/2006WR005583

Chapter 5 Conclusions and Outlook

5.1 Summary and Conclusions

This thesis explores the nearshore hydrodynamics of a shallow turbulent flow entering a laterally unconfined open water with a sloping bottom boundary, focusing on the development of the mean flow, shear layers and coherent structures. The neutrally (tidal jet) and negatively buoyant (hyperpycnal plume) situations are investigated. For the tidal jet, the focus is the influence of the sloping bottom boundary because it is usually examined over horizontal bottoms and considered quasi two-dimensional in the literature (Chapter 2). As for the hyperpycnal plume, the focus is the 3D plunging behavior of a laterally unconfined plume different from a confined plume (Chapter 3). These two types of flows (tidal jet and hyperpycnal plume) are then compared to determine the impacts of negative buoyancy on the development of side shear layers and Kelvin Helmholtz-type coherent structures (KHCS) induced by shearing (Chapter 4).

A tidal jet flowing over an 8° sloping bottom boundary spreads vertically (i.e., increasing thickness) when it transports longitudinally. The sudden change in bottom boundary (from 0° in the inlet channel to 8° in the receiving water body) induces a sharp decrease in centerline velocity near the channel mouth and forms a low-velocity zone inside the jet close to the bottom boundary. An increase in the jet thickness leads to the lateral convergence of the jet near the channel mouth. On the other hand, this increase also enhances the entrainment of ambient water from the sides of the jet. After a certain distance, the lateral entrainment becomes large enough that the jet diverges laterally thereafter. Similar to a quasi-2D plane jet, the sloping bottom jet transfers gradually from the flow establishment zone with a top-hat transverse velocity profile into the established flow zone with a Gaussian profile. However, given that the jet undergoes a lateral contraction near the channel mouth, the transition point between the two zones is much closer to the channel mouth than quasi-2D plane jet under the influence of the sloping bottom. That is, the longitudinal length of the flow

establishment zone is significantly reduced.

The hyperpycnal plume undergoes an even more complicated 3D process. Owing to the influence of negative buoyancy, the hyperpycnal plume slumps laterally when it is transported longitudinally. As a result, the plume converges near the water surface (forming a triangular shape) but diverges near the bottom boundary. The near-bottom lateral spreading of the plume generates secondary circulations on both of its sides. This behavior is reported experimentally for the first time because the commonly used laterally confined experimental configuration in the literature completely restrains the development of a plume in the lateral direction. A low-velocity zone is observed inside the plunging plume due to the sudden change in the sloping boundary at the river mouth (from 0 to β). The plunging entrainment coefficient observed in a laterally unconfined plume is considerably larger than that of a laterally confined plume. The inflow densimetric Froude number $Fr_{d\text{-}0}$ and the bottom slope β in the receiving water body are the dominant control parameters of an unconfined plunging process. The plunge location is closer to the river mouth with a smaller $Fr_{d\text{-}0}$ or larger β. For laterally unconfined plunging, the plunge location is the place where two sides of the plume meet at the centerline on the water surface rather than the place where the densimetric Froude number decreases to the critical value (~0.5) as in confined plunging. Thus, the plunging densimetric Froude number of laterally unconfined plunging can be much larger than 0.5 or even larger than unity.

Shear layers develop at the sides of the tidal jet and at the sides of the laterally unconfined hyperpycnal plume. In the sloping bottom jet, with increasing offshore distance, shear layers at both sides converge towards the centerline because of jet contraction and then merge with each other at the transition point from the flow establishment zone to established flow zone. An even stronger convergence of the side shear layers towards the centerline is observed on the water surface of the hyperpycnal plume, which arises from the lateral slumping mechanism due to negative buoyancy. The lateral growth of the shear layers is evident for both the tidal jet and hyperpycnal plume, which means that the momentum thickness increases with offshore distance.

However, in hyperpycnal plumes, the negative buoyancy significantly suppresses the growth of the shear layers. KHCS develop inside the shear layers, generating velocity and concentration fluctuations. For the tidal jet, as the jet spreads vertically, the vertical thickness of KHCS increases with offshore distance. Given that the jet-ambient interface is always vertical, the direction of shear-induced vorticity is vertical as well. By contrast, negative buoyancy twists the plume-ambient interface into a hooked face for the hyperpycnal plume. Thus, the direction of shear-induced vorticity changes gradually from vertical on the water surface to horizontal near the bottom boundary and the KHCS present a half crescent shape in transects. Although the KHCS develop longitudinally, their nondimensionalized frequency (i.e., Strouhal number) remains nearly constant and close to 0.079 for the tidal jet. Under the influence of negative buoyancy, the Strouhal number decreases with increasing local Richardson number for hyperpycnal plumes. KHCS considerably contribute to mass and momentum transfer in shear layers. The coherent region formed by KHCS contributes about 40% of the total mixing of the jet or hyperpycnal plume with ambient water in the nearshore region before the two shear layers meet at the centerline.

5.2 Future work

The natural prototypes of this thesis are ebb tidal jets and hyperpycnal river plumes. A comparison of the experimental and numerical tidal jet along with direct field observations in harbors and straits (e.g., Otago Harbor and Naruto Strait) can help to identify the potential limitations of present experimental and numerical configurations. Field observations may include remote sensing images and in situ flow field measurements. Preliminary comparison of the presented experimental and numerical hyperpycnal plume results along with remote sensing images obtained from the Rhône River mouth (Lake Geneva) suggests the presence of other mechanisms in the field, which are not considered in the present experiments and numerical model. More detailed field measurement of velocity, temperature, sediment concentration and bathymetry at the Rhône River mouth will help identify these mechanisms. Several potentially important mechanisms excluded in the experiment and model setup of this

thesis are listed, which may be considered in future studies.

- **Suspended sediment**

Suspend sediment is an important contributor of jet or plume density, especially for turbid river plumes. The deposition and resuspension of sediments decrease and increase flow density, respectively, thus significantly change jet or plume hydrodynamics because of changes in buoyancy. Future laboratory studies with sediments can help in evaluating the influence of sediment deposition or resuspension on jet or plume behavior. The present numerical model can be improved with two-phase methods (e.g., SedFOAM) to capture sediment behavior and answer the following questions. Does a turbid plume behave differently from a temperature or salinity induced hyperpycnal plume? Can the estimation of x_p shown in Fig. A3.1 be improved after the sediment behavior is considered?

- **Morphology**

The bottom geometry significantly influences plume or jet behavior. The nearshore morphology in natural coastal areas is usually not a constant slope and also nonuniform transversally. A numerical model with a bottom topography same as the field bathymetry is required to study the realistic flow hydrodynamics in the field. More importantly, natural bedforms can change depending on the deposition and resuspension of sediments. For example, the sediment deposition in the low-velocity zone (Figs. 2.3d and 3.5c) may change the bottom slope there. In contrast, the underflow may pick up sediment from the bed leading to local scour. Future experimental and numerical studies may apply a movable bed and focus on the following questions. In which region does the sediment deposit and resuspend, respectively? How does the bathymetry change with time and how does the bathymetry evolution influence the flow hydrodynamics?

- **Longshore currents**

Longshore currents driven by radiation stress divergence transport parallel to the coast and thus perpendicular to an offshore jet or plume. They probably push the offshore jet

or plume towards one side and destroy the symmetry of the system, changing the entire hydrodynamics. The interaction between longshore currents and offshore jets or plumes needs to be further investigated. For example, how does the longshore currents influence the entrainment of ambient water into the offshore jet or plume? How does the longshore currents influence the nearshore transportation and dispersion of materials (e.g., sediment, nutrition and pollution)?

- **Unsteady inflow conditions**

Steady inflow conditions of jets or plumes are used in the present thesis. However, unsteady inflow conditions are commonly observed in the field. For example, inflow discharge and velocity vary during flood or tidal propagation, and an upstream landslide can cause abrupt increases in inflow sediment concentration and inflow density. Unsteady inflow conditions can be introduced in future experimental and numerical studies. It is interesting to study the hydrodynamics, sediment behavior and geomorphology evolution during different time periods of a flood propagation. For example, when does the sediment deposit and when does the flow erose the bed? It is also interesting to study the influence of an upstream landslide on the hydrodynamics at the downstream river or tidal mouth.

Bibliography

Akiyama, J., & Stefan, H. G. (1984). Plunging flow into a reservoir: Theory. *Journal of Hydraulic Engineering*, *110*(4), 484–499. https://doi.org/10.1061/(ASCE)0733-9429(1984)110:4(484)

Akula, B., Suchandra, P., Mikhaeil, M., & Ranjan, D. (2017). Dynamics of unstably stratified free shear flows: An experimental investigation of coupled Kelvin–Helmholtz and Rayleigh-Taylor instability. *Journal of Fluid Mechanics*, *816*, 619–660. https://doi.org/10.1017/jfm.2017.95

An, R., & Li, J. (2010). Characteristic analysis of the plunging of turbidity currents. *Journal of Hydrodynamics*, *22*(2), 274–282. https://doi.org/10.1016/S1001-6058(09)60055-X

Antonia, R. A., Browne, L. W. B., Rajagopalan, S., & Chambers, A. J. (1983). On the organized motion of a turbulent plane jet. *Journal of Fluid Mechanics*, *134*(1), 49-66. https://doi.org/10.1017/S0022112083003213

Arita, M., & Nakai, M. (2008). Plunging conditions of two-dimensional negative buoyant surface jets released on a sloping bottom. *Journal of Hydraulic Research*, *46*(3), 301–306. https://doi.org/10.3826/jhr.2008.2714

Athanasiou, P., van Dongeren, A., Giardino, A., Vousdoukas, M., Gaytan-Aguilar, S., & Ranasinghe, R. (2019). Global distribution of nearshore slopes with implications for coastal retreat. *Earth System Science Data*, *11*, 1515–1529. https://doi.org/10.5194/essd-11-1515-2019

Baas, J. H., McCaffrey, W. D., Haughton, P. D. W., & Choux, C. (2005). Coupling between suspended sediment distribution and turbulence structure in a laboratory turbidity current. *Journal of Geophysical Research*, *110*(C11), C11015. https://doi.org/10.1029/2004JC002668

Baas, J. H., Van Kesteren, W., & Postma, G. (2004). Deposits of depletive high-density turbidity currents: A flume analogue of bed geometry, structure and texture. *Sedimentology*, *51*(5), 1053–1088. https://doi.org/10.1111/j.1365-3091.2004.00660.x

Bagherimiyab, F., & Lemmin, U. (2018). Large-scale coherent flow structures in rough-bed open-channel flow observed in fluctuations of three-dimensional velocity, skin friction and bed pressure. *Journal of Hydraulic Research*, *56*(6), 806–824. https://doi.org/10.1080/00221686.2017.1416686

Best, J. L., Kostaschuk, R. A., Peakall, J., Villard, P. V., & Franklin, M. (2005). Whole flow field dynamics and velocity pulsing within natural sediment-laden underflows. *Geology*, *33*(10), 765-768. https://doi.org/10.1130/G21516.1

Biron, P. M., Buffin-Bélanger, T., & Martel, N. (2019). Three-dimensional turbulent structures at a medium-sized confluence with and without an ice cover. *Earth Surface Processes and Landforms*, *44*(15), 3042–3056. https://doi.org/10.1002/esp.4718

Blanckaert, K. (2015). Flow separation at convex banks in open channels. *Journal of Fluid Mechanics*, *779*, 432–467. https://doi.org/10.1017/jfm.2015.397

Bonamy, C., Chauchat, J., Augier, P., Mathieu, A., Clemencot, Q., Chassagne, R., et al. (2020). fluiddyn/fluidfoam: Release v0.2.3 (v0.2.3). https://doi.org/10.5281/zenodo.6453090

Branch, R. A., Horner-Devine, A. R., Kumar, N., & Poggioli, A. R. (2020). River plume liftoff dynamics and surface expressions. *Water Resources Research*, *56*. e2019WR026475 https://doi.org/10.1029/2019WR026475

Broekema, Y. B., Labeur, R. J., & Uijttewaal, W. S. J. (2018). Observations and analysis of the horizontal

structure of a tidal jet at deep scour holes. *Journal of Geophysical Research: Earth Surface*, *123*(12), 3162–3189. https://doi.org/10.1029/2018JF004754

Brown, G. L., & Roshko, A. (1974). On density effects and large structure in turbulent mixing layers. *Journal of Fluid Mechanics*, *64*(4), 775–816. https://doi.org/10.1017/S002211207400190X

Brown, C. A., Jackson, G. A., & Brooks, D. A. (2000). Particle transport through a narrow tidal inlet due to tidal forcing and implications for larval transport. *Journal of Geophysical Research: Oceans*, *105*(C10), 24141–24156. https://doi.org/10.1029/2000JC000211

Buonaiuto, F. S., & Bokuniewicz, H. J. (2008). Hydrodynamic partitioning of a mixed energy tidal inlet. *Journal of Coastal Research*, *245*, 1339–1348. https://doi.org/10.2112/07-0869.1

Canestrelli, A., Nardin, W., Edmonds, D., Fagherazzi, S., & Slingerland, R. (2014). Importance of frictional effects and jet instability on the morphodynamics of river mouth bars and levees. *Journal of Geophysical Research: Oceans*, *119*(1), 509–522. https://doi.org/10.1002/2013JC009312

Cantero, M. I., Balachandar, S., & Garcia, M. H. (2007). High-resolution simulations of cylindrical density currents. *Journal of Fluid Mechanics*, *590*, 437–469. https://doi.org/10.1017/S0022112007008166

Chen, S. N., Geyer, W. R., & Hsu, T. J. (2013). A numerical investigation of the dynamics and structure of hyperpycnal river plumes on sloping continental shelves: Dynamics of hyperpycnal river plumes. *Journal of Geophysical Research: Oceans*, *118*(5), 2702–2718. https://doi.org/10.1002/jgrc.20209

Churchill, J. H., Hench, J. L., Luettich, R. A., Blanton, J. O., & Werner, F. E. (1999). Flood tide circulation near Beaufort Inlet, North Carolina: Implications for larval recruitment. *Estuaries*, *22*(4), 1057-1070. https://doi.org/10.2307/1353083

Cohen, C. (2012). Shallow-water plane and tidal jets. Unpublished Ph.D. thesis. *University of Otago*. Otago, New Zealand. https://ourarchive.otago.ac.nz/handle/10523/2493

Cortés, A., Fleenor, W. E., Wells, M. G., de Vicente, I., & Rueda, F. J. (2014). Pathways of river water to the surface layers of stratified reservoirs. *Limnology and Oceanography*, *59*(1), 233–250. https://doi.org/10.4319/lo.2014.59.1.0233

Cowen, E. A., Monismith, S. G., Cowen, E. A., & Monismith, S. G. (1997). A hybrid digital particle tracking velocimetry technique. *Experiments in Fluids*, *22*(3), 199–211. https://doi.org/10.1007/s003480050038

Crookshanks, S., & Gilbert, R. (2008). Continuous, diurnally fluctuating turbidity currents in Kluane Lake, Yukon Territory. *Canadian Journal of Earth Sciences*, *45*(10), 1123–1138. https://doi.org/10.1139/E08-058

Curray, J. R., Emmel, F. J., & Moore, D. G. (2002). The Bengal Fan: Morphology, geometry, stratigraphy, history and processes. *Marine and Petroleum Geology*, *19*(10), 1191–1223. https://doi.org/10.1016/S0264-8172(03)00035-7

Dai, A., & Huang, Y. L. (2020). Experiments on gravity currents propagating on unbounded uniform slopes. *Environmental Fluid Mechanics*, *20*(6), 1637–1662. https://doi.org/10.1007/s10652-020-09758-2

De Cesare, G., & Schleiss, A. (1999). Physical and numerical modelling of turbidity currents. *Proceedings XXVIII IAHR Congress*, Graz, Austria. https://www.iahr.org/library/infor?pid=13822

Bibliography

De Cesare, G., Schleiss, A., & Hermann, F. (2001). Impact of turbidity currents on reservoir sedimentation. *Journal of Hydraulic Engineering*, *127*(1), 6–16. https://doi.org/10.1061/(ASCE)0733-9429(2001)127:1(6)

De Lorenzis, L., & Düster, A. (2020). Modeling in engineering using innovative numerical methods for solids and fluids. CISM International Centre for Mechanical Sciences (Vol. 599). *Springer International Publishing*, Cham, Switzerland. https://doi.org/10.1007/978-3-030-37518-8

Deo, R. C., Mi, J., & Nathan, G. J. (2007). The influence of nozzle-exit geometric profile on statistical properties of a turbulent plane jet. *Experimental Thermal and Fluid Science*, *32*(2), 545–559. https://doi.org/10.1016/j.expthermflusci.2007.06.004

Deo, R. C., Mi, J., & Nathan, G. J. (2008). The influence of Reynolds number on a plane jet. *Physics of Fluids*, *20*(075108). https://doi.org/10.1063/1.2959171

Dimotakis, P. E. (1991). Turbulent free shear layer mixing and combustion. In: High speed flight propulsion systems (pp. 265–340). *American Institute of Aeronautics and Astronautics*. Washington DC, USA. https://doi.org/10.2514/4.866104

Dracos, T., Giger, M., & Jirka, G. H. (1992). Plane turbulent jets in a bounded fluid layer. *Journal of Fluid Mechanics*, *241*, 587–614. https://doi.org/10.1017/S0022112092002167

Duguay, J., Biron, P. M., & Lacey, J. (2022). Impact of density gradients on the secondary flow structure of a river confluence. *Water Resources Research*, *58*. e2022WR032720. https://doi.org/10.1029/2022WR032720

Dupuis, V., Schraen, L., & Eiff, O. (2023). Shear layers in two-stage compound channels investigated with LS-PIV. *Experiments in Fluids*, *64*(2), 24. https://doi.org/10.1007/s00348-022-03557-9

Farrell, G. J., & Stefan, H. G. (1988). Mathematical modeling of plunging reservoir flows. *Journal of Hydraulic Research*, *26*(5), 525–537. https://doi.org/10.1080/00221688809499191

Fischer, H. B., List, E., Koh, R., Imberger, J., & Brooks, N. (1979). Mixing in inland and coastal waters. *Academic Press*, San Diego, California. USA. https://doi.org/10.1016/C2009-0-22051-4

Fleenor, W. (2001). Effects and control of plunging inflows on reservoir hydrodynamics and downstream releases. Unpublished Ph.D. thesis. *University of California, Davis*, Davis, California, USA. https://search.library.ucdavis.edu/permalink/01UCD_INST/9fle3i/alma990021089970403126

Fujiwara, T., Nakata, H., & Nakatsuji, K. (1994). Tidal-jet and vortex-pair driving of the residual circulation in a tidal estuary. *Continental Shelf Research*, *14*(9), 1025–1038. https://doi.org/10.1016/0278-4343(94)90062-0

Garrett, B. (1960). Hydrodynamics (Second Edition). *Princeton University Press*. Princeton, New Jersey, USA. https://press.princeton.edu/books/ebook/9781400877775/hydrodynamics

Georgoulas, A. N., Angelidis, P. B., Panagiotidis, T. G., & Kotsovinos, N. E. (2010). 3D numerical modelling of turbidity currents. *Environmental Fluid Mechanics*, *10*(6), 603–635. https://doi.org/10.1007/s10652-010-9182-z

Ghisalberti, M., & Nepf, H. (2005). Mass transport in vegetated shear flows. *Environmental Fluid Mechanics*, *5*(6), 527–551. https://doi.org/10.1007/s10652-005-0419-1

Ghisalberti, M., & Nepf, H. (2006). The structure of the shear layer in flows over rigid and flexible canopies. *Environmental Fluid Mechanics*, *6*(3), 277–301. https://doi.org/10.1007/s10652-006-0002-4

Bibliography

Gray, D. D., & Giorgini, A. (1976). The validity of the Boussinesq approximation for liquids and gases. *International Journal of Heat and Mass Transfer*, *19*(5), 545–551. https://doi.org/10.1016/0017-9310(76)90168-X

Guan, D., Agarwal, P., & Chiew, Y. M. (2018). Quadrant analysis of turbulence in a rectangular cavity with large aspect ratios. *Journal of Hydraulic Engineering*, *144*(7), 04018035. https://doi.org/10.1061/(ASCE)HY.1943-7900.0001480

Giger, M., Dracos, T., & Jirka, G. H. (1991). Entrainment and mixing in plane turbulent jets in shallow water. *Journal of Hydraulic Research*, *29*(5), 615–642. https://doi.org/10.1080/00221689109498980

Haigh, R., Taylor, F. J. R., & Sutherland, T. F. (1992). Phytoplankton ecology of Sechelt Inlet, a fjord system on the British Columbia coast. I. General features of the nano- and microplankton. *Marine Ecology Progress Series*, *89*(2/3), 117–134. https://www.jstor.org/stable/24831781

Härtel, C., Meiburg, E., & Necker, F. (2000). Analysis and direct numerical simulation of the flow at a gravity-current head. Part 1. Flow topology and front speed for slip and no-slip boundaries. *Journal of Fluid Mechanics*, *418*, 189–212. https://doi.org/10.1017/S0022112000001221

Hauenstein, W. (1982). *Zuflussbedingte Dichteströmungen in Seen*. Unpublished Ph.D. thesis. *ETH Zürich*. Zürich, Switzerland. https://eth.swisscovery.slsp.ch/permalink/41SLSP_ETH/lshl64/alma990003139310205503

Hauenstein, W., & Dracos, Th. (1984). Investigation of plunging density currents generated by inflows in lakes. *Journal of Hydraulic Research*, *22*(3), 157–179. https://doi.org/10.1080/00221688409499404

He, Z., Han, D., Lin, Y. T., Zhu, R., Yuan, Y., & Jiao, P. (2022). Propagation, mixing, and turbulence characteristics of saline and turbidity currents over rough and permeable/impermeable beds. *Physics of Fluids*, *34*(6), 066604. https://doi.org/10.1063/5.0095354

He, Z., Xu, B., Okon, S. U., & Li, L. (2022). Numerical investigation of the sediment hyperpycnal flow in the Yellow River estuary. *Journal of Marine Science and Engineering*, *10*(7), 943. https://doi.org/10.3390/jmse10070943

Hearn, C., Hunter, J., Imberger, J., & D. van, S. (1985). Tidally induced jet in Koombana Bay, Western Australia. *Marine and Freshwater Research*, *36*(4), 453-479. https://doi.org/10.1071/MF9850453

Heskestad, G. (1965). Hot-wire measurements in a plane turbulent jet. *Journal of Applied Mechanics*, *32*(4), 721–734. https://doi.org/10.1115/1.3627309

Hinze, J. O. (1975). Turbulence (2nd Edition). *McGraw-Hill Inc.* US. https://openlibrary.org/books/OL5186579M/Turbulence

Ho, C. M, & Huerre, P. (1984). Perturbed free shear layers. *Annual Review of Fluid Mechanics*, *16*(1), 365–422. https://doi.org/10.1146/annurev.fl.16.010184.002053

Ho, C. M., & Huang, L. S. (1982). Subharmonics and vortex merging in mixing layers. *Journal of Fluid Mechanics*, *119*, 443–473. https://doi.org/10.1017/S0022112082001438

Hogg, C. A. R., Marti, C. L., Huppert, H. E., & Imberger, J. (2013). Mixing of an interflow into the ambient water of Lake Iseo. *Limnology and Oceanography*, *58*(2), 579–592. https://doi.org/10.4319/lo.2013.58.2.0579

Howard, L. N. (1961). Note on a paper of John W. Miles. *Journal of Fluid Mechanics*, *10*(04), 509-512. https://doi.org/10.1017/S0022112061000317

Huai, W. X., Zhang, J., Wang, W. J., & Katul, G. G. (2019). Turbulence structure in open channel flow with partially covered artificial emergent vegetation. *Journal of Hydrology*, *573*, 180–193. https://doi.org/10.1016/j.jhydrol.2019.03.071

Jasak, H. (2009). OpenFOAM: Open source CFD in research and industry. *International Journal of Naval Architecture and Ocean Engineering*, *1*(2), 89–94. https://doi.org/10.2478/IJNAOE-2013-0011

Jiménez-Robles, A. M., Ortega-Sánchez, M., & Losada, M. A. (2016). Effects of basin bottom slope on jet hydrodynamics and river mouth bar formation. *Journal of Geophysical Research: Earth Surface*, *121*(6), 1110–1133. https://doi.org/10.1002/2016JF003871

Jirka, G. H. (1994). Shallow jets. In: Davies, P.A., Neves, M.J.V. (eds). Recent research advances in the fluid mechanics of turbulent jets and plumes: Vol. 255. (pp. 157–175). *Springer.* Dordrecht. https://doi.org/10.1007/978-94-011-0918-5_10

Jirka, G. H. (2001). Large scale flow structures and mixing processes in shallow flows. *Journal of Hydraulic Research*, *39*(6), 567–573. https://doi.org/10.1080/00221686.2001.9628285

Johnson, T. R., Ellis, C. R., Farrell, G. J., & Stefan, H. G. (1987). Negatively buoyant flow in a diverging channel. II: 3-d flow field descriptions. *Journal of Hydraulic Engineering*, *113*(6), 731–742. https://doi.org/10.1061/(ASCE)0733-9429(1987)113:6(731)

Johnson, T. R., Ellis, C. R., & Stefan, H. G. (1989). Negatively buoyant flow in diverging channel, IV: Entrainment and dilution. *Journal of Hydraulic Engineering*, *115*(4), 437–456. https://doi.org/10.1061/(ASCE)0733-9429(1989)115:4(437)

Johnson, T. R., Farrell, G. J., Ellis, C. R., & Stefan, H. G. (1987). Negatively buoyant flow in a diverging channel. I: Flow regimes. *Journal of Hydraulic Engineering*, *113*(6), 716–730. https://doi.org/10.1061/(ASCE)0733-9429(1987)113:6(716)

Joshi, P. B. (1982). Hydromechanics of tidal jets. *Journal of the Waterway, Port, Coastal and Ocean Division*, *108*(3). 239-253. https://doi.org/10.1061/JWPCDX.0000302

Kim, W. W., & Menon, S. (1995). A new dynamic one-equation subgrid-scale model for large eddy simulations. *33rd Aerospace Sciences Meeting and Exhibit*. Reno, Nevada, USA. https://doi.org/10.2514/6.1995-356

Knight, D. W., & Shiono, K. (1990). Turbulence measurements in a shear layer region of a compound channel. *Journal of Hydraulic Research*, *28*(2), 175–196. https://doi.org/10.1080/00221689009499085

Kostaschuk, R., Nasr-Azadani, M. M., Meiburg, E., Wei, T., Chen, Z., Negretti, M. E., Best, J., Peakall, J., & Parsons, D. R. (2018). On the causes of pulsing in continuous turbidity currents. *Journal of Geophysical Research: Earth Surface*, *123*(11), 2827–2843. https://doi.org/10.1029/2018JF004719

Lamb, M. P., McElroy, B., Kopriva, B., Shaw, J., & Mohrig, D. (2010). Linking river-flood dynamics to hyperpycnal-plume deposits: Experiments, theory, and geological implications. *Geological Society of America Bulletin*, *122*(9–10), 1389–1400. https://doi.org/10.1130/B30125.1

Lamb, M. P., & Mohrig, D. (2009). Do hyperpycnal-flow deposits record river-flood dynamics? *Geology*, *37*(12), 1067–1070. https://doi.org/10.1130/G30286A.1

Landel, J. R., Caulfield, C. P., & Woods, A. W. (2012). Meandering due to large eddies and the statistically self-similar dynamics of quasi-two-dimensional jets. *Journal of Fluid Mechanics*, *692*,

347–368. https://doi.org/10.1017/jfm.2011.518

Lee, H., & Yu, W. (1997). Experimental study of reservoir turbidity current. *Journal of Hydraulic Engineering*, *123*(6), 520–528. https://doi.org/10.1061/(ASCE)0733-9429(1997)123:6(520)

Lewis, Q. W., & Rhoads, B. L. (2015). Resolving two-dimensional flow structure in rivers using large-scale particle image velocimetry: An example from a stream confluence. *Water Resources Research*, *51*(10), 7977–7994. https://doi.org/10.1002/2015WR017783

Li, D., Liu, M., & Huai, W. (2022). Modeling transverse momentum exchange in partially vegetated flow. *Physics of Fluids*, *34*(2), 025124. https://doi.org/10.1063/5.0081202

Maggi, M. R., Negretti, M. E., Hopfinger, E. J., & Adduce, C. (2023). Turbulence characteristics and mixing properties of gravity currents over complex topography. *Physics of Fluids*, *35*(1), 016607. https://doi.org/10.1063/5.0132830

Martin, A., Negretti, M. E., & Hopfinger, E. J. (2019). Development of gravity currents on slopes under different interfacial instability conditions. *Journal of Fluid Mechanics*, *880*, 180–208. https://doi.org/10.1017/jfm.2019.713

Mayeli, P., & Sheard, G. J. (2021). Buoyancy-driven flows beyond the Boussinesq approximation: A brief review. *International Communications in Heat and Mass Transfer*, *125*, 105316. https://doi.org/10.1016/j.icheatmasstransfer.2021.105316

Meiburg, E., & Kneller, B. (2010). Turbidity currents and their deposits. *Annual Review of Fluid Mechanics*, *42*(1), 135–156. https://doi.org/10.1146/annurev-fluid-121108-145618

Miles, J. W. (1961). On the stability of heterogeneous shear flows. *Journal of Fluid Mechanics*, *10*(04), 496-508. https://doi.org/10.1017/S0022112061000305

Mulder, T., Syvitski, J. P. M., Migeon, S., Faugères, J. C., & Savoye, B. (2003). Marine hyperpycnal flows: Initiation, behavior and related deposits. A review. *Marine and Petroleum Geology*, *20*(6–8), 861–882. https://doi.org/10.1016/j.marpetgeo.2003.01.003

Negretti, M. E., Flòr, J. B., & Hopfinger, E. J. (2017). Development of gravity currents on rapidly changing slopes. *Journal of Fluid Mechanics*, *833*, 70–97. https://doi.org/10.1017/jfm.2017.696

Negretti, M. E., Socolofsky, S. A., & Jirka, G. H. (2008). Linear stability analysis of inclined two-layer stratified flows. *Physics of Fluids*, *20*(9), 094104. https://doi.org/10.1063/1.2980351

Nezu, I., & Nakagawa, H. (1993). Turbulence in open-channel flows. *IAHR, A.A. Balkema*, Rotterdam, Netherlands. https://doi.org/10.1201/9780203734902

Odier, P., Chen, J., & Ecke, R. E. (2012). Understanding and modeling turbulent fluxes and entrainment in a gravity current. *Physica D: Nonlinear Phenomena, 241*(3), 260–268. https://doi.org/10.1016/j.physd.2011.07.010

Old, C. P., & Vennell, R. (2001). Acoustic Doppler current profiler measurements of the velocity field of an ebb tidal jet. *Journal of Geophysical Research: Oceans*, *106*(C4), 7037–7049. https://doi.org/10.1029/1999JC000144

Oler, J. W., & Goldschmidt, V. W. (1982). A vortex-street model of the flow in the similarity region of a two-dimensional free turbulent jet. *Journal of Fluid Mechanics, 123,* 523–535. https://doi.org/10.1017/S0022112082003188

Onishi, S. (1984). Study of vortex structure in water surface jets by means of remote sensing. In *Elsevier Oceanography Series* (Vol. 38, pp. 107–132). Elsevier. https://doi.org/10.1016/S0422-9894(08)70607-X

Ooi, S. K., Constantinescu, G., & Weber, L. (2009). Numerical simulations of lock-exchange compositional gravity current. *Journal of Fluid Mechanics*, *635*, 361–388. https://doi.org/10.1017/S0022112009007599

Ortega-Sánchez, M., Losada, M. A., & Baquerizo, A. (2008). A global model of a tidal jet including the effects of friction and bottom slope. *Journal of Hydraulic Research*, *46*(1), 80–86. https://doi.org/10.1080/00221686.2008.9521845

Özgökmen, T. M., Fischer, P. F., Duan, J., & Iliescu, T. (2004). Three-dimensional turbulent bottom density currents from a high-order nonhydrostatic spectral element model. *Journal of Physical Oceanography*, *34*(9), 2006–2026. https://doi.org/10.1175/1520-0485(2004)034<2006:TTBDCF>2.0.CO;2

Özsoy, E., & Ünlüata, Ü. (1982). Ebb-tidal flow characteristics near inlets. *Estuarine, Coastal and Shelf Science*, *14*(3), 251-IN3. https://doi.org/10.1016/S0302-3524(82)80015-7

Parker, G., Fukushima, Y., & Pantin, H. M. (1986). Self-accelerating turbidity currents. *Journal of Fluid Mechanics*, *171*(1), 145. https://doi.org/10.1017/S0022112086001404

Parker, G., & Toniolo, H. (2007). Note on the analysis of plunging of density flows. *Journal of Hydraulic Engineering*, *133*(6), 690–694. https://doi.org/10.1061/(ASCE)0733-9429(2007)133:6(690)

Parker, J. P., Caulfield, C. P., & Kerswell, R. R. (2019). Kelvin–Helmholtz billows above Richardson number. *Journal of Fluid Mechanics*, *879*, R1. https://doi.org/10.1017/jfm.2019.725

Piton, V., Soulignac, F., Ulrich, L., Graf, B., Wynn, H. K., Blanckaert, K., & Barry, D. A. (2022). Tracing unconfined nearfield spreading of a river plume interflow in a large lake (Lake Geneva): Hydrodynamics, suspended particulate matter and associated fluxes. *Frontiers in Water*, *4*, 943242. https://doi.org/doi: 10.3389/frwa.2022.943242

Pohl, F., Eggenhuisen, J. T., Kane, I. A., & Clare, M. A. (2020). Transport and burial of microplastics in deep-marine sediments by turbidity currents. *Environmental Science & Technology*, *54*(7), 4180–4189. https://doi.org/10.1021/acs.est.9b07527

Poletto, R., Craft, T., & Revell, A. (2013). A new divergence free synthetic eddy method for the reproduction of inlet flow conditions for LES. *Flow, Turbulence and Combustion*, *91*(3), 519–539. https://doi.org/10.1007/s10494-013-9488-2

Pope, E. L., Cartigny, M. J. B., Clare, M. A., Talling, P. J., Lintern, D. G., Vellinga, A., et. al., (2022). First source-to-sink monitoring shows dense head controls sediment flux and runout in turbidity currents. *Science Advances*, *8*(20), eabj3220. https://doi.org/10.1126/sciadv.abj3220

Pope, S. B. (2000). Turbulent flows. *Cambridge University Press*. Cambridge, UK. https://doi.org/10.1017/CBO9780511840531

Prasad, A. K., Adrian, R. J., Landreth, C. C., & Offutt, P. W. (1992). Effect of resolution on the speed and accuracy of particle image velocimetry interrogation. *Experiments in Fluids*, *13*(2–3), 105–116. https://doi.org/10.1007/BF00218156

Proust, S., Fernandes, J. N., Leal, J. B., Rivière, N., & Peltier, Y. (2017). Mixing layer and coherent structures in compound channel flows: Effects of transverse flow, velocity ratio, and vertical confinement. *Water Resources Research*, *53*(4), 3387–3406. https://doi.org/10.1002/2016WR019873

Bibliography

Roache, P. J. (1994). Perspective: a method for uniform reporting of grid refinement studies. *Journal of Fluids Engineering*, *116*(3), 405–413. https://doi.org/10.1115/1.2910291

Rogers, M. M., & Moser, R. D. (1992). The three-dimensional evolution of a plane mixing layer: The Kelvin–Helmholtz rollup. *Journal of Fluid Mechanics*, *243,* 183-226. https://doi.org/10.1017/S0022112092002696

Roache, P. J. (1997). Quantification of uncertainty in computational fluid dynamics. *Annual Review of Fluid Mechanics*, *29*(1), 123–160. https://doi.org/10.1146/annurev.fluid.29.1.123

Rowland, J. C., Stacey, M. T., & Dietrich, W. E. (2009). Turbulent characteristics of a shallow wall-bounded plane jet: Experimental implications for river mouth hydrodynamics. *Journal of Fluid Mechanics*, *627*, 423–449. https://doi.org/10.1017/S0022112009006107

Scheu, K. R., Fong, D., Monismith, S. G., & Fringer, O. B. (2018). Modeling sedimentation dynamics of sediment-laden river intrusions in a rotationally-influenced, stratified lake. *Water Resources Research*, *54*(6), 4084–4107. https://doi.org/10.1029/2017WR021533

Schuch, F. N., Pinto, L. C., Silvestrini, J. H., & Laizet, S. (2018). Three-dimensional turbulence-resolving simulations of the plunge phenomenon in a tilted channel. *Journal of Geophysical Research: Oceans*, *123*(7), 4820–4832. https://doi.org/10.1029/2018JC014027

Sequeiros, O. E. (2012). Estimating turbidity current conditions from channel morphology: A Froude number approach. *Journal of Geophysical Research: Oceans*, *117*(C4), C04003. https://doi.org/10.1029/2011JC007201

Sequeiros, O. E., Naruse, H., Endo, N., Garcia, M. H., & Parker, G. (2009). Experimental study on self-accelerating turbidity currents. *Journal of Geophysical Research, 114*(C5), C05025. https://doi.org/10.1029/2008JC005149

Shi, H., Negretti, M. E., Chauchat, J., Blanckaert, K., Lemmin, U., & Barry, D. A. (2022). Unconfined plunging of a hyperpycnal river plume over a sloping bed and its lateral spreading: laboratory experiments and numerical modeling. *Water Resources Research*, *58*. e2022WR032633. https://doi.org/10.1029/2022WR032633

Shi, H., Negretti, M. E., Chauchat, J., Blanckaert, K., Lemmin, U., & Barry, D. A. (2023). Tracking the as yet unknown nearfield evolution of a shallow, neutrally-buoyant plane jet over a sloping bottom boundary. Submitted to *Water Resources Research*. (Under Review).

Shi, H., Zhang, J., & Huai, W. (2023). Experimental study on velocity distributions, secondary currents, and coherent structures in open channel flow with submerged riparian vegetation. *Advances in Water Resources, 173*, 104406. https://doi.org/10.1016/j.advwatres.2023.104406

Singh, B., & Shah, C. R. (1971). Plunging phenomenon of density currents in reservoirs. *La Houille Blanche*, *1*, 59–64. https://doi.org/10.1051/lhb/1971005

Shih, T. H., Liou, W. W., Shabbir, A., Yang, Z., & Zhu, J. (1995). A new k-ϵ eddy viscosity model for high Reynolds number turbulent flows. *Computers & Fluids*, *24*(3), 227–238. https://doi.org/10.1016/0045-7930(94)00032-T

Shin, J. O., Dalziel, S. B., & Linden, P. F. (2004). Gravity currents produced by lock exchange. *Journal of Fluid Mechanics*, *521*, 1–34. https://doi.org/10.1017/S002211200400165X

Shiono, K., & Knight, D. W. (1991). Turbulent open-channel flows with variable depth across the channel. *Journal of Fluid Mechanics*, *222*(1), 617-646. https://doi.org/10.1017/S0022112091001246

Socolofsky, S. A., & Jirka, G. H. (2004). Large-scale flow structures and stability in shallow flows.

Journal of Environmental Engineering and Science, 3(5), 451–462.
https://doi.org/10.1139/s04-032

Soulignac, F., Lemmin, U., Ziabari, S. M. H., Wynn, H. K., Graf, B., & Barry, D. A. (2021). Rapid changes in river plume dynamics caused by advected wind-driven coastal upwelling as observed in Lake Geneva. *Limnology and Oceanography*, *66*(8), 3116–3133.
https://doi.org/10.1002/lno.11864

Spiers, K. C., Healy, T. R., & Winter, C. (2009). Ebb-Jet dynamics and transient eddy formation at Tauranga Harbour: Implications for entrance channel shoaling. *Journal of Coastal Research*, *25*(1), 234–247. https://doi.org/10.2112/07-0947.1

Spigel, R. H., Howard-Williams, C., Gibbs, M., Stephens, S., & Waugh, B. (2005). Field calibration of a formula for entrance mixing of river inflows to lakes: Lake Taupo, North Island, New Zealand. *New Zealand Journal of Marine and Freshwater Research*, *39*(4), 785–802.
https://doi.org/10.1080/00288330.2005.9517353

Stefan, H. G., & Johnson, T. R. (1989). Negatively buoyant flow in diverging channel. III: Onset of underflow. *Journal of Hydraulic Engineering*, *115*(4), 423–436.
https://doi.org/10.1061/(ASCE)0733-9429(1989)115:4(423)

Stocchino, A., & Brocchini, M. (2010). Horizontal mixing of quasi-uniform straight compound channel flows. *Journal of Fluid Mechanics*, *643*, 425–435.
https://doi.org/10.1017/S0022112009992680

Taborda, C., Fael, C., Ricardo, A. M., & Ferreira, R. M. L. (2022). Wave-like motion and secondary currents in arrays of emergent cylinders induced by large scale eddying motion. *Environmental Fluid Mechanics*, *22*(2–3), 403–428. https://doi.org/10.1007/s10652-022-09863-4

Talling, P. J., Baker, M. L., Pope, E. L., Ruffell, S. C., Jacinto, R. S., Heijnen, M. S., et al. (2022). Longest sediment flows yet measured show how major rivers connect efficiently to deep sea. *Nature Communications*, *13*(1), 4193. https://doi.org/10.1038/s41467-022-31689-3

Tennekes, H., & Lumley, J. L. (1972). A first course in turbulence. *The MIT Press*. Cambridge, Massachusetts and Longdon, England. https://mitpress.mit.edu/9780262536301/a-first-course-in-turbulence/

Thomas, F. O., & Goldschmidt, V. W. (1986). Structural characteristics of a developing turbulent planar jet. *Journal of Fluid Mechanics*, *163*, 227–256. https://doi.org/10.1017/S0022112086002288

Tominaga, Y., & Stathopoulos, T. (2007). Turbulent Schmidt numbers for CFD analysis with various types of flow field. *Atmospheric Environment*, *41*(37), 8091–8099.
https://doi.org/10.1016/j.atmosenv.2007.06.054

Truong, S. H., & Uijttewaal, W. S. J. (2019). Transverse momentum exchange induced by large coherent structures in a vegetated compound channel. *Water Resources Research*, *55*(1), 589–612.
https://doi.org/10.1029/2018WR023273

Tseng, C. Y., & Chou, Y. J. (2018). Nonhydrostatic simulation of hyperpycnal river plumes on sloping continental shelves: Flow structures and nonhydrostatic effect. *Ocean Modelling*, *124*, 33–47.
https://doi.org/10.1016/j.ocemod.2018.02.003

Turner, E. R., Rabalais, N. N., & Zhang, Z. N. (1990). Phytoplankton biomass, production and growth limitations on the Huanghe (Yellow River) continental shelf. *Continental Shelf Research*, *10*(6), 545–571. https://doi.org/10.1016/0278-4343(90)90081-V

Uijttewaal, W. S. J., & Booij, R. (2000). Effects of shallowness on the development of free-surface mixing layers. *Physics of Fluids*, *12*(2), 392–402. https://doi.org/10.1063/1.870317

Vandekerkhove, E., Bertrand, S., Crescenzi Lanna, E., Reid, B., & Pantoja, S. (2020). Modern sedimentary processes at the heads of Martínez Channel and Steffen Fjord, Chilean Patagonia. *Marine Geology*, *419*, 106076. https://doi.org/10.1016/j.margeo.2019.106076

Variano, E. A., & Cowen, E. A. (2013). Turbulent transport of a high-Schmidt-number scalar near an air–water interface. *Journal of Fluid Mechanics*, *731*, 259–287. https://doi.org/10.1017/jfm.2013.273

Vennell, R. (2006). ADCP measurements of momentum balance and dynamic topography in a constricted tidal channel. *Journal of Physical Oceanography*, *36*(2), 177–188. https://doi.org/10.1175/JPO2836.1

Wallace, J. M. (2016). Quadrant analysis in turbulence research: History and evolution. *Annual Review of Fluid Mechanics*, *48*(1), 131–158. https://doi.org/10.1146/annurev-fluid-122414-034550

Wang, H., Bi, N., Wang, Y., Saito, Y., & Yang, Z. (2010). Tide-modulated hyperpycnal flows off the Huanghe (Yellow River) mouth, China. *Earth Surface Processes and Landforms*, *35*(11), 1315–1329. https://doi.org/10.1002/esp.2032

Weir, A. D., Wood, D. H., & Bradshaw, P. (1981). Interacting turbulent shear layers in a plane jet. *Journal of Fluid Mechanics*, *107*(1), 237-260. https://doi.org/10.1017/S0022112081001766

Weller, H. G., Tabor, G., Jasak, H., & Fureby, C. (1998). A tensorial approach to computational continuum mechanics using object-oriented techniques. *Computers in Physics*, *12*(6), 620-631. https://doi.org/10.1063/1.168744

Wells, M. G., & Dorrell, R. M. (2021). Turbulence processes within turbidity currents. *Annual Review of Fluid Mechanics*, *53*(1), 59–83. https://doi.org/10.1146/annurev-fluid-010719-060309

White, B. L., & Nepf, H. M. (2007). Shear instability and coherent structures in shallow flow adjacent to a porous layer. *Journal of Fluid Mechanics*, *593*, 1–32. https://doi.org/10.1017/S0022112007008415

White, B. L., & Nepf, H. M. (2008). A vortex-based model of velocity and shear stress in a partially vegetated shallow channel. *Water Resources Research*, *44*, W01412. https://doi.org/10.1029/2006WR005651

Willmarth, W. W., & Lu, S. S. (1972). Structure of the Reynolds stress near the wall. *Journal of Fluid Mechanics*, *55*(1), 65–92. https://doi.org/10.1017/S002211207200165X

Wolanski, E., Drew, E., Abel, K. M., & O'Brien, J. (1988). Tidal jets, nutrient upwelling and their influence on the productivity of the alga Halimeda in the Ribbon Reefs, Great Barrier Reef. *Estuarine, Coastal and Shelf Science*, *26*(2), 169–201. https://doi.org/10.1016/0272-7714(88)90049-2

Wright, L. D., Yang, Z. S., Bornhold, B. D., Keller, G. H., Prior, D. B., & Wiseman, W. J. (1986). Hyperpycnal plumes and plume fronts over the Huanghe (Yellow River) delta front. *Geo-Marine Letters*, *6*(2), 97–105. https://doi.org/10.1007/BF02281645

Yuan, Y., & Horner-Devine, A. R. (2017). Experimental investigation of large-scale vortices in a freely spreading gravity current. *Physics of Fluids*, *29*(10), 106603. https://doi.org/10.1063/1.5006176

Yue, W., Meneveau, C., Parlange, M. B., Zhu, W., Van Hout, R., & Katz, J. (2007). A comparative quadrant analysis of turbulence in a plant canopy. *Water Resources Research*, *43*. W05422.

https://doi.org/10.1029/2006WR005583

Zhang, R., Wu, B., & Zhang, B. (2023). Sensitivity analysis of a three-dimensional simulation of turbidity currents in a sloping flume. *Journal of Hydraulic Research*, *61*(1), 18–33. https://doi.org/10.1080/00221686.2022.2106590

Curriculum Vitae

Ph.D. candidate: **Haoran Shi**   Tel: (+41) 788485177

Faculty of Architecture, Civil and Environmental Engineering (ENAC)   Email: haoran.shi@epfl.ch

École Polytechnique Fédérale de Lausanne (EPFL), Switzerland

Haoran Shi - Google Scholar

Education

École Polytechnique Fédérale de Lausanne (EPFL), Switzerland

2019.09–2023.09 Ph.D.   Civil and Environmental Engineering

Okinawa Institute of Science and Technology, Japan

2019.01–2019.03 Research Intern   Fluid Mechanics Research Unit

Wuhan University, China

2016.09–2019.06 MPhil   Hydraulics and River Dynamics

Wuhan University, China

2012.09–2016.06 BEng   Port, Coast and River-Regulating Engineering

Research Interests

- Plunging process of hyperpycnal river plumes
- Hydrodynamics of ebb tidal jets
- Flow-vegetation interaction

Selected Papers

- **Shi, H.**, Negretti, M. E., Chauchat, J., Blanckaert, K., Lemmin, U., & Barry, D. A. Impacts of negative buoyancy on the development of shear layers and coherent structures at the interface between a hyperpycnal plume and the quiescent receiving ambient. *To be submitted*.
- **Shi, H.**, Negretti, M. E., Chauchat, J., Blanckaert, K., Lemmin, U., & Barry, D. A. Tracking the as yet known nearfield evolution of a shallow, neutrally-buoyant plane jet over a sloping bottom boundary. *Under review*, submitted to *Water Resources Research*.
- **Shi, H.**, Negretti, M. E., Chauchat, J., Blanckaert, K., Lemmin, U., & Barry, D. A. (2022). Unconfined plunging of a hyperpycnal river plume over a sloping bed and its lateral spreading: Laboratory experiments and numerical modeling. *Water Resources Research*, *58*, e2022WR032633. https://doi.org/10.1029/2022WR032633

- **Shi, H.**, Zhang, J., & Huai, W. (2023). Experimental study on velocity distributions, secondary currents, and coherent structures in open channel flow with submerged riparian vegetation. *Advances in Water Resources*, 173(104406). https://doi.org/10.1016/j.advwatres.2023.104406
- **Shi, H.**, Liang, X., Huai, W., & Wang, Y. (2019). Predicting the bulk average velocity of open-channel flow with submerged rigid vegetation. *Journal of Hydrology*, *572*, 213-225. https://doi.org/10.1016/j.jhydrol.2019.02.045
- Huai, W., **Shi, H.**, Yang, Z., & Zeng, Y. (2018). Estimating the transverse mixing coefficient in laboratory flumes and natural rivers. *Water, Air, & Soil Pollution*, *229*(8), 1-17. https://doi.org/10.1007/s11270-018-3893-z
- Huai, W., **Shi, H.**, Song, S., & Ni, S. (2018). A simplified method for estimating the longitudinal dispersion coefficient in ecological channels with vegetation. *Ecological indicators*, *92*, 91-98. https://doi.org/10.1016/j.ecolind.2017.05.015
- Li, S., **Shi, H.**, Xiong, Z., Huai, W., & Cheng, N. (2015). New formulation for the effective relative roughness height of open channel flows with submerged vegetation. *Advances in Water Resources*, *86*, 46-57. https://doi.org/10.1016/j.advwatres.2015.09.018

Conferences

- **Shi, H.**, Negretti, M. E., Chauchat, J., Blanckaert, K., Lemmin, U., & Barry, D. A. (2022). Three-dimensional process of laterally unconfined hyperpycnal current plunging. Thesis-2022 Two-phase modeling for sediment dynamics. Les Houches, France (Oral presentation).
- **Shi, H.**, Negretti, M. E., Chauchat, J., Blanckaert, K., Lemmin, U., & Barry, D. A. (2022). The surface pattern of unconfined, hyperpycnal river plume plunging. 7th IAHR Europe Congress. Athens, Greece (Oral presentation).
- **Shi, H.**, Huai, W. (2018). Flow Structure of open channel flow with partly submerged vegetation. 12th International Symposium on Eco-hydraulics. Tokyo, Japan (Oral presentation, Best Student Paper).

Skills

- Linux (Ubuntu), OpenFOAM (LES), python
- Experienced with PIV, ADV and LDV

Teaching experience

- Teaching assistant of Modflow course

Review Services

Reviewer of *Water Resources Management* and *Journal of Hydrodynamics, Ser B*